Dynamics and Fluctuations in Single-Electron Tunneling Devices

Analytical and Numerical Methods for Time-Dependent Quantum Transport in Interacting Nanosystems

Von der Fakultät für Mathematik, Informatik und Naturwissenschaften der RWTH Aachen University zur Erlangung des akademischen Grades eines Doktors der Naturwissenschaften genehmigte Dissertation

vorgelegt von

Niklas Dittmann, M. Sc. Physik
aus Oldenburg (Niedersachsen)

Berichter: Dr. Nicole Helbig
Prof. Dr. Janine Splettstoesser
Prof. Dr. Volker Meden

Tag der mündlichen Prüfung: 28. September 2018

Diese Dissertation ist auf den Internetseiten der Universitätsbibliothek online verfügbar.

Thesis for the degree of Doctor of Philosophy

Dynamics and Fluctuations in Single-Electron Tunneling Devices

Analytical and Numerical Methods for Time-Dependent Quantum Transport in Interacting Nanosystems

Niklas Dittmann

Department of Microtechnology and Nanoscience MC2
Chalmers University of Technology

Göteborg, Sweden 2018

Dynamics and Fluctuations in Single-Electron Tunneling Devices
Analytical and Numerical Methods for Time-Dependent Quantum Transport in Interacting Nanosystems

ISBN 978-91-7597-828-4
Doktorsavhandlingar vid Chalmers tekniska högskola
Ny series nr 4509
ISSN 0346-718X

Technical Report MC2
Series number 404
ISSN 1652-0769

Applied Quantum Physics Laboratory
Department of Microtechnology and Nanoscience – MC2
Chalmers University of Technology, SE-412 96 Göteborg, Sweden
Phone +46 (0) 31 772 1000

Doctoral Thesis

Department of Microtechnology and Nanoscience MC2
Chalmers University of Technology

Institute for Theory of Statistical Physics
RWTH Aachen University

List of Publications

1. *Clocked single-spin source based on a spin-split superconductor*
   Niklas Dittmann, Janine Splettstoesser, Francesco Giazotto
   New J. Phys. **18** 083019 (2016)

2. *Nonadiabatic dynamics in single-electron tunneling devices with time-dependent density-functional theory*
   Niklas Dittmann, Janine Splettstoesser, Nicole Helbig
   Phys. Rev. Lett. **120** 157701 (2018)

3. *Equilibrium finite-frequency noise of an interacting mesoscopic capacitor studied in time-dependent density functional theory*
   Niklas Dittmann, Janine Splettstoesser, Nicole Helbig
   J. Phys.: Conf. Ser. **969** 012145 (2018)

4. *Finite-frequency noise of interacting single-electron emitters: spectroscopy with higher noise harmonics*
   Niklas Dittmann, Janine Splettstoesser
   Phys. Rev. B **98** 115414 (2018)

5. *Dynamics of the Anderson impurity model: benchmarking a non-adiabatic exchange-correlation potential in TDDFT*
   Niklas Dittmann, Nicole Helbig, Dante Kennes
   Preprint: *arXiv:1810.00183* (2018)

6. *Nonadiabatic dynamics of a biased quantum dot with time-dependent density-functional theory*
   Niklas Dittmann, Nicole Helbig
   in preparation

Acknowledgements

Many people supported me during the writing of this thesis and made the last years a very enjoyable experience. First and foremost, I thank my wife Cornelia for her permanent motivation and love, the readiness to move with me to Gothenburg and Aachen and for countless discussions on physics. I thank my two supervisors, Janine Splettstoesser and Nicole Helbig, for the opportunity to work on exciting projects and to spend extended periods at two universities, and for providing a lot of helpful guidance into the scientific world. Then, I would like to thank all my colleagues from the Chalmers University for the inspirational environment, with special thanks to Jens Schulenborg, Maciek Misiorny and Patrick Holmvall. I am also very thankful for my friends Andreas Schindler and Laura Schüppel, who hosted me numerous times during my frequent visits in Gothenburg. I furthermore thank all my colleagues from the RWTH Aachen University, with special thanks to Jovan Odavic, Timo Reckling and Jan Rentrop, and I thank Volker Meden and his group for their hospitality. I also thank my coworkers from the Research Training Group 1995 for all inspirational discussions we had during the Friday seminars (with thanks to all volunteers who made these seminars possible). Further thanks go to my collaborators, Francesco Giazotto and Dante Kennes, for the possibility of working together on fascinating projects, and Neepa Maitra and Francesco Parmentier, for inviting me to New York and Paris for discussions. Finally, I thank my parents and all my family for their steady support, and I thank my friends, including many of the mentioned names as well as Philipp Comanns, Daniel & Sybille Ehrhard, David & Janika Irle, Claudia Komitsch, Florina Lachmann and all friends from Vinyard Aachen for all encouragement and for the distraction from physics they always joyfully provided.

Abstract

In recent years, it has been routinely achieved to build nanoscale electronic devices, which generate current pulses carrying only a single elementary charge. Realizations of these single-electron emitters are based on time-dependently driven quantum dots, on single-electron turnstiles built from superconductor/normal-metal hybrid structures, and also on nanosystems employing Lorentzian voltage pulses or surface acoustic waves. In this thesis, we present theoretical studies of single-electron transport in nanoscale devices of this kind. A central focus—besides extending the understanding of the physics in these devices—is the development and application of complementary theoretical methods. This multi-method approach allows us to highlight the assets and limitations of different theories, to compare the accuracy of results and the necessary analytical/computational efforts, and, most importantly, to find novel and fruitful method combinations.

In this thesis, we first propose a novel clocked spin-current source, which consists of a superconducting island tunnel coupled to two superconducting contacts via a ferromagnetic insulator layer. We demonstrate that this nanostructure can be operated as an emitter of a precise quantized spin current and we point out its working principle as well as its experimental feasibility.

The second device we analyze is a single-electron source, which is built from an interacting quantum dot with tunnel coupling to a single contact. The single-electron emission is triggered by a slow time-dependent gate-voltage driving, and we present a comprehensive study of the noise spectrum of the emitted current signal. The noise contains information on the system's excitation spectrum and its dynamics, and it also reveals signatures of Coulomb interaction. To derive the noise spectra over a large frequency range, we extend a

real-time diagrammatic perturbative method in the tunnel coupling to finite noise frequencies in the presence of the slow time-dependent drive. We then perform a harmonic decomposition of the noise spectra, present an interpretation of the noise in terms of individual fluctuation processes, and point out characteristic signatures for the interplay between Coulomb interaction and the time-dependent driving.

Third, we turn to time-dependent density-functional theory, which is a numerical method, and we transfer insights from the diagrammatic calculations to this theory. This novel combination of methods allows us to develop a nonadiabatic (i. e. time-nonlocal) approximation of this theory's exchange-correlation potential. We relate properties of the exchange-correlation potential to physical time scales of the electron dynamics and we apply it to obtain numerical time evolutions of single and multiple quantum dots coupled to a shared electron reservoir. In addition, we extend this combination of methods to another nanosystem, namely an interacting quantum dot coupled to two contacts and exposed to time-dependent gate and bias voltages. The results presented in this part of the thesis constitute a significant step towards the application of time-dependent density-functional theory for the description of charge dynamics in complex single-electron tunneling devices.

Deutsche Zusammenfassung

Heutzutage existiert die Technologie elektrische Ströme in Nanoschaltungen zu erzeugen, welche nur eine einzelne Elementarladung durch einen Festkörper transportieren. Typische Realisierungen dieser Einzel-Elektronen Quellen basieren auf zeitabhängig getriebenen Quantenpunkten, Einzel-Elektronen Schleusen bestehend aus supraleitenden und metallischen Hybridstrukturen, Spannungspulsen in Lorentz-Form oder akustischen Oberflächenwellen. Das Thema der vorliegenden Doktorarbeit sind theoretische Studien des Einzel-Elektronen Transportes in Nanostrukturen dieser Art. Darüber hinaus ist ein weiterer Schwerpunkt die Weiterentwicklung und Anwendung komplementärer Methoden der theoretischen Physik. Ich verwende in dieser Arbeit mehrere Methoden, um die Stärken und Schwächen verschiedener theoretischer Ansätze darzulegen und um die Qualität berechneter Ergebnisse und die dafür notwendigen analytischen und numerischen Kosten zu bewerten. Des Weiteren ermöglicht mir diese Herangehensweise neue und ergebnisreiche Methodenkombinationen zu entwickeln. Diese Doktorarbeit besteht aus mehreren eng miteinander verbundenen Teilen, welche ich im Folgenden kurz zusammenfasse.

Als erstes diskutiere ich eine neuartige Einzel-Elektronen Schleuse, bestehend aus einem supraleitenden Körnchen im Nanobereich und zwei ebenfalls supraleitenden makroskopischen Kontakten. Zwischen diesen drei Strukturen befinden sich zwei Tunnelbarrieren, gebildet aus einem ferromagnetischen Isolator. Ich zeige, dass diese hier neu vorgeschlagene Nanostruktur als Quelle eines quantisierten Spinstromes eingesetzt werden kann, erkläre das Arbeitsprinzip der Spinstrom-Erzeugung und verdeutliche die experimentelle Machbarkeit.

Die zweite von mir studierte Nanostruktur ist eine Einzel-Elektronen Quelle, basierend auf einem Quantenpunkt mit Tunnelkopplung an

ein einzelnes Elektronenreservoir. Der hier betrachtete Quantenpunkt emittiert einzelne Elektronen auf Grund einer angelegten elektrischen Steuerspannung mit langsamer Zeitabängigkeit. Eine informative Messgröße für dieses System ist neben dem emittierten Ladungsstrom das Rauschen dieses Stromes, welches ich in dieser Arbeit ausführlich analysiere. Das Rauschen beinhaltet Informationen über Anregungszustände des Systems, über die Dynamik und über die Auswirkungen von Coulomb Wechselwirkung. Um die verschiedenen Frequenzen im Rauschspektrum zu untersuchen, erweitere ich eine zeitaufgelöste diagrammatische Störungstheorie in der Tunnelkopplung zu endlichen Rauschfrequenzen, unter Berücksichtigung der zeitabhängigen Steuerspannung. Anschließend zerlege ich das Rauschspektrum in seine Harmonische, beschreibe eine Interpretation des Rauschens in Form von individuellen Fluktuationsprozessen und zeige charakteristische Merkmale für das Zusammenspiel zwischen Coulomb Wechselwirkung und Zeitabhängigkeit.

Als Drittes wende ich mich der zeitabhängigen Dichtefunktionaltheorie zu und transferiere Einsichten aus den vorherigen diagrammatischen Rechnungen zu dieser numerischen Methode. Diese neuartige Methodenkombination erlaubt es mir, eine nichtadiabatische (d. h. zeitnichtlokale) Näherung des Austausch-Korrelations-Potentials dieser Theorie zu entwickeln. Ich identifiziere physikalische Zeitskalen der Elektronendynamik in dem hergeleiteten Potential und demonstriere die Anwendung des Potentials, um numerische Zeitpropagationen von einzelnen und mehreren Quantenpunkten mit Kopplung an ein gemeinsames Elektronenreservoir zu berechnen. Darüber hinaus erweitere ich die beschriebene Methodenkombination auf ein weiteres Nanosystem, bestehend aus einem Quantenpunkt mit Tunnelkopplungen an zwei benachbarte Kontakte. Hierbei betrachte ich den Quantenpunkt in der Gegenwart von zeitabhängigen Steuer- und Bias-Spannungen. Die Ergebnisse der hier dargelegten Methodenkombination sind ein signifikanter Fortschritt im Hinblick auf zukünftige numerische Dichtefunktional-Simulationen der Ladungsdynamik in komplexen Einzel-Elektron Tunnel-Anordnungen.

Contents

1 Introduction

In 1911, Millikan's oil-drop experiment verified that electric charge is quantized into individual electrons [1, 2]. In electric circuits, however, this quantization did not play a major role for the next 70 years, until a breakthrough experimental work was published by Fulton and Dolan in 1987 [3]. By measuring current-voltage curves of a nano-sized aluminum island, coupled to several contacts by aluminum-oxide tunnel junctions, they found signatures attributed to the charging (or discharging) of the island by a single electron. Over the following decades, and facilitated by the steady progress in semiconductor and lithographic technologies, we witnessed many advances in the controlled manipulation of *single electrons* in electric circuits on the nanoscale. It is nowadays possible to build nanoscale devices, which emit electrons one-by-one into a mesoscopic conductor [4–7]. The first single-electron emitters were reported in the 90's based on metallic islands [8, 9] as well as semiconductor quantum dots [10].[1] Geerligs et al. [8] realized a single-electron turnstile by employing an array of four tunnel junctions, which defined three metallic islands. In analogy to the oil droplets of Millikan's experiment, the metallic islands hereby represent nearly isolated regions in the nanoscale circuit, which are largely occupied by integer numbers of electrons [16–18]. Charge transfer occurs via electron tunneling across the junctions [3]. Importantly, each tunnel junction also resembles a tiny capacity, and, as a consequence, different charge configurations in nanostructures of this kind can be separated by as much as several meV, which equals a temperature of roughly

[1] Quantum dots are artificial nanostructures which confine electrons in all three dimensions (the number of free electrons ranges between a few to a few thousand). They can be realized, e. g., in semiconductor setups [11–14] or with nanotubes [15].

10 Kelvin [4]. Hence, at sufficiently low temperatures, the tunneling even of a single electron can be energetically blocked (Coulomb blockade). In the experiment by Geerligs et al., the energy required for periodic changes in the charge configuration is provided by applying a bias voltage across the array as well as an ac gate voltage to the middle island. During the ac drive, the occupation of the middle island first increases by one electron coming from the left hand side, and then decreases by one electron emitted to the right. The additional left and right islands thereby serve as energy filters, which suppress any steady-state current through the device. This turnstile principle leads to a *quantized* current, $I = ef$, with the driving frequency f of the ac gate voltage, and the elementary charge e [4, 8].

The first single-electron emitters had several drawbacks, most importantly a low precision due to higher-order tunneling and a poor energy resolution of the emitted electrons [4]. Achieving a high precision, in combination with a large current output, is crucial for their application as ultra-precise current sources to define a new SI standard for the ampere [4, 19, 20]. Furthermore, having control over the energy of emitted electrons is relevant, e. g., for flying-qubit applications, which anticipate to use individual coherently-transported electrons as carriers of quantum information [6]. Several new and improved device geometries emerged to adress these issues. For example, in 2007, Feve et al. realized an on-demand ac single-electron source [21] built from a quantum dot coupled to a single contact [22] and driven by a time-periodic gate voltage. The setup is based on a two-dimensional electron gas (2DEG), which manifests at GaAsAl/GaAs heterojunctions. An illustration is shown in Fig. 1.1 (a). Since the experiment is conducted in the integer quantum Hall regime, where the propagation of emitted electrons (and holes) is confined into one-dimensional edge channels due to a strong magnetic field, it allows for novel electron quantum-optics experiments [23–28]. In the same year, Blumenthal et al. reported a single-electron pump [29], again based on a 2DEG setup. In their device, single-electron emission is achieved via a temporal quantum dot, which is defined by applying several gate voltages to a mesoscopic conductor, see Fig. 1.1 (b). In each period of an ac drive, the quantum dot is generated and filled from one side of the conductor, and then annihilated and emptied towards the other side, see also Ref. [30–34] (and Ref. [35] for a device based on sili-

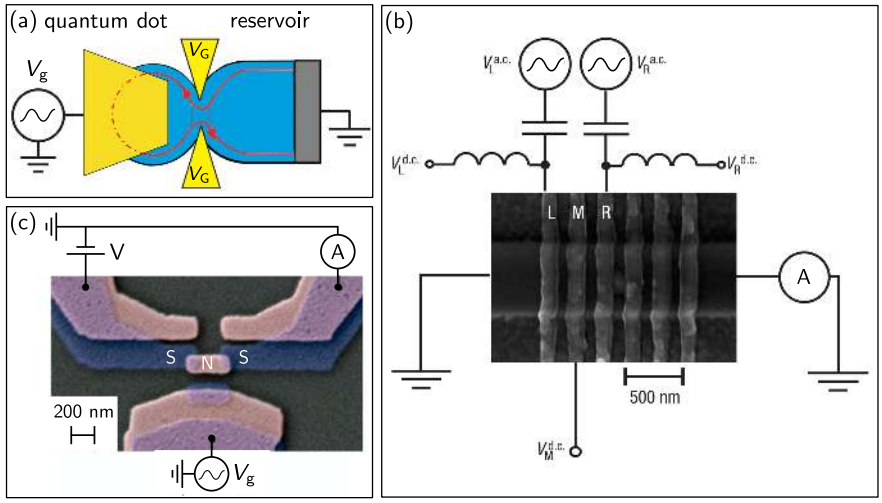

Figure 1.1: Selection of nanoscale devices which emit single electrons: (a) Sketch of a 2DEG quantum dot coupled to an electron reservoir by a weak tunnel barrier (a quantum-point contact defined by the voltage V_G); (b) Scanning electron-microscope (SEM) image of a single electron pump, where a temporal quantum dot is created via three gates (L,M,R) placed on top of a quantum wire. (c) SEM image of a single-electron turnstile, consisting of a normal-metal island (N) and two superconducting (S) contacts (current in (b)-(c) measured at A); The shown images are adapted from Refs. [21, 29, 37], reprinted with permission from (a) AAAS and (b)-(c) Springer Nature.

con). A year later, in 2008, Pekola et al. implemented an improved version of the single-electron turnstile principle, by employing a single metallic island coupled to two superconducting contacts [36–38], as shown in Fig. 1.1 (c). The gap in the BCS density-of-states of the superconductors hereby suppresses error mechanisms stemming from higher-order tunneling [39–42], which limit the precision in metallic turnstile setups. Note that further recently realized single-electron sources exploit, e. g., Lorentzian-shaped voltage pulses [43], surface acoustic waves [44, 45], a quantum dot coupled to two superconductors [46] or two atoms placed in a nanojunction [47].

In this thesis, we present comprehensive theoretical analyses of the electron dynamics in several of these single-electron sources. A particular focus, besides investigating physical questions, is the application of multiple theoretical approaches. This not only allows us to compare the performance of different theories in single-electron transport calculations, but it also makes it possible to find novel and fruitful method combinations, as we demonstrate throughout this thesis.

To characterize single-electron emitters, it is useful to study the generated time-dependent current and also its fluctuations, the current noise [48–50]. The latter, which is a quantity of recent theoretical [51–55] as well as experimental efforts [56, 57], is, e. g., relevant to identify the precision of a quantized electron source. Over the last decades, many different theoretical methods have been developed to calculate time-dependent quantum-transport properties, such as the current and the noise, of these systems. Prominent examples are given by the (Floquet) scattering-matrix theory [58–60], the non-equilibrium Green's-function formalism [61–63] and perturbation theory in the tunnel coupling [64–68].

It is important to emphasize that the choice to apply a specific method to a problem at hand always includes a trade-off. All theoretical approaches differ in their regime of applicability, the costs of analytical or numerical calculations, and the achievable accuracy. To provide an example of this issue, let us begin with Floquet scattering-matrix theory [58–60]. This theory is applicable to a wide range of systems and parameters, but it is a single-particle theory, and thus cannot describe strong electron-electron repulsion. On the contrary, interaction is well described when we apply perturbation theory in the tunneling [64–68], but the performed perturbative expansion is only justified when the system's temperature is sufficiently large compared to the tunnel-coupling strength. A possible path to access lower temperatures is provided by renormalization-group techniques [69], e. g., the time-dependent density-matrix renormalization group (td-DMRG) [70–73], which excels in accuracy. However, as we will see in Sec. 8.2.2, this method is numerically very demanding, which limits its applicability.

Another quantum many-body method, which is less prominent in single-electron transport, is given by time-dependent density-functional theory (TDDFT) [74]. This theory is the time-dependent extension of

density-functional theory [75, 76], one of the most popular methods to analyze electronic properties of condensed matter systems [77]. For time-dependent quantum transport, TDDFT is particularly promising, because its simple numerical implementation offers the prospects of analyzing complex nanoscale devices, which are not (or hardly) accessible with the majority of theoretical methods [78, 79], see also Ref. [80]. The reason for its numerical efficiency is that TDDFT simulates the electron dynamics by an effective system of noninteracting electrons [81], thanks to the so-called exchange-correlation (XC) potential. The application of TDDFT to simulate nanoscale devices is mainly hindered by the fact that approximations of the XC potential are barely developed to a stage of practical use in this field [82]. However, we note that TDDFT is successfully applied in other branches of physics, e. g., to calculate electronic excitations or to investigate molecules in strong laser fields [78, 79, 83].

To introduce the project presented in this thesis, we emphasize that it consists of two parts, which are closely connected. In the first part, we provide profound theoretical studies of two experimentally relevant quantized electron emitters. These studies contribute to the understanding of the physics in these devices and help to guide future experiments. In particular, we begin by proposing a novel superconducting turnstile device, which not only produces a quantized charge but also a quantized spin current [84]. We discuss its working principle as well as possible error sources for the spin-current emission. By setting up a master-equation calculation, which is a perturbative approach in the tunnel coupling, we derive the emitted charge and spin currents and discuss experimental feasibility of the device. We then turn to a second nanosystem, namely a single-electron source based on a quantum dot coupled to a single contact, see Ref. [21]. Here, we apply a real-time diagrammatic perturbative approach in the tunnel coupling [64–68], and calculate finite-frequency current noise spectra [49, 50] in the presence of a slow time-dependent gate-voltage driving as well as Coulomb repulsion on the quantum dot [55]. This extends previous noise studies, which either considered no interaction [52, 53] or zero-frequency noise averaged over the (periodic) driving [54]. Importantly, the noise of a time-dependent system is a function of frequency and time, and we show that a harmonic decomposition of this time dependence provides a useful spectroscopic

tool to investigate specific fluctuation processes. Additionally, we find that the combination of time-dependent driving and Coulomb interaction leads to a unique noise feature, which is a non-vanishing first noise harmonic at zero noise frequency. By also performing a noise calculation in Floquet scattering-matrix theory, we validate the diagrammatic results in the limit of vanishing interaction.

In the second part, we switch to TDDFT and investigate how insights from the prior perturbative calculations can be used to develop and improve XC potentials. The goal of this part is to push forward TDDFT simulations of time-dependently driven single-electron tunneling devices. Specifically, we derive a XC potential based on a master-equation description of the electron dynamics in the previously analyzed single-contact quantum dot. The derived XC potential turns out to include a time-nonlocal dependence on the quantum-dot electron density [80, 85]. This is a major step forward, because, to our knowledge, all previous XC approximations for this system neglect time non-locality [86–92] (also, note that time non-locality is neglected in almost all available XC potentials in TDDFT in general). We provide an extensive study of the derived XC potential in the nonlinear- and linear-response regime, and show that it contains physical charge-relaxation time scales. In TDDFT simulations of the single-electron source, we find that the time-nonlocal density dependence is crucial for the dynamics. Furthermore, the TDDFT data matches results obtained with td-DMRG, which emphasizes that the developed TDDFT approach is highly accurate on long time scales as well as in the regime of transient dynamics. We finish by discussing the prospects of TDDFT for more complex devices, in particular, by studying many quantum dots coupled to a shared electron reservoir and a quantum dot coupled to two contacts and exposed to possibly time-dependent gate and bias voltages.

Note that a central component in both parts of this thesis is method development. In part one, for the spin-current source, we derive a master-equation description of the charge and spin currents in the proposed nanodevice, and for the noise calculations of quantum-dot based single-electron emitters, we extend the real-time diagrammatic approach to simultaneously include slow time-dependent driving and finite noise frequencies. In part two, we explain the application of TDDFT for single-electron tunneling devices and present a novel way

to include memory dependence in employed XC potentials.

This thesis is structured in the following way. In Chap. 2, we discuss the single-electron source based on a quantum dot and introduce the Anderson Hamiltonian, which we employ for its theoretical description. Besides that, we outline the working principle of the hybrid single-electron turnstile reported in Refs. [36, 37], where a single metallic island is coupled to two superconducting contacts. The latter provides a background for the proposed single-spin source studied in Chap. 4. Prior to that, in Chap. 3, we introduce two theoretical techniques, namely real-time diagrammatic perturbation theory and TDDFT, and we compare both methods with respect to their performance in time-dependent quantum-transport calculations. The diagrammatic method is applied in Chap. 5, to derive finite-frequency noise spectra of the time-dependently driven interacting quantum dot. The results of these calculations are presented in Chap. 6. We then turn to TDDFT and, in Chap. 7, begin by explaining a computational implementation of TDDFT for single-electron tunneling devices. The derivation of the time-nonlocal XC potential as well as its application in TDDFT simulations are outlined in Chap. 8, and an extension for a two-contact quantum dot is discussed in Chap. 9. We conclude this thesis in Chap. 10, where we also collect future research questions opened up by this work. The appendices A and B present technical details, respectively, related to the calculations of Chaps. 4 and 5.

Finally, we note that some results presented here are (or will be) published in scientific journals, see the list of publications on page vii. All published sections are indicated as such.

2 Nanoscale Devices as Quantized Electron Emitters

In this chapter, which provides the background for the theoretical studies presented later, we introduce two mesoscopic systems and outline their working principle as quantized electron emitters. First, a single-electron source based on a quantum dot with weak tunnel coupling to a metallic contact is explained in Secs. 2.1 and 2.2. This device is studied in Chaps. 5-6, where we investigate its finite-frequency current noise. It also serves as an instructive example in Chaps. 7-8, where we apply time-dependent density-functional theory to describe electron dynamics in single-electron tunneling devices. Second, a charge turnstile realized with a hybrid superconductor/normal-metal single-electron transistor (SET) is outlined in Sec. 2.3. This device sets the stage for a modified superconducting SET with spin-active elements, which we propose as a nanodevice for accurate spin-current emission in Chap. 4.

2.1 Quantum dots and the Anderson model

The first mesoscopic system we introduce is motivated by single-electron emitters based on quantum dots[1] [21, 29]. In this section, we describe the system and motivate the Anderson model for its theoretical description, and we discuss single-electron emission and

[1] A quantum dot denotes an artificial nanostructure which confines electrons in all three dimensions. See Refs. [11–15] and references therein for an introduction.

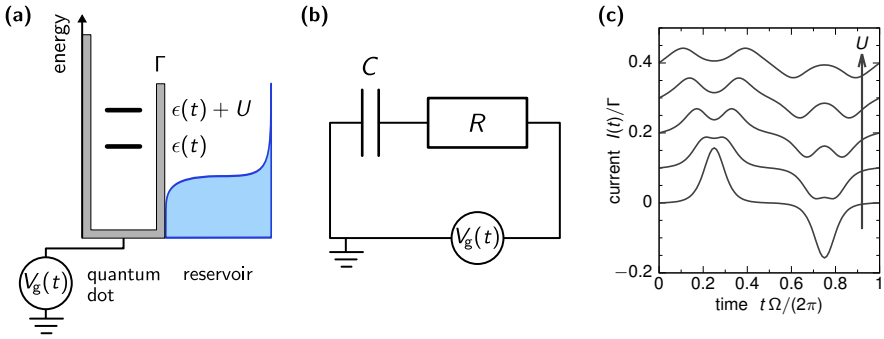

Figure 2.1: (a) Sketch of a (spin-symmetric) quantum dot tunnel coupled to an electron reservoir with strength Γ. Shown is a single quantum-dot energy level, $\epsilon(t)$, where U denotes an on-site interaction. (b) The classical analog of (a) is the RC circuit with capacitance C and resistance R. (c) Current in the reservoir of setup (a) for a slow harmonic gate-voltage driving and interaction strengths $U/(2\delta\epsilon) = 0, 0.2, ..., 0.8$, plotted as bottom to top lines, shifted for visibility. Further parameters are $\beta = 1/(2\Gamma)$, $\epsilon(t) = -U/2 + \delta\epsilon\cos(\Omega t)$, $\delta\epsilon = 10\Gamma$ and $\Omega \ll \Gamma$, see Eq. (3.6).

related experiments in the next Sec. 2.2. The system we aim to study consists of an interacting quantum dot, which is tunnel coupled to a single contact acting as an electron reservoir, see the illustration in Fig. 2.1 (a).[2] The single reservoir is in thermal equilibrium with the surrounding environment and we assume a temperature lower than the level separation of the quantum dot. Therefore, we expect the discreteness of the quantum-dot's energy spectrum to significantly influence physical properties. As indicated in Fig. 2.1 (a), the positions of the quantum-dot energy levels, with respect to the Fermi energy of the reservoir, can be shifted by a gate voltage, $V_g(t)$. This leads to electron tunneling between the reservoir and the quantum dot, and the dot can thus be charged or discharged. In other words, the system acts as a *mesoscopic capacitor* or quantum capacitor [93–95]. The classical analog of the setup in panel (a) is the RC circuit shown

[2]Note that in this common illustration, the reservoir is sketched via a Fermi function, describing the occupation of the reservoir's single-particle states, while the indicated quantum-dot energies are many-particle energies of a decoupled dot.

in panel (b). In this classical setup, the charging and discharging dynamics is described by exponential functions, with the RC time scale given by $\tau_{\mathrm{RC}} = RC$. Importantly, in contrast to the *macroscopic* (geometric) capacitor in panel (b), electron dynamics in the mesoscopic capacitor in (a) is governed by quantum mechanics, which leads to surprising phenomena.[3] For example, in Ref. [93] it is derived that the capacity of the mesoscopic capacitor becomes sensitive to the density-of-states (DOS), and that the resistance becomes a universal quantity at zero temperature, taking the value[4] of $h/(4e^2)$ [22, 94, 96].

We now introduce a theoretical model for this setup. We hereby make the Born-Oppenheimer approximation and assume that the electron dynamics is separable from the dynamics of the atomic nuclei, due to a separation of the respective time scales. Therefore, our model only takes the electronic degrees-of-freedom (including spin) into account. Besides that, we consider the common experimental situation that electrons are fully screened inside the reservoir, i. e., Coulomb repulsion is only included for electrons occupying the quantum dot. We exploit that the level separation of the quantum dot is large compared to the reservoir temperature, and describe the quantum dot by a single energy level, which can be occupied by zero, one or two electrons. A standard model for this setting is the Anderson Hamiltonian,

$$H(t) = H_{\mathrm{dot}}(t) + H_{\mathrm{res}} + H_{\mathrm{T}} \tag{2.1}$$

with

$$H_{\mathrm{dot}}(t) = \sum_{\sigma} \epsilon_{\sigma}(t) d_{\sigma}^{\dagger} d_{\sigma} + U d_{\uparrow}^{\dagger} d_{\uparrow} d_{\downarrow}^{\dagger} d_{\downarrow}, \tag{2.2a}$$

$$H_{\mathrm{res}} = \sum_{k,\sigma} \epsilon_k c_{k\sigma}^{\dagger} c_{k\sigma}, \tag{2.2b}$$

$$H_{\mathrm{T}} = \sum_{k,\sigma} \gamma c_{k\sigma} d_{\sigma}^{\dagger} + \mathrm{H.\,c.}\ . \tag{2.2c}$$

In Eqs. (2.2), the quantum-dot level is given by $\epsilon_{\sigma}(t)$ with spin index $\sigma = \uparrow / \downarrow$ and creation/annihilation operators $d_{\sigma}^{\dagger}/d_{\sigma}$. For the

[3] The quantities R and C for the quantum system sketched in Fig. 2.1 (a) are defined by performing a low-frequency expansion of the admittance and comparing the outcome to the low-frequency admittance of the classical setup shown in panel (b), i. e., $G(\omega) = -i\omega C + \omega^2 C^2 R$, see also Sec. 8.3.5.

[4] For spinless electrons, the universal resistance is $h/(2e^2)$.

spin-symmetric case, $\epsilon_\uparrow(t) = \epsilon_\downarrow(t)$, we write $\epsilon(t)$ instead of $\epsilon_\sigma(t)$. The quantum-dot level is a time-dependent quantity due to the presence of the gate voltage, $V_\mathrm{g}(t)$, see Fig. 2.1 (a). Here, we assume that the dot level depends linearly on the gate voltage, $\epsilon_\sigma(t) = \bar{\epsilon}_\sigma - \alpha V_\mathrm{g}(t)$, with $\alpha > 0$ and where $\bar{\epsilon}_\sigma$ defines the level position for zero gate voltage. The Coulomb repulsion between electrons for the case of double occupation of the quantum dot is modeled as a (constant) on-site interaction [97], included by the Hubbard-interaction term with strength U. For the reservoir, we include a single energy band, ϵ_k, with momentum k and creation/annihilation operators $c^\dagger_{k\sigma}/c_{k\sigma}$. The equilibrium occupation of the reservoir is characterized by the Fermi function, $f^+(\epsilon) = 1/(1 + e^{\beta\epsilon})$, with the inverse temperature[5] β and with $e, \hbar$ and k_B set to one throughout this thesis unless otherwise indicated. The Fermi energy of the reservoir is in the following used as a reference point for the definition of energy values. Tunneling between the quantum dot and the reservoir is described by H_T in Eq. (2.2c), where γ is the (spin-independent) tunnel coupling, which we consider as energy independent on the scales relevant for the dynamics (wide-band limit). The tunnel-coupling strength is defined as $\Gamma = 2\pi|\gamma|^2\nu_0$, with the DOS in the reservoir ν_0. We always focus on the case of weak reservoir-dot coupling, $\beta\Gamma \ll 1$, where the energy levels of the quantum dot are only weakly broadened by the coupling to the reservoir. Furthermore, we assume strong-correlation effects ('Kondo physics') to be absent, i. e., we consider $\beta^{-1} \gg T_\mathrm{K}$ with T_K being the Kondo temperature.

2.2 Quantum dots as single-electron emitters

The single-contact quantum dot introduced in the previous section can be operated as a nanoscale quantum device, which generates on-demand single-electron pulses in the nearby reservoir [4, 6, 21, 98]. This is illustrated in Fig. 2.1 (c), showing time-dependent currents[6] emerging for a slow harmonic drive of the gate voltage. Without interaction, the system periodically absorbs and emits two electrons per pulse during the drive (lowest line), where the pulse broadening is caused by the temperature. The on-site interaction U separates the

[5] In this work, T refers to driving periods and β to inverse temperatures.

[6] The calculation of the current is postponed to Sec. 3.1.

current pulses into two peaks each, corresponding to the first and the second electron being absorbed or emitted (upper lines).

A single-electron emitter based on this setup has first been realized by Feve et al. [21], see also Fig. 1.1 (a). In this experiment, a (semiconductor) quantum dot is created by confining a two-dimensional electron gas, which builds up at GaAsAl/GaAs heterojunctions, in space. The confinement is achieved by applying electrostatic fields via top gates, which deplete the electron gas in the volume below the gates. The experiment is carried out in the quantum Hall regime, where a strong magnetic field perpendicular to the electron gas constrains the electron propagation into one-dimensional channels along the edges. This pioneering work triggered theoretical investigations into the role of Coulomb interaction[7] in similar devices, see e. g. [27, 99, 100]. Further motivation was provided by the realization of single-electron emitters based on temporary quantum dots [29], in which Coulomb repulsion plays a major role [Fig. 1.1 (b)]. As noted in the introduction, these on-demand single-electron emitters [21, 29, 43] are relevant as ultra-precise charge-current sources for metrology [4, 31, 32] and for experiments in the emerging fields of electron quantum-optics [23–28] and flying qubits [6]. For these and further applications, a detailed understanding of the electron dynamics in single-electron emitters of this kind is important. We note that an insightful quantity, e. g., to characterize the emission process and the accuracy of a device, is provided by the charge-current noise [48–50, 56, 57]. This is discussed further in Chaps. 5-6, where we present a comprehensive study of the current noise of the introduced single-electron emitter and the influence of Coulomb interaction on its noise spectra.

2.3 Hybrid single-electron turnstile

Controlled single-electron emission in a solid-state setup is also realized in experiments based on hybrid superconductor/normal-metal single-electron transistors (SETs) [4, 36, 37]. The hybrid SET consists of a nano-sized metallic grain, known as an *island*, which is coupled to two adjacent (BCS-type) superconducting contacts, see Fig. 1.1 (c).

[7] Note that Coulomb interaction on the quantum dot is reasonably assumed to be screened by a large metallic top gate in the specific setup used in Ref. [21].

The energy landscape is sketched in Fig. 2.2 (a), which also shows the gapped BCS DOS of the superconducting parts with (momentum-independent) gap Δ, as well as different charge configurations of the metallic island. The working principle of this electron emitter is related to the turnstile concept of the purely metallic setup employed by Geerligs et al. [8]: during an ac drive of the gate voltage, the island is first charged by one electron tunneling onto the island from the left contact, and later discharged by one electron leaving the island towards the right. This is achieved, because tunneling in the 'wrong' direction is strongly suppressed, as we explain below. Prior to that, let us emphasize that the level spacing on the island is typically significantly smaller than the level spacing of the semiconductor quantum dots discussed previously. Still, the island can obtain a discrete many-particle energy spectrum with well separated energies, thanks to the presence of Coulomb interaction. Here, we make use of the constant-interaction model [97, 101], and parametrize the Coulomb repulsion between an additional island electron and all other electrons in the system by defining the total capacitance of the island C_Σ. Due to the tiny size of the island, its capacitive coupling with the surrounding environment is small, which results in a large charging energy, $E_\mathrm{c} = e^2/(2C_\Sigma)$. In a Hamiltonian-description of the electronic degrees-of-freedom (see Chap. 4), we include this charging effect in terms of

$$H_\mathrm{c}(t) = E_\mathrm{c}\left[\hat{n} - n_\mathrm{g}(t)\right]^2, \tag{2.3}$$

where $\hat{n}$ is the charge-number operator of the island and $n_\mathrm{g}(t)$ is defined as the offset charge number, which depends linearly on the gate voltage. At sufficiently low temperatures, $\beta E_\mathrm{c} \gg 1$, the charging energy dominates the dynamics and, e. g., leads to the phenomenon of Coulomb blockade, where a significant bias voltage is necessary to start a current flow through the system [3, 16–18]. The characteristic Coulomb-diamond pattern, emerging for the current as a function of bias and gate voltages, is illustrated in Fig. 2.2 (b) for a SET with metallic contacts and in Fig. 2.2 (c) for the hybrid SET discussed here. In panel (c), compared to panel (b), the superconducting contacts result in enlarged Coulomb-blockade regions, the additional white areas, where the two neighboring charge states are both stable. The regions appear due to the sequential electron-tunneling being strongly suppressed by the gap in the DOS (note that higher-order tunneling

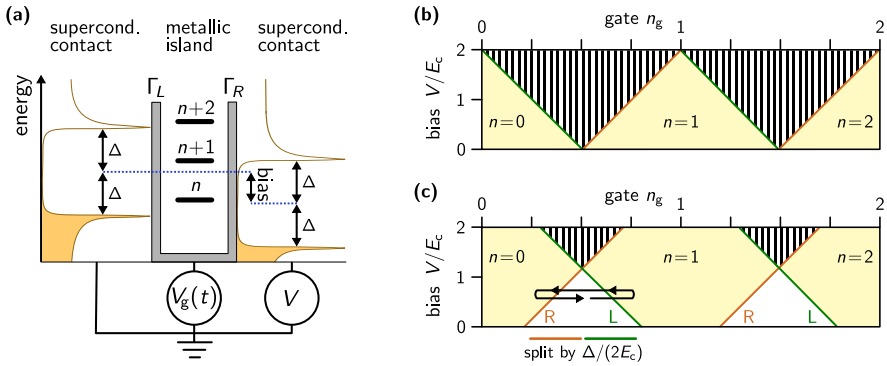

Figure 2.2: (a) Energy landscape of a hybrid SET: a metallic island with charge number n is tunnel coupled to two superconducting contacts, whose DOS is of BCS-type with gap Δ. (b) Sketch of the current for a SET with metallic contacts, showing the Coulomb-diamond pattern: the current is suppressed outside the shaded regions. (c) Similar to (b) for the hybrid SET shown in (a): in the white regions, both neighboring charge states are stable; the black arrow indicates the operation mode as a charge turnstile [4].

leads to small residue currents even in the Coulomb-blockade regions). Only when the green/red lines in panel (c) are crossed towards the yellow regions, e. g., by adjusting the gate voltage, the island charge configuration changes by one. Importantly, the responsible sequential-tunneling event is only energetically allowed at the left *or* the right contact, as indicated by R and L. This has been exploited in an experiment by Pekola et al. [36, 37], who set up a charge turnstile by applying a constant bias and a harmonic gate voltage to the hybrid SET, see the black arrow in Fig. 2.2 (c).[8] In each period of the drive the charge state changes periodically between zero and one, and a single electron is transfered across the device. The consequence is a very precise charge current, $I = ef$, where f is the driving frequency. Nanodevices of this kind are currently in demand for metrological purposes [4, 36, 37], where they are anticipated to provide a new current standard [19, 20].

[8] Single-electron turnstiles require an applied bias voltage to rectify the generated current, in contrast to electron pumps, see, e. g., Refs. [21, 29–32, 35, 47, 102].

To study the electron dynamics in nanodevices similar to the ones described here, we continue, in the next chapter, by introducing the theoretical techniques which we use in this thesis.

3 Time-Dependent Quantum Transport

The focus of this thesis are single-electron transport setups, where a nanoscale constituent (quantum dot, island) is weakly tunnel coupled to one or multiple macroscopic reservoirs. For nanosystems of this kind, we are interested in analyzing the electron dynamics in the presence of Coulomb interaction as well as a time-dependent driving of system parameters. We now introduce the methods which we use in the theoretical studies presented in this thesis, and we provide the theoretical background, which is helpful to follow the discussion in the subsequent chapters.

To analyze the electron dynamics in a nanoscale device, we consider the electronic degrees-of-freedom only (including spin), see Chap. 2, and we describe the electrons using quantum mechanics. Let us first remind ourselves that the time evolution of a quantum system is given by the von Neumann equation,

$$i\partial_t \rho(t) = [H(t), \rho(t)]\,, \tag{3.1}$$

where the (possibly mixed) quantum state at time t is described by the density matrix $\rho(t)$. In this equation, the Hamiltonian $H(t)$ contains the description of the whole system, which we consider to consist of a time-dependently driven nanoscale part, macroscopic electron reservoirs and tunneling in between: $H(t) = H_{\mathrm{nano}}(t) + H_{\mathrm{res}} + H_{\mathrm{T}}$, compare also to Eq. (2.1). A crucial assumption for many theoretical methods applied to Eq. (3.1) is the existence of an initial time t_0, at which the nanoscale part and the reservoirs are uncoupled and the reservoirs in thermal equilibrium. The initial state can then be

written as $\rho(t_0) = \rho_{\mathrm{nano}}(t_0) \otimes \rho_{\mathrm{res}}^{\mathrm{eq}}$, where $\rho_{\mathrm{nano}}(t_0)$ denotes the initial configuration of the nanoscale part and $\rho_{\mathrm{res}}^{\mathrm{eq}} = e^{-\beta H_{\mathrm{res}}}/\mathrm{Tr}\left[e^{-\beta H_{\mathrm{res}}}\right]$, with inverse reservoir temperature β.

A strategy to obtain an observable, e. g., the time-dependent charge current in reservoir α, is to first derive the density matrix $\rho(t)$ with Eq. (3.1), and afterwards to evaluate the trace, $\langle I_\alpha(t)\rangle = \mathrm{Tr}\left[I_\alpha \rho(t)\right]$, with the current operator I_α (see below). However, the problem which forbids a straightforward solution of Eq. (3.1) is that the many-particle Hilbert space of the considered quantum system is very large (or even infinite) and a treatment of the full density matrix thus becomes impractical. Furthermore, if many-body interactions are present, less complicated descriptions of the time evolution in terms of single-particle wave functions cannot be applied.[1]

To describe the complex physics of these systems, it is typically necessary to choose between complementary theoretical approaches, which describe different parameter regimes and also differ in analytical and numerical complexity. In this thesis, we apply the following two theoretical methods of quantum many-body physics. First, we consider a real-time diagrammatic technique, which is based on a partial trace over the reservoir degrees-of-freedom and a perturbative expansion in the tunnel Hamiltonian, H_{T}. The partial trace strongly reduces the degrees-of-freedom of the system which have to be treated directly, and results in a time-nonlocal kinetic equation for the reduced density-matrix of the nanoscale constituent. Note that this equation [given in Eq. (3.4) for the system of Eq. (2.1)] is still a general description of the dynamics, because it is derived from Eq. (3.1) without any approximation [64–67]. In order to employ this approach further, one possibility is to subsequently perform a perturbative expansion in the tunnel coupling, as done in this thesis. Second, we turn back to the time evolution of the whole system and simulate it by numerically time propagating an auxiliary system of noninteracting electrons in the framework of time-dependent density-functional theory (TDDFT). This auxiliary system is build in a way that the time-dependent electron density is identical to the density in the interacting system. Although we deal with a single-particle Hilbert space in TDDFT, we additionally

[1] For noninteracting systems, a convenient method for time-dependent quantum-transport calculations is given by the Floquet scattering-matrix theory, see Sec. 5.5.

have to reduce the degrees-of-freedom to make the method numerically feasible, which means that we only include a discrete and finite number of states for the reservoirs, see Chap. 7.

We now introduce the methods real-time diagrammatic perturbation theory and TDDFT in Secs. 3.1 and 3.2, respectively. Their differences as well as their strengths and limitations are compared in Sec. 3.3. Note that we base the discussion in the following sections on the single-electron emitter built from a quantum dot, which is an instructive example and also a main focus of this thesis, see Sec. 2.1.

3.1 Real-time diagrammatic method

3.1.1 Kinetic equation for occupation and current

We begin with the Hamiltonian of the single-level Anderson model in Eq. (2.1) and calculate the quantum-dot occupation and the charge current which emerges due to a time-dependent gate voltage. Calculations of further observables (in particular the current noise) are postponed to later chapters. To evaluate the occupation and the current, we now explain a non-equilibrium real-time diagrammatic technique, which is based on a perturbative expansion in the reservoir-dot coupling strength. This method has been developed and mainly employed for stationary systems by Schoeller, Schön, König and Schmid in Refs. [64–66]. It has later been extended to systems with a slow periodic time dependence by Splettstoesser et al. [67]. Note that the applied series expansion in the reservoir-dot coupling is reasonable for weak coupling and high temperature, $\beta\Gamma \ll 1$, as considered here, see Sec. 2.1. In this regime, successive tunnel events between the dot and the reservoir become independent of each other (sequential tunneling), which means that leading terms in this series already capture the system's dynamics. Corrections to the sequential-tunneling picture can be included by calculating higher orders in the expansion series (e. g. Ref. [99]).

The time evolution of the quantum dot is described by its reduced density matrix, which we obtain by tracing out the reservoir degrees-of-freedom. Since spin is conserved during tunneling events, the evolution of the diagonal part of the reduced density matrix decouples from the one for the off-diagonal part (coherences) for the system studied here,

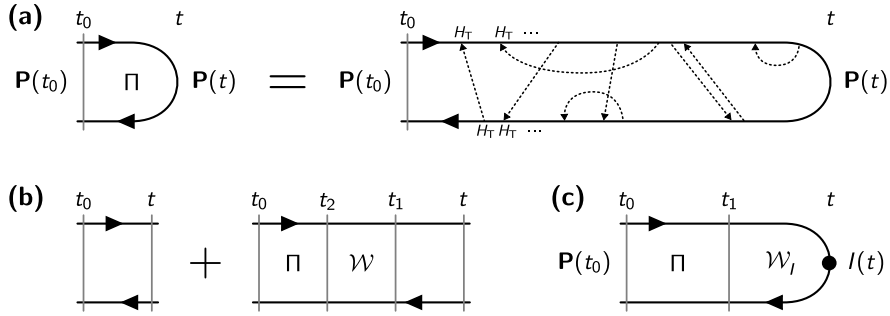

Figure 3.1: Time evolution on the Keldysh time contour sketched for (a) the occupation-vector Eq. (3.2); (b) the propagator Eq. (3.3); (c) the current Eq. (3.5). Note that the time arguments of propagators and kernels are suppressed for readability.

see Ref. [66]. For the calculation of the current[2] it is then sufficient to consider the diagonal part only, which is given by the occupation probabilities of the dot states. We write these occupation probabilities in terms of the *occupation vector*, $\boldsymbol{P}(t) = \left[P_0(t), P_\uparrow(t), P_\downarrow(t), P_2(t)\right]^{\mathrm{T}}$, where the subscript denotes the charge/spin configuration of the quantum dot (empty, singly occupied with spin up/down or doubly occupied). The time evolution of the occupation vector is given by

$$\boldsymbol{P}(t) = \Pi(t, t_0)\boldsymbol{P}(t_0). \tag{3.2}$$

The propagator $\Pi(t, t_0)$ takes tunneling between the dot and the reservoir into account. Note that we assume correlations between the reservoir and the quantum dot to be absent at the initial time, t_0.

As outlined in Refs. [64–66, 103], Eq. (3.2) can be depicted on the Keldysh time contour, in which the forward (backward) part of the time evolution of the reduced density matrix is represented by a forward (backward) time line, see Fig. 3.1 (a). The perturbative treatment of the tunnel Hamiltonian, H_{T} in Eq. (2.1), is captured by the insertion of tunnel vertices on both parts of the contour. When tracing out the reservoir degrees-of-freedom, the tunnel vertices become pair-wise contracted (Wick's theorem), which is indicated by tunneling lines in the diagrammatic language. An example is shown in the

[2]The same applies to the calculation of the current noise, see Chap. 5.

right part of panel (a). By collecting all *irreducible* diagrams into the kernel, $\mathcal{W}(t_1, t_2)$, i. e., all diagrams in which any vertical cut crosses a tunneling line, we derive the Dyson equation for the propagator,

$$\Pi(t, t_0) = \mathbf{1} + \int_{t_0}^{t} dt_1 \int_{t_0}^{t_1} dt_2 \, \mathcal{W}(t_1, t_2)\Pi(t_2, t_0). \tag{3.3}$$

This Dyson equation is sketched in Fig. 3.1 (b), where the first term in the figure as well as the right-hand side of the second term correspond to free parts of the contour. The time evolution of the occupation vector is derived by inserting Eq. (3.3) into Eq. (3.2) and taking a time derivative [64, 66, 103]. We obtain the kinetic equation

$$\partial_t \boldsymbol{P}(t) = \int_{-\infty}^{t} dt_1 \mathcal{W}(t, t_1)\boldsymbol{P}(t_1), \tag{3.4}$$

where the initial time t_0 has been sent to minus infinity, assuming that it is far away from the measurement time t. The diagrammatic method also leads to a related equation for the charge current, with the charge-current operator $I = -i \sum_{\sigma k} \left(\gamma d_\sigma^\dagger c_{\sigma k} - \gamma^* c_{\sigma k}^\dagger d_\sigma\right)$. We find

$$\langle I(t)\rangle = \frac{\boldsymbol{e}^{\mathrm{T}}}{2} \int_{-\infty}^{t} dt_1 \mathcal{W}_I(t, t_1)\boldsymbol{P}(t_1), \tag{3.5}$$

with $\boldsymbol{e}^{\mathrm{T}} = (1, 1, 1, 1)$. The current kernel, $\mathcal{W}_I(t, t_1)$ in Eq. (3.5), contains all irreducible diagrams in which an additional current vertex is placed at the time t, as indicated in Fig. 3.1 (c). For details on the derivations of Eqs. (3.4) and (3.5) we refer, e. g., to Ref. [66]. The calculation of kernels as well as explicit expressions are discussed in App. B.5. To calculate the current for the single-contact quantum dot, we point out that we can also exploit the continuity equation of charge conservation, $\langle I(t)\rangle = -\partial_t \langle n(t)\rangle$, with the quantum-dot electronic density, $\langle n(t)\rangle = (0, 1, 1, 2)\, \boldsymbol{P}(t)$.

3.1.2 Born-Markov master equation

To obtain the time evolution of the quantum-dot's occupation vector, based on Eq. (3.4), we now introduce the Born-Markov approximation [104]. This scheme is used in Chap. 8 of this thesis as input to extend TDDFT calculations (see Sec. 3.2). It is also applied in Chap. 4

for a different mesoscopic system, a superconducting single-electron transistor with spin-active tunnel barriers, for which we study time-dependent charge and spin currents. Note that in Chap. 5, where we employ the diagrammatic method to derive current noise of a slowly driven interacting quantum dot, we apply a different approximation scheme, namely a slow-driving expansion, see Sec. 5.4 for details.

The Born-Markov approximation consists of two parts. On the one hand, the *Born* approximation refers to the leading order in the tunnel-coupling strength, i. e., we derive the kernel in Eq. (3.4) in the sequential-tunneling picture. This is a valid approach for the high temperatures considered here, $\beta\Gamma \ll 1$. On the other hand, the *Markov* approximation concerns the time scales of the electron dynamics. At finite temperature, the kernel $\mathcal{W}(t, t_1)$ in Eq. (3.4) decays, when the time difference $|t - t_1|$ exceeds the memory time β of the reservoir. The latter, therefore, sets a first time scale. A second time scale is given by Γ^{-1}, which describes the time scale of electron tunneling. Additional time scales are introduced by the time-dependent driving scheme itself, such as the inverse driving frequency and the time span on which the dot level crosses the Fermi energy. With this in mind, we define the Markov approximation as neglecting the finite memory time of the reservoir. Since the reservoir memory time sets the support of the kernel in Eq. (3.4), we approximate the kernel as being proportional to a delta distribution centered at time t. This means that, instead of the time integral on the right-hand side in Eq. (3.4), we evaluate the occupation vector at the measurement time t, and we calculate the kernel with parameters frozen at this time. We obtain the Markovian master equation

$$\partial_t \boldsymbol{P}(t) = \mathcal{W}_t^{(\mathrm{i})} \boldsymbol{P}(t), \tag{3.6}$$

with the Laplace-transformed kernel in the limit of zero Laplace frequency, $\mathcal{W}_t^{(\mathrm{i})} = \lim_{z\to 0^+} \int_0^\infty d(t - t_1) e^{-z(t-t_1)} \mathcal{W}^{(\mathrm{i})}(t - t_1)$. The frozen part of the kernel in Eq. (3.4) is written as $\mathcal{W}^{(\mathrm{i})}(t - t_1)$ with the superscript (i) for instantaneous, see also App. B.5. The master Eq. (3.6) describes the dynamics of a slowly driven quantum dot, where the memory time β is the smallest time scale, but also the long-time dynamics ($t \gg \beta$) after a sudden step-pulse change of the gate voltage [99, 105]. As an example, we already applied Eq. (3.6) to calculate the

time-dependent current of a slowly driven interacting quantum dot in Fig. 2.1 (c). Note that $\mathcal{W}_t^{(\mathrm{i})}$ contains the Fermi golden-rule tunnel rates between different quantum-dot configurations.

3.2 Time-dependent density-functional theory

We now turn to the second theoretical method which is largely applied throughout this thesis, namely TDDFT [78, 79, 82]. In the following, we first provide a short general introduction to TDDFT in Sec. 3.2.1 and to adiabatic approximations in Sec. 3.2.2. We discuss the specific application of TDDFT to the Anderson model of Eq. (2.1) in Secs. 3.2.3 and 3.2.4.

3.2.1 Introduction to TDDFT

TDDFT is the time-dependent extension of density-functional theory (DFT) [75, 76]—one of the most successful methods for the computation of electronic properties in condensed-matter systems (also beyond model Hamiltonians) [77]. Today, it is a favored method in physics as well as in physical chemistry, e. g., to obtain the electronic excitation spectrum of large molecules or clusters, to study molecules in strong laser fields or to simulate the impact of high-energy protons in solids [78, 79, 83]. On the contrary, TDDFT is barely applied for studies of single-electron transport in nanodevices, mainly due to the insufficiency of available approximations [82] (see also Ref. [106]).

The theoretical foundation of TDDFT has been led by Runge and Gross in Ref. [74]. In this seminal paper, they consider a closed quantum system, which consists of interacting electrons confined in an external potential $v_{\mathrm{ext}}(\boldsymbol{r}, t)$, which is Taylor expandable in time and where $\boldsymbol{r}$ is a spatial coordinate. For this system, their theorem says that the knowledge of the (pure) initial state, $|\psi(t_0)\rangle$, together with the evolution of the *electron density*, $n(\boldsymbol{r}, t)$, between the times t_0 and t, is sufficient to uniquely[3] define the time-dependent potential, $v_{\mathrm{ext}}(\boldsymbol{r}, t)$, which leads to the prescribed density evolution. Since the expectation values of all observables are fixed by knowing the external potential and the initial state, this means that we can write any observable

[3] $v_{\mathrm{ext}}(\boldsymbol{r}, t)$ is unique up to a purely time-dependent function.

of the system as a functional of $n(\boldsymbol{r},t)$ and $|\psi(t_0)\rangle$. The one-to-one correspondence between densities and potentials is typically exploited by constructing a Kohn-Sham (KS) system [81]. The KS system, with initial state $|\phi(t_0)\rangle$, is an unphysical auxiliary system of *noninteracting* electrons, with the crucial property that its time-dependent density is identical with the density in the (physical) interacting system. This is possible thanks to the nontrivial KS potential, here written as

$$v_{\mathrm{KS}}\big[n,|\psi(t_0)\rangle,|\phi(t_0)\rangle\big](\boldsymbol{r},t) = v_{\mathrm{ext}}(\boldsymbol{r},t) + v_{\mathrm{H}}[n](\boldsymbol{r},t) + v_{\mathrm{XC}}\big[n,|\psi(t_0)\rangle,|\phi(t_0)\rangle\big](\boldsymbol{r},t). \tag{3.7}$$

Besides $v_{\mathrm{ext}}(\boldsymbol{r},t)$, the KS potential contains the Hartree (H) potential, describing electrostatic effects, and the exchange-correlation (XC) potential, which is defined as the difference between the sum $v_{\mathrm{ext}}(\boldsymbol{r},t)+v_{\mathrm{H}}(\boldsymbol{r},t)$ and $v_{\mathrm{KS}}(\boldsymbol{r},t)$. Uniqueness of the latter is provided by the Runge-Gross theorem [74], while existence of the KS potential for a density $n(\boldsymbol{r},t)$ which is Taylor expandable in time (at all times) has been demonstrated by van Leeuwen in Ref. [81], see also Refs. [107, 108] for extensions.[4] As a consequence, the XC potential is a functional of the electron density and the initial states in the interacting and the KS systems, as already indicated in Eq. (3.7). Furthermore, it is a universal quantity for a given two-body interaction, which means that it is independent of the external potential defining the specific model under consideration. The main drawback of TDDFT, aside of developing approximations[5] of $v_{\mathrm{XC}}(t)$ for practical purposes, is that the KS system is unphysical. Therefore, many observables cannot be calculated directly from the KS state. Important exceptions are—by construction—the time-dependent electron density $n(\boldsymbol{r},t)$ and related observables.

The procedure to compute the electron density for a quantum system with external potential $v_{\mathrm{ext}}(\boldsymbol{r},t)$ and initial state $|\psi(t_0)\rangle$ is as follows: (1) we determine a KS initial state, $|\phi(t_0)\rangle$, which leads to the correct initial density, $n(\boldsymbol{r},t_0)$, and also its time derivative; (2) we numerically time evolve the KS wave function using the KS potential, where we continuously update the latter based on the approximation of the XC potential which is used in the calculation; (3) from the KS

[4] A density for which $v_{\mathrm{KS}}(\boldsymbol{r},t)$ exists is called noninteracting v-representable.

[5] Note that several exact conditions of $v_{\mathrm{XC}}(t)$ have been found in Refs. [109–112].

wave function $|\phi(t)\rangle$ we extract the KS electron density, which provides an approximate solution for the density of the interacting system.

A key benefit of the TDDFT approach is its numerical efficiency, since we only need to time propagate the noninteracting KS system. For this reason, it can be applied not only for model Hamiltonians, but also to analyze many-electron systems beyond models, for which the majority of theoretical methods is no longer directly implementable [78, 79]. Importantly, besides discretization of the Hamiltonian for the numerical time propagation, we only approximate the XC potential in a TDDFT calculation. The quality of available XC approximations is therefore crucial for the accuracy of a calculation, and it is of key importance to explore and open up new ways which ultimately result in more accurate XC potentials.

We point out that TDDFT also provides the proper framework to extract linear-response quantities from a DFT calculation [78, 79, 82], without the need of a time evolution. In TDDFT linear-response theory, many of the unphysical linear-response quantities calculated from a KS equilibrium state are linked, via Dyson equations, to physical observables of the associated interacting system. For more details we refer to Sec. 8.3, where we apply TDDFT linear-response theory to derive finite-frequency admittances of a single-contact quantum dot.

3.2.2 Adiabatic approximation of the XC potential

The difficulty to approximate the XC potential of TDDFT hinders its application in many areas of condensed-matter physics. For example, almost all TDDFT calculations make use of *adiabatic* XC potentials. These are defined by evaluating an XC potential from DFT time-locally at the electron density of the time-dependent system. A frequent choice is the adiabatic local-density approximation (ALDA), defined by

$$v_{\mathrm{XC}}^{\mathrm{ALDA}}[n](\boldsymbol{r},t) = v_{\mathrm{XC}}^{\mathrm{LDA}}[n](\boldsymbol{r},t)\big|_{n(\boldsymbol{r})=n(\boldsymbol{r},t)}\,, \tag{3.8}$$

where $v_{\mathrm{XC}}^{\mathrm{LDA}}[n](\boldsymbol{r},t)$ is the famous local-density approximation of DFT, which stems from the homogeneous electron gas. XC potentials of this type are popular not only for their simple numerical implementation and fulfilling of exact properties [109]. A reason is also that *nonadiabatic* XC potentials are hardly developed to a stage, where they are of practical use [82]. However, we emphasize that adiabatic XC potentials

suffer from two key failures. First, they neglect a dependence on the initial states [see Eq. (3.7)], which has been shown to be relevant for time evolutions starting from an excited[6] state [111, 113, 114]. Second, the XC potential of TDDFT depends time-nonlocally on the electron density and the time-local adiabatic approximation is thus a severe simplification, which is only justifiable for systems with adiabatically slow time dependence. If a system's time evolution is instead beyond the adiabatic evolution, adiabatic approximations often fail, as we show, e. g., in Sec. 8.2.1 for a time-dependently driven interacting quantum dot, see also Ref. [115]. Although this drawback is well known [82], it remains a nontrivial task—and a main focus of this thesis—to include time-nonlocal density dependence in approximate XC potentials, see also Refs. [109–112, 116]. It is important to point out that this history dependence is caused by the mathematical construction of the KS system. Therefore, it should not be confused with physical memory effects of an open quantum system, i. e., the part of the dynamics, which is neglected in the Markov approximation defined in Sec. 3.1.2. On the one hand, a TDDFT time evolution based on an adiabatic XC potential still includes non-Markovian dynamics, because no approximation is made with respect to the time propagation itself, see also Sec. 8.2.2. On the other hand, as we present in Sec. 8.2.1, an adiabatic XC potential can perform significantly worse than a Markovian time evolution [80].

We now leave the general discussion of TDDFT and describe how the theory is specifically employed in this thesis.

3.2.3 Kohn-Sham Anderson model

In this thesis, we push forward the (nonstandard) application of TDDFT for describing electron dynamics in model Hamiltonians of mesoscopic physics. A main focus and instructive starting point is the single-contact quantum dot modeled by the Anderson Hamiltonian of Eq. (2.1).[7] Note that we consider a spin symmetric quantum dot in

[6] If the initial states are ground states, the Hohenberg-Kohn theorem [75] ensures that $|\psi(t_0)\rangle$ and $|\phi(t_0)\rangle$ are functionals of the initial density, $n(\boldsymbol{r}, t_0)$.

[7] Extensions of this model, describing more complex single-electron tunneling devices such as many quantum dots coupled to a shared electron reservoir as well as a quantum dot coupled to two reservoirs, are introduced throughout Chaps. 7-9.

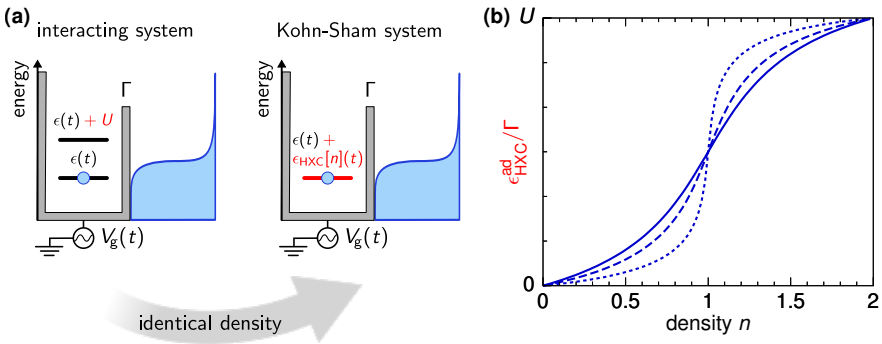

Figure 3.2: (a) Sketch of an interacting single-contact quantum dot (left) and the related KS system (right). (b) Adiabatic HXC (H plus XC) potential from Ref. [88] for the setup shown in (a), plotted for three different inverse temperatures, $\beta = 1/(2\Gamma), 1/(4\Gamma), 1/(6\Gamma)$, as short dashed, long dashed and solid lines with interaction $U = 16\Gamma$.

this section as well as in Chaps. 7-9, i. e., $\epsilon(t) = \epsilon_\uparrow(t) = \epsilon_\downarrow(t)$.

In order to employ TDDFT for the Anderson model, we first define a corresponding KS auxiliary system of noninteracting electrons. To obtain the Hamiltonian of this KS system, we set the interaction parameter U in Eq. (2.1) to zero. Additionally, we take the H and XC potentials into account as a combined shift of the single energy level by the amount $\epsilon_{\mathrm{HXC}}[n](t)$, which we consider to only depend on the quantum-dot electron density, $n(t_1)$, with $t_0 \leq t_1 \leq t$, thus allowing for history dependence.[8] We find the KS Anderson Hamiltonian

$$H_{\mathrm{KS}}(t) = \sum_\sigma \left[\epsilon(t) + \epsilon_{\mathrm{HXC}}[n](t)\right] d_\sigma^\dagger d_\sigma + \sum_{k,\sigma} \epsilon_k c_{k\sigma}^\dagger c_{k\sigma} + \sum_{k,\sigma} \left(\gamma c_{k\sigma} d_\sigma^\dagger + \mathrm{H.\,c.}\right), \tag{3.9}$$

see also Fig. 3.2 (a). As mentioned in Sec. 3.2.1, the KS system shares the identical electron density with the interacting system defined in Eq. (2.1). Therefore, to obtain the charge current of the interacting system in response to a time-dependent variation of the energy

[8] Note that this includes the additional assumption that the reservoir-dot couplings are equal in the interacting and the KS systems, which turns out to be justified by the results presented in Chap. 8.

level, $\epsilon(t)$, we numerically time propagate the KS system, using an approximate XC potential, and compute the charge current in the KS system.

Importantly, from now on we consider mixed (thermal equilibrium) states instead of pure states as initial configurations in the interacting as well as the KS systems.[9] The temperature of the reservoir is thereby always defined at the initial time.

3.2.4 Development of XC potentials for the Anderson model

The Anderson model of Eq. (2.1) is an instructive system to investigate properties of the XC potential in the presence of a strong localized Coulomb repulsion [117]. We now review efforts to develop an (adiabatic) XC potential for this model. This provides a context for the new development of a nonadiabatic XC potential, presented in Sec. 8.1 of this thesis, see also Sec. 9.2.1.

First, we remind that the Runge-Gross theorem [74] only ensures system independence of the XC potential for a fixed electron-electron interaction. This means that XC potentials derived for realistic systems with long-ranged Coulomb interaction cannot be applied to model Hamiltonians containing a Hubbard interaction. Nevertheless, it is a reasonable strategy to transfer concepts which work well for first-principle calculations to model Hamiltonians. For example, a LDA for a Hubbard interaction has been proposed in Ref. [118], based on the Bethe-ansatz solution for a homogeneous Hubbard chain. This Bethe-ansatz LDA (BALDA) has later been applied as an adiabatic XC potential in TDDFT calculations for a 1D Hubbard model [119], and it has also been tried in studies of the Anderson Hamiltonian [86, 87].

A crucial feature of BALDA, in contrast to LDA, is that the former has a derivative discontinuity (DD) [120]—a step at integer values of the density. This step is not only well-known in DFT, where it yields an important correction to the band gaps of solids [121]. It is also highly relevant in non-equilibrium calculations [122–125], e. g., to obtain Coulomb blockade [86, 126, 127] or Kondo physics [88] in a KS system. Interestingly, in nonadiabatic TDDFT time propagations, further steps besides the DD have been reported for the

[9] A rigorous proof for the existence of a (finite-temperature) ensemble TDDFT in analogy to the Runge-Gross theorem is still an open research problem [83].

exact XC potential of a two-electron system with long-ranged Coulomb interaction [116, 123, 128, 129] as well as for a 1D semiconductor [130].

Besides adiabatic BALDA, Ref. [88] proposes an adiabatic XC potential specifically tailored to the Anderson model and based on a single energy level coupled to a thermal bath. This XC potential is plotted in Fig. 3.2 (b), which shows that it features a DD smeared out by temperature [88, 127, 131]. For stationary systems with temperatures larger than the tunnel-coupling strength it provides a good description of the equilibrium density reached after a long time evolution, see Sec. 8.2. In a follow-up work [89], this XC potential has been modified towards lower temperatures as well as attractive interactions. However, modifications beyond the *adiabatic approximation* are less explored. This is a focus of Chap. 8, where we use master equations to include history dependence in the XC potential of Ref. [88].

Another recently proposed DFT method for transport calculations in mesoscopic systems has been named i-DFT [90, 91]. This method describes a time-stationary model system coupled to two contacts in terms of the density and the *steady-state current* through the system. The KS system in i-DFT not only takes into account the XC potential, but also an XC correction to an applied constant bias voltage (from now on referred to as the XC bias) [90, 132, 133]. While the original framework only includes steady-state physics, a first step towards a time-dependent i-DFT, based on a memory-less XC approximation, has been reported in Ref. [92].[10] In Chap. 9, we discuss a way to include memory in the XC approximation of a two-contact quantum dot as well, by generalizing the method outlined in Chap. 8.

3.3 Motivation for the multi-method approach

In the remainder of this thesis, we present several theoretical studies of single-electron transport in interacting nanodevices. An additional focus is to apply and extend *multiple* theoretical methods for the description of these systems. The motivation for this multi-method

[10] With this in mind, we note that the results presented in Chaps. 8-9 can be understood in two ways: in terms of TDDFT with a nonadiabatic XC potential, or, similarly, as a memory-full extension of time-dependent i-DFT. We discuss this point further in Chap. 9, see also Refs. [80, 134].

approach is manifold. On the one hand, by comparing the outcome of different calculations, we obtain a more precise picture of the physics in these devices and we also understand more the assets and limitations of different theoretical methods. On the other hand, by having in-depth experience with more than one theoretical approach, we can find situations, where insights from one method are useful to extend and improve a second method. We realize these ideas in different parts of this thesis, where we mainly apply the two methods introduced in this chapter: real-time diagrammatic perturbation theory and TDDFT.

First, to validate the results presented in later chapters, we present comparisons with additional theoretical methods. In Sec. 6.2.3, we compare noise spectra of an interacting quantum dot, which we calculate using the real-time diagrammatic approach, with data obtained in Floquet-scattering matrix theory, see also Sec. 5.5. Furthermore, to validate the TDDFT time evolutions of single-electron tunneling devices, which we present in Chap. 8, we compare the TDDFT data with accurate time-dependent density-matrix renormalization-group calculations (td-DMRG) in Sec. 8.2.2. Important differences between these four theories, in the context of single-electron transport, are discussed in these sections as well. Additionally, the main tools employed in this thesis, i. e., the diagrammatic approach and TDDFT, are compared in the second half of the present section.

Second, in Chaps. 8-9, we exploit insights from the diagrammatic perturbative method as an input to extend the aforementioned TDDFT calculations. As outlined in Sec. 3.2.2 as well as in Sec. 3.2.4, a key issue of TDDFT is that almost all available approximations of the XC potential are *adiabatic* [82]. This severely limits the applicability of TDDFT for systems with nonadiabatic time dependence, as we, e. g., show in Sec. 8.2. Importantly, we find in this thesis that it is possible to derive a *nonadiabatic* XC approximation for a Hubbard interaction on a quantum dot, by using master-equation descriptions of the dynamics, see Chaps. 8-9. The derived nonadiabatic XC approximation strongly improves the TDDFT description of a single-contact quantum dot and related systems in the linear [85] and nonlinear response regime [80]. This emphasizes the significance of having a multi-method perspective, to further advance theoretical methods in mesoscopic physics.

In the following, we compare real-time diagrammatic perturbation theory and TDDFT, while considering their application for describing

	real-time diagrammatic perturbation theory (in tunneling)	**time-dependent density-functional theory**
main application	transport properties of open quantum systems	electronic excitations, molecules in strong laser fields, ...
calculations	mainly analytical	numerical
system size	large systems are analytically/numerically demanding or impossible	applicable to very large systems and beyond model Hamiltonians
observables	no restrictions	provides electron density and related quantities, care must be taken for other observables
interaction	no further approximation beyond choice of the model	approximated by the XC potential
temperature	restrictions arise from perturbative expansion	restrictions can arise from XC approximation (regime of applicability)
tunneling	weak, depending on the expansion order (sequential tunneling, co-tunneling, ...)	fully included (in the KS system)
time evolution	in applications typically approximated (Markov, slow-driving expansion, ...)	fully included (in the KS system)

Table 3.1: Comparison between real-time diagrammatic perturbation theory (Sec. 3.1) and TDDFT (Sec. 3.2) for the description of time-dependent quantum transport in the mesoscopic systems studied here.

time-dependently driven nanoscale electronic devices. First, we once more point out that TDDFT is today hardly applied in this context, see Sec. 3.2.1. On the contrary, the diagrammatic approach has been specifically developed to study transport physics and open-system dynamics. Another key difference is that TDDFT time propagations are typically solved numerically, while the diagrammatic theory can produce analytic results, which allow for more physical interpretation.

Various properties of the two theories are listed and compared in Tab. 3.1. The table reveals a key benefit of TDDFT, when contrasted with the diagrammatic method. In TDDFT, we solve the time propagation of the KS system without further approximation[11] and, therefore, the theory includes non-Markovian dynamics as well as tunneling processes in all orders. This means that TDDFT—depending on the employed XC potential—can describe coherent transport at low temperatures and also strong reservoir-dot coupling [86, 88, 91], which can both be difficult when applying pertubation theory in the tunnel coupling. Besides that, a further asset of TDDFT is its numerical efficiency, as already pointed out in Sec. 3.2.1, which allows for calculations of very large systems. However, TDDFT also has a severe drawback, which is the nontrivial development of accurate XC potentials, especially, when we want to address nonadiabatic dynamics and/or strong correlation in a nanoscale device.

In contrast, the development and interpretation of approximations is a particular asset of the real-time diagrammatic method. In the diagrammatic language, approximations can typically be understood by studying which physical processes they include. Furthermore, the diagrammatic method allows us to calculate observables beyond those directly related to the electron density (unlike TDDFT). For example, in Chap. 5, we apply the diagrammatic approach to derive current-noise spectra of a time-dependently driven interacting quantum dot. Accessing this observable, which includes a two-time correlation function (see Sec. 5.3.1), is difficult in TDDFT, where the basic variable is the electron density.

At the end of this chapter, let us briefly remind the reader how the remainder of this thesis is structured. In the following, we first apply

[11] In practice, we typically discretize the Hamiltonian, which can lead to numerical inaccuracies, see also Sec. 7.4.

the diagrammatic method to analyze two different nanosystems. In Chap. 4, we present a theoretical study of a novel nanostructure, which we propose as an experimentally feasible quantized spin-current source. In Chaps. 5-6, we turn from analyses of currents to an analysis of the (charge) current noise, and we study the latter for single-electron emitters based on quantum dots. Afterwards, in Chaps. 7-9, we switch from the diagrammatic method to TDDFT, however, still applying insights from the diagrammatic calculations in order to develop nonadiabatic XC potentials. Here, to demonstrate the practical use of the developed XC potentials, we present TDDFT time propagations of single and multiple interacting quantum dots coupled to contacts and driven by time-dependent fields. Note that the subsequent chapters all contain parts where we focus on physical questions, as well as sections more devoted to method development.

4 A Clocked Single-Spin Source

In this chapter we present a theoretical study of a novel single-electron tunneling device, which can be operated as an on-demand single-*spin* emitter. We describe the working principle of the device and develop a theoretical framework for the calculation of charge and spin currents, based on a master-equation description of the dynamics. Note that the present chapter and the related Apps. A.1-A.3 are in major parts published in *New Journal of Physics* **18** 083019 (2016).

The nanodevice we investigate is based on a superconductor/ ferromagnetic-insulator (S/FI) hybrid structure, which is driven by a constant bias and a time-dependent ac gate voltage, see Fig. 4.1. This structure is motivated by similar superconductor/normal-metal (S/N) turnstiles, which have successfully been implemented to realize single-*electron* emission in solid-state setups [36, 37], as discussed in Sec. 2.3. On the contrary, although a number of relevant applications of spintronic devices exists [135, 136], we find that the implementation of spintronics at the single-spin level is still weakly explored. Only recently, the transfer of single spins between two quantum dots was experimentally reported with a fidelity of 30% [137]. Previous efforts to realize a cyclic electronic pure-spin current source at the single-spin level, instead of stationary spin sources and spin batteries using rotating magnetic fields [138, 139], are based on a spin ratchet [140]. However, to our knowledge, single-spin sources with high accuracy are still missing, although their successful implementation would offer many opportunities. For instance, they could be used to emit in a controlled way single quasiparticles with a defined spin into a supercon-

ducting contact. This is of interest for spintronics at the single-particle level [141, 142], for controlled quantum operations (e. g. on flying (spin)-qubits) [6], and for the fundamental research on single-particle characteristics. Furthermore, a clocked spin pump, relating the spin current directly to a driving frequency, would provide a very precise spin-current source.

Besides that, in superconductors, when compared to typical semiconducting materials, the quasiparticle spin lifetime is largely enhanced [141, 143–146]. This is one of the several reasons why superconducting spintronics [141, 146, 147] has recently become highly attractive. Notably, the here proposed accurate high-frequency spin source works in the absence of any applied magnetic field, see Fig. 4.1. The entirely superconducting structure furthermore avoids the technologically difficult combination of superconductors with ferromagnetic metals or halfmetals and is based on realizable material combinations and device parameters [148–150], as discussed below. Additionally, an important characteristic of the FI layer is that it improves the turnstile precision by strongly suppressing Cooper-pair tunneling and related higher-order processes.[1]

This chapter is organized in the following way. In Sec. 4.1 we outline the proposed nanostructure and in Sec. 4.2 we describe the working principle of its spin-turnstile operation mode. The calculation of charge and spin currents is explained in Sec. 4.3. We then present the main results in Sec. 4.4, discuss possible error sources of the device in Sec. 4.5 and analyze additional features in the pumped charge and spin currents in Sec. 4.6. A conclusion is given in Sec. 4.7.

4.1 Superconducting turnstile with ferromagnetic insulator layer

To realize an accurate spin emitter, we propose to use a quantized turnstile, which acts as a clocked spin source thanks to the presence of a FI layer. The SFISFIS setup, consisting of a S island tunnel coupled to two S leads via the FI layer is illustrated in Fig. 4.1. The island

[1] As a consequence, we expect FI tunnel barriers to be equally beneficial for the precision of pure *charge* turnstiles based on S/N nanostructures [36, 37], which are promising candidates for a new current standard [4], see also Sec. 2.3.

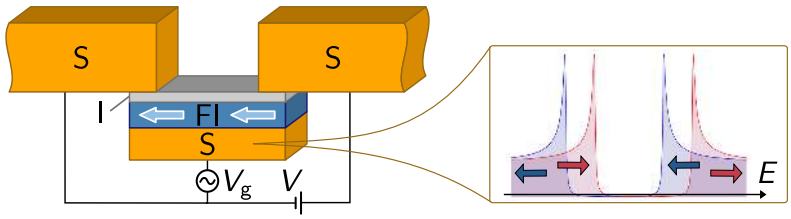

Figure 4.1: Sketch of the turnstile (left); the ferromagnetic insulator (FI) layer covering the entire thin superconducting (S) island induces a spin-split density of states (right) due to exchange interaction. Coupling the island to S contacts via the same FI layer provides spin-selective tunneling barriers. An additional non-magnetic insulator (I) layer prevents a local exchange field in the S contacts [154].

is characterized by a strong charging energy, which, together with weak tunnel coupling [151], implies that the transport of charge and spin through the nanostructure takes place by sequential-tunneling processes. As a result of the compact design, the FI layer induces a spin-split density of states (DOS) in the small island [148, 149, 152, 153], leading to a high spin polarization of quasiparticles, and, at the same time, it provides strongly spin-polarized tunneling barriers.[2]

We describe the superconducting elements of the turnstile by a standard Bardeen-Cooper-Schrieffer-Hamiltonian with an energy gap Δ (momentum-independent).[3] The system is modeled by the Hamiltonian $H = H_{\rm res} + H_{\rm island} + H_{\rm T}$ with the contact (reservoir) part

$$H_{\rm res} = \sum_{\alpha={\rm L,R}} \sum_{\sigma,k} \epsilon_{\alpha k} c^\dagger_{\alpha\sigma k} c_{\alpha\sigma k} - \sum_{\alpha,k} \left(\Delta_\alpha c^\dagger_{\alpha\uparrow k} c^\dagger_{\alpha\downarrow -k} + \Delta^*_\alpha c_{\alpha\downarrow -k} c_{\alpha\uparrow k} \right), \tag{4.1a}$$

[2] An alternative setup might use thin FI/I layers at the interfaces between the (serial) S elements as spin-polarized barriers and an additional thick FI layer on top of the S island to induce the split-field. While this involves changes in the device design, it does not change the following theoretical investigation.

[3] Note that the parameters Δ and Δ_α attributed to the island and the contacts are complex numbers and can in principle differ in phase, which does, however, not influence the following discussion (we always consider the charging energy of the island to dominate over the Josephson energies of the tunnel barriers).

the island part

$$H_{\text{island}} = \sum_{\sigma,k} (\epsilon_k - \sigma h)\, d^\dagger_{\sigma k} d_{\sigma k} - \sum_k \left(\Delta d^\dagger_{\uparrow k} d^\dagger_{\downarrow -k} + \Delta^* d_{\downarrow -k} d_{\uparrow k} \right) + E_{\text{c}} \left[\hat{n} - n_{\text{g}}(t) \right]^2 , \tag{4.1b}$$

and the tunnel-coupling part,[4]

$$H_{\text{T}} = \sum_{\alpha=\text{L,R}} \sum_{\sigma,k,l} \left(t^{\alpha\sigma}_{kl} c_{\alpha\sigma l} d^\dagger_{\sigma k} + \text{H. c.} \right). \tag{4.1c}$$

In Eq. 4.1, the $d^{(\dagger)}_{\sigma k}$ and $c^{(\dagger)}_{\alpha\sigma k}$ are electron annihilation (creation) operators for the island and for the contacts with momentum index k and l, respectively. All energies are defined with respect to a common reference chemical potential $\mu = 0$. The subscript $\sigma = \uparrow, \downarrow$ indicates the electron spin (parallel/antiparallel to the magnetization of the FI layer), and takes the values ± 1 when used as a variable. The interaction between the localized magnetic moments of the FI layer and the conduction electrons in the superconductor yields an effective exchange-field h in the S island that decays away from the interface over the superconducting coherence length ξ_0 [155] ($\simeq$ 100nm in Al). We assume the island thickness to be smaller than ξ_0 and, therefore, the induced DOS spin-splitting as being spatially uniform across the entire island [148, 149, 151–153]. Similar to the discussion in Sec. 2.3, the island features a strong charging energy, characterized by $E_{\text{c}} = e^2/(2C_\Sigma)$ with overall capacitance C_Σ, where the electron charge is $-e$. The charging energy depends on the number of excess charges on the island n (accounted for by the operator $\hat{n}$) with respect to the induced offset charge number $n_{\text{g}} = C_{\text{g}} V_{\text{g}}$, where C_{g} is the gate capacitance and V_{g} the gate voltage.[5] The Hamiltonian in Eq. (4.1) is diagonalized by a standard Bogoliubov transformation, leading to a description of the system's excitations in terms of quasiparticles. This and further technical details are presented in App. A.1. As a result, the dimensionless DOS of the island, as sketched in Fig. 4.1, can be

[4] In this chapter we use $t^{\alpha\sigma}_{kl}$ for tunnel couplings, because γ is reserved for the Dynes parameter defined below.

[5] C_Σ equals $C_{\text{g}} + C_{\text{L}} + C_{\text{R}}$ with the $C_{\text{L/R}}$ being the capacitances attributed to the coupling between the island and the left/right contacts.

written as

$$g_\sigma(E) = \frac{\nu_\sigma(E)}{\nu_0} = \left| \mathrm{Re}\left[\frac{E + \sigma h + i\gamma}{\sqrt{(E + \sigma h + i\gamma)^2 - |\Delta|^2}} \right] \right|, \tag{4.2}$$

where ν_0 is the DOS per spin at the Fermi level in the normal state. The dimensionless DOS of the left and right contacts, $g_\alpha(E)$ for $\alpha = \mathrm{L}, \mathrm{R}$, is obtained by setting $h = 0$ in Eq. (4.2). The Dynes parameter γ [41, 156, 157] accounts for a finite broadening in the superconductors.[6] The tunneling barriers between island and contacts have spin-dependent contact resistances $R_{\alpha\sigma} = 1/(2\pi|t^{\alpha\sigma}|^2\nu_0^2 V_\alpha V_\mathrm{I})$ with the volumes V_α (contact) and V_I (island), and $t^{\alpha\sigma}_{kl} = t^{\alpha\sigma}$ is assumed to be momentum independent. Furthermore, we assume $R_{\mathrm{L}\sigma} = R_{\mathrm{R}\sigma} \equiv R_\sigma$ for simplicity. The barrier polarization is defined as $P = (R_\downarrow - R_\uparrow) / (R_\downarrow + R_\uparrow)$.

From the experimental point of view, materials such as EuO or EuS, which can provide barrier polarizations as high as $\sim 98\%$ [158], in contact with superconducting aluminum (Al) are suitable candidates for the implementation of the spin turnstile. Depending on the thickness of the Al layer and the quality of the interface, the value for h in such FIS structures ranges from $\sim 0.2\Delta$ up to $\sim 0.6\Delta$ [149, 159–161]. Alternatively, ferromagnetic GdN barriers combined with superconducting NbN could be used with the advantage of a higher critical temperature of ~ 15 K [162, 163]. In all plots shown below, we set $P = 90\%$ and $h \leq 0.3\Delta$. Increasing these parameters would even further improve the turnstile operation. We furthermore assume the Dynes parameter to be of the order of $10^{-5}\Delta$ down to $10^{-6}\Delta$. In analogous devices with non-spin-split superconducting elements, the Dynes parameter can reach values down to $10^{-7}\Delta$, favored by the opaque tunnel barriers and further improved by appropriately curing the electromagnetic-field environment [41]. Here, we presume that similar values can be obtained in mesoscopic devices with spin-split superconductors.

[6] We choose the Dynes parameters of island and contacts to be equal for simplicity and we also assume $\Delta = \Delta_\alpha$ with Δ being a positive real number. The expected differences in a real device do not change the turnstile working principle, see also footnote 3. The same is true for the symmetric choice of contact resistances.

4.2 Working principle of the spin turnstile

We now analyze the working principle of the spin turnstile. A bias voltage V is symmetrically applied across the structure and the island's gate voltage is time-dependently modulated, $V_\mathrm{g}(t) = \bar{V}_\mathrm{g} + \delta V_\mathrm{g} A(t)$, and respectively $n_\mathrm{g}(t) = \bar{n}_\mathrm{g} + \delta n_\mathrm{g} A(t)$, where the zero-time-average function $A(t)$ describes the shape of the driving signal [36, 37]. This causes tunneling of charges across the device. The addition energies for a charge entering (+) or leaving (−) the island, initially occupied with n excess charges, via the left contact are

$$\delta E_+^{\mathrm{L},n} = E_\mathrm{c}\left[(n+1-n_\mathrm{g})^2 - (n-n_\mathrm{g})^2\right] - \frac{V}{2}, \tag{4.3a}$$

$$\delta E_-^{\mathrm{L},n} = E_\mathrm{c}\left[(n-1-n_\mathrm{g})^2 - (n-n_\mathrm{g})^2\right] + \frac{V}{2}, \tag{4.3b}$$

($V/2$ must be replaced by $-V/2$ for tunnel events via R). Charge tunneling goes along with the creation or annihilation of quasiparticles on the island and in the reservoirs. Note that at sufficiently low temperatures, the island can be initialized in a state essentially free of quasiparticle excitations [150]. During the described turnstile operation, a quasiparticle is generated on the island by an *incoming* charge in the first half of the driving cycle. Since a single quasiparticle on a superconductor can not relax, which is known as the parity effect [150, 164–166], the island continues to be occupied by one quasiparticle until an annihilation process takes place in the second half of the driving cycle. This is accompanied by an *outgoing* charge and results in a controlled flow of single particles. Spin polarization of the generated single-particle current is partially already achieved by the spin-polarized tunneling barriers. However, here we show that the spin-split DOS of the island is the crucial ingredient for a complete spin-polarization of the emitted particles over a wide range of driving frequencies and parameter configurations. Importantly, to account for the parity effect in the theoretical description, we have to carefully keep track of the number of quasiparticles on the island.[7] In contrast, in the macroscopic reservoirs the distribution of quasiparticles is well

[7] To fix the convention, we set the state of zero excess charges to be a state with an even number of quasiparticles throughout this chapter. Then, even/odd charge states are always states with an even/odd number of quasiparticles.

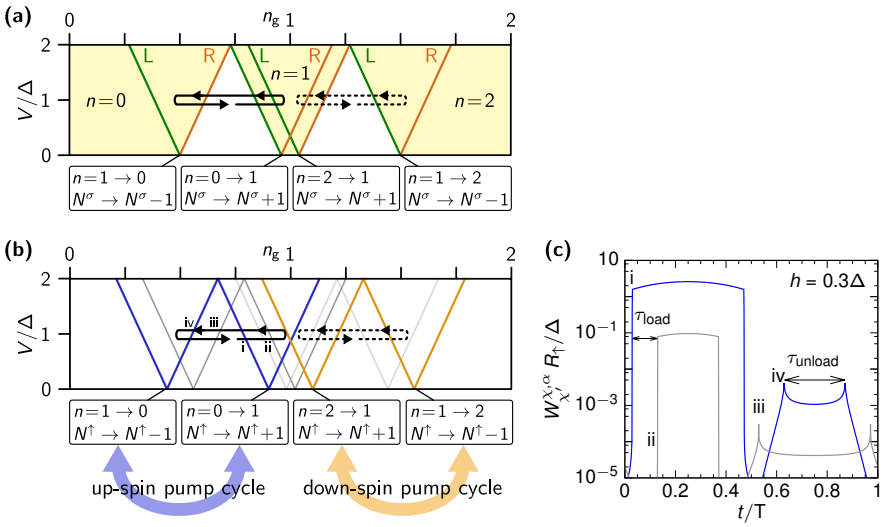

Figure 4.2: (a) Stability diagram of a SISIS structure for $E_c = 2.2\Delta$. Pairs of diagonal lines indicate the set-in of energetically possible tunneling processes: Creation/annihilation of island quasiparticles is marked as $N^\sigma \to N^\sigma \pm 1$. (b) Equivalent to (a) for a SFISFIS structure with a spin-split island DOS characterized by $h = 0.3\Delta$. Blue/orange lines show processes involving changes in $N^\uparrow$ contributing to pumping of up-spins/down-spins. Grey lines indicate changes in $N^\downarrow$, irrelevant for the shown pumping cycles. (c) Time-evolution of the tunneling rates, where i, ii, iii, iv correspond to crossings of the solid black loop in (b) with threshold lines of the same color [panel (c) is discussed in Sec. 4.4]. Further parameters are $V = \Delta$, $1/\beta = 0.01T_c$, $\gamma = 10^{-6}\Delta$, $V_I = 1.5 \cdot 10^5 \mathrm{nm}^3$, $\nu_0 = 1.45 \cdot 10^{47} \mathrm{m}^{-3}\mathrm{J}^{-1}$ [150], $R_\uparrow = 100\mathrm{k}\Omega$, $P = 90\%$, with critical temperature $T_c = 1.3\mathrm{K}$ and $\Delta = 200\mu\mathrm{eV}$ (aluminum).

described by a Fermi-function with the inverse temperature β, i. e., $f^+(E) = 1/(1 + e^{\beta E})$. For temperatures of the order of tens of mK, as considered here, the occupation of quasiparticles in the reservoirs is strongly suppressed. Hence, a sequential tunnel event that turns an even island charge state into an odd one necessarily breaks up a Cooper pair in the island or in one of the contacts. In order to allow

that energetically, the addition energy for adding a quasiparticle to the island has to equal -2Δ. However, when the DOS is spin-split as proposed here, see Eq. (4.2), the required energy, $-2\Delta + \sigma h$, differs for different spin species. In contrast, when the initial island charge state is odd (namely, occupied by one quasiparticle with spin σ), a sequential tunnel process that annihilates this quasiparticle becomes favorable when the addition energy is σh (respectively 0 for the nonmagnetic case).

The turnstile cycle makes use of the above described tunneling processes. This is visualized in the stability diagram for an SISIS charge turnstile in Fig. 4.2 (a), which is shown for a comparison, and for an SFISFIS spin turnstile in Fig. 4.2 (b). Compare also to the stability diagram of experimentally realized SINIS charge turnstiles [36, 37], which is discussed in Fig. 2.2 (c). In all three figures, the respective turnstile cycles are indicated as black loops, where the full line shows cycles involving charge transitions between 0 and 1. Let us briefly describe the turnstile cycle in Fig. 4.2 (a) of the SISIS setup. In the first half of this driving cycle, tunneling from the left contact increases the island charge by 1 and a quasiparticle is generated on the island. Due to the presence of the charging energy, further tunneling is suppressed. In the second half of the cycle, one charge leaves the island towards the right lead, while an existing quasiparticle is annihilated. In this chapter, we focus on a clocked *spin pump* with a spin-split island DOS. The onset of a tunneling process therefore depends on the spin of the participating quasiparticle, as shown in Fig. 4.2 (b). The result is an *up-spin* pump cycle between the charge states $0 \leftrightarrow 1$. The black dashed loop in Fig. 4.2 (a) and (b) shows a second possible driving cycle between the charge states $1 \leftrightarrow 2$, leading to *down-spin* pumping in the SFISFIS structure. However, we will show that the up-spin pump cycle is favored by the spin-selective tunnel resistances.

4.3 Calculation of charge and spin currents

For a quantitative analysis of the clocked spin pump, we investigate the probabilities $P(n, N^{\uparrow}, N^{\downarrow})$ that the island holds n excess charges and $N^{\uparrow}$ and $N^{\downarrow}$ quasiparticle excitations of respective spin. Since the parity of excess charges equals the parity of quasiparticles, the occupation

probabilities are restricted to the ones, where n and $N^{\uparrow}+N^{\downarrow}$ are both even or both odd. Similarly to previous studies on S/N hybrid structures, see, e. g., Ref. [166] and App. A.3, we derive a master equation in the sequential-tunneling limit, describing the time evolution of the occupation probabilities in the SFISFIS setup,

$$\partial_t P(\chi) = \sum_{\chi'} \Big[W_{\chi}^{\chi'} P(\chi') - W_{\chi'}^{\chi} P(\chi) \Big]. \tag{4.4}$$

Here, $W_{\chi'}^{\chi} = \sum_{\alpha=\mathrm{L,R}} W_{\chi'}^{\chi;\alpha}$ is a transition rate from χ to χ', with $\chi = (n, N^{\uparrow}, N^{\downarrow})$, via quasiparticle tunneling between island and contacts. These rates contain the superconducting DOS of both island and contacts and the number of already excited quasiparticles on the island via the distribution functions F_{N^σ}. For instance, the rate for tunneling of a charge towards the island with simultaneous increase of $N^{\uparrow}$ reads as

$$\begin{aligned} W_{n+1,N^{\uparrow}+1,N^{\downarrow}}^{n,N^{\uparrow},N^{\downarrow}} = \frac{1}{R_{\uparrow}} \sum_{\alpha=\mathrm{L,R}} \int_0^{\infty} dE\, g_{\uparrow}(E) \left[1 - F_{N^{\uparrow}}(E)\right] \\ \times g_{\alpha}(E + \delta E_{+}^{a,n})\, f^{+}(E + \delta E_{+}^{a,n})\,. \end{aligned} \tag{4.5}$$

We model the quasiparticle distribution functions, F_{N^σ}, by Fermi functions with an *effective* temperature T_{N^σ} [150, 166, 167] (details are shown in App. A.2). This temperature is implicitly set by fixing the island's quasiparticle number

$$N^{\sigma} = 2\,\nu_0 V_{\mathrm{I}} \int_0^{\infty} dE\, g_{\sigma}(E) F_{N^\sigma}(E), \tag{4.6}$$

with the island's volume V_{I}. With the help of the transition rates and the occupation probabilities obtained from Eq. (4.4), the charge current through the island can be written as

$$\begin{aligned} I = -\frac{1}{2} \sum_{\alpha=\mathrm{L,R}} \sum_{\sigma} {\sum_{n,N^{\uparrow},N^{\downarrow}}}' \alpha P(n, N^{\uparrow}, N^{\downarrow}) \Big[W_{n+1,N^{\sigma}+1}^{n,N^{\sigma};\alpha} \\ + W_{n+1,N^{\bar{\sigma}}-1}^{n,N^{\bar{\sigma}};\alpha} - W_{n-1,N^{\sigma}-1}^{n,N^{\sigma};\alpha} - W_{n-1,N^{\bar{\sigma}}+1}^{n,N^{\bar{\sigma}};\alpha} \Big], \end{aligned} \tag{4.7}$$

and the spin current as

$$J = \frac{1}{4} \sum_{\alpha=\mathrm{L,R}} \sum_{\sigma} \sum_{n,N^{\uparrow},N^{\downarrow}}{}' \alpha\sigma P(n,N^{\uparrow},N^{\downarrow}) \Big[W^{n,N^{\sigma};\alpha}_{n+1,N^{\sigma}+1} + W^{n,N^{\bar{\sigma}};\alpha}_{n+1,N^{\bar{\sigma}}-1} - W^{n,N^{\sigma};\alpha}_{n-1,N^{\sigma}-1} - W^{n,N^{\bar{\sigma}};\alpha}_{n-1,N^{\bar{\sigma}}+1} \Big]. \tag{4.8}$$

Here, we introduced $\sum'_{n,N^{\uparrow},N^{\downarrow}} = \sum_{n,N^{\uparrow},N^{\downarrow} \text{ with } p(n)=p(N^{\uparrow}+N^{\downarrow})}$ as a short-hand notation, and also $\bar{\sigma} = -\sigma$. The index α of all tunnel rates in Eqs. (4.7) and (4.8) denotes that these rates are taken only for transfer via the α lead, where α takes the values ± 1 for L/R, when used as a variable. Besides that, we abbreviated $W^{n,N^{\uparrow},N^{\downarrow};\alpha}_{n+1,N^{\uparrow}+1,N^{\downarrow}}$ and $W^{n,N^{\uparrow},N^{\downarrow};\alpha}_{n+1,N^{\uparrow},N^{\downarrow}+1}$ by $W^{n,N^{\sigma};\alpha}_{n+1,N^{\sigma}+1}$, suppressing the index of the quasiparticle number which remains unchanged in the tunneling process, and similarly also for the other transition rates. Remarkably, the spin current in Eq. (4.8) can be interpreted as a sum over spin-polarized charge currents, although it is known that in a superconductor the spin current is in general determined by the quasiparticle current [153]. However, owing to the even-odd parity effect on the small island, a change in the number of island charges by ± 1 causes a change in the number of quasiparticles; therefore in the regime of weak coupling and large charging energy analyzed here, spin-polarized charge currents are a meaningful quantity. We present technical details about the master equation and the transition rates in Apps. A.1-A.3.

4.4 Clocked spin-polarized transport

To illustrate the working principle of the clocked spin pump, it is insightful to plot the evolution of the relevant spin-dependent transition rates over one period of the time-dependent drive. The relevant rates are presented in Fig. 4.2 (c) along the black solid driving cycle shown in Fig. 4.2 (b). We find that the rate for a charge tunneling onto the island by creating an up-spin quasiparticle is largely increased compared to the one for a down-spin during the time span τ_{load}. Only when the energy for creating a down-spin quasiparticle on the island can be brought up, the respective tunnel rate increases. However, the island has already been occupied by an additional charge during τ_{load} with

a high probability, making this rate basically irrelevant. In addition, it remains small due to the strongly spin-polarized tunnel resistances, and can even be fully suppressed by adjusting the driving cycle such that the crossing at (ii) is avoided. In the second half of the driving cycle, the rate for annihilating a down-spin quasiparticle sets in before the corresponding rate for an up-spin quasiparticle becomes relevant. Since, however, no down-spin quasiparticle is occupying the island, also this rate is irrelevant for the turnstile operation. Consequently, during the time span τ_{unload}, an up-spin quasiparticle together with one charge leaves the island.

We proceed by analyzing the generated charge and spin current over a large range of working points, $\bar{n}_{\mathrm{g}}$, and driving amplitudes, δn_{g}, in order to point out regimes, where a precise spin current is achieved. Figure 4.3 displays the results for the pumped charge ($\bar{I}$) and spin ($\bar{J}$) averaged over the sinusoidal driving cycle. Let us first analyze the left panels in Fig. 4.3, where the Dynes parameter $\gamma = 10^{-6}\Delta$ suppresses contributions which arise from the leakage current. Here, the transferred charge is quantized in the triangular regions, which are expected from the stability diagrams illustrated in Fig. 4.2 (a)-(b). The upper row in Fig. 4.3 shows that the spin-dependent tunnel resistances already lead to a partially spin-polarized current, even when the split field is neglected. However, as clearly visible in the line cuts shown below, the amount of polarization strongly depends on the driving frequency and the chosen working point. Besides that, the line-cuts for $P = 99\%$ show that an increase in the barrier polarization can even be detrimental for the turnstile precision. This is a consequence of the spin blockade effect, which occurs if a *down*-spin quasiparticle which has entered the island does not tunnel out during the time τ_{unload}, due to fast driving and the reduced tunnel rate for down-spin quasiparticles. The advantage of a finite split field h caused by the FI layer is apparent in the second row and the related line cut below: the spin-pumping precision is greatly enhanced in the left yellow region. This corresponds to the up-spin pump cycle indicated in Fig. 4.2 (b), where the transfer of down-spin particles is energetically blocked. Furthermore, the left plateau in the line cuts shows that the precision of this fully spin-polarized clocked current is little sensitive to the driving frequency as well as to small deviations in the working point and the barrier polarization, as long as the turnstile operation is enabled. This is in

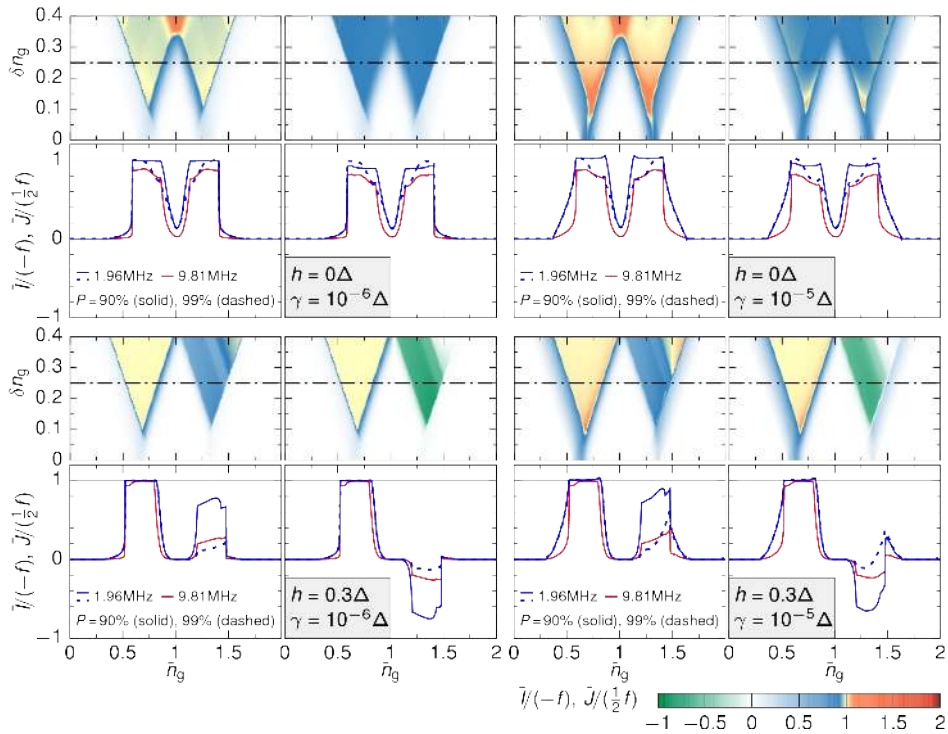

Figure 4.3: Density plots of the pumped charge ($\bar{I}$) and spin ($\bar{J}$) per period as a function of the average gate charge $\bar{n}_\mathrm{g}$ and the driving amplitude δn_g without and with split field h (upper and lower panels) and with $\gamma = 10^{-6}\Delta$ and $\gamma = 10^{-5}\Delta$ (left and right). Here, we set $A(t) = \sin(2\pi f t)$, with driving frequency $f = 1.96\mathrm{MHz}$, $E_\mathrm{c} = 2.2\Delta$, $V = \Delta$, $1/\beta = 0.01 T_\mathrm{c}$, $V_\mathrm{I} = 1.5 \cdot 10^5 \mathrm{nm}^3$, $\nu_0 = 1.45 \cdot 10^{47} \mathrm{m}^{-3}\mathrm{J}^{-1}$, $T_\mathrm{c} = 1.3\mathrm{K}$, $\Delta = 200\mu\mathrm{eV}$, $R_\uparrow = 100\mathrm{k}\Omega$ and $P = 90\%$. The dashed-dotted line in each density plot indicates the respective cut which is shown below, for different driving frequencies and barrier polarizations.

contrast to the green region on the right of the plot, where the turnstile operates as a down-spin pump [see Fig. 4.2 (b)]. Here, depending on the spin polarization of the tunnel resistances, the performance is severely limited.

The right panel of Fig. 4.3, compared to the left panel, demonstrates

the effect of a larger Dynes parameter γ [$10^{-5}\Delta$ instead of $10^{-6}\Delta$]. Consequently, the leakage current is enhanced in the right set of plots. A comparison between the left and the right panels reveals regions where the leakage current yields a significant contribution to the pumped charge per cycle. This is in particular the case for the additional features occurring at amplitudes $\delta n_{\mathrm{g}} \lesssim 0.1$. Also, a smoother transition between regions of vanishing and finite pumped charge and spin can be observed. In the triangular regions of quantized charge and spin transfer, the enhanced leakage current due to the increased Dynes parameter only leads to slight inaccuracies, which can be reduced by increasing the frequency of the periodic driving. Additional features visible in the density plots in Fig. 4.3 are discussed in Sec. 4.6.

4.5 Error sources

Let us outline possible error sources of the proposed up-spin turnstile. A relevant time scale, setting a limit to the operation precision, is given by the inverse of the rate for a charge to tunnel *off* the island by annihilating a quasiparticle. During the time τ_{unload}, indicated in Fig. 4.2 (c), this rate is roughly $W_{\mathrm{unload}} \approx (2R_{\uparrow}\nu_0 V_{\mathrm{I}})^{-1} \approx 9\mathrm{Mhz}$ (for the parameters in Fig. 4.3). Caused by the large DOS of the island, this rate is orders of magnitude lower than the rate for tunneling *on* the island with simultaneous creation of a quasiparticle [see Fig. 4.2 (c)]. For a precise clocked spin pump, the driving frequency is required to be small enough to provide $\tau_{\mathrm{unload}} \gtrsim 1/W_{\mathrm{unload}}$. However, if the driving frequency is too small, errors might get facilitated due to pair breaking on the island (with a rate of the order of a few kHz [150]), to spin flips (which we here expect to be absent due to the spin-split DOS and the absence of magnetic impurities) and to leakage currents as discussed above (with rates of the order of $\gamma/R_{\sigma} \approx 10\mathrm{kHz}$ (100kHz) for the parameters in the left (right) panels in Fig. 4.3 and $\sigma = \uparrow$). Consequently, the described spin-pump operation can only be achieved if $\gamma/R_{\sigma} \ll W_{\mathrm{unload}}$, which restricts the Dynes parameter to be below $10^{-4}\Delta$, for all other parameters taken as in Fig. 4.3. Also, a small driving frequency risks to reduce the magnitude of the spin-polarized current to the noise level of the measurement. This issue can be solved

by optimizing the driving cycle. The rate W_{unload} can be increased by decreasing the island size, which we here estimate to be of volume $V_I = 200 \times 50 \times 15\,\mathrm{nm}^3$. A way to increase the time τ_{unload} without decreasing the driving frequency is to design the shape of the driving signal appropriately. Furthermore, an increase in the generated spin current can also be achieved by operating multiple spin turnstiles in a synchronized way [38].

In addition to these limitations, higher-order tunnel processes potentially induce errors, because they enable the tunneling of multiple charges per cycle. The dominant processes in second-order tunneling are cotunneling and Andreev reflection. However, cotunneling is exponentially suppressed for $V < 2\Delta$ [39], as it is the case here. Importantly, the structure proposed here is well protected against Andreev reflection and other detrimental higher-order processes that involve tunneling of Cooper pairs, because the spin-polarized tunnel barriers suppress the tunneling of particles with opposite spins. For instance, we estimate the tunnel rate for Andreev reflection to be suppressed by a factor of $(1-P)/(1+P)$, when compared to the Andreev tunnel rate through a non-magnetic barrier [39]. A detailed quantitative analysis of higher-order processes in the presence of spin-polarized barriers and their level of importance is left for future research.

4.6 Additional features in the pumped charge and spin currents

Finally, we discuss additional features visible in the pumped charge and spin per cycle shown in Fig. 4.3, which are however irrelevant for the proposed spin-turnstile operation. The first feature which we want to point out occurs in the vicinity of $\bar{n}_{\mathrm{g}} = 1$ for $\delta n_{\mathrm{g}} > 0.3$, as it can be seen in the upper panel for the pumped charge for $h = 0$. In this region the pumping cycle is large enough to transfer two charges through the device, as indicated in Fig. 4.4 (a), by combining both driving cycles shown in Fig. 4.2 (b). For the parameters shown, the transferred charge remains less than 2 since the tunneling of the down-spin is suppressed by the polarized tunnel barriers.

Besides that, two features appear in the upper right part of the density plots for a finite split field (lower panels in Fig. 4.3). Towards

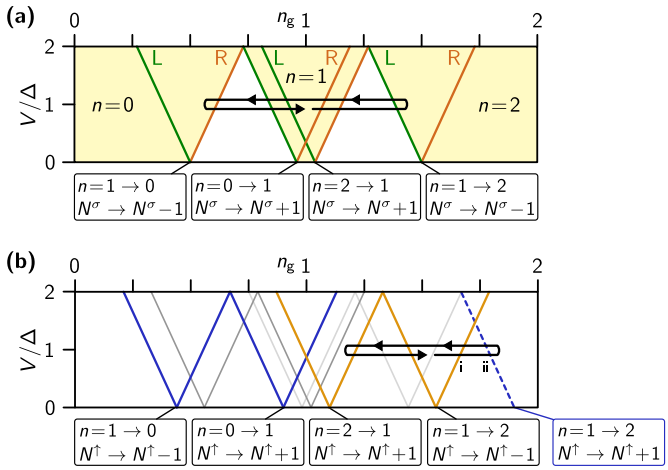

Figure 4.4: (a) Similar to Fig. 4.2 (a). The black loop indicates a pump cycle leading to the pumping of two charges per period. (b) Similar to Fig. 4.2 (b). The black loop indicates a pump cycle where the transition $n = 1 \to 2$ via the *creation* of a quasiparticle (blue dashed line) can occur, in the case that the transition $n = 1 \to 2$ via the *annihilation* of a quasiparticle did not take place earlier in the pump cycle (e.g. due to fast driving). Crossings with the threshold lines for processes $(n = 1 \to 2, N^\uparrow \to N^\uparrow - 1)$ via the right contact and $(n = 1 \to 2, N^\uparrow \to N^\uparrow + 1)$ via the left contact are marked by i and ii.

increasing drive amplitude δn_g and for working points $\bar{n}_g > 1$, we first find a region where the amount of pumped charge and spin slightly decreases (also visible in the line cuts in the lower panels in Fig. 4.3). The decrease is a consequence of the pumping cycle crossing the transition line $(n = 1 \to 2, N^\uparrow \to N^\uparrow - 1)$ also for the *right* contact. Furthermore, for even larger drive amplitude and for working points $\bar{n}_g > 1$, we find a region where again one charge is pumped per cycle. The onset of this region coincides with the crossing of the pumping cycle with the transition line $(n = 1 \to 2, N^\uparrow \to N^\uparrow + 1)$, which is shown Fig. 4.4 (b). This means that, in this region, the occupation probability $P(2, 2, 0)$ for two up-spin quasiparticles occupying the island becomes finite and contributes to the pumped charge current.

Importantly, the pumped spin is suppressed in this region, since both the tunneling of an up-spin and of a down-spin is finite there. Note that this process is only possible if the island can be occupied by two up-spin quasiparticles which do not relax, i. e., recombination processes following a spin flip have to be suppressed, as assumed in the model calculation.

4.7 Conclusive remarks

In this chapter, we proposed a clocked, accurate source for single spins, based on the parity effect in a S island with S contacts operated as a turnstile. The special spin properties of the structure originate from the presence of a ferromagnetic insulator layer, which splits the quasiparticle DOS of the island, and at the same time provides strongly spin-polarized tunneling barriers, while leaving the contacts nonmagnetic. We emphasize that it is the combination of these effects, which provides the possibility of reaching fully polarized, clocked spin currents for spintronic applications over a significant range of driving frequencies and working points.

In addition, we expect these FIS layers to be highly advantageous also for charge turnstiles, which—if the precision can be enhanced—are promising candidates for a novel SI current standard [4, 19, 20]. In these SINIS devices elastic and inelastic cotunneling effects are successfully blocked. However, they suffer [36, 37] from errors stemming from third-order Cooper-pair-electron cotunneling [39] and photon-assisted-tunneling induced Andreev reflection [42]. We therefore suggest a setup, where the insulating barriers are replaced by FI layers to suppress Andreev reflection with the help of strongly spin-polarized barriers. This could greatly enhance the precision of clocked charge currents by up to two orders of magnitude for realistic barrier polarizations of $P = 98\%$.

Besides that, we note that the analysis of charge and spin currents in this chapter was based on current *expectation* values. We identified parameter regions, where the currents generated during the turnstile operation are barely influenced by small variations of the employed working point and driving amplitude. This is a key property for an accurate turnstile, because these variations would occur in a real

device. However, even in these regions, the turnstile precision is altered by charge and spin *fluctuations*, which produce a current noise. To characterize the emission process and the precision of spin (or charge) turnstiles, it is, therefore, crucial to also investigate the noise of the emitted currents in the presence of the time-dependent driving.

In the next chapter, we derive this finite-frequency current noise for a different single-electron tunneling device, namely for a single-electron source based on a time-dependently driven single-contact quantum dot. For the calculations, we extend the real-time diagrammatic pertubative approach in the tunnel coupling, which is introduced in Secs. 3.1, see also Sec. 5.4. It would be an interesting future project, to also conduct a detailed analysis of the spin- and charge-current noise in the SFISFIS turnstile, e. g., using the real-time diagrammatic method.

5 Noise of Interacting Single-Electron Emitters

A central quantity for the characterization of charge transport through single-electron tunneling devices is provided—besides the current itself—by the current noise [48–50]. In this chapter and the subsequent Chap. 6, we analyze the current noise of single-electron emitters, which are built from time-dependently driven interacting quantum dots, see Secs. 2.1 and 2.2. A paper which includes parts of Secs. 5.2-5.4 and the related Apps. B.1-B.6 (and parts of Chap. 6) is published in Phys. Rev. B **98** 115414 (2018). We begin the present chapter by motivating an analysis of the current noise of single-electron tunneling devices in Sec. 5.1. The subsequent sections are outlined at the end of this section.

5.1 Current noise in single-electron transport

The charge current which is emitted from a nanoelectric device typically contains noise [49, 50]. The origin of this current noise are thermal and quantum fluctuations of the charge configuration in the system. This leads to fluctuations in the current signal, i. e., the actual current deviates from a time-averaged mean value. The current-noise spectrum can reveal how two of these current fluctuations, which occur at different times t and t', are correlated, e. g., due to the Pauli exclusion

principle or to Coulomb repulsion in the nanosystem. [56, 57, 168].[1]

In experiments, the current noise is often detrimental to the desired application of a nanoscale device. However, it also constitutes an interesting signal in itself [48], containing information on the system's excitation spectrum, on time scales of the electron dynamics and on interaction. A prominent example is that the zero-frequency noise of a current, which flows through a tunnel junction, reveals the charge of the charge carriers in the system [49]. This so-called shot noise has been used to measure the charge fractionalization in the fractional quantum Hall effect [169, 170]. Furthermore, the frequency dependence of the noise spectrum can be related to energy emission and absorption processes, which has been demonstrated in transport through nanoscale devices in the stationary regime [168, 171, 172].

In single-electron transport, the finite-frequency noise has been measured, e. g., by Ubbelohde et al., to determine a temporal correlation between current pulses. In Ref. [168], they studied a quantum dot with weak coupling to two electron reservoirs, and they applied a bias voltage across the dot, leading to the sequential tunneling of single electrons through the device. In this setup, due to electron-electron repulsion, an electron which tunnels onto the dot blocks the tunneling of further incoming charges, until one electron has tunneled out (Coulomb blockade). The consequence is a correlation between the emitted electrons, and the measured noise spectrum thus deviates from a frequency-independent *white* noise spectrum, showing that electron emission in this setup is not a purely stochastic process [49].

In addition to the stationary system studied by Ubbelohde et al., the finite-frequency noise of a time-dependently driven quantum dot has been investigated by Mahe et al. in Ref. [56]. In this work, they reported the measurement of the finite-frequency current noise of a single-contact quantum dot, which is exposed to an ac gate-voltage driving [21], see also Sec. 2.2. By comparing the noise measurements with theoretical calculations, they identified a regime, where the system acts as an ac single-electron source, i. e., it emits a single electron and a single hole per periodic driving cycle. This operation as a single-electron emitter leads to a measurable decrease in the current-noise

[1] Note that the frequency dependence of the noise spectrum stems from a Fourier transform of the correlation function between two current fluctuations, with respect to $t' - t$. All noise quantities studied in this thesis are defined in Sec. 5.3.

signal at finite frequencies. The remaining noise contributions are attributed to fluctuations in the emission times (phase noise), see also Ref. [57]. This experiment emphasizes the importance of noise measurements, to ensure that a single-electron source, which generates a quantized current on average, actually emits a quantized number of electrons/holes in each period of an ac drive.

In this chapter, as well as in Chap. 6, we provide a comprehensive theoretical analysis of the finite-frequency noise spectrum of on-demand single-electron emitters. For the theoretical description, we focus on devices similar to the ones studied by Mahe et al. [21, 56, 57], which are built from a quantum dot with tunnel coupling to a single electron reservoir, see Secs. 2.1-2.2. Theoretically, finite-frequency current noise of quantum dots has been analyzed mostly in the stationary regime [173–186], and the study of time-dependent setups [51–53, 187] has so far been limited to systems where Coulomb interaction seems to play no major role. Therefore, we emphasize that a particular focus of this work is to investigate the impact of Coulomb repulsion on the quantum dot to finite-frequency noise spectra. This is relevant to obtain a complete picture of the finite-frequency noise in these systems, where interaction can be strong [29], and to point out unambiguous signatures of interaction in the noise spectra. We also take into account a slow time-periodic driving of a gate voltage, which triggers the emission of single electrons (and holes) into the reservoir, and we study the noise in the presence of this driving.

Importantly, in contrast to previous works, in which the stationary regime was studied, we here also have to treat the time scale of the driving with care. We investigate the noise for slowly driven system parameters, focusing on the instantaneous contribution to the noise, where the system is considered to always follow the driving. In addition, we analyze the first-order correction, namely the adiabatic response, which takes into account the lag of the system state with respect to the time-dependent drive. One generic consequence of the driving, independent of these approximation schemes, is that the finite-frequency noise also depends on time. We show that the study of the zeroth and first *harmonic* of this time-dependent function is particularly insightful—a quantity that has attracted little attention so far [188].

The remainder of this chapter is structured as follows. In Sec. 5.2,

we define the studied model and introduce the method employed for the noise calculations, which is based on the real-time diagrammatic technique of Sec. 3.1. In Sec. 5.3, we explain all noise quantities analyzed in this thesis. In Sec. 5.4, we outline the diagrammatic noise calculations for the interacting quantum dot, and in Sec. 5.5, we briefly describe a related calculation for a noninteracting quantum dot, performed, for comparison, in Floquet scattering-matrix theory. Note that in the present chapter, we mostly focus on the technical aspects of the noise calculations, and we present the main physical results in Chap. 6.

5.2 Model and real-time diagrammatic method

We consider a quantum dot with possibly strong on-site Coulomb interaction and weak tunnel coupling to a single electron reservoir, as illustrated in Fig. 5.1 (b). The working principle of this single-electron emitter is shown in Fig. 5.1 (a). A time-periodic gate voltage leads to a time-dependent modulation of the quantum-dot levels, which makes tunneling processes out of or into the quantum dot energetically accessible. The finite-frequency noise of this single-electron source contains information not only on the device's precision, but also on temporal delays in the described emission process [56, 57] and has recently even been used for quantum-state tomography of the emitted particles [188]. As mentioned in the previous section, we want to show that Coulomb interaction can have a significant impact on such noise spectra. To unambiguously identify interaction-induced features in the noise, we compare the results to a noninteracting quantum dot, both in the spin-degenerate case as shown in Fig. 5.1 (c), as well as in the presence of a strong magnetic field, see Fig. 5.1 (d). As a theoretical model for the single-contact quantum dot, we employ the Anderson Hamiltonian introduced in Sec. 2.1, see Eq. (2.1). This Hamiltonian describes a single time-dependent quantum-dot level $\epsilon_\sigma(t)$, with on-site interaction U and tunnel coupling Γ to the nearby electron reservoir. We consider a harmonic gate-voltage driving, leading to the time-dependent energy level $\epsilon_\sigma(t) = \bar{\epsilon}_\sigma + \epsilon_\mathrm{g}(t)$ with the cosine contribution $\epsilon_\mathrm{g}(t) = \delta\epsilon\cos(\Omega t)$, where Ω denotes the driving frequency and $\delta\epsilon$ the driving amplitude.

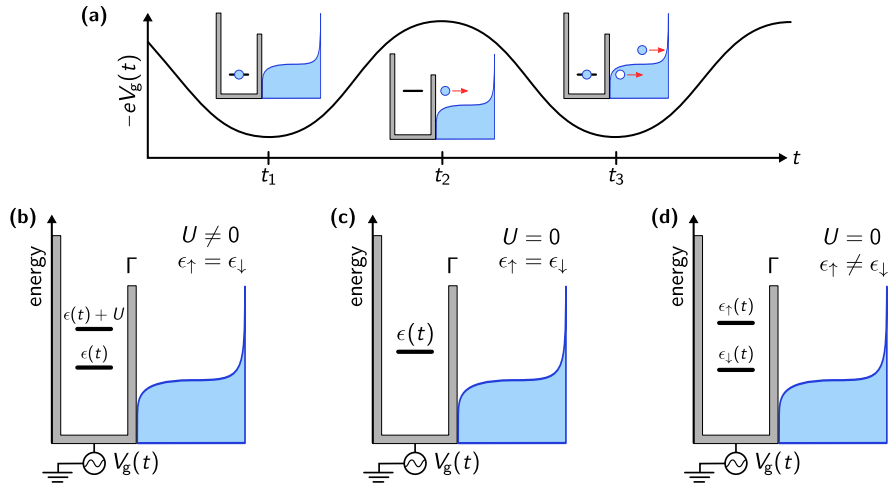

Figure 5.1: (a) Working principle of the single-electron emitter: A harmonic gate voltage, $V_g(t)$, results in the periodic emission of single electrons and holes into the reservoir at crossings between the dot's and the reservoir's electrochemical potentials. (b) Energy landscape of a spin-degenerate quantum dot with on-site Coulomb interaction U, tunnel coupled to an electron reservoir with coupling strength Γ. Similar setups with vanishing Coulomb interaction are shown in (c) for a spin-degenerate and in (d) for a spin-split energy level.

For the finite-frequency noise calculations, we extend a real-time diagrammatic technique [64–67], see also Sec. 3.1. This method is based on a perturbative expansion in the tunnel coupling between the quantum dot and the reservoir. For stationary systems, it has, e. g., been applied to study the finite-frequency noise of a single-electron transistor [173], a quantum-dot spin valve [175] and a quantum dot coupled to normal and superconducting contacts [183]. For systems with slow periodic time dependence, as considered here, Ref. [54] analyzes the noise of adiabatic quantum pumps. This calculation is however restricted to the (long-time) zero-frequency noise, which vanishes when the dot is in contact with a single reservoir only. In the next two sections, we extend the approach of Ref. [54] to finite noise frequencies. In the calculations of the finite-frequency noise,

we distinguish a high, an intermediate and a low noise-frequency regime, $\omega \gg \Gamma$, $\omega \sim \Gamma$ and $\omega \ll \Gamma$, with noise frequency ω, and we discuss appropriate approximation schemes for these three regimes. We continue by defining the noise quantities studied in this thesis.

5.3 General properties of the noise

5.3.1 Finite-frequency noise and noise harmonics

The main topic in this and the subsequent chapter is given by the current noise, namely fluctuations in the charge current emitted by the time-dependently driven quantum dot. The current operator, measuring the charge current into the tunnel-coupled reservoir, is given by $I = -i \sum_{\sigma k} \left(\gamma d_\sigma^\dagger c_{\sigma k} - \gamma^* c_{\sigma k}^\dagger d_\sigma\right)$. Using this expression we define the current-fluctuation operator, $\delta I = I - \langle I \rangle$, and its symmetrized two-time correlator $\mathcal{C}(t,\tau) = \langle \{\delta I(t), \delta I(t+\tau)\} \rangle$. The time t is taken as the reference measurement time and τ is the time difference between two current measurements at t and $t' = t + \tau$. Here, curly brackets denote an anti-commutator, and the time dependence of operators is treated following the Heisenberg picture. As usual, the finite-frequency current-noise spectrum is obtained by a Fourier transform of this correlator with respect to the *time difference*,

$$S(t;\omega) = \int_{-\infty}^{\infty} d\tau e^{i\omega\tau} \mathcal{C}(t,\tau). \tag{5.1}$$

However, in contrast to standard treatments, this finite-frequency noise still depends on the time t. This is caused by the time-dependent driving of the quantum dot, breaking time-translational invariance. We refer to the quantity defined in Eq. (5.1) as the *time-resolved finite-frequency noise*. The study of this quantity gives us, to some extend, an intuitive understanding of the effect of time-dependent driving and the response times on the noise spectrum, as demonstrated in Sec. 6.1. However, it is at the same time hard to disentangle various effects governing this quantity and it is also expected to be difficult to measure in a realistic experiment. In addition to the time-resolved finite-frequency noise, we therefore promote the study of the symmetric

quantity	brief description	reference
$S(t;\omega)$	time-resolved finite-frequency noise	Eq. (5.1)
$\mathcal{S}(n=0;\omega)$	time-averaged noise spectrum	Eq. (5.2)
$\mathcal{S}(n\neq 0;\omega)$	nth noise harmonic	Eq. (5.2)
$\tilde{S}(t;\omega)$	auxiliary function for diagrammatic noise calculations	Eq. (5.4)
$\boldsymbol{P}(t)$	quantum-dot occupation vector	Sec. 3.1
$\boldsymbol{F}^{(i)}(t)$	instantaneous fluctuation vector	Eqs. (6.2), (6.7), (6.10)

Table 5.1: List of quantities analyzed in Chaps. 5 and 6.

current-noise harmonics,

$$\mathcal{S}(n;\omega)=\int_0^T\frac{dt}{T}\int_{-\infty}^{\infty}d\tau e^{in\Omega t+i\omega\tau}\mathcal{C}(t,\tau), \tag{5.2}$$

with index n. Studying these noise harmonics, in particular the case $n=1$, is a main focus of Chap. 6. There, we investigate temporal correlations between the driving signal and the noise spectrum. Equation (5.2) also defines the more standardly studied *time-averaged noise spectrum*, $\mathcal{S}(n=0;\omega)$. This quantity has, e. g., proven to be helpful to characterize the precision of single-electron emitters [56, 57]. Here, we show that information on fluctuation processes, which is hard to extract from these time-averaged noise spectra, can be accessed by analyzing the first noise harmonic. The main quantities investigated in this and the subsequent chapter are listed in Tab. 5.1.

5.3.2 Auxiliary function for the diagrammatic noise calculation

In Chap. 6 we analyze both the noise harmonics [Eq. (5.2)] and the time-resolved finite-frequency noise [Eq. (5.1)] of the quantum dot, while the dot is operated as an on-demand electron emitter. As explained in Sec. 5.4, we therefore extend a real-time diagrammatic perturbative approach for weakly coupled quantum dots. For this purpose, as well as for an expansion in small driving frequencies which is detailed below,

it turns out to be helpful to rewrite the noise harmonics as

$$\mathcal{S}(n;\omega) = \int_0^T \frac{dt}{T} e^{in\Omega t} \left[\tilde{S}\,(t;\omega) + \tilde{S}\,(t;n\Omega-\omega)\right], \tag{5.3}$$

with the *auxiliary function*,

$$\tilde{S}\,(t;\omega) = \int_{-\infty}^{t} dt' e^{i\omega(t'-t)} \Big[\big\langle \{I(t), I(t')\} \big\rangle - 2\,\langle I(t)\rangle \big\langle I(t')\big\rangle \Big]. \tag{5.4}$$

See App. B.1 for the derivation of this expression. The advantage of this rewriting is that all other times, $t' = t + \tau$, lie in the past with respect to the reference time t.

5.3.3 Expansion for slow gate-voltage driving

As discussed before, we consider the emission and absorption of single electrons by the quantum dot to be triggered by a slow time-dependent driving of the gate voltage, namely $\delta\epsilon\,\Omega\beta/\Gamma \ll 1$. This condition ensures that the system has enough time for electron emissions/absorptions to occur during each level crossing caused by the drive. This justifies an expansion of the noise expression in Eq. (5.3) in terms of the small parameter $\delta\epsilon\,\Omega\beta/\Gamma$, see, e. g., Refs. [54, 67]. In the next paragraph, we outline the main idea of this expansion, which should suffice to follow the discussions of results in Chap. 6. For technical aspects we refer to Sec. 5.4, where we explain all steps of the noise derivations in detail.

In order to obtain the noise-harmonics expression in Eq. (5.3) for slow driving, we expand the auxiliary function as $\tilde{S}(t;\omega) \to \tilde{S}^{(\mathrm{i})}(t;\omega) + \tilde{S}^{(\mathrm{a})}(t;\omega) + \dots$. The first term in this series is the *instantaneous* contribution, marked with a superscript (i). It contains the zeroth order in the expansion in the slow-driving parameter, $\delta\epsilon\,\Omega\beta/\Gamma$. In zeroth order, the slow driving expansion describes the time evolution of a system, which always follows its instantaneous stationary state. Hence, to derive the instantaneous contribution to the auxiliary noise function, we consider a stationary quantum dot with parameters frozen at time t. The second term in the series above contains the first order in the slow-driving expansion, which takes into account a small retarded response of the system with respect to the time-dependent driving. Therefore, we call terms of this type, indicated with the superscript (a),

the *adiabatic response*. By inserting the expansion of the auxiliary function into Eq. (5.3) and expanding rigorously up to first order in the small-driving parameter, we obtain the instantaneous noise and its adiabatic response,

$$\mathcal{S}^{(\mathrm{i})}(n;\omega) = \int_0^T \frac{dt}{T} e^{in\Omega t}\Big[\tilde{S}^{(\mathrm{i})}(t;\omega) + \tilde{S}^{(\mathrm{i})}(t;-\omega)\Big] \tag{5.5a}$$

$$\begin{aligned}\mathcal{S}^{(\mathrm{a})}(n;\omega) = \int_0^T \frac{dt}{T} e^{in\Omega t}\Big[&\tilde{S}^{(\mathrm{a})}(t;\omega) + \tilde{S}^{(\mathrm{a})}(t;-\omega) \\ &+ \Omega n\, \partial_x \tilde{S}^{(\mathrm{i})}(t;x)\big|_{x=-\omega}\Big].\end{aligned} \tag{5.5b}$$

As pointed out before, the technical calculations of the expressions $\tilde{S}^{(\mathrm{i})}(t;\omega)$ and $\tilde{S}^{(\mathrm{a})}(t;\omega)$ are presented in Sec. 5.4. Prior to these derivations, we now discuss some general properties of the instantaneous and adiabatic-response contributions to the noise harmonics [Eqs. (5.5)].

5.3.4 Instantaneous finite-frequency noise

The instantaneous contribution to the noise can in many respects be understood as the noise of a stationary equilibrium system (due to the presence of only a single reservoir). The time t merely enters as a parameter, and the instantaneous noise therefore inherits a number of properties that are known for these kind of stationary systems.

First of all, the symmetrized and time-averaged instantaneous finite-frequency noise, Eq. (5.5a) with $n = 0$, is always real. The technical reason is that the auxiliary function, Eq. (5.4), fulfills $\tilde{S}(t;\omega) = \tilde{S}^*(t;-\omega)$, which also holds for the instantaneous and adiabatic-response parts separately. Furthermore, because we consider a cosine driving of the gate voltage, we find that the instantaneous part of the auxiliary function, $\tilde{S}^{(\mathrm{i})}(t;\omega)$, is an even function in t. We conclude that all noise harmonics in instantaneous order, Eq. (5.5a) with $n \neq 0$, are real quantities. The same is then true for the time-resolved finite-frequency noise, Eq. (5.1), in instantaneous order.

The instantaneous part of the time-resolved finite-frequency noise, being the one of an equilibrium system with parameters frozen at the reference time t, is furthermore expected to fulfill a fluctuation-dissipation theorem. Here, we give its explicit shape and show an interesting extension for the first noise harmonic. More specifically, the

instantaneous contribution to the noise fulfills a fluctuation-dissipation theorem [189] at every fixed level position $\epsilon_\sigma(t)$, where t serves as a parametrization,

$$S^{(\mathrm{i})}(t;\omega) = 2\omega \coth\left(\frac{\beta\omega}{2}\right) \mathrm{Re}\, G(\{\epsilon_\sigma(t)\};\omega). \tag{5.6}$$

It connects the equilibrium noise spectrum at time t, $S^{(\mathrm{i})}(t;\omega)$, to the real part of the finite-frequency linear-response admittance (i. e. the conductance) $G(\{\epsilon_\sigma(t)\};\omega) = \frac{\partial I(\omega)}{\partial \epsilon_\mathrm{g}(\omega)}\Big|_{\{\epsilon_\sigma(t)\}}$, evaluated for the system being in equilibrium at the level positions given by $\{\epsilon_\sigma(t)\}$.

We now use the expression given in Eq. (5.6), in order to derive extensions of the fluctuation-dissipation theorem for zeroth and first noise harmonics. For $n = 0$, we find

$$\mathcal{S}^{(\mathrm{i})}(0;\omega) = \int_0^T \frac{dt}{T} 2\omega \coth\left(\frac{\beta\omega}{2}\right) \mathrm{Re}\, G(\{\epsilon_\sigma(t)\};\omega). \tag{5.7}$$

In the same way, we derive the fluctuation-dissipation theorem for the first noise harmonic, $n = 1$. For the cosine gate-voltage driving, $\epsilon_\mathrm{g}(t) = \delta\epsilon\cos(\Omega t)$, we make a parameter replacement using ϵ_g instead of time, such that the relation reads

$$\mathcal{S}^{(\mathrm{i})}(1;\omega) = \frac{2\omega}{\pi} \coth\left(\frac{\beta\omega}{2}\right) \int_{-\delta\epsilon}^{\delta\epsilon} d\epsilon_\mathrm{g} \sqrt{1 - \frac{\epsilon_\mathrm{g}^2}{\delta\epsilon^2}}\, \mathrm{Re}\frac{\partial G(\epsilon_\mathrm{g};\omega)}{\partial \epsilon_\mathrm{g}}. \tag{5.8}$$

This shows that, while the zeroth noise harmonic is directly related to an average over the finite-frequency conductance of the system, the first harmonic reveals nonlinearities (namely first-order derivatives of the conductance, equivalent to second-order derivatives of the current). In the limit in which the driving amplitude, $\delta\epsilon$, is smaller than the scale on which variations in the conductance occur, Eq. (5.8) simplifies to

$$\mathcal{S}^{(\mathrm{i})}(1;\omega) \approx \delta\epsilon\, \omega \coth\left(\frac{\beta\omega}{2}\right) \mathrm{Re}\frac{\partial G(\epsilon_\mathrm{g};\omega)}{\partial \epsilon_\mathrm{g}}\Big|_{\epsilon_\mathrm{g}=0}, \tag{5.9}$$

and the first noise harmonic is proportional to this nonlinearity.

In Chap. 6 we use these relations to interpret the instantaneous contribution to the finite-frequency noise. Similar extensions of the

fluctuation-dissipation theorem, connecting noise harmonics to derivatives of the finite-frequency conductance, also hold for $n \geq 2$. In these cases, higher derivatives as well as products of derivatives of different order would appear. Importantly, no such extension of the fluctuation-dissipation theorem is expected to hold for the adiabatic-response contribution to the noise [54].

5.3.5 Adiabatic-response contribution to the noise

We also want to collect a few general properties of the adiabatic-response contribution to the noise. We first point out that the adiabatic-response correction of the zeroth noise harmonic always vanishes for the considered system. This result is a consequence of having a single contact and single-parameter driving, $\epsilon_{\mathrm{g}}(t)$, which leads to an integrand in Eq. (5.5b) which is linear in $\partial_t \epsilon_{\mathrm{g}}(t)$ and otherwise depends on $\epsilon_{\mathrm{g}}(t)$. Due to the periodicity, $\epsilon_{\mathrm{g}}(0) = \epsilon_{\mathrm{g}}(T)$, we derive $\mathcal{S}^{(\mathrm{a})}(0;\omega) = 0$. Importantly, non-vanishing contributions occur in the adiabatic response of higher noise harmonics and hence in the time-resolved finite-frequency noise.

Besides that, the adiabatic response of the auxiliary function, $\tilde{S}^{(\mathrm{a})}(t,\omega)$, turns out to be an odd function in t, because it contains a factor $\partial_t \epsilon_{\mathrm{g}}(t)$ in front of an otherwise even expression, see also Sec. 5.4. Since, however, the third term on the right-hand side in Eq. (5.5b) remains an even function, the harmonics of the adiabatic-response contribution to the noise are generally complex valued. When the latter term does not contribute, which, as we explain in Sec. 6.1, is for instance the case for high noise frequencies, we find that $\mathcal{S}^{(\mathrm{a})}(n=1;\omega)$ is purely imaginary. Consequently, we also find that the adiabatic-response contribution to the time-resolved finite-frequency noise in Eq. (5.1) is generally complex valued (and real in the high noise-frequency regime). The reason that these contributions to the symmetrized noise can become complex is due to the lag of the system. In any non-zero order in the expansion in the small parameter $\delta\epsilon\,\Omega\beta/\Gamma$, the two constituents on the right-hand side in Eq. (5.3) are not each others complex conjugates.[2]

The general properties of the noise are summarized in Tab. 5.2.

[2] We note that $\tilde{S}(t;\omega)$ is an auxiliary function and should not be confused with the unsymmetrized noise.

quantity	general property
$S^{(\mathrm{i})}(t;\omega)$	real
$S^{(\mathrm{a})}(t;\omega)$	complex (real for $\omega \gg \Gamma$)
$\mathcal{S}^{(\mathrm{i})}(n;\omega)$	real for zero and non-zero harmonics
$\mathcal{S}^{(\mathrm{a})}(n=0;\omega)$	vanishes for one-parameter driving
$\mathcal{S}^{(\mathrm{a})}(n\neq 0;\omega)$	complex (imaginary for $\omega \gg \Gamma$ and $n=1$)

Table 5.2: Properties of the time-resolved finite-frequency noise and the noise harmonics for a cosine driving of the gate voltage, see Sec. 5.3.3.

5.4 Derivation of the finite-frequency noise

We now outline the derivation of the finite-frequency noise and the noise harmonics for the time-dependently driven, interacting quantum dot. Further details are given in respective appendices. To derive the finite-frequency current noise, we extend a non-equilibrium real-time diagrammatic technique, which is based on a perturbative expansion in the reservoir-dot coupling strength Γ, see Refs. [64–67]. For weak coupling and high temperature, $\beta\Gamma \ll 1$, as considered here, the system dynamics is well described by leading terms in this series. An introduction to this method is given in Sec. 3.1. As discussed there, we describe the time evolution of the dot state in terms of the occupation vector, $\boldsymbol{P}(t) = \big[P_0(t), P_\uparrow(t), P_\downarrow(t), P_2(t)\big]^{\mathrm{T}}$, which is the diagonal part of the reduced quantum-dot density matrix (and which decouples from the off-diagonal part). The kinetic equation for the occupation vector is written in Eq. (3.4). We now proceed to derive the finite-frequency noise defined in Eq. (5.2) using the real-time diagrammatic method.

5.4.1 Real-time diagrammatic noise calculation

We calculate the finite-frequency noise based on the auxiliary function defined in Eq. (5.4). Using the diagrammatic language introduced in Sec. 3.1, we depict all contributions to this function on the Keldysh contour with a forward and backward time line. The auxiliary function consists of correlation functions of two current operators at time t and an earlier time t', which have to be placed as external vertices along the contour (at the turning point and, respectively, on the forward

or backward contour). Illustrations of two possible configurations are shown in Fig. 5.2. In total, we write the auxiliary function as

$$\begin{aligned}\tilde{S}(t;\omega) = \lim_{t_0\to-\infty} \frac{\boldsymbol{e}^{\mathrm{T}}}{2}\Bigg(&\int_{t_0}^{t} dt_1 \mathcal{W}_{II}(t,t_1;\omega)\boldsymbol{P}(t_1) \\ &+ \int_{t_0}^{t} dt_1 \int_{t_0}^{t_1} dt_2 \int_{t_0}^{t_2} dt_3 \\ &\times \mathcal{W}_I^{<}(t,t_1;\omega)\Pi(t_1,t_2;\omega)\mathcal{W}_I^{>}(t_2,t_3;\omega)\boldsymbol{P}(t_3) \\ &- \int_{t_0}^{t} dt_1 \int_{t_0}^{t} dt_2 \int_{t_0}^{t_1} dt_3 e^{i\omega(t_1-t)} \\ &\times \mathcal{W}_I(t,t_2)\boldsymbol{P}(t_2) \otimes \boldsymbol{e}^{\mathrm{T}}\mathcal{W}_I(t_1,t_3)\boldsymbol{P}(t_3)\Bigg).\end{aligned} \tag{5.10}$$

The first term of this complex expression contains all diagrams in which the two current vertices are part of the same irreducible kernel, indicated by $\mathcal{W}_{II}(t,t_1;\omega)$, see the upper plot in Fig. 5.2. The exponential function in Eq. (5.4) enters as an additional frequency line [173, 175] going from t to t' and carrying the noise frequency ω, hence the frequency dependence of the kernel. In App. B.5, we explain how this frequency line modifies the calculation of kernels in comparison to a zero-frequency noise calculation [54].

The lower sketch of Fig. 5.2 is an example for all those contributions in which the current vertices are part of two irreducible current kernels separated by a propagator. This is summarized in the second expression of Eq. (5.10). The first factor of this term, $\mathcal{W}_I^{<}(t,t_1;\omega)$, contains all irreducible diagrams which include a single current vertex and a frequency line, which enters the diagram from the left-hand side and ends at the current vertex. The third factor, $\mathcal{W}_I^{>}(t,t_1;\omega)$, is of similar nature, but here the frequency line begins at the current vertex and leaves the diagram to the right. The kernels are separated by a propagator with an external frequency line, $\Pi(t,t_1;\omega)$, for which we write the modified Dyson equation

$$\begin{aligned}\Pi(t,t_1;\omega) = \mathbf{1}\, e^{i\omega(t_1-t)} + \int_{t_1}^{t} dt_2 \int_{t_1}^{t_2} dt_3\, e^{i\omega(t_2-t)} \\ \times \mathcal{W}(t_2,t_3;\omega)\Pi(t_3,t_1;\omega),\end{aligned} \tag{5.11}$$

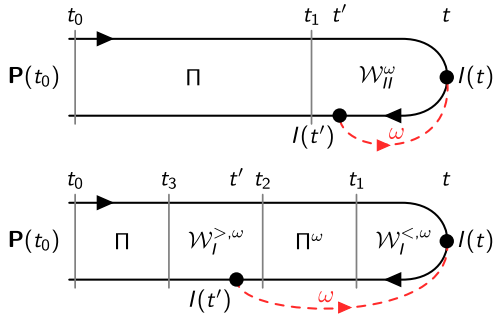

Figure 5.2: Time evolution on the Keldysh time contour sketched for two possible contributions to the auxiliary function for the finite-frequency-noise calculation, see Eq. (5.10) and also Fig. 3.1. Note that the time arguments of propagators and kernels are suppressed and frequency arguments are indicated by superscripts.

with the kernel $\mathcal{W}(t_2, t_3; \omega) = e^{i\omega(t_3-t_2)}\mathcal{W}(t_2, t_3)$. Equation (5.11) is given by Eq. (3.3) multiplied with the factor $e^{i\omega(t_1-t)}$. This factor takes into account the part of the frequency line between the two current vertices which runs over the propagator, see the lower sketch in Fig. 5.2.

Finally, the third term of Eq. (5.10) stems from the second term of the auxiliary function in Eq. (5.4), consisting of a product of current expectation values, see Eq. (3.5). Importantly, the limit $t_0 \to -\infty$ is not taken separately for the different terms in Eq. (5.10), because the terms do not converge independently. This problem is caused by the propagator, $\Pi(t, t_1; \omega)$, which does not decay for large time differences, $t \gg t_1$. To solve this issue, we split the propagator into a decaying, *reduced* part [54, 190], defined by

$$\overline{\Pi}(t, t_1; \omega) = \Pi(t, t_1; \omega) - \boldsymbol{P}(t) \otimes \boldsymbol{e}^{\mathrm{T}} e^{i\omega(t_1-t)}, \tag{5.12}$$

and a non-decaying part. The reduced propagator approaches zero for $t \gg t_1$, on a time scale given by the relaxation dynamics of the occupation vector, i. e., roughly on the scale Γ^{-1}.

abbr.	definition	brief description	details
(i)	instant. contribution	instantaneous response of the system to the time-dependent change of parameters	Sec. 5.4.2, Apps. B.2-B.4
(a)	adiabatic response	first order retarded response of the system to the time-dep. change of parameters	Sec. 5.4.2, Apps. B.2-B.4
(s)	resummed adiabatic expansion	sum of all orders in the slow-driving expansion, valid for driving frequencies not exceeding the tunneling rate	Sec. 6.1.5

abbr.	definition	employed approximation scheme	details
(HF)	high noise frequencies ($\omega \gg \Gamma$)	order-by-order scheme of the Γ expansion: observables are expanded in leading order in Γ	Secs. 5.4.3 and 6.1, App. B.6
(LF)	low noise frequencies ($\omega \ll \Gamma$)	crossover scheme of the Γ expansion with neglected frequency dependence of kernels	Secs. 5.4.3 and 6.2
none	all noise frequencies	when the noise-frequency regime is not specified, we employ the crossover scheme of the Γ expansion: only kernels are expanded in leading order in Γ	Secs. 5.4.3 and 6.3

Table 5.3: List of abbreviations, indicating the applied approximation scheme when used as a superscript.

5.4.2 Expansion for slow gate-voltage driving

We now come to the expansion for slow driving as introduced in Sec. 5.3.3. Note that we perform this expansion not only for the noise, but also for the occupation vector and the current (in contrast to the calculations of Chap. 4, where we employed the Born-Markov approximation, see Sec. 3.1.2). To justify the slow-driving expansion, we make an assumption concerning the time scale of the gate-voltage driving with respect to the response time of the system and the reservoirs, summarized in the condition $\delta\epsilon\Omega\beta/\Gamma \ll 1$. In the following

description, we closely follow the lines of Refs. [54, 67]. Thereby, we take into account the typical time scale for the support of kernels, which is given by the reservoir correlation time, β, as well as for changes in the occupation, $\boldsymbol{P}(t)$, given by Γ^{-1} (which sets the support of the reduced propagator).

We start by setting up the slow-driving expansion for the kinetic equation (3.4), which determines the evolution of the occupation vector, $\boldsymbol{P}(t)$. Therefore, we first expand the occupation vector $\boldsymbol{P}(t_1)$ in the integrand on the right hand side of Eq. (3.4) around the reference time t. In addition, an expansion of the kernel, describing a time evolution governed by time-dependently driven parameters, is performed, $\mathcal{W}(t,t_1) \to \mathcal{W}_t^{(\mathrm{i})}(t-t_1) + \mathcal{W}_t^{(\mathrm{a})}(t-t_1) + \ldots$. See Refs. [54, 67] for details. Here, the superscript (i) indicates that the kernel in lowest order describes a system that *instantaneously* follows the time-dependent driving. In other words, parameters are frozen at time t. In contrast, the superscript (a) refers to the *adiabatic response*, taking into account the finite lag of the system with respect to the gate-voltage driving. The subscript t indicates the reference time at which all time-dependent parameters are evaluated. Consistently replacing $\boldsymbol{P}(t) \to \boldsymbol{P}^{(\mathrm{i})}(t) + \boldsymbol{P}^{(\mathrm{a})}(t) + \ldots$ and collecting all terms of the same order in the slow-driving expansion in the kinetic equation leads to

$$0 = \big\{\mathcal{W}\boldsymbol{P}\big\}_t^{(\mathrm{i})}, \tag{5.13a}$$

$$\partial_t \boldsymbol{P}^{(\mathrm{i})}(t) = \big\{\mathcal{W}\boldsymbol{P}\big\}_t^{(\mathrm{a})}. \tag{5.13b}$$

Equations (5.13) use the compact curly-bracket notation [54, 191]

$$\big\{AB\big\}_t^{(\mathrm{i})} = A^{(\mathrm{i})}(t)B^{(\mathrm{i})}(t), \tag{5.14a}$$

$$\big\{AB\big\}_t^{(\mathrm{a})} = A^{(\mathrm{i})}(t)B^{(\mathrm{a})}(t) + A^{(\mathrm{a})}(t)B^{(\mathrm{i})}(t) + \partial A^{(\mathrm{i})}(t)\,\dot{B}^{(\mathrm{i})}(t), \tag{5.14b}$$

for two generic functions, $A(t)$ and $B(t)$. Here, in addition to the occupation vector, this involves the Laplace transforms of the kernels, $\mathcal{W}_t^{(i/a)}(z) = \int_0^\infty d(t-t_1)e^{-z(t-t_1)}\mathcal{W}_t^{(i/a)}(t-t_1)$, and derivatives thereof, in the limit of zero Laplace frequency, which is abbreviated by $\mathcal{W}_t^{(i/a)} = \lim_{z\to 0}\mathcal{W}_t^{(i/a)}(z)$ and $\partial\mathcal{W}_t^{(i)} = \lim_{z\to 0}(\partial\mathcal{W}_t^{(i)}(z)/\partial z)$ (equivalent notations apply to current and noise kernels used later). Equation (5.13), together with the normalization conditions $\boldsymbol{e}^{\mathrm{T}}\cdot\boldsymbol{P}^{(\mathrm{i})}(t) = 1$

and $\boldsymbol{e}^{\mathrm{T}} \cdot \boldsymbol{P}^{(\mathrm{a})}(t) = 0$, determines the instantaneous and adiabatic-response contributions to the occupation vector.

Furthermore, by applying the same line of arguments to the time-dependent current, Eq. (3.5), we find

$$\langle I(t)\rangle^{(\mathrm{i})} = \frac{\boldsymbol{e}^{\mathrm{T}}}{2}\big\{\mathcal{W}_I \boldsymbol{P}\big\}_t^{(\mathrm{i})}, \tag{5.15a}$$

$$\langle I(t)\rangle^{(\mathrm{a})} = \frac{\boldsymbol{e}^{\mathrm{T}}}{2}\big\{\mathcal{W}_I \boldsymbol{P}\big\}_t^{(\mathrm{a})}. \tag{5.15b}$$

Note that $\langle I(t)\rangle^{(\mathrm{i})}$ vanishes for the single-contact quantum dot considered here, while $\langle I(t)\rangle^{(\mathrm{a})}$ describes the non-vanishing adiabatic-response of the current.

An equivalent expansion can be performed for the auxiliary function of the finite-frequency noise, Eq. (5.10). This expansion is described in detail in Apps. B.2-B.4. It leads to the results

$$\begin{aligned}\tilde{S}^{(\mathrm{i})}(t;\omega) = {} & \frac{\boldsymbol{e}^{\mathrm{T}}}{2}\Big\{\mathcal{W}_I^{<}\overline{\Pi}\mathcal{W}_I^{>}\boldsymbol{P}\Big\}_{t;\omega}^{(\mathrm{i})} \\ & + \frac{\boldsymbol{e}^{\mathrm{T}}}{2}\Big\{\mathcal{W}_{II}\boldsymbol{P}\Big\}_{t;\omega}^{(\mathrm{i})} - 2\Big\{\tilde{I}I\Big\}_{t;\omega}^{(\mathrm{i})},\end{aligned} \tag{5.16a}$$

$$\begin{aligned}\tilde{S}^{(\mathrm{a})}(t;\omega) = {} & \frac{\boldsymbol{e}^{\mathrm{T}}}{2}\Big\{\mathcal{W}_I^{<}\overline{\Pi}\mathcal{W}_I^{>}\boldsymbol{P}\Big\}_{t;\omega}^{(\mathrm{a})} \\ & + \frac{\boldsymbol{e}^{\mathrm{T}}}{2}\Big\{\mathcal{W}_{II}\boldsymbol{P}\Big\}_{t;\omega}^{(\mathrm{a})} - 2\Big\{\tilde{I}I\Big\}_{t;\omega}^{(\mathrm{a})}.\end{aligned} \tag{5.16b}$$

The curly brackets with four operators can be obtained by successively applying Eq. (5.14), see also Eq. (B.5). The additional subscript ω indicates that the frequency-dependent functions $\mathcal{W}_I^{<}, \mathcal{W}_I^{>}, \overline{\Pi}$ and $\tilde{I}$ are evaluated at this frequency. The functions

$$\tilde{I}^{(\mathrm{i})}(t;\omega) = \frac{\boldsymbol{e}^{\mathrm{T}}}{2i\omega}\Big[\{\mathcal{W}_I\boldsymbol{P}\}_t^{(\mathrm{i})} - \{\mathcal{W}_I\boldsymbol{P}\}_{t;\omega}^{(\mathrm{i})}\Big], \tag{5.17a}$$

$$\tilde{I}^{(\mathrm{a})}(t;\omega) = \frac{\boldsymbol{e}^{\mathrm{T}}}{2i\omega}\Big[\{\mathcal{W}_I\boldsymbol{P}\}_t^{(\mathrm{a})} - \{\mathcal{W}_I\boldsymbol{P}\}_{t;\omega}^{(\mathrm{a})}\Big] \tag{5.17b}$$

are derived in App. B.3, and expressions for the instantaneous and adiabatic-response contributions to the reduced propagator are given in App. B.4.

Using Eqs. (5.16) together with Eqs. (5.5), the instantaneous and the adiabatic-response contributions to the time-resolved finite-frequency noise and its harmonics can be evaluated. These quantities are the objects of our main interest. An additional resummation of higher-order contributions in the slow-driving expansion of the noise is only considered in the special case of noise at high frequencies, as presented in Sec. 6.1.5 and indicated by (s). A list of superscripts denoting different approximation schemes is provided in Tab. 5.3.

5.4.3 Expansion in the tunnel-coupling strength

On top of the adiabatic expansion outlined in the previous section, we perform a perturbative expansion in the tunnel-coupling strength Γ. Since we are interested in a weakly coupled quantum dot, $\beta\Gamma \ll 1$, we restrict the following discussion to the sequential-tunneling limit, where first-order tunneling processes govern the dynamics of the driven quantum dot. We expect that second or higher order processes are reasonably suppressed for the system of interest.[3]

While an order-by-order expansion in Γ (see the end of this section for more details), has been applied for the calculation of the pumping current [67] and the zero-frequency noise of these systems [54], it is in general not applicable for the calculation of the finite-frequency noise, see, e. g., Refs. [173, 175, 183]. The reason is that the frequency-dependent propagator in Eq. (5.12) can, in general, not be expanded order-by-order in Γ, which can be understood from the Dyson equation (5.11) and in particular from its determining equations given in Eq. (B.12). To evaluate the finite-frequency noise we therefore use a different scheme, which we refer to as the *crossover scheme*. It means that only kernels are expanded in the tunnel-coupling strength, while for other objects resulting from them—like the reduced propagator—we keep all orders in Γ. Specifically, we first derive the adiabatic expansion of Eqs. (3.4), (3.5) and (5.10), as outlined in Sec. 5.4.2. We then keep all terms on the right-hand sides of the resulting equations which include kernels in first order in Γ. For explicit expressions we refer to App. B.5.

[3] For a time-dependently driven, interacting quantum dot, effects of second order in the tunnel coupling have been studied for the relaxation dynamics [99], the pumping current [67] and the zero-frequency pumping-current noise [54].

While this scheme is in principle applicable for all noise frequencies, it turns out to be in some cases overcomplicated. Furthermore, for noise frequencies of the order of the tunnel-coupling, $\omega \sim \Gamma$, care has to be taken to consistently treat higher-order coupling terms [173], see App. B.5 for details. We therefore only employ this full crossover scheme when calculating the finite-frequency noise for intermediate noise frequencies, which is done in Sec. 6.3. For the regime of low noise frequencies ($\omega \ll \Gamma$), as well as for the regime of high noise frequencies ($\omega \gg \Gamma$), simplified schemes for the perturbative approximation can be employed, as we explain in the following.

Low noise frequencies, $\omega \ll \Gamma$

We find that for low noise frequencies, $\omega \ll \Gamma$, it is reasonable to neglect the frequency dependence of kernels in Eq. (5.16) and to only keep the frequency dependence of the propagator, see also Ref. [175]. Any correction in ω to the zero-frequency kernel would be smaller than the neglected cotunneling terms, as long as $\omega \ll \Gamma$. Specifically, we keep the frequency dependence of free parts of the contour only, which means that also the kernel in the Dyson equation (5.11) is evaluated at zero frequency. This is justified because for low noise frequencies the time scales of fluctuations is much larger than the support of the kernels (given by β). The frequency line in the propagator is therefore expected to rather play a role for free parts of the propagation. The physical picture is that during the (long) duration of a fluctuation, ω^{-1}, the system mostly propagates freely: the time span where the system is in intermediate states, due to additionally occurring tunnel events described by the kernel in the Dyson equation, is negligible at low noise frequencies. Quantities calculated in this regime are indicated by a superscript (LF).

High noise frequencies, $\omega \gg \Gamma$

In the high noise-frequency regime, $\omega \gg \Gamma$ indicated by (HF), it turns out that the previously mentioned order-by-order scheme can be employed. The technical reason for is that the frequency-dependent propagator in Eq. (5.16) is well described by the frequency-dependent *free* propagator in this regime, see also Eqs. (B.12). Physically, this

regime is characterized by the electron dynamics being much slower than the time scale of a fluctuation, ω^{-1}, see also the introduction of Chap. 6. The order-by-order scheme is then consistently applied to the kinetic equation (5.13), to the current in Eq. (5.15), as well as to the auxiliary function in Eq. (5.16), after the adiabatic expansion has been performed. After expanding all contributions to these equations up to first order in the tunnel coupling, we sort all terms on the left- and the right-hand sides of the resulting equations by their order in the tunnel-coupling strength and keep the leading contributions only. For the auxiliary function in Eq. (5.10), this turns out to be

$$\tilde{S}^{(l,\mathrm{HF})}(t;\omega) = \frac{\boldsymbol{e}^{\mathrm{T}}}{2}\mathcal{W}^{(\mathrm{i})}_{II}(t;\omega)\,\boldsymbol{P}^{(l,\mathrm{HF})}(t), \tag{5.18}$$

with $l = \mathrm{i/a}$ for the instantaneous contribution and the adiabatic response, respectively. The derivation of Eq. (5.18) is outlined in App. B.6, and the equation is applied in Sec. 6.1, where we analyze noise and noise harmonics evaluated at high noise frequencies.

The simplicity of Eq. (5.18) makes it possible to go beyond the first-order (adiabatic-response) approximation for the slow driving, by employing the same strategy as discussed up to here. This is relevant to describe the noise of single-electron emitters which employ faster driving schemes. In the sequential-tunneling regime (for weak coupling Γ), the kinetic equation (5.13) and the current formula, Eq. (5.15), can be extended to higher orders in the slow-driving expansion by keeping the instantaneous kernel and taking successively higher-order terms in the slow-driving expansion for the occupation vector, see also Ref. [105, 192]. Importantly, we here find that this extension is also possible for the auxiliary function of Eq. (5.18), hence the parameter l, denoting the expansion order. The case where all higher-order contributions to the slow-driving expansion are resummed is studied in Sec. 6.1.5 and indicated by the superscript (s). A list of different orders in the slow-driving expansion and of all employed approximation schemes for the Γ expansion is provided in Tab. 5.3.

5.5 Noise in Floquet scattering-matrix theory

For the special case of a noninteracting and spin-symmetric quantum dot, we also perform a finite-frequency noise calculation in *Floquet*

scattering-matrix theory, see Ref. [60] for an introduction. The results are useful to cross-check the numerical implementation of the real-time-diagrammatic noise expressions in this limit (and at low noise frequencies, see below). We now briefly summarize this additional noise calculation, where we closely follow Refs. [52, 53], see also Ref. [193]. Note that the scattering-matrix approach relies on a single-particle picture and thus cannot account for many-body interactions.

The concept of scattering-matrix theory—as the name says—is to describe electron transport in a mesoscopic system in terms of scattering processes of single-electron wave functions. For the reservoir, we write incoming and outgoing electronic states with creation and annihilation operators, $a^\dagger(E)/a(E)$ and $b^\dagger(E')/b(E')$, respectively, see the sketch in Fig. 5.3. The quantum dot, as indicated in the figure, is modeled by a unitary Floquet scattering-matrix, $S_\mathrm{F}(E', E)$, which defines how incoming electrons with energy E are scattered into outgoing electronic states with energy E'. Due to the harmonically driven gate voltage $V_\mathrm{g}(t)$, which we consider here, the energies E' and E can differ by multiples of the driving frequency Ω. This is a consequence of the Floquet theorem, which says that the (quasi-) energy in a time-periodic quantum system can only be defined modulo the driving frequency [60, 194]. The Floquet scattering matrix connects incoming and outgoing states as

$$b(E) = \sum_{n=-\infty}^{\infty} S_\mathrm{F}(E, E + n\Omega) a(E + n\Omega), \tag{5.19a}$$

$$b^\dagger(E) = \sum_{n=-\infty}^{\infty} S_\mathrm{F}^*(E, E + n\Omega) a^\dagger(E + n\Omega). \tag{5.19b}$$

The current in the reservoir is obtained from the expression

$$I(t) = \frac{1}{2\pi} \int dE \int dE' e^{i(E-E')t} \left[b^\dagger(E) b(E') - a^\dagger(E) a(E') \right], \tag{5.20}$$

see Ref. [60]. The strategy to evaluate this and further scattering-matrix theory expression is the following. We first replace outgoing electrons with incoming ones by inserting Eqs. (5.19) into Eq. (5.20). In a second step, we consider a thermal distribution for the incoming electrons, $\langle a^\dagger(E) a(E') \rangle = f^+(E) \delta(E - E')$, with $f^+(E)$ being the Fermi

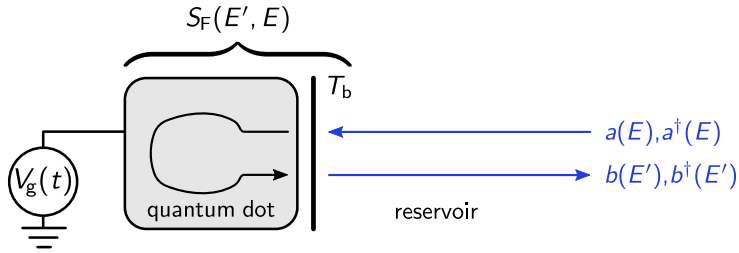

Figure 5.3: Sketch of a quantum dot tunnel-coupled to a reservoir, as described in Floquet scattering-matrix theory. The scattering matrix, $S_F(E', E)$, models the tunnel barrier with transmission T_b as well as the quantum dot.

function of the reservoir. To define the symmetric finite-frequency current noise in the language of Floquet scattering-matrix theory, we apply the definitions written in Eqs. (5.1) and (5.2) and replace the current operator in these expressions by the one given in Eq. (5.20). In the following, we only provide key steps of the noise calculation and refer to Refs. [52, 53, 60] for details.

Let us first remind ourselves that we focus on a slow driving of the gate voltage, $V_g(t)$. This means that any time-dependent variation of the gate voltage is considered to be slow compared to the time span which an electron typically spends in the quantum dot. In this case, the Floquet scattering matrix is closely related to the scattering matrix of a stationary system, in which all parameters are evaluated at a frozen time t. The relation between this *frozen* scattering matrix, $S(E, t)$, and the Floquet scattering matrix, $S_F(E', E)$, is derived by performing an expansion of the latter in powers of the driving frequency Ω, as outlined in Ref. [60]. In zeroth order in this expansion, the Floquet scattering matrix turns out to be equal to the frozen scattering matrix, after a Fourier transform has been performed. Including also the first order, the relation for the single-contact quantum dot reads as

$$S_F(E, E + n\Omega) \approx \frac{\Omega}{2\pi} \int_0^T dt e^{-in\Omega t} \left[1 - \frac{n\Omega\partial_E}{2}\right] S(E, t). \qquad (5.21)$$

To calculate the frozen scattering matrix for our system, we assume the aforementioned constant gate voltage over the time an electron

spends in the dot. After some calculations [60], this leads to

$$S(E,t) = -e^{-i\theta_\mathrm{r}} \frac{T_\mathrm{b} + 2i\tau\big[E - V_\mathrm{g}(t)\big]}{T_\mathrm{b} - 2i\tau\big[E - V_\mathrm{g}(t)\big]}, \tag{5.22}$$

with $V_\mathrm{g}(t) = \bar{V}_\mathrm{g} + \delta V_\mathrm{g}\cos(\Omega t)$. The strength of the tunnel barrier is given by the transmission T_b. Furthermore, the parameter τ is known as the round-trip time and essentially defines the separation between quantum-dot energy levels. Note that θ_r, which is the additional phase of a reflected electron, drops out of the final noise expression.

By inserting Eq. (5.21) into the noise-harmonics expression in Eq. (5.2) and using Eqs. (5.19), we derive the noise in Floquet scattering-matrix theory. This calculation has first been outlined by Moskalets and Büttiker in Refs. [52, 53]. Note that the calculation is based on a series expansion around the noise frequency $\omega = 0$ in quadratic order, which means that the final noise result is only valid for very low noise frequencies. Besides that, we assume high temperatures, $\beta^{-1} \gg \omega, \Omega$, and expand combinations of Fermi functions, which appear in the derivation, around the energy E, see Ref. [52]. After standard manipulations, we obtain the final result for the noise harmonics derived in Floquet scattering-matrix theory. We write the result as

$$\mathcal{S}(n;\omega) = 4P(n; n\Omega - \omega), \tag{5.23}$$

where we define

$$P(n;\omega) = \frac{2\pi\omega(n\Omega - \omega)}{\beta} \int dE \left(\partial_E f^+(E)\right) [\nu^2(E)]_{-n}, \tag{5.24}$$

with $[\nu^2(E)]_{-n} = \frac{\Omega}{2\pi}\int dt e^{-in\Omega t}\nu^2(E,t)$. The so-called frozen density-of-states, $\nu(E,t) = \frac{i}{2\pi}S(E,t)\partial_E S^*(E,t)$, evaluated with Eq. (5.22) becomes

$$\nu(E,t) = \frac{2\Gamma_\tau^2(E)\tau}{\pi T_\mathrm{b}} \sum_{\alpha=\pm} \frac{1}{\Gamma_\tau^2(E) + [t - t_\alpha(E)]^2}, \tag{5.25}$$

in the limit where only a single quantum-dot level is close to the Fermi energy [60]. During the driving, the level crosses the Fermi energy at the times $t_\pm(E) = \pm\frac{1}{\Omega}\arccos\left(\frac{E-\bar{V}_\mathrm{g}}{\delta V_\mathrm{g}}\right)$, and the two crossings occur on the time scales $\Gamma_\tau(E) = \frac{T_\mathrm{b}}{2\tau\Omega\sqrt{\delta V_\mathrm{g}^2 - (E-\bar{V}_\mathrm{g})^2}}$.

In Sec. 6.2.3, the scattering-theory result of Eq. (5.23) is compared to the noise derived in real-time diagrammatic perturbation theory. Since, in the diagrammatic approach, we assume a single-level quantum dot and a weak tunnel barrier, we also choose $T_\mathrm{b} \ll 1$, and a value for τ which leads to a large level separation. For a quantitative comparison, we match the value of T_b/τ, which defines the level broadening due to the tunnel barrier, to the tunnel-coupling strength Γ in the real-time diagrammatic perturbation theory.

Finally, we note that the difference between the discussion in this section and the result of Refs. [52, 53] is that we explicitly keep the energy dependence of the frozen density-of-states in Eq. (5.25). This is necessary for the computation of the finite-frequency noise at the (rather high) temperatures considered in this thesis.

In the next chapter, we proceed by presenting detailed analyses of the noise expressions which we derived in this chapter using the real-time diagrammatic method.

6 Noise Spectra and their Harmonics

We investigate the finite-frequency current noise of an interacting quantum dot coupled to a single electron reservoir, when the system is subject to a slow harmonic gate-voltage driving. By extending a perturbative real-time diagrammatic technique in Chap. 5, we set up a framework to access instantaneous as well as adiabatic-response contributions to the noise over a large range of noise frequencies. Here, we use this approach to analyze time-resolved finite-frequency noise spectra and, importantly, also their decomposition into individual noise harmonics. Note that parts of this chapter (except Sec. 6.2.3) are included in the publication Phys. Rev. B **98** 115414 (2018).

To begin with the noise analysis, we first of all emphasize that we are able to interpret many of the presented results, by comparing the time scales which are present in the single-contact quantum dot. First, the relaxation dynamics of the dot is controlled by the time scale of electron tunneling, i. e., Γ^{-1}. This scale also defines the time scale on which the occupation vector varies, when the quantum dot is operated as a single-electron emitter. For the finite-frequency noise results presented here, this scale has to be compared with a second time scale, namely the time span of charge fluctuations. We associate the time ω^{-1} to charge fluctuations with frequency ω, where a hole or electron excitation is momentarily created in the reservoir, paired with an electron entering or leaving the quantum dot.

Depending on the ratio Γ/ω we distinguish three different noise regimes in this chapter. At high noise frequencies, $\omega \gg \Gamma$, dynamical changes in the system are much slower than the time span of

a fluctuation. Consequently, we find that the current noise in this regime is closely related to the noise of a stationary system. It is, however, evaluated with a non-equilibrium occupation caused by the time-dependent driving. We show that this leads to simple noise expressions in the high noise-frequency regime, which allow us to identify dominating fluctuation processes in the instantaneous first noise harmonic. This intuitive picture fails at intermediate frequencies, $\omega \sim \Gamma$, as well as at low frequencies, $\omega \ll \Gamma$, where the noise depends on an interplay of relaxation and fluctuation dynamics. The reason to also distinguish the regimes of intermediate and low frequencies is that, in the latter, the time span of a fluctuation is much larger than the memory time scale β of the reservoir. This simplifies the noise calculations in the low noise-frequency regime, because β also sets the support of the kernels, see Sec. 5.4.3. A key result, which we find at low noise frequencies, is that the combination of strong Coulomb interaction and periodic driving leads to a non-vanishing imaginary part in the adiabatic response of the first noise harmonic. We also demonstrate that this contribution provides unambiguous evidence of Coulomb interaction in the low-frequency noise of the driven quantum dot: for a noninteracting and possibly spin-split quantum dot, both the instantaneous and the adiabatic-response contributions to the first noise harmonic vanish, when the noise-frequency approaches zero.

We now present the results sorted in the three noise-frequency regimes. First, we explain the high noise-frequency regime in Sec. 6.1. Here, we begin in Sec. 6.1.1 by deriving analytic high-frequency noise expressions and we discuss their physical interpretation in terms of fluctuation processes. This is followed by a detailed discussion of time-resolved noise spectra in Secs. 6.1.2-6.1.3, which is helpful to get an intuitive understanding of the instantaneous and the adiabatic-response noise of the driven quantum dot. We continue with analyzing the noise harmonics in Sec. 6.1.4, where we identify dominating fluctuation processes in the instantaneous first noise harmonic. Finally, in Sec. 6.1.5, we present a re-summation of the slow-driving expansion of the noise, which allows us to obtain high-frequency noise spectra for faster driving schemes. This is especially relevant for experiments, since a faster gate-voltage driving increases many of the noise signatures discussed up to there. Second, we investigate the low noise-frequency regime in Sec. 6.2, by analyzing instantaneous (Sec. 6.2.1)

and adiabatic-response (Sec. 6.2.2) noise harmonics. In Sec. 6.2.2, we also present the aforementioned noise contribution, which reveals the presence of interaction in combination with the time-dependent driving. Additionally, in Sec. 6.2.3, we cross-check the diagrammatic noise results in the limit of vanishing interaction by comparing with data obtained in Floquet scattering-matrix theory. Third, we study the intermediate noise-frequency regime in Sec. 6.3, showing that the there employed crossover scheme of the tunnel-coupling expansion combines and extends the previous results, which we derived using the high and low-frequency approximations, see Sec. 5.4.3. A summary of this chapter is provided in Sec. 6.4.

6.1 Noise at high frequencies

We start by considering high noise frequencies, $\omega \gg \Gamma$, indicated in the following by the superscript (HF). Here, the competition between the described time scales means that we can think of fluctuations as temporary processes, which occur much faster than any variations of the occupation vector caused by relaxation dynamics in response to the gate-voltage driving. This intuitive picture agrees with the explicit high-frequency noise expressions, as we now outline.

6.1.1 Noise expressions and fluctuation vector

In the noise calculations outlined in Sec. 5.4, a central object is given by the auxiliary function, $\tilde{S}(t;\omega)$, defined in Eq. (5.4). The relation between this function and the general noise-harmonics expression is given in Eq. (5.3). To discuss the noise at high frequencies in this section, we first remind ourselves that we derived a simple high-frequency expression for this auxiliary function in Eq. (5.18), which we now employ. Following the procedure of the order-by-order scheme explained in Sec. 5.4.3, we insert this equation into Eqs. (5.5) and only keep leading-order terms in Γ. We then obtain for the instantaneous

noise ($l = 0$) and its adiabatic response ($l = 1$) the two expressions[1]

$$\mathcal{S}^{(\mathrm{i,HF})}(n;\omega) = \int_0^T \frac{dt}{T} e^{in\Omega t}\, \boldsymbol{F}^{(\mathrm{i,HF})}(t;\omega)\boldsymbol{P}^{(\mathrm{i,HF})}(t), \tag{6.1a}$$

$$\mathcal{S}^{(\mathrm{a,HF})}(n;\omega) = \int_0^T \frac{dt}{T} e^{in\Omega t}\, \boldsymbol{F}^{(\mathrm{i,HF})}(t;\omega)\boldsymbol{P}^{(\mathrm{a,HF})}(t), \tag{6.1b}$$

Equations (6.1) can be applied to calculate time-averaged noise spectra, $n = 0$, as well as noise harmonics, $n \neq 0$, of the slowly driven interacting quantum dot. Both equations contain the vector

$$\boldsymbol{F}^{(\mathrm{i,HF})}(t;\omega) = \frac{\boldsymbol{e}^{\mathrm{T}}}{2}\Big[\mathcal{W}^{(\mathrm{i})}_{II}(t;\omega) + \mathcal{W}^{(\mathrm{i})}_{II}(t;-\omega)\Big], \tag{6.2}$$

which we denote as the *instantaneous fluctuation vector*. As written before, the explicit form of Eqs. (6.1) can be seen as a consequence of the fact that high-frequency fluctuations occur much faster than any relaxation dynamics of the quantum dot. Hence, the fluctuation vector appearing in Eqs. (6.1) is given by the instantaneous one, defined in Eq. (6.2), where the contributing kernels are evaluated with parameters frozen at time t. The retarded response of the system to the time-dependent driving enters only in terms of the lag of the occupation vector itself: the instantaneous occupation appears in Eq. (6.1a), while Eq. (6.1b) is evaluated with its adiabatic response.

We continue by studying the instantaneous fluctuation vector in more detail, leading us towards an intuitive picture of noise spectra in the high noise-frequency regime. For the model introduced in Eq. (2.1) (and $\epsilon_\uparrow = \epsilon_\downarrow$) we derive

$$\frac{\boldsymbol{F}^{(\mathrm{i,HF})}(t;\omega)}{\Gamma} = \begin{pmatrix} 2f^+\big(\epsilon(t);\omega\big) \\ f^-\big(\epsilon(t);\omega\big) + f^+\big(\epsilon(t)+U;\omega\big) \\ f^-\big(\epsilon(t);\omega\big) + f^+\big(\epsilon(t)+U;\omega\big) \\ 2f^-\big(\epsilon(t)+U;\omega\big) \end{pmatrix}^{\mathrm{T}}, \tag{6.3}$$

with $f^\pm(x;\omega) = f^\pm(x+\omega) + f^\pm(x-\omega)$, where $f^\pm(x) = (1+e^{\pm\beta x})^{-1}$. The extension of Eq. (6.3) to the spin-split case is provided in Eq. (B.23).

[1] The third term on the right-hand side of Eq. (5.5b) does not contribute to Eq. (6.1b) in leading order in the order-by-order Γ expansion.

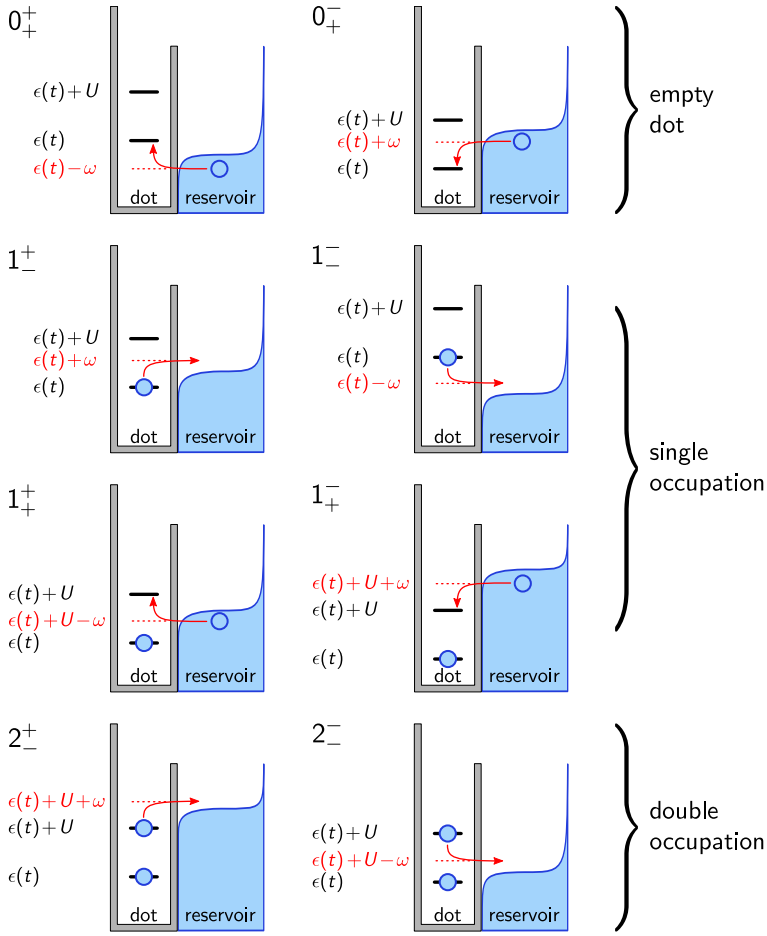

Figure 6.1: Sketch of fluctuation processes which are included in the instantaneous fluctuation vector in Eq. (6.3) for the spin-symmetric case, $\epsilon_\uparrow = \epsilon_\downarrow$ ('single occupation' refers to mixed states of $\uparrow$ and $\downarrow$). The processes are denoted as $0^\pm_+, 1^\pm_\pm$ and $2^\pm_-$, where the superscript indicates the temporal absorption or emission of the energy ω during the fluctuation, while the subscript indicates if the occupation momentarily increases or decreases by one electron. Probabilities for individual processes are proportional to the occupation of the reservoir at the relevant energies. An additional Zeeman splitting would split each of the shown processes in two [see Fig. 6.3 (j)].

The explicit form of the instantaneous fluctuation vector in Eq. (6.3) can be understood by studying the possible fluctuation processes. As an example, let us consider the first entry of this vector, which, in Eqs. (6.1), is multiplied by the first entry of the instantaneous (adiabatic-response) occupation vector, i. e., the probability of the empty quantum-dot configuration. A fluctuation originating from an empty dot involves an electron, which momentarily tunnels from the reservoir onto the dot and back. The first entry on the right-hand side of Eq. (6.3) represents two possible scenarios for this fluctuation: the tunneling electron either absorbs or emits the energy quantum ω temporarily for the time span of the fluctuation. Both fluctuation processes are sketched in Fig. 6.1 in the panels indicated by 0^+_+ and 0^-_+. Since we consider an energy-independent tunnel coupling, the probability that one of the two processes occurs is proportional to the occupation of the reservoir at the initial energy of the tunneling electrons. This occupation is what is described by the first entry of the instantaneous fluctuation vector in Eq. (6.3), where the factor 2 stems from the spin degree-of-freedom. In analogy, fluctuation processes with respect to the other dot occupations can be assigned to the further entries of the fluctuation vector, see the remaining panels in Fig. 6.1. Fluctuations in which an electron tunnels momentarily from the quantum dot into an empty reservoir state lead to Fermi functions with the superscript '$-$'.

We now turn to numerically evaluated high-frequency noise spectra of the quantum dot for a harmonically driven gate voltage, with $\epsilon_g(t) = \delta\epsilon\cos(\Omega t)$, and discuss features related to the processes shown in Fig. 6.1 as well as to the extended fluctuation-dissipation theorem of Sec. 5.3.4.

6.1.2 Time-resolved finite-frequency noise – noninteracting quantum dot

We start by discussing time-resolved finite-frequency-noise spectra, considering the simplest case of a noninteracting spin-symmetric quantum dot as a reference system for the spin-split as well as the interacting dots studied in the next sections. The quantum-dot energy level is driven harmonically around the working point $\bar{\epsilon} = 0$, with amplitude $\delta\epsilon = 10\Gamma$, which results in the periodic emission and absorption of two

electrons by the dot during each period of the drive. We first present results for the instantaneous part of the noise.

The instantaneous time-resolved finite-frequency noise of this setup is plotted in Fig. 6.2 (a), for three different times t, and in Fig. 6.2 (b) as a function of time and frequency. In both figures we find a smeared-out step roughly centered at the noise frequency $\omega = |\epsilon(t)|$, see also the thick dashed and thick dashed-dotted lines in (b). This step structure at every instant of time is expected, since the strength of an individual fluctuation process strongly depends on the occupation of the reservoir at a specific energy, compare to Fig. 6.1. As a consequence, the appearance of a particular step indicates that a related fluctuation processes (or several processes) become energetically possible or suppressed.

In the line cuts shown in Fig. 6.2 (a), this step is clearly visible for the dotted line, showing the noise spectrum at time $t = 0$, where the level position is given by $\epsilon(0) = 10\Gamma$. The instantaneous dot occupation at this point in time is given by the empty configuration, which means that only the two processes $0^{\pm}_{+}$ of Fig. 6.1 can in principle contribute to the noise. Since the process 0^{-}_{+} is suppressed for all noise frequencies whenever the energy level is above the Fermi energy, we find that the fluctuation process 0^{+}_{+} is responsible for the observed noise spectrum. However, also this process is suppressed in the case $\omega < \epsilon(0)$, which leads to the visible step.

During the time-dependent drive, the quantum-dot level first moves towards the Fermi energy and, consequently, the step approaches lower and lower noise frequencies, as shown by the short dashed and long dashed lines in Fig. 6.2 (a).[2] After the Fermi-energy crossing at $t = T/4$, the quantum-dot level moves to even lower energies and the dot tends towards double occupation. The dominating fluctuation process is now given by 2^{+}_{-}, because the second possibility, 2^{-}_{-}, is suppressed by the Fermi function of the reservoir, and therefore a step appears for $\omega < -\epsilon(t) = |\epsilon(t)|$, see Fig. 6.2 (b).

For very high noise frequencies, $\omega \gg |\epsilon(t)|$, the instantaneous time-resolved finite-frequency noise reaches a plateau value of 2Γ. The technical reason for this is that in this regime the instantaneous fluctuation vector becomes time independent and is well described by

[2] At $t = T/4$ the step is not visible in this plot, which does not continue to zero noise-frequency. At zero frequency, $\omega = 0$, the instantaneous time-resolved finite-frequency noise always vanishes due to charge conservation.

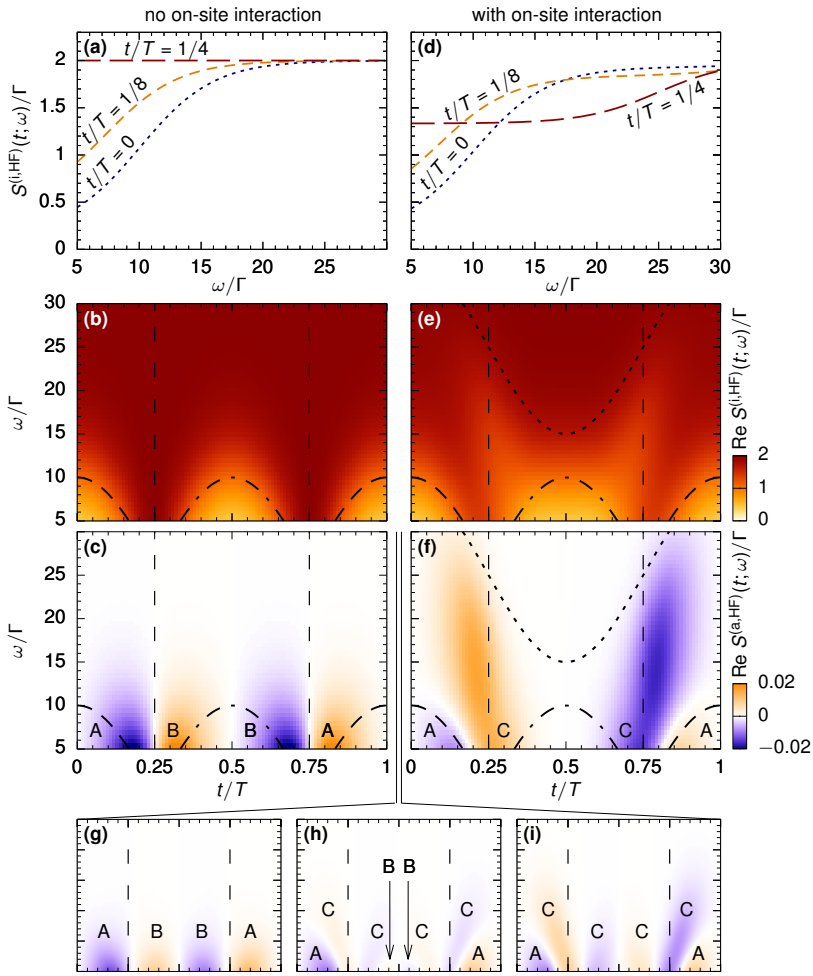

Figure 6.2: (a)-(b) Instantaneous time-resolved finite-frequency noise (HF regime) for a harmonic gate voltage and $U = 0\Gamma$; panel (a) presents cuts of (b) for times $t = 0, T/8, T/4$ (dotted, short dashed, long dashed lines). (c) Adiabatic response to the time-resolved finite-frequency noise (HF regime) for a harmonic gate voltage and $U = 0\Gamma$. Additional lines in (b)-(c) show $\epsilon(t)$ and $-\epsilon(t)$ (thick dashed and dashed-dotted) and zero-crossings of $\epsilon(t)$ (thin dashed). (d)-(f) Similar to (a)-(c) with $U = 25\Gamma$ and $\epsilon(t) + U$ shown by the thick dotted line. Further parameters are $\beta = 1/(3\Gamma)$, $\epsilon_\uparrow = \epsilon_\downarrow$, $\bar{\epsilon} = 0\Gamma$, $\delta\epsilon = 10\Gamma$ and $\Omega = 0.03\Gamma$. (g)-(i) Similar to (f) for intermediate interaction strengths, $U = 3\Gamma, 6\Gamma, 9\Gamma$.

$2\Gamma \boldsymbol{e}^{\mathrm{T}}$ with $\boldsymbol{e}^{\mathrm{T}} = (1,1,1,1)$. More intuitively, it is explained by the fact that all fluctuation processes which temporarily absorb the energy ω, i. e. the ones in the left column in Fig. 6.1, can contribute to the noise, while processes which emit the energy ω are suppressed by the vanishing occupation of the reservoir at energies far above the Fermi energy.

The instantaneous noise studied in the previous paragraph does not account for the fact that the occupation of the driven system slightly lags behind the driving signal. To investigate this, we turn to the adiabatic-response contribution $S^{(\mathrm{a,HF})}(t;\omega)$. The adiabatic response is plotted in Fig. 6.2 (c). A first observation are the alternating signs going along with the fact that the time average of the adiabatic-response noise vanishes, which is a consequence of the one-parameter driving considered here, see Sec. 5.3.5. More specifically, the sign of the adiabatic-response noise changes whenever the energy level crosses the Fermi energy during the drive (thin dashed lines). The regions indicated by A/B in panel (c) mark regions where the empty/double configuration of the dot dominates in the quasi-stationary state, respectively. We find that the adiabatic response reduces the time-resolved noise before the crossing (blue regions) and increases the noise after the crossing (orange regions) leading to a slight shift of the total time-resolved noise, which reflects the lag of the occupation vector. The adiabatic-response contribution to the noise is suppressed when the noise frequency is larger than the drive amplitude, $\delta\epsilon$, i. e., when the noise probes the reservoir occupation far away from the Fermi energy, see the Fermi functions in Eq. (6.3). Naturally, at these energies the fluctuations are not sensitive to the time-dependent modulation of the energy level. In this regime, as explained in the previous paragraph, the instantaneous fluctuation vector is approximately given by $2\Gamma \boldsymbol{e}^{\mathrm{T}}$, because here all fluctuation processes which absorb the energy ω are energetically allowed. This leads to a vanishing integrand in Eq. (6.1b), because the adiabatic response of the occupation vector fulfills the normalization constraint $\boldsymbol{e}^{\mathrm{T}} \cdot \boldsymbol{P}^{(\mathrm{a})}(t) = 0$.

6.1.3 Time-resolved finite-frequency noise – interacting quantum dot

One of the main questions we want to address is how an on-site interaction U changes finite-frequency noise spectra of the driven quantum dot. Since an interacting quantum dot, due to the effect of Coulomb blockade, can be *singly occupied* over a large range of parameters, we expect the fluctuation processes $1^{\pm}_{\pm}$ of Fig. 6.1 to play a major role, leading to additional steps in the noise spectra. As before, we begin with the instantaneous time-resolved finite-frequency noise, which is presented in Fig. 6.2 (d) and (e) for the interacting quantum dot. We consider the interaction strength to be larger than the driving amplitude, which has the consequence that the quantum dot emits and absorbs only a single electron during one period of the drive. The step at $\omega < |\epsilon(t)|$, which is also seen for the noninteracting dot, is now caused by the fluctuation processes 0^{+}_{+} and 1^{+}_{-}, instead of 0^{+}_{+} and 2^{+}_{-} in the noninteracting case. In addition, we find in Fig. 6.2 (d), as expected, a step centered roughly at $\omega \approx |\epsilon(t) + U|$. It emerges when the quantum dot occupation is mostly non-zero. Indeed, this new step is visible for the long dashed line, which shows the spectrum evaluated at time $t = T/4$, where $\epsilon(T/4) + U = 25\Gamma$ (the first step with $\epsilon(T/4) = 0$ is not shown due to the frequency range chosen for this plot). The generating fluctuation process turns out to be 1^{+}_{+}. Note that for a quantum-dot level far below the Fermi energy, a step appears at $\omega = -\big(\epsilon(t) + U\big)$, generated by the process 2^{+}_{-}. In Fig 6.2 (e), we see how these steps evolve in time: both steps are indicated by the thick dashed, dashed-dotted and dotted lines.

Let us now discuss how a finite on-site Coulomb interaction modifies the adiabatic response of the time-resolved finite-frequency noise, see Fig. 6.2 (f). When we gradually change the system from noninteracting to interacting, using the parameters of Fig. 6.2, we find that the two regions marked with A and B in panel (c) separate and two new colored regions, C, related to a singly-occupied dot, emerge in between, see panel (f). Here, we also observe that the regions B, associated with a doubly-occupied dot, have disappeared. See also the additional plots in panels (g)-(i), where the behavior for intermediate interaction strengths is shown. This disappearance of the regions B is caused by the strong interaction, which prevents the occupation of the

quantum dot with two electrons. Interestingly, the regions C extend to much larger noise frequencies than the regions A and B, because only when the noise frequency exceeds the value $|\epsilon(t) + U|$, the noise always probes the reservoir occupation far away from the Fermi energy and the effect of the driving disappears in the noise. Additionally, we find that the boundary between the regions A and C now shows a frequency-dependent bending, which is linked to the fact that the single-occupied dot is doubly degenerate, in contrast to the empty dot. The consequence is that, in the case where double occupation is suppressed by the strong on-site interaction, fluctuations which originate from the empty configuration can in principle contribute more strongly to the noise than fluctuations beginning from a singly-occupied dot. For example, at $\epsilon(t) = 0$ and $\omega \lesssim U$, the first entry of the instantaneous fluctuation vector in Eq. (6.3) roughly doubles the value of the second (third) entry. Furthermore, since the adiabatic response of the occupation vector, $\boldsymbol{P}^{(\mathrm{a,HF})}(t)$, is proportional to $(1, -1/2, -1/2, 0)^{\mathrm{T}}$, when evaluated in the vicinity of the energy-level's zero-crossing, the boundary between A and C reveals the difference between the first and the second (third) entry of the instantaneous fluctuation vector. The boundary line indicates points where fluctuation processes originating from an empty and a singly occupied dot are of equal magnitude, see also Eq. (6.1b). If the dot is noninteracting, the additionally allowed fluctuations between single and double occupation result in a cancellation of this frequency dependence, as it is visible in panel (c). Note that for strong Coulomb interaction on the quantum dot, the described boundary generally differs from the point, where the *tunnel rates* which change the instantaneous dot occupation from empty to single and vice versa are equal. The latter leads to the known condition $\epsilon(t) = \log(2)/\beta$, which defines the emission and absorption times of the first electron (the second electron is emitted and absorbed at $\epsilon(t) = -\log(2)/\beta - U$).

6.1.4 Noise harmonics – noninteracting, interacting and spin-split quantum dot

We in particular want to promote the study of *noise harmonics* as a tool to identify particular fluctuation processes in the finite-frequency noise. The aim is to thereby identify interaction physics from a combination

with time-dependent driving. For this purpose, a central object is the decomposition of the time-resolved finite-frequency current noise, $S(t;\omega)$, in individual current-noise harmonics, $\mathcal{S}(n;\omega)$, as introduced in Eq. (5.2). We hereby focus on the first noise harmonic in addition to the more standardly considered zeroth harmonic, i. e., the average of the noise over one driving period. The first noise harmonic can, e. g., be accessed in experiments by multiplying the noise with the driving signal [27].

In this section, we show that contributions to the first noise harmonic can be linked to individual fluctuation processes. Furthermore, specific patterns appear when Coulomb interaction is present on the quantum dot, which can be clearly distinguished from a sequence of two resonances due to a Zeeman splitting. Another benefit of noise harmonics is that any constant background noise cancels for harmonics with $n \geq 1$. Besides that, we already proved in Sec. 5.3.5 that the time-averaged adiabatic-response noise of the considered model system always vanishes, and thus it is natural to analyze the first harmonic of the adiabatic response.

In Fig. 6.3, we present noise harmonics for three different scenarios: a noninteracting spin-symmetric quantum dot, an interacting spin-symmetric quantum dot and a noninteracting spin-split quantum dot. The comparison of these three cases allows us to unanimously identify effects due to the many-body Coulomb interaction. All harmonics are plotted as a function of the noise frequency and the working point, $\bar{\epsilon}$, of the harmonic gate-voltage drive. In the first row of Fig. 6.3 we plot instantaneous parts of *zeroth* noise harmonics. These represent time averages of time-resolved finite-frequency noise spectra similar to the ones shown in Fig. 6.2 (b) and (e). We see that the zeroth noise harmonic is finite whenever the noise frequency exceeds the distance between the Femi energy of the reservoir and a dot addition energy. As mentioned before, the related adiabatic-response contributions of the zeroth noise harmonics vanish.

We now turn to *first* noise harmonics, which are shown in the second and third row of Fig. 6.3, and which we use to study the effect of time-dependent driving on the noise.

As expected from the extension of the fluctuation-dissipation theorem to the first noise harmonics, Eq. (5.8), the panels in the middle row in Fig. 6.3 are closely related to the first derivative, with respect

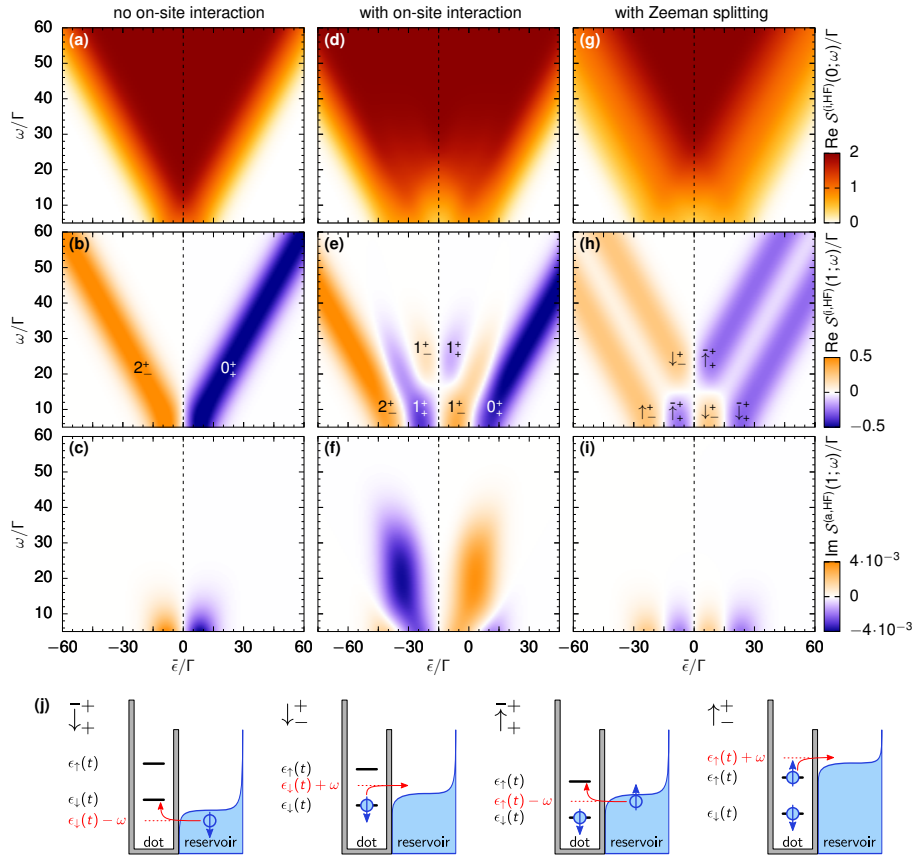

Figure 6.3: (a)-(i) Noise harmonics (HF regime) for a harmonic gate voltage. Shown is the zeroth harmonic of the instantaneous noise (first row), the first harmonic of the instantaneous noise (second row) and the first harmonic of the adiabatic-response noise (third row) for $\beta = 1/(3\Gamma)$, $\delta\epsilon = 10\Gamma$ and $\Omega = 0.02\Gamma$ and (a)-(c) $U = 0\Gamma$, (d)-(f) $U = 30\Gamma$, (g)-(i) $U = 0\Gamma$ and $\bar{\epsilon}_\uparrow - \bar{\epsilon}_\downarrow = 30\Gamma$. Dotted lines indicate the electron-hole symmetric point. (j) Fluctuation processes for a spin-split quantum dot. The abbreviations $\downarrow/\bar{\downarrow}$ denote processes where an electron with respective spin projection leaves/enters the quantum dot during the fluctuation (similarly for $\uparrow/\bar{\uparrow}$). The sup-/superscripts $\pm$ are defined as in Fig. 6.1.

to $\bar{\epsilon}$, of the noise shown in the upper row in the same figure. Interestingly, we can assign a single fluctuation process, which generates the contribution to the first noise harmonic, namely to each of the colored regions. Fig. 6.3 (b) presents the instantaneous noise contribution of a noninteracting spin-symmetric quantum dot. In this figure, we find two straight, broadened lines centered around $\omega = \pm\bar{\epsilon}$. Their widths are given by twice the amplitude of the gate-voltage drive. The dominant processes are 2^+_- and 0^+_+, as defined in Fig. 6.1 and indicated in Fig. 6.3 (b). The reason that the first harmonic clearly differentiates between these processes is that all fluctuations involving reservoir states far away from the Fermi energy cannot contribute: the magnitudes of the latter are not sensitive to the gate-voltage drive. In other words, the first noise harmonic only includes fluctuations, where the fluctuating electron comes from or tunnels into a reservoir state close to the Fermi energy. From these fluctuations, the occupation vector in Eq. (6.1a) then selects the processes 2^+_- and 0^+_+ in the two colored lines in Fig. 6.3 (b). We find that for the related adiabatic-response noise (purely imaginary at high noise frequencies) in Fig. 6.3 (c), no clear identification of fluctuation processes is possible, because the adiabatic-response of the quantum-dot occupation allows for several processes to contribute with comparable strengths in Eq. (6.1b). Here, a nonzero first harmonic not only requires the condition that reservoir states in the vicinity of the Fermi energy take part, but also that the quantum-dot occupation itself strongly varies during the drive. To fulfill the second condition, the quantum-dot level needs to be close to the Fermi energy, additionally requiring $|\bar{\epsilon}| \lesssim \delta\epsilon$ for the working points.

Coulomb interaction on the quantum dot strongly modifies the first noise harmonic. To study its impact, it is instructive to compare the first column of Fig. 6.3 with the second column, where a strong on-site interaction U has been included. In the instantaneous part of the first noise harmonic in panel (e), we again find two straight lines with widths set by twice the driving amplitude, but now centered[3] around $\omega - \bar{\epsilon} = \log(2)/\beta$ and $\omega - \bar{\epsilon} = -U - \log(2)/\beta$. In the region bounded by these (external) lines, we observe a new pattern, which

[3]We recall that $\epsilon(t) = \log(2)/\beta$ and $\epsilon(t) = -U - \log(2)/\beta$ set the times for electron emission/absorption from the interacting quantum dot.

turns out to be specific to the presence of on-site Coulomb interaction. The new pattern is anti-symmetric with respect to the electron-hole symmetric point (dotted lines) and it tends to zero, when the noise frequency exceeds the value of U. Again, we can assign a dominating fluctuation process to each region in Fig. 6.3 (e) as indicated. An important difference with respect to the noninteracting case is that dominant processes for the first noise harmonic not only depend on the working point, but also on the noise frequency. This additional dependency occurs in the region where the dot is mostly singly occupied, because here fluctuations between empty/single occupation and single/double occupation are both possible but contribute at different noise frequencies.

The adiabatic response to the first noise harmonic, Fig. 6.3 (f), also shows additional contributions when compared to Fig. 6.3 (c). Here, the strongest contributions appear if the system is driven around the working points $\bar{\epsilon} = \log(2)/\beta$ and $\bar{\epsilon} = -U - \log(2)/\beta$, which are the points where the occupation vector changes most strongly during the drive. This first harmonic of the adiabatic-response noise exhibits the characteristic features of the interplay between time-dependent driving and strong Coulomb interaction, which we have previously identified in the time-resolved finite-frequency noise: we see the bent line of the sign change as a function of noise frequency and working point as well as non-vanishing noise regions extended to a value set by the Coulomb interaction U.

As a third scenario, we analyze the impact of a magnetic field on the noninteracting quantum dot, leading to a spin splitting of the energy level. In a measurement limited to currents, this spin-splitting could be confused with the two split dot resonances due to Coulomb interaction. Here, we show that the first noise harmonic constitutes an unambiguous way to distinguish the two cases. The zeroth and first noise harmonics of this system are shown in the third row of Fig. 6.3. By comparing panels (g)-(i) with panels (a)-(c) in the same figure, we find that the spin splitting doubles the structures which are seen in the noise harmonics of the noninteracting quantum dot. The dominant fluctuation processes for the instantaneous first harmonic of the spin-split case are indicated in panel (h) and sketched in panel (j). It is instructive to analyze the difference between the instantaneous first noise harmonic of the spin-split quantum dot in panel (h) and

the interacting quantum dot in panel (e). While the instantaneous contributions are qualitatively similar for noise frequencies with $\omega \lesssim \frac{U}{2}$, they differ strongly for higher noise frequencies. The main reason is that processes which contain a 1 in Fig. 6.3 (e) can only occur when a single electron already occupies the quantum dot. On the contrary, for the processes $\bar{\downarrow}_+^+$ and $\bar{\uparrow}_+^+$ in Fig. 6.3 (h) only the occupation of either down or up electrons is relevant, respectively, independent of the occupation with electrons of opposite spin direction. For the adiabatic-response noise in panel (i), which doubles the pattern visible in panel (c), we again find that no clear identification of fluctuation processes is possible, because the adiabatic-response occupation vector selects several processes with comparable strengths in Eq. (6.1b).

6.1.5 Noise spectra beyond the adiabatic response

In the previous sections we analyzed either instantaneous contributions to the noise or adiabatic-response contributions, the latter describing corrections to the instantaneous noise as a consequence of a small retarded response of the system. Both contributions rely on a slow driving of the quantum dot. In an experimental realization, such a slow driving might reduce the magnitude of the signal to be detected. It is therefore of interest to find out whether the driving frequency can be increased without modifying the features described in the previous sections. Interestingly, in the high noise-frequency regime, it turns out that the results of Secs. 6.1.1-6.1.4 are transferable to faster driving schemes, i. e., beyond the adiabatic response. This is possible as long as the time scale of fluctuations, ω^{-1}, is smaller than both the scale of quantum-dot relaxation dynamics and any time scales introduced by the driving scheme. In this case, the auxiliary noise function of Eq. (5.4) obtains the simple form given in Eq. (5.18), see also App. B.6. As discussed in Sec. 5.4.3, this equation not only holds for instantaneous, $l = 0$, and adiabatic-response contributions, $l = 1$, but also in all orders in l of the slow-driving expansion. By summing up this expansion series, we obtain the generalized auxiliary function

$$\tilde{S}^{(\mathrm{s,HF})}(t;\omega) = \frac{\boldsymbol{e}^{\mathrm{T}}}{2} \mathcal{W}_{II}^{(\mathrm{i})}(t;\omega)\, \boldsymbol{P}^{(\mathrm{s,HF})}(t), \tag{6.4}$$

marked with the additional superscript (s) for 'sum', see Tab. 5.3. Similarly, we write for the occupation vector

$$\partial_t \boldsymbol{P}^{(\mathrm{s,HF})}(t) = \mathcal{W}_t^{(\mathrm{i})} \boldsymbol{P}^{(\mathrm{s,HF})}(t). \tag{6.5}$$

Note that this equation is derived by summing up the slow-driving expansion of the kinetic equation, while keeping the leading-order in Γ for each order in l, see Ref. [105], but it also equals the Born-Markov master equation given in Eq. (3.6). We find the generalized noise formula,

$$\mathcal{S}^{(\mathrm{s,HF})}(n;\omega) = \int_0^T \frac{dt}{T} e^{in\Omega t}\, \boldsymbol{F}^{(\mathrm{i,HF})}(t;\omega) \boldsymbol{P}^{(\mathrm{s,HF})}(t), \tag{6.6}$$

where the instantaneous fluctuation vector is the one defined in Eq. (6.2) and the occupation vector is derived using Eq. (6.5), see App. B.6 for details. Besides the restrictions to high noise frequencies and weak tunnel coupling, we expect Eq. (6.6) to be valid for $\Omega \lesssim \Gamma$ [54, 105]. Therefore, in comparison to the instantaneous and adiabatic-response noise in Eqs. (6.1), the generalized noise formula in Eq. (6.6) can be applied to study faster driving schemes. What is more, since the equations share a similar structure, Eq. (6.6) generalizes the results outlined in Secs. 6.1.1-6.1.4.

In Fig. 6.4, we present the time-resolved finite-frequency noise of a noninteracting and an interacting spin-symmetric quantum dot calculated from Eq. (6.6). The figure shows the summed-up noise in panels (a) and (c) as well as the difference between the latter and the instantaneous noise in panels (b) and (d). The parameters are similar to the ones used in Fig. 6.2, except that the driving frequency in Fig. 6.4 has been increased by an order of magnitude. As expected, we find that the density plots in both figures show a similar qualitative behavior. However, what might be of importance for experimental realizations: the differences between the instantaneous and the summed-up noise, shown in Fig. 6.4 (b) and (d), are an order of magnitude larger than the adiabatic-response noise, presented in Fig. 6.2 (c) and (f), respectively. We find a similar behavior for zeroth and first noise harmonics (not shown).

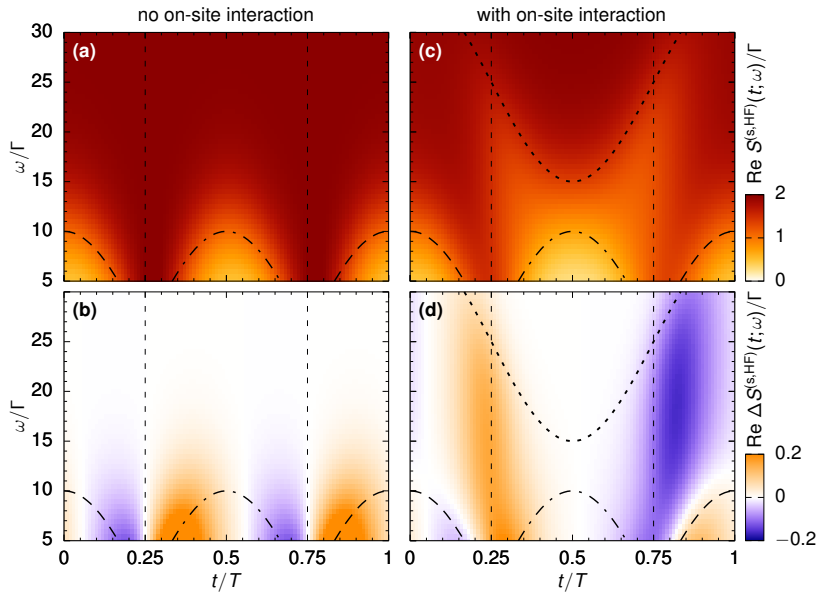

Figure 6.4: (a) Summed-up time-resolved finite-frequency noise (HF regime) for a harmonic gate voltage and $U = 0\Gamma$. (b) Same as (a) with instantaneous time-resolved finite-frequency noise subtracted. Additional lines in (a)-(b) show $\epsilon(t)$, $-\epsilon(t)$ and $\epsilon(t)+U$ (thick dashed, dashed-dotted and dotted) and zero-crossings of $\epsilon(t)$ (thin dashed). (c)-(d) Similar to (a)-(b) with $U = 25\Gamma$. Further parameters are $\beta = 1/(3\Gamma)$, $\epsilon_\uparrow = \epsilon_\downarrow$, $\bar{\epsilon} = 0\Gamma$, $\delta\epsilon = 10\Gamma$ and $\Omega = 0.3\Gamma$.

6.2 Low noise frequencies

We now turn to low noise frequencies, $\omega \ll \Gamma$, where the time scale of fluctuations exceeds the time scale of relaxation dynamics of the quantum dot. This means that the current noise in this regime is generated by an interplay of relaxation and fluctuation dynamics, which cannot be separated as in the high frequency regime. The consequence is that it is difficult to obtain an intuitive interpretation of the derived low-frequency noise spectra in analogy to the interpretation outlined in Sec. 6.1 for high noise frequencies. However, the noise at low frequencies and, in particular, the case of zero frequency, is what is

often measured in related experiments, and it is therefore important to analyze this regime in detail, as we do in this section.

6.2.1 Noise harmonics – instantaneous contribution

We start by analyzing the instantaneous contribution to the low-frequency noise, Eqs. (5.5a) and (5.16a).

By employing the crossover scheme of the Γ expansion, while additionally neglecting the frequency dependence of kernels, see Secs. 5.4.2 and 5.4.3, we can derive a compact analytical expression for the instantaneous low-frequency noise:

$$\mathcal{S}^{(\mathrm{i,LF})}(n;\omega) = \int_0^T \frac{dt}{T} e^{in\Omega t}\, \boldsymbol{F}^{(\mathrm{i,LF})}(t;\omega)\cdot \boldsymbol{P}^{(\mathrm{i})}(t). \tag{6.7}$$

The fluctuation vector occurring here is given by the expression

$$\boldsymbol{F}^{(\mathrm{i,LF})}(t;\omega) = \frac{\omega^2}{\lambda_{\mathrm{c}}(t)^2+\omega^2}\, \boldsymbol{F}^{(\mathrm{i,HF})}(t;0). \tag{6.8}$$

It differs from the one at high noise frequencies, Eq. (6.2), in two ways. First, due to the different time scales of the fluctuations considered here, it contributes only at $\omega = 0$, and second, it features a factor $\omega^2/(\lambda_{\mathrm{c}}(t)^2+\omega^2)$. This frequency-dependent Lorentzian factor suppresses the noise when the time scale associated with a fluctuation, ω^{-1}, exceeds the time scale $\lambda_{\mathrm{c}}^{-1}(t)$, which equals the physical charge relaxation time for a system with parameters frozen at time t [99, 105],

$$\lambda_{\mathrm{c}}(t) = \Gamma\left[1 + f^{+}\big(\epsilon(t)\big) - f^{+}\big(\epsilon(t)+U\big)\right]. \tag{6.9}$$

In the first two rows of panels in Fig. 6.5, we show the zeroth and first noise harmonic of this instantaneous contribution to the low-frequency noise for the three different scenarios, which for high noise frequencies were displayed in Fig. 6.3 of Sec. 6.1.4: a non-interacting spin-symmetric dot, an interacting spin-symmetric dot and a non-interacting spin-split dot. Two important remarks about these figures need to be made. First, we clearly see the features prescribed by the fluctuation-dissipation theorem, Eqs. (5.7) and (5.8), for the zeroth and first harmonic of the instantaneous noise: these noise contributions are directly related to the finite-frequency conductance and its derivative.

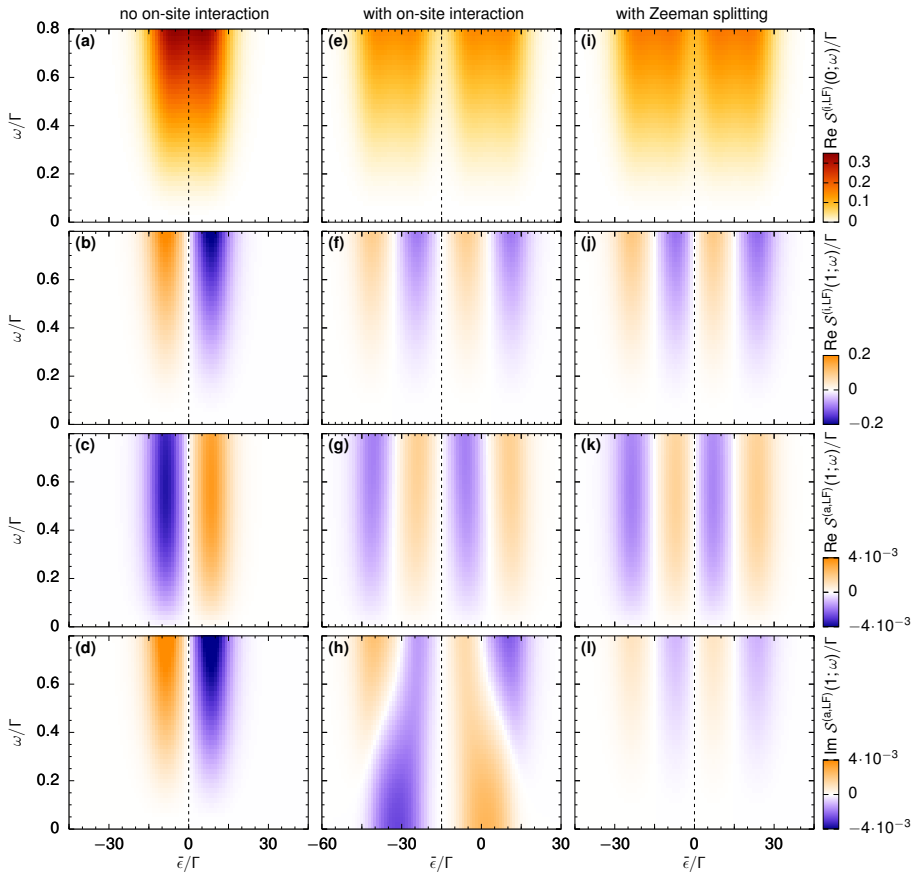

Figure 6.5: Noise harmonics for a time-dependently driven noninteracting quantum dot for low noise frequencies (LF). Dotted lines indicate the electron-hole symmetric point. First row (a), (e), (i): zeroth harmonic of the instantaneous part. Second row (b), (f), (j): first harmonic of the instantaneous part. Third row: (c), (g), (k): real part of the first harmonic of the adiabatic response. Fourth row: (d), (h), (l): imaginary part of the first harmonic of the adiabatic response. Parameters are $\beta = 1/(3\Gamma)$, $\delta\epsilon = 10\Gamma$ and $\Omega = 0.02\Gamma$. Furthermore, different values of the interaction strength and the Zeeman splitting are chosen for the different columns: first column (a)-(d): $U = 0\Gamma$ with $\bar{\epsilon}_\uparrow - \bar{\epsilon}_\downarrow = 0$; second column (e)-(h): $U = 30\Gamma$ with $\bar{\epsilon}_\uparrow - \bar{\epsilon}_\downarrow = 0$; third column (i)-(l): $U = 0\Gamma$ with $\bar{\epsilon}_\uparrow - \bar{\epsilon}_\downarrow = 30\Gamma$.

Furthermore, in agreement with these fluctuation-dissipation theorems, both noise harmonics vanish in the limit of $\omega \to 0$, as dictated by the vanishing zero-frequency conductance of the single-contact quantum dot.

Importantly, from the noise features displayed in these two rows, no clear distinction is possible between the case of finite interaction and no magnetic field, and vanishing interaction and finite magnetic field. This is different when studying the adiabatic-response contribution.

6.2.2 Noise harmonics – adiabatic-response

For the adiabatic-response noise at low frequencies, no compact analytical expression for $\mathcal{S}^{(\mathrm{a,LF})}(n;\omega)$ is accessible[4] and it is more insightful to analyze the plots of this function given in the third and fourth rows of Fig. 6.5. Since the adiabatic-response of the first harmonic, $\mathcal{S}^{(\mathrm{a,LF})}(1;\omega)$, is a complex quantity, we show its real and imaginary part separately.

For the first harmonic of the noise, the real part of the adiabatic response behaves very similar to the instantaneous part, even though the order of magnitude is much smaller. In both cases, the noise vanishes with decreasing frequencies and the overall behavior with alternating signs is equivalent, however, with an opposite overall sign. In contrast, the imaginary part of the adiabatic response, displayed in the fourth row of panels in Fig. 6.5, shows a very different behavior.

For the noninteracting dot, both in the presence and in the absence of a Zeeman field, the difference between real and imaginary part are merely opposite signs and a stronger suppression for low frequencies in the imaginary part. However, a key finding of this thesis is that the *interacting* quantum dot behaves completely differently: the imaginary part of the adiabatic response of the first harmonic stays finite even at zero noise frequency, as it is evident from Fig. 6.5 (h). This effect is unique to strong Coulomb interaction and cannot be mimicked by a

[4] The reason is that the time-dependent driving causes a retarded response not only of the occupation vector, but of all objects which appear in the auxiliary function in Eq. (5.10). While these additional terms hardly contribute at high noise frequencies—they can be neglected in the order-by-order scheme—these terms strongly influence the low frequency noise. The final expression for the adiabatic response related to Eq. (6.7) is too large to be shown here, and we therefore analyze it numerically.

Zeeman splitting with equal magnitude. Importantly, it is only visible when combined with the time-dependent driving: it is not visible in the time-averaged noise, i. e., the zeroth harmonic, where the adiabatic response vanishes, see Sec. 5.3.5. The described feature is also absent in the zeroth as well as the first harmonic of the instantaneous noise in Fig. 6.5 (e)-(f). We attribute the signature of non-vanishing noise in the adiabatic response to its sensitivity to the modified charge-relaxation rate, Eq. (6.9), due to interaction and the resulting difference in degeneracy of the quantum-dot ground states. This is also at the origin of deviations from the equilibrium fluctuation-dissipation theorem in the adiabatic response of interacting quantum-dot pumps, see Ref. [54].

The contribution to $\mathcal{S}^{(\mathrm{a,LF})}(1;\omega)$ for the interacting dot evolves from two features with a sign change to two resonant contributions with a single maximum (or minimum) with decreasing noise frequencies. These features are situated around working points in the vicinity of $\bar{\epsilon} = \log(2)/\beta$ or $\bar{\epsilon} = -U - \log(2)/\beta$, i. e., when the dot is driven around energies at which electrons are emitted and absorbed. The sign of the contribution, when approaching zero noise frequency, reveals if the quantum dot is driven between the empty configuration and the singly occupied state or between the singly and the doubly occupied states, see Fig. 6.5 (h), namely whether the ground-state degeneracy increases or decreases with the working-point position, see also Ref. [195].

6.2.3 Comparison with scattering-matrix theory

We briefly show a comparison of the real-time diagrammatic noise data at low noise frequencies and vanishing interaction with results derived in Floquet scattering-matrix theory. See Sec. 5.5 for a brief introduction and Ref. [60] for further details. This comparison is helpful to cross-check the (rather tedious) numerical implementation of the real-time-diagrammatic noise expressions, in particular, of the adiabatic response [e. g. Eq. (5.16b)]. For the comparison, we use the noise formula written in Eq. (5.23), which is derived in Floquet scattering-matrix theory in the limit of slow driving, and expanded around zero noise-frequency, see also Refs. [52, 53].

In Fig. 6.6 (a)-(c) we plot the zeroth and first noise harmonics computed in both theories, with the real-time diagrammatic data shown as lines and the Floquet scattering-matrix data shown as triangles.

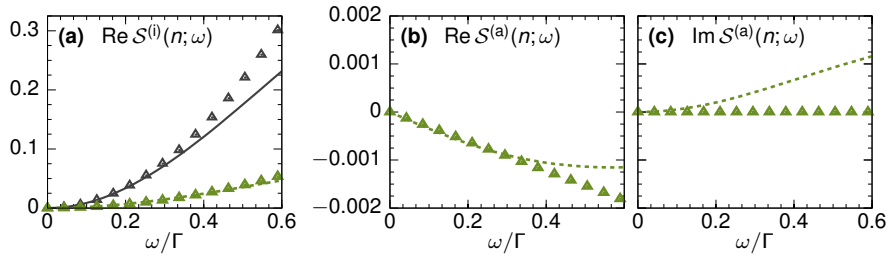

Figure 6.6: Comparison of low-frequency noise harmonics calculated in real-time diagrammatic perturbation theory (LF, lines) with results from Floquet scattering-matrix theory (triangles). Shown are (a) instantaneous contributions and (b)-(c) real and imaginary adiabatic-response contributions to the zeroth ($n = 0$, black solid) as well as to the first noise harmonic ($n = 1$, green dotted). Note that the real-time diagrammatic results are line cuts of Fig. 6.5 (a)-(d) at the working point $\bar{\epsilon} = -2\Gamma$. Further parameters are $T_\mathrm{b} = 0.01$ with $T_\mathrm{b}/\tau = \Gamma$ and $\beta = 1/(3\Gamma)$, $\epsilon_\uparrow = \epsilon_\downarrow$, $\delta\epsilon = 10\Gamma$, $\Omega = 0.02\Gamma$.

As expected, we find that both methods agree well at very low noise frequencies, i. e., in the left parts of panels (a)-(c), thereby confirming the validity of the diagrammatic calculations in the noninteracting low-frequency limit. Deviations start with increasing noise frequency in the right parts of the plots. This can be attributed to the series expansion around $\omega = 0$, which is performed in Floquet scattering-matrix theory, but not for the real-time diagrammatic expressions, where we instead keep the full frequency dependence for free parts of the Keldysh contour, see Sec. 5.4.3. Due to this expansion, the scattering-matrix theory result in Eq. (5.23) is quadratic (linear) in the noise frequency when evaluating the zeroth (first) noise harmonic. Consequently, the regime of applicability is more restricted for this scattering-matrix theory result, compared to the real-time diagrammatic noise expressions. Note that the asset of the diagrammatic noise calculations, besides the broad range of accessible noise frequencies, is that it accounts for interaction on the quantum dot.

6.3 Noise at intermediate frequencies

We finally present results for arbitrary noise frequencies—calculated in the real-time diagrammatic approach—and we use them to show how the transition from high to low noise frequencies takes place. This is particularly relevant in the range where the time scale of fluctuations is similar to the time scale on which the dot occupation probabilities change, $\omega \sim \Gamma$. The main finding is that noise spectra and noise harmonics derived in this range connect well the high and low noise-frequency results, which have been discussed in the previous sections. In this section, we focus on a spin-symmetric quantum dot.

6.3.1 Noise harmonics – instantaneous contribution

In order to calculate the noise at intermediate noise frequencies, we employ the technically more challenging full crossover scheme of the expansion in the tunnel coupling, as outlined in Sec. 5.4.3. For the instantaneous noise this leads to the expression

$$\mathcal{S}^{(\mathrm{i})}(n;\omega) = \int_0^T \frac{dt}{T} e^{in\Omega t}\, \boldsymbol{F}^{(\mathrm{i})}(t;\omega) \cdot \boldsymbol{P}^{(\mathrm{i})}(t). \tag{6.10}$$

In this equation, $\boldsymbol{F}^{(\mathrm{i})}(t;\omega) = \frac{\omega^2}{\lambda_{\mathrm{c}}(t;\omega)^2+\omega^2}\, \boldsymbol{F}^{(\mathrm{i,HF})}(t;\omega)$, and

$$\lambda_{\mathrm{c}}(t;\omega) = \Gamma \left(1 + \frac{f^+\big(\epsilon(t);\omega\big) - f^+\big(\epsilon(t)+U;\omega\big)}{2} \right), \tag{6.11}$$

with $f^+(x;\omega)$ defined below Eq. (6.3). Equation (6.10) combines and extends the instantaneous noise expressions which we derived previously, i. e., in the high and low noise-frequency regimes, see Eqs. (6.1a) and (6.7). Again, we find that the instantaneous noise can be expressed in terms of the instantaneous quantum-dot occupation, $\boldsymbol{P}^{(\mathrm{i})}(t)$, and an instantaneous fluctuation vector, $\boldsymbol{F}^{(\mathrm{i})}(t;\omega)$, as written in Eq. (6.10). The instantaneous fluctuation vector in Eq. (6.10) differs from its high-frequency limit, $\boldsymbol{F}^{(\mathrm{i,HF})}(t;\omega)$, by a frequency-dependent factor, which suppresses the noise for frequencies $\omega < \lambda_{\mathrm{c}}(t;\omega)$. The difference compared to the result at low noise frequencies [Eq. (6.9)] is that the quantity $\lambda_{\mathrm{c}}(t;\omega)$ in Eq. (6.11) is now frequency dependent itself. It equals the physical charge relaxation rate of the quantum

dot [99, 105] only in the limit $\omega \to 0$. For general noise frequencies, $\lambda_c(t;\omega)$ can be expressed as the average of two charge relaxation rates, namely the rates associated with quantum-dot levels frozen at $\epsilon(t) \pm \omega$. Importantly, for a noninteracting quantum dot, the quantity $\lambda_c(t;\omega)$ remains frequency independent and the suppression factor in Eq. (6.10) becomes a Lorentzian, as for the low-frequency noise discussed before. For the noninteracting dot the transition between the high- and low-frequency noise is therefore expected to be trivial and we focus on the interacting dot, when displaying the results in Fig. 6.7. The result for the instantaneous contribution to the noise in Fig. 6.7 (a) shows the suppression of the noise with decreasing frequencies.

6.3.2 Noise harmonics – adiabatic response

To also investigate the adiabatic response of the noise, we again find that it is more insightful to analyze numerical results. It turns out, that the adiabatic response is more sensitive to the frequency dependence of the noise than the instantaneous contribution.

The real and imaginary part of the adiabatic response of the first harmonic are shown in Figs. 6.7 (b) and (c). We again find that the results present a smooth connection between the high- and low-frequency-noise results. A minor deviation is visible in column (b), where the crossover scheme gives a small contribution even at higher frequencies, which is not captured by the order-by-order scheme employed in the upper plot of this column. Note, however, that the non-vanishing contribution visible in the upper part of the middle plot in column (b) turns out to be further suppressed, if we choose a higher temperature than the one applied here [$\beta = 1/(3\Gamma)$].

The center panels of Figs. 6.7 (b) and (c) show a shifting of features (such as maxima and sign changes) as a function of the working-point position depending on the noise frequencies. The reason for this is the delicate interplay between time scales given by the time-dependent driving, the time scale of fluctuations, and the charge relaxation time, where the latter is only working-point dependent in the case of Coulomb interaction, see Eq. (6.9).

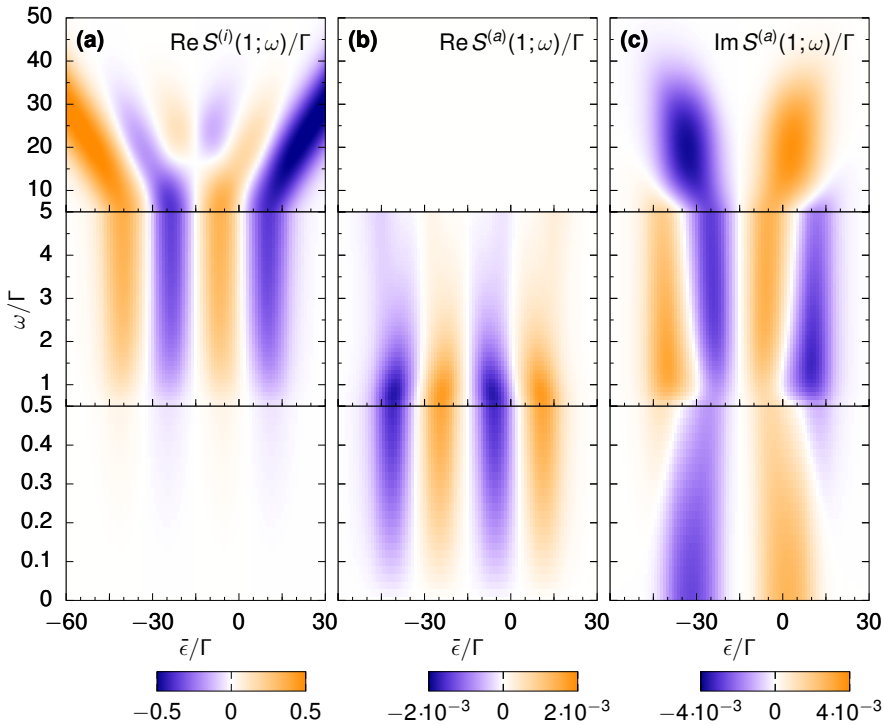

Figure 6.7: Full frequency dependence of the finite-frequency noise for a strongly interacting quantum dot. We show results for the first noise harmonic displaying (a) the instantaneous contribution and (b)-(c) the real and imaginary part of the adiabatic response. The high- and low-frequency results repeat the ones discussed in Secs. 6.1 and 6.2, while the middle row is obtained by employing the full crossover scheme required for the regime of intermediate frequencies. Parameters are $U = 30\Gamma$, $\beta = 1/(3\Gamma)$, $\epsilon_\uparrow = \epsilon_\downarrow$, $\delta\epsilon = 10\Gamma$ and $\Omega = 0.02\Gamma$.

6.4 Summary of the noise results

In summary, this chapter provided a comprehensive analysis of finite-frequency current-noise spectra as well as noise harmonics, which are emitted from an interacting quantum dot that is slowly driven in time. In the case of high noise frequencies, where the time scale of fluctuations is much smaller than the time scale of the quantum-dot

relaxation dynamics, we found simple noise expressions, which allowed us to identify dominating fluctuation processes in the instantaneous first noise harmonic. In the opposite limit of low noise frequencies, a main result is that the combination of strong Coulomb interaction and periodic driving leads to a unique signature in the noise, namely a non-vanishing imaginary part in the adiabatic response of the first noise harmonic. We emphasize that this noise contribution provides unambiguous evidence of Coulomb interaction, because it is absent for a noninteracting and possibly spin-split quantum dot.

The results presented here thus promote the study of noise harmonics not only as a spectroscopic tool to access contributions of individual fluctuation processes, but also to identify Coulomb interaction in the noise of the time-dependently driven quantum dot. We expect both to be of use in future related experiments. Besides that, the detailed noise calculations outlined in Chap. 5 can be readily adapted to investigate further nanosystems, e. g., to study the finite-frequency noise of adiabatic quantum pumps, consisting of a quantum dot with coupling to two adjacent electron reservoirs (see Ref. [54] for a zero-frequency noise calculation).

This concludes the presentation of finite-frequency noise results in this thesis. In the next chapters, the focus switches to the numerical description of the electron dynamics in time-dependently driven quantum dots, for which we employ time-dependent density-functional theory (TDDFT), see Sec. 3.2. The insights gained from the diagrammatic approach, which we employed so far, are used in the remainder of this thesis to extend the TDDFT description of single-electron tunneling devices.

7 | Time-Dependent DFT for Single-Electron Tunneling Devices

This chapter marks the beginning of the second part of this thesis. In this and the following chapters, we take into account an additional quantum many-body method, which is time-dependent density-functional theory (TDDFT), see Sec. 3.2 for an introduction. We focus on the description of charge transport in time-dependently driven single-electron tunneling devices, in which Coulomb repulsion is modeled by Hubbard-interaction terms. The latter is motivated by the observation that basic physics in these devices can often be described in this way, see also the introduction of Chap. 8. Note that this is a rather nonstandard application of TDDFT, and the investigation of the respective exchange-correlation (XC) potential is an active research field, as outlined in Sec. 3.2.4. In the present and the subsequent chapters we advance this discussion by deriving a *nonadiabatic* (i. e. time-nonlocal) XC potential based on the Anderson model (Sec. 2.1) and inspired by insights obtained from the real-time diagrammatic method (Sec. 3.1). The derivation of the XC potential and application in TDDFT time propagations are presented in Chap. 8. In the following, we set the stage for these calculations by explaining the numerical implementation of TDDFT for single-electron tunneling devices, which is employed in this thesis. Major parts of this chapter are included, as supplemental material, in the publication *Phys. Rev. Lett.* **120** 157701 (2018).

As outlined in Sec. 3.2, the key concept of TDDFT is to define an auxiliary Kohn-Sham (KS) system of noninteracting electrons, which

move in an effective potential, given by the external potential of the interacting system plus the (trivial) Hartree (H) and (nontrivial) XC contributions. Importantly, the electron density in the KS system is identical to the physical electron density in the interacting system. We now focus on this KS system and numerically compute its time evolution, which is described by the von Neumann Eq. (3.1), in which we insert the KS Hamiltonian. At this point, a severe simplification arises from the fact that the KS system is noninteracting, which means that we can treat the time evolution of the many-particle KS density matrix as a single-particle problem: we determine a complete set of single-particle states at the initial time, $\{|\psi(t_0)\rangle\}$, and compute their time evolution using the KS Schrödinger equation, $i\partial_t |\psi(t)\rangle = H_{\mathrm{KS}}(t) |\psi(t)\rangle$. At the end, each of these states appears with a time-independent weight, p_ψ, in the many-particle KS density matrix. To calculate ensemble averages of single-particle observables, such as the density, at time t, we sum up the values obtained from $\{|\psi(t)\rangle\}$ taking into account the weights $\{p_\psi\}$ (see below).

7.1 Single-electron tunneling devices

The main focus is the single-electron emitter introduced in Secs. 2.1-2.2, which consists of a time-dependently driven and interacting quantum dot coupled to a single contact, see the Anderson model in Eq. (2.1). However, to remain more general, we here discuss the extended scenario of N_{dot} interacting quantum dots coupled to a shared electron reservoir.[1] The latter is used in Chap. 8 to investigate an experiment by Beckel et al. [196], where a self-assembled layer of quantum dots is located on top of a two-dimensional electron gas [see Fig. 8.1 (b)]. We begin with the generalized Anderson Hamiltonian

$$H(t) = \sum_{l,\sigma} \epsilon_l(t) d_{l\sigma}^\dagger d_{l\sigma} + \sum_l U_l d_{l\uparrow}^\dagger d_{l\uparrow} d_{l\downarrow}^\dagger d_{l\downarrow} + \sum_{k,\sigma} \epsilon_k c_{k\sigma}^\dagger c_{k\sigma} + \sum_{k,l,\sigma} \gamma_{kl} \left(c_{k\sigma} d_{l\sigma}^\dagger + \mathrm{H.c.} \right), \tag{7.1}$$

[1] In Chap. 9 we present another extension: an interacting quantum dot coupled to two contacts and exposed to a (possibly time-dependent) bias voltage.

with quantum-dot index $l = 1, \ldots, N_{\mathrm{dot}}$. Compared to Eq. (2.1), we also keep the energy dependence of the tunnel couplings, γ_{kl} in Eq. (7.1). This is important to take care of the quantum-dots' real-space positions, $\{r_l\}$, which we model by an energy-dependent phase of the reservoir-dot couplings, $\gamma_{kl} = \gamma_l \exp(ik \cdot r_l)$, where γ_l is assumed as energy independent, see, e. g., Ref. [197]. This modeling allows us to analyze specific spatial geometries of quantum dots coupled to a shared reservoir. Note that we always consider a one-dimensional reservoir for simplicity, but extensions to two or three dimensions are possible.

Along the lines of Sec. 3.2.3, we define the Hamiltonian of the related noninteracting KS system as

$$H_{\mathrm{KS}}(t) = \sum_{l,\sigma} \left[\epsilon_l(t) + \epsilon_{\mathrm{HXC},l}[n](t)\right] d_{l\sigma}^\dagger d_{l\sigma} + \sum_{k,\sigma} \epsilon_k c_{k\sigma}^\dagger c_{k\sigma} + \sum_{k,l,\sigma} \left(\gamma_{kl} c_{k\sigma} d_{l\sigma}^\dagger + \mathrm{H.\,c.}\right), \tag{7.2}$$

which includes Eq. (3.9) as the case $N_{\mathrm{dot}} = 1$. Again, the H and XC contributions to the energy level of the lth quantum dot are modeled by a shift of this level by the amount $\epsilon_{\mathrm{HXC},l}[n](t)$, which is assumed to only depend on the electron density and its historic evolution. To calculate the electronic density on the lth quantum dot, we evaluate $n_l(t) = \sum_\sigma \left\langle d_{l\sigma}^\dagger d_{l\sigma} \right\rangle (t)$, with $n(t) = \sum_l n_l(t)$, by time propagating the KS single-particle orbitals.

7.2 Open-boundary Schrödinger equation

For the numerical time propagation of KS single-particle wave functions we implemented a TDDFT code, which we based on an open-boundary approach to the Schrödinger equation [198], see also Refs. [199, 200]. This open-boundary Schrödinger equation only describes the nanoscale part of the system directly, i. e., the quantum dots (see Fig. 8.1 (a)-(b) for illustrations of the systems studied here). The reservoir is fully included in terms of a boundary condition for the wave functions projected onto the quantum-dot region. Since we only keep track of these quantum-dot parts of the wave functions during a time propagation, this method is natural to use for time-dependent quantum-transport

problems, where we are typically less interested in details of the electron dynamics in the reservoir. The technical benefit is computational speed-up, because we only store and time propagate the projected wave functions. We now outline this approach applied to the many quantum-dot system defined in Eq. (7.1). We also point out that we work with a reservoir discretized in k-space.[2]

To derive the open-boundary Schrödinger equation, we first partition the KS Hamiltonian of Eq. (7.2), expressed in the single-particle basis given by the quantum-dot and reservoir KS orbitals, as

$$H_{\mathrm{KS}}(t) = \begin{pmatrix} H_{\mathrm{cc}}(t) & H_{\mathrm{cr}} \\ H_{\mathrm{rc}} & H_{\mathrm{rr}} \end{pmatrix}, \tag{7.3}$$

where $H_{\mathrm{cc}}(t)$ [H_{rr}] acts on the quantum dot [reservoir] degrees of freedom, while H_{cr} and H_{rc} describe tunneling between the quantum dot and the reservoir. Since the spin sector factorizes for the KS Hamiltonian in Eq. (7.2), we restrict the following discussion to a single spin species. Furthermore, we also express a KS single-particle state $|\psi(t)\rangle$ in the basis given by the quantum-dot and reservoir KS orbitals, and thus write it as a vector $\psi(t) = (\psi_{\mathrm{c}}(t), \psi_{\mathrm{r}}(t))^{\mathrm{T}}$, where $\psi_{\mathrm{c/r}}(t)$ denotes the quantum-dot/reservoir part of the wave function. As outlined in Ref. [198], the time-dependent Schrödinger equation for a KS single-particle state, $|\psi(t)\rangle$, projected onto the quantum-dot region, $\psi_{\mathrm{c}}(t)$, can then be written as

$$\begin{aligned} i\partial_t \psi_{\mathrm{c}}(t) = {} & H_{\mathrm{cc}}(t)\psi_{\mathrm{c}}(t) \\ & + \int_{t_0}^{t} dt' \Sigma(t,t')\psi_{\mathrm{c}}(t') + iH_{\mathrm{cr}} g_{\mathrm{r}}(t,t_0)\psi_{\mathrm{r}}(t_0), \end{aligned} \tag{7.4}$$

with $\Sigma(t,t') = H_{\mathrm{cr}} g_{\mathrm{r}}(t,t') H_{\mathrm{rc}}$ and the reservoir Green's function $g_{\mathrm{r}}(t,t')$. The two additional terms on the right-hand side of Eq. (7.4), respectively the memory and the source term, are due to the presence of the reservoir. The reservoir Green's function is defined as the solution of the equation $(i\partial_t - H_{\mathrm{rr}})\, g_{\mathrm{r}}(t,t') = \delta(t-t')$, with initial value $g_{\mathrm{r}}(t^+,t) = -i$, which is

$$g_{\mathrm{r}}(t,t') = \frac{1}{2\pi} \int d\omega e^{-i\omega(t-t')} \left(\omega - H_{\mathrm{rr}} + i\eta\right)^{-1}, \tag{7.5}$$

[2] An alternative possibility is a discretization based on a tight-binding chain.

with $\eta \to 0$. Inserting the partitioned Hamiltonian and the reservoir Green's function into Eq. (7.4), we obtain, for the lth entry,

$$\begin{aligned} i\partial_t \psi_{\mathrm{c},l}(t) = & \left[\epsilon_l(t) + \epsilon_{\mathrm{HXC},l}[n](t)\right]\psi_{\mathrm{c},l}(t) \\ & - i\int_{t_0}^{t} dt' \sum_{l',k} \gamma_l \gamma_{l'}^* e^{ik(r_l - r_{l'}) + i\epsilon_k(t'-t)} \psi_{\mathrm{c},l'}(t') \\ & + \sum_k \gamma_l e^{ikr_l - i\epsilon_k(t-t_0)} \psi_{\mathrm{r},k}(t_0), \end{aligned} \tag{7.6}$$

where $\psi_{\mathrm{r},k}(t_0)$ is the kth component of the vector $\psi_{\mathrm{r}}(t_0)$. Since in this thesis, we always assume a reservoir with a one-dimensional flat energy band, we rewrite the product $k(r_l - r_{l'})$ in Eq. (7.6) as $\mathrm{sgn}(k)\epsilon_k(\bar{t}_l - \bar{t}_{l'})$, with $\bar{t}_l = \frac{|r_l|}{v_{\mathrm{F}}}$, and v_{F} and sgn being the Fermi velocity and the sign function. Moreover, we write the first sum over k as an integral over a constant density of states, which leads to a delta distribution. We derive the final expression,

$$\begin{aligned} i\partial_t \psi_{\mathrm{c},l}(t) = & \left[\epsilon_l(t) + \epsilon_{\mathrm{HXC},l}[n](t) - \frac{i\Gamma_l}{2}\right]\psi_{\mathrm{c}}(t) \\ & - \frac{i}{2}\sum_{l\neq l'} \Gamma_{ll'} \psi_{\mathrm{c},l'}\left(t - |\bar{t}_l - \bar{t}_{l'}|\right) \theta\left(t - t_0 - |\bar{t}_l - \bar{t}_{l'}|\right) \\ & + \sum_k \gamma_l e^{i\mathrm{sgn}(k)\epsilon_k \bar{t}_l - i\epsilon_k(t-t_0)} \psi_{\mathrm{r},k}(t_0), \end{aligned} \tag{7.7}$$

with $\Gamma_{ll'} = 2\pi\nu_0 \gamma_l \gamma_{l'}^*$, the tunnel-coupling strengths $\Gamma_l = \Gamma_{ll}$, the density of states at the Fermi energy ν_0 and with θ denoting the Heaviside step function. For $N_{\mathrm{dot}} = 1$ we furthermore define $\Gamma = \Gamma_1$. Equation (7.7) is applied in all TDDFT calculations shown in this thesis (except the linear-response calculations of Sec. 8.3, which are based on TDDFT linear-response theory). Notably, the second line in Eq. (7.7) only contributes if the propagation time, $t - t_0$, is larger than $|\bar{t}_l - \bar{t}_{l'}|$ for any combination $l' \neq l$.

7.3 Discretization and initial conditions

As initial condition at time t_0, we consider the equilibrium density matrix of the uncoupled KS system ($\gamma_l = 0$). The initial occupation

of the reservoir orbital related to ϵ_k is, therefore, given by $f^+(\epsilon_k)$ in the spin-less system, and $2f^+(\epsilon_k)$ in the spin-full system, where $f^+(E) = 1/(1+e^{\beta E})$ is the Fermi function with inverse temperature β. The initial occupation of the quantum dots has been chosen arbitrarily in the calculations in this thesis. Unless otherwise noted, presented TDDFT densities are shown for $t \gg t_0$, where any current due to the initial quantum-dot occupations has decayed.[3] The density on the lth quantum dot reads as $n_l(t) = \sum_{\{\psi\}} p_\psi |\psi_{\mathrm{c},l}(t)|^2$, where the sum goes over all KS orbitals and p_ψ is the initial occupation of each orbital. In practice, we use a discrete number N_{res} of KS orbitals by considering reservoir energy levels, ϵ_k, equally distributed over an energy interval, I_{res}, in accordance with the flat-band approximation. For each value of ϵ_k we include two reservoir states, respectively, for the two signs of k. Numerical inaccuracies which are introduced by the discretization are discussed further in Sec. 7.4. The discretization of the system is illustrated in Fig. 7.1 for a single quantum dot coupled to a reservoir. In the calculations shown in this thesis we are restricted to the case where distances between neighboring dots are sufficiently large, which allows us to drop the term in the second line of Eq. (7.7) in the time evolution. However, it would be an interesting extension of the calculations to also include this term, in order to investigate coupling between the quantum dots mediated by the reservoir, see also the outlook in Chap. 10. Notably, we expect the importance of this term to be reduced by processes which lead to decoherence in the reservoir, e. g., electron-electron or electron-phonon scattering, which are not included in the calculations. The insightful task to analyze, e. g., two interacting quantum dots which are close to each other in a TDDFT time evolution, based on Eq. (7.7), is left for future research.

7.4 Time propagation and numerical aspects

The KS orbitals are numerically propagated in time by applying Eq. (7.7) with a discretized time step. After each step, we adjust the HXC potential by evaluating, with the updated densities, the approximation used for $\epsilon_{\mathrm{HXC},l}[n](t)$.

[3] We could also perform a self-consistent DFT calculation to find, as initial state, the equilibrium configuration at inverse temperature β.

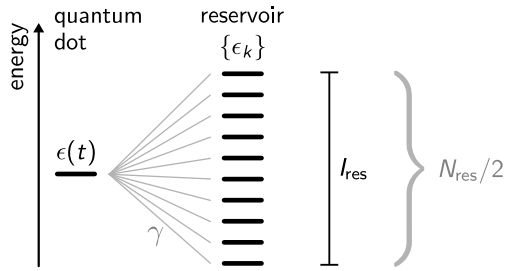

Figure 7.1: Sketch of a single energy level tunnel-coupled to a discretized reservoir. Each of the energy values shown for the reservoir corresponds to two single-particle states with opposite momentum, as explained in Sec. 7.3.

In this section, we briefly comment on numerical aspects, which are relevant for an accurate time evolution. In this paragraph, we analyze a noninteracting system, for which the implementation described in this chapter obtains the exact time evolution, if the numerical data is properly converged. As mentioned in Sec. 7.3, the numerical accuracy of the calculations is essentially controlled by three parameters, namely the time step, Δt, the number of reservoir states, N_{res}, and the interval, I_{res}, on which the reservoir states are distributed. While the time step clearly must be chosen sufficiently small to converge a calculation, it is more interesting to study the impact of the number of reservoir states on the outcome of a time propagation. This is exemplified in Fig. 7.2, showing the density and current evolution calculated for a single energy level coupled to a discretized reservoir for three values of N_{res}. Since the initial occupation of the dot is not the equilibrium occupation in these calculations, we find that the density begins to decay towards its equilibrium value in the time interval $0 < t\Gamma < 2$ (solid line). A sudden change of the energy-level position at $t\Gamma = 2$ triggers a strong increase of the density in the following time evolution. By also analyzing the dashed lines in Fig. 7.2, we conclude that a large number of reservoir states is crucial to delay the onset of back reflection, where the finite size of the discretized reservoir starts to influence the density and current evolution. This effect is more pronounced for the current shown in Fig. 7.2 (b), where additional current peaks appear when N_{res} is too small. To avoid this finite-size effect, we have to increase

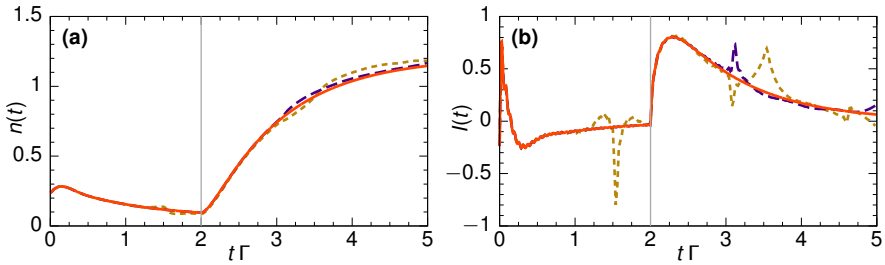

Figure 7.2: (a) Density and (b) current evolution of a single energy level coupled to N_{res} reservoir states and subject to a step-pulse gate voltage (unconverged data to illustrate numerical issues). The position of the energy level changes suddenly from $\epsilon(t\Gamma < 2) = 5\Gamma$ to $\epsilon(t\Gamma \geq 2) = -5\Gamma$ (thin line). Shown are results for $N_{\mathrm{res}} = 100$ (short dashed), $N_{\mathrm{res}} = 200$ (long dashed) and $N_{\mathrm{res}} = 400$ (solid). Further parameters are $\beta = 1/(2\Gamma)$, $I_{\mathrm{res}} = [-100\Gamma, 100\Gamma]$, $\Delta t = 2 \cdot 10^{-5}/\Gamma$.

N_{res} depending on the maximum propagation time we want to achieve. Besides that, we also observe in panel (b) (solid line) that the current oscillates quickly, with very small amplitude, around a time-dependent mean value. We find that these oscillations are suppressed further if we increase I_{res}, while keeping the ratio $N_{\mathrm{res}}/I_{\mathrm{res}}$ constant. Note that extending the energy interval for the reservoir states implies that a smaller time step is necessary for the calculation to converge, which can strongly affect the computation time.

In the next chapter, we employ the TDDFT implementation outlined here to calculate TDDFT time evolutions of single and multiple quantum dots. To separate the discussion of technical issues (this chapter) from the TDDFT results presented there, we end this section by providing the numerical parameters, which we used to compute the results presented in Chap. 8. In Fig. 8.3 (a) we show densities which are calculated by propagating 1600 reservoir orbitals, distributed in $I_{\mathrm{res}} = [-900\Gamma, 900\Gamma]$, with the time step $\Delta t = 10^{-5}/\Gamma$. The currents in Fig. 8.3 (b) are obtained with 1000 reservoir orbitals (lowest drive frequency with 1300 orbitals), $I_{\mathrm{res}} = [-100\Gamma, 100\Gamma]$ and $\Delta t = 3 \cdot 10^{-5}/\Gamma$. For Figs. 8.4 and 8.5 we used 2500 reservoir orbitals distributed in $I_{\mathrm{res}} = [-600\Gamma, 600\Gamma]$ and with $\Delta t = 10^{-5}/\Gamma$. To compute Fig. 8.6, we applied 1600 orbitals, $I_{\mathrm{res}} = [-200\Gamma, 200\Gamma]$ and $\Delta t = 3 \cdot 10^{-5}/\Gamma$.

8 XC Potential from Master Equations and Applications

We apply time-dependent density-functional theory (TDDFT) to describe the electron dynamics in time-dependently driven single-electron tunneling devices. In this chapter, we study two different systems: a single quantum dot coupled to a single contact and many quantum dots coupled to a single contact, see Fig. 8.1 (a)-(b). To take into account Coulomb repulsion on the quantum dot(s), we derive an exchange-correlation (XC) potential from master equations, based on a reverse-engineering procedure developed below. Note that we published major parts of this introduction and of Secs. 8.1-8.2 (excluding Sec. 8.2.2) in *Phys. Rev. Lett.* **120** 157701 (2018); Sec. 8.3 (except Sec. 8.3.5) is published in *J. Phys.: Conf. Ser.* **969** 012145 (2018); Besides that, a preprint of a paper which includes Secs. 8.2.2 and 8.3.5 is available with the reference *arXiv:1810.00183*.

To begin, we emphasize that a central goal of this chapter is to put forward the concept of simulating interacting single-electron tunneling devices with TDDFT. The idea is based on the observation that the basic physics in these devices can, in many cases, be well described by model Hamiltonians with Hubbard interaction terms. But, even when relying on model Hamiltonians, it can be a challenge to obtain the dynamics in the presence of interaction, see, e. g., Refs. [27, 100]. For this reason, we believe that the method outlined in this chapter benefits both, the mesoscopic-transport and the TDDFT community, because (1) it opens up TDDFT simulations of experimentally relevant

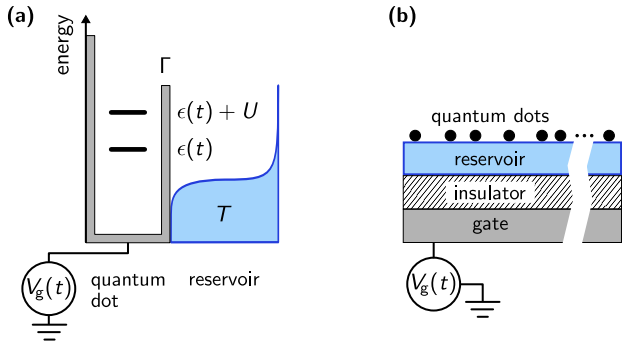

Figure 8.1: (a) Energy diagram of a single-level quantum dot with tunnel coupling, Γ, to a reservoir. (b) Sketch of many quantum dots coupled to a shared reservoir.

nanoscale devices, and (2) it leads to analytical expressions of XC potentials, from which we can understand properties that are essential for the accuracy of TDDFT. In particular, the XC potential derived below turns out to be *nonadiabatic* (i. e. time-nonlocal), which is a property that is of key interest for current TDDFT development, see Sec. 3.2.2.

The first system we investigate is the single-electron source based on a time-dependently driven single-contact quantum dot, see Sec. 2.1. To describe the single-contact quantum dot in TDDFT, we develop a nonadiabatic XC potential for this system, by using insights obtained from perturbation theory.[1] To find this XC potential, we begin with the Anderson model in Eq. (2.1) and the related Kohn-Sham (KS) system, defined in Eq. (3.9). We then describe the dynamics in both systems with Markovian master equations, see Sec. 3.1.2. In a next step, we exploit the fact that the densities in both systems are identical, to reverse-engineer an XC potential which depends on the quantum-dot's density and its first time derivative.

This chapter is organized in the following way. In Sec. 8.1 we discuss the derivation of the nonadiabatic XC potential for the single-contact quantum dot. We then apply this XC potential in Sec. 8.2, not only

[1] We remind that we already analyzed the single-electron emitter in Chaps. 5-6, where we derived current-noise spectra of this system with real-time diagrammatic perturbation theory.

to describe the single-electron source, but also to simulate a system consisting of multiple quantum dots coupled to a shared electron reservoir, as illustrated in Fig. 8.1 (b). This setup has been realized in a recent experiment [196], and the example here demonstrates the applicability of the XC potential to larger systems. To validate—for the single-contact quantum dot—the quality of the TDDFT results, we present a comparison with accurate time-dependent density-matrix renormalization-group data in Sec. 8.2.2. Besides that, in Sec. 8.3, we analyze the developed XC potential in the framework of linear-response theory and calculate finite-frequency admittances. The results of this chapter are summarized in Sec. 8.4. Note that a generalization for a two-contact quantum dot is presented in Chap. 9.

8.1 XC potential from master equations

8.1.1 Interacting system

We begin by describing the time-dependent dynamics of the quantum dot coupled to a single reservoir in terms of a master equation. We consider the regime of weak reservoir-dot coupling, $\beta\Gamma \ll 1$, where the dynamics is Markovian whenever the reservoir memory time, $\tau_\mathrm{r} = \beta$, is smaller than time scales [67, 99, 105, 201] introduced by the particular driving scheme. In this regime, the dynamics of the single-electron source is well described by the sequential-tunneling picture [101], which has the advantage of yielding an explicit analytic expression for the nonadiabatic XC potential derived below. We note that the formalism can be extended to include higher-order tunneling corrections and also corrections with respect to non-Markovian dynamics, by applying the real-time diagrammatic technique developed in Refs. [64–67], see also Sec. 3.1. One anticipated generalization is, e. g., to include second-order tunneling in the derivations outlined here [99].

We consider the reduced density matrix, $\rho_\mathrm{dot}(t)$, of the quantum dot, which is related to the full density matrix $\rho(t)$ of the reservoir-dot system by a partial trace over the reservoir degrees of freedom. The reduced Hilbert space includes the many-particle states $\{|0\rangle, |\uparrow\rangle, |\downarrow\rangle, |2\rangle\}$ denoting an empty, singly (with spin $\uparrow, \downarrow$) and doubly occupied dot. The diagonal part of $\rho_\mathrm{dot}(t)$ defines the vector of occupation probabilities, $\boldsymbol{P}(t) = [P_0(t), P_1(t), P_2(t)]^\mathrm{T}$, where $P_1(t) = P_\uparrow(t) + P_\downarrow(t)$ cap-

tures both possible spin configurations for single occupation.[2] The electronic density on the quantum dot is $n(t) = \boldsymbol{n}^{\mathrm{T}}\boldsymbol{P}(t)$, with $\boldsymbol{n}^{\mathrm{T}} = [0, 1, 2]$. The first step of the reverse-engineering procedure is to express the occupation vector in terms of the density, $n(t)$, and a further degree of freedom, $p(t)$, which is related to the parity of the quantum dot [202], by

$$\boldsymbol{P}(t) = \begin{pmatrix} 1 - n(t) \\ n(t) \\ 0 \end{pmatrix} + p(t) \begin{pmatrix} 1 \\ -2 \\ 1 \end{pmatrix}, \tag{8.1}$$

with $n(t)/2 \geq p(t) \geq \max\big(0, n(t) - 1\big)$. For the spin-degenerate system, the time evolution of the occupation vector decouples from the off-diagonal elements in $\rho_{\mathrm{dot}}(t)$ [65], and is well approximated by the Markovian master equation[3]

$$\partial_t \boldsymbol{P}(t) = \mathcal{W}_t^{(\mathrm{i})} \boldsymbol{P}(t), \tag{8.2}$$

see also Eq. (3.6). The superscript (i) for 'instantaneous' at the kernel $\mathcal{W}_t^{(\mathrm{i})}$ denotes that the latter is derived with parameters frozen at time t. The kernel reads

$$\frac{\mathcal{W}_t^{(\mathrm{i})}}{\Gamma} = \begin{bmatrix} -2f^+(\epsilon) & f^-(\epsilon) & 0 \\ 2f^+(\epsilon) & -f^-(\epsilon) - f^+(\epsilon + U) & 2f^-(\epsilon + U) \\ 0 & f^+(\epsilon + U) & -2f^-(\epsilon + U) \end{bmatrix}, \tag{8.3}$$

with $\epsilon = \epsilon(t)$. In the next subsection, we exploit the well-known Eqs. (8.2) and (8.3) to develop a nonadiabatic XC potential for the noninteracting KS system given in Eq. (3.9) (which equals Eq. (7.2) for $N_{\mathrm{dot}} = 1$). In addition, we use them as a reference for the time evolution of the interacting system in Sec. 8.2.

8.1.2 Kohn-Sham system and reverse engineering

We now describe the dynamics of the single-electron source in TDDFT. Therefore, as explained in Sec. 3.2.3, we assume noninteracting v-representability and consider the KS Hamiltonian defined in Eq. (3.9).

[2] Compare also to Secs. 3.1 and 5.4, where we keep the spin degree-of-freedom.

[3] The initial time has been sent to minus infinity and any information of the initial condition has decayed.

In this equation, the HXC (Hartree+XC) potential is modeled by the level shift $\epsilon_{\mathrm{HXC}}[n](t)$. To derive a nonadiabatic approximation of this HXC potential, we express the dynamics of the KS system also in terms of a master equation. This step is a necessary for the analytical reverse-engineering shown below. Note that this requires the additional assumption of Markovian dynamics to hold also in the KS system, see also the discussion in Sec. 3.1.2. Its time evolution is then given by

$$\partial_t \boldsymbol{P}_{\mathrm{KS}}(t) = \mathcal{W}^{(\mathrm{i})}_{\mathrm{KS},t}\, \boldsymbol{P}_{\mathrm{KS}}(t), \tag{8.4}$$

with the KS occupation vector, $\boldsymbol{P}_{\mathrm{KS}}(t)$, and the quantum-dot electronic density, $n(t) = \boldsymbol{n}^{\mathrm{T}} \boldsymbol{P}_{\mathrm{KS}}(t)$. The KS kernel, $\mathcal{W}^{(\mathrm{i})}_{\mathrm{KS},t}$, is calculated by setting $U \to 0$ and $\epsilon(t) \to \epsilon(t) + \epsilon^{\mathrm{M}}_{\mathrm{HXC}}[n](t)$ in the expression in Eq. (8.3). The superscript M on the HXC potential reminds that the Markov approximation is applied in Eqs. (8.2) and (8.4).

Based on the master equations (8.2) and (8.4), we now derive a nonadiabatic approximation of the HXC potential. The key observation is that the position of the quantum dot energy level is uniquely fixed by the density and its first time derivative. In the interacting system, the latter is written, with Eq. (8.2), as $\dot{n}(t) = \boldsymbol{n}^{\mathrm{T}} \mathcal{W}(t) \boldsymbol{P}(t)$. Inserting the representation of the occupation vector (8.1) into this equation, only the contribution stemming from the first term on the right-hand side of Eq. (8.1) remains [202]. This means that the time-dependent energy level of the quantum dot, $\epsilon(t)$, only depends on $n(t)$ and $\dot{n}(t)$. Explicitly, we write $\epsilon(t)$ as a function, g, with

$$\epsilon(t) = g\big(n(t), \dot{n}(t), \Gamma, \beta, U\big), \tag{8.5}$$

where Γ, β and U are constants. The same inversion in the noninteracting KS system leads to

$$\epsilon(t) + \epsilon^{\mathrm{M}}_{\mathrm{HXC}}[n](t) = g\big(n(t), \dot{n}(t), \Gamma, \beta, 0\big), \tag{8.6}$$

where we have used the fact that the KS and the interacting system have the same density, $n(t)$. Solving Eqs. (8.5) and (8.6) for $\epsilon^{\mathrm{M}}_{\mathrm{HXC}}$, we obtain

$$\epsilon^{\mathrm{M}}_{\mathrm{HXC}}\big(n(t), \dot{n}(t)\big)(t) = \frac{1}{\beta} \log\Big\{ C\big(n(t), \dot{n}(t)\big)\Big\}, \tag{8.7}$$

with

$$C(n,\dot{n}) = \frac{\xi_1(n,\dot{n})}{\xi_2(n,\dot{n}) - \sqrt{\xi_2(n,\dot{n})^2 - \xi_3(n,\dot{n})}} \tag{8.8}$$

and the additional abbreviations

$$\xi_1(n,\dot{n}) = 2e^{\beta U}\big(\dot{n} + \Gamma(n-2)\big), \tag{8.9a}$$

$$\xi_2(n,\dot{n}) = \dot{n} + e^{\beta U}\big(\dot{n} + 2\Gamma(n-1)\big), \tag{8.9b}$$

$$\xi_3(n,\dot{n}) = 4e^{\beta U}\left((\dot{n} + \Gamma n)^2 - 2\Gamma(\dot{n} + \Gamma n)\right). \tag{8.9c}$$

Equation (8.7) is a first key result of this section. It defines an HXC potential, which is nonadiabatic due to its dependence on the first time derivative of the density. We remark that a general functional dependence is denoted by $[n]$, but, in this specific approximation, the HXC potential becomes a function of $n(t)$ and $\dot{n}(t)$. Importantly, for vanishing $\dot{n}(t)$, the expression in Eq. (8.7) equals the adiabatic HXC potential derived in Ref. [88], $\epsilon^{\mathrm{ad}}_{\mathrm{HXC}}\big(n(t)\big)(t) = \epsilon^{\mathrm{M}}_{\mathrm{HXC}}\big(n(t),0\big)(t)$, which we use for comparison in the subsequent sections.

8.1.3 Properties of the nonadiabatic XC potential

To outline nonadiabatic properties of the HXC potential derived in Eq. (8.7), we first compare its form to the related adiabatic HXC potential. Both potentials are presented in Fig. 8.2 (a)-(b). As visible in (b), and already discussed in Sec. 3.2.4, the adiabatic potential shows a step, denoted as derivative discontinuity (DD) [120–125], which is centered at the electron-hole symmetric point, $n = 1$, and smeared out[4] by temperature [88, 127, 131]. This step is, e. g., relevant to reproduce Coulomb-blockade physics in a non-interacting KS system [86, 126, 127]. In the nonadiabatic HXC potential, this feature is strikingly modified, see the density plot in Fig. 8.2 (a). Here, a non-zero time derivative of the density shifts the position of the step to different density values, giving rise to a dynamical step. Importantly, we find that this *dynamical* step improves the TDDFT description by impeding electron tunneling in the KS system, see also Ref. [129]. Related dynamical steps have been reported for two-electron systems

[4] In Fig. 3.2 (b), the adiabatic HXC potential is plotted for different temperatures.

with long-range Coulomb interaction [116, 123, 128, 129] and for a 1D semiconductor [130]. For the Anderson model studied here, this dynamical step clearly emerges from the DD of the stationary system. Besides that, the analytic expression for $\epsilon_{\mathrm{HXC}}^{\mathrm{M}}$ allows us to connect this step to electronic time scales by identifying charge relaxation rates of the single-electron source in the evolution of this step. The position of the dynamical step as a function of the time-derivative of the density reads as

$$n = 1 - \dot{n}\left(\tau_{\mathrm{c}}^{U=0} - \tau_{\mathrm{c}}^{U\neq 0}\right), \tag{8.10}$$

where $\tau_{\mathrm{c}}^{U=0} = \Gamma^{-1}$ denotes the time scale of charge relaxation in the noninteracting system, while $\tau_{\mathrm{c}}^{U\neq 0} = \lambda_{\mathrm{c}}^{-1}(-U/2)$ denotes the respective time scale in the interacting system, evaluated at the electron-hole symmetric point. The charge relaxation rate of the interacting system, written as a function of the level position, is given by $\lambda_{\mathrm{c}}(\epsilon) = \Gamma\big[1 + f^{+}(\epsilon) - f^{+}(\epsilon + U)\big]$ [99, 105]. This link of the dynamical step to *physical* time scales of electron dynamics is a second key result of this chapter.[5] What is more, Eq. (8.10) shows that only if the second term on the right-hand side is small during the full time propagation, $|\dot{n}| \ll \left|\tau_{\mathrm{c}}^{U=0} - \tau_{\mathrm{c}}^{U\neq 0}\right|^{-1}$, the dynamical step is always close to $n = 1$ and the adiabatic HXC potential, $\epsilon_{\mathrm{HXC}}^{\mathrm{ad}}$, becomes a sufficient approximation.

8.2 Nonadiabatic dynamics with TDDFT

8.2.1 Dynamics of a single-electron source

We proceed by investigating the performance of the nonadiabatic HXC potential developed in the last section. As a first application, we employ it in TDDFT simulations of the interacting single-electron source, which we used to derive the HXC potential of Eq. (8.7). Note that a successful TDDFT description of this system opens up a variety

[5] We point out that this charge-relaxation rate also plays a significant role in Chap. 6 of this thesis, where we study the finite-frequency noise of single-electron emitters. There, it appears as a scale which competes with the noise frequency and which leads to a suppression of the instantaneous noise for very low frequencies, see, e. g., Eqs. (6.7) and (6.10).

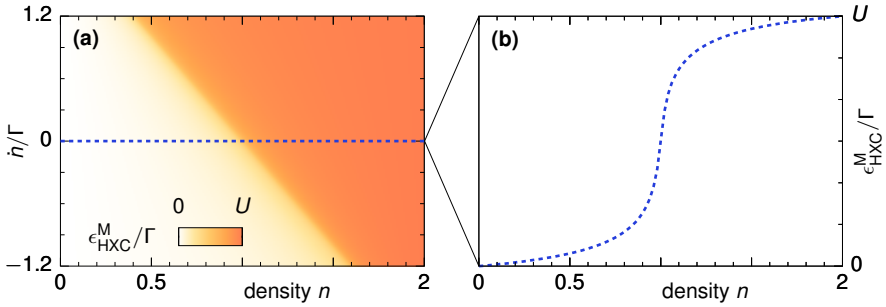

Figure 8.2: (a) Nonadiabatic HXC potential of Eq. (8.7) for $U = 16\Gamma$, $\beta = 1/(2\Gamma)$. (b) Line cut at $\dot{n} = 0$, showing the potential step at integer occupation, which becomes a dynamical step if $\dot{n} \neq 0$.

of future studies. First of all, it is insightful to investigate in which way the TDDFT results deviate from the master-equation data. This point is studied in this section, and, in particular, in the subsequent Sec. 8.2.2, where we show that the TDDFT description is significantly more accurate in nonadiabatic time propagations than the master equation used initially. Furthermore, due to the numerical efficiency of TDDFT, we can anticipate calculations, e. g., of several independent single-electron sources which emit electrons into a shared reservoir. A first step in this direction is presented in Sec. 8.2.3 and we discuss further possibilities for future studies in Chap. 10, see also Chap. 9.

For the numerical calculations of the single-electron source, we assume a finite but sufficiently large number of states for the reservoir and propagate the KS density matrix of the combined reservoir-dot system in time until periodicity has been established. For details on the numerical implementation we refer to Chap. 7. The ensemble TDDFT calculations presented here begin with an equilibrium KS density matrix with finite inverse temperature β. Since the KS system is noninteracting, this involves the time propagation of single-particle wave functions using a continuously updated KS Hamiltonian. We remind that the HXC potential is the only approximation in a TDDFT calculation besides the discretization of the Hamiltonian, and no further approximations, e. g., with respect to weak tunnel coupling or to Markovian dynamics, are made for the time propagation. We compare the results to the ones obtained by applying the adiabatic

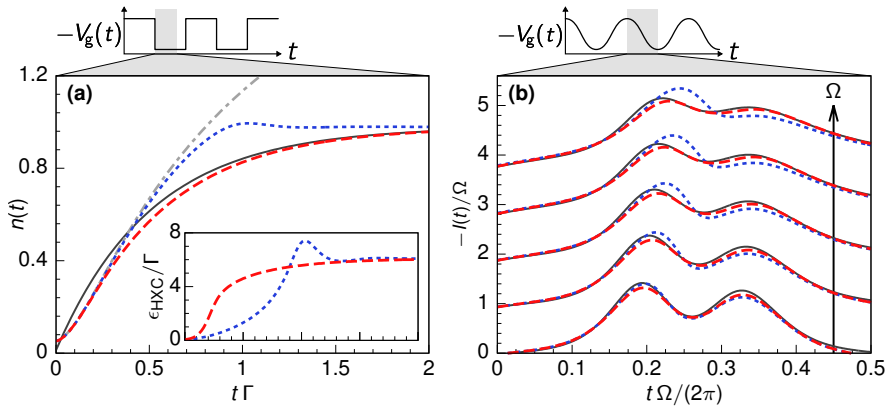

Figure 8.3: Comparison of TDDFT results obtained using $\epsilon_{\mathrm{HXC}}^{\mathrm{ad}}$ (dotted lines), $\epsilon_{\mathrm{HXC}}^{\mathrm{M}}$ (dashed lines) and no HXC potential (dashed-dotted lines) with analytic results from Eq. (8.2) (solid lines). (a) Densities of the quantum dot subject to a square pulse (inset: HXC potentials) with parameters $U = 16\Gamma$, $\beta = 1/(2\Gamma)$, $\epsilon(t < 0) = 10\Gamma$, $\epsilon(t > 0) = -6\Gamma$. (b) Currents in the case of a harmonic gate-voltage drive plotted for driving frequencies in the range $[0.1\Gamma, 0.5\Gamma]$ with $\Delta\Omega = 0.1\Gamma$ (note that for visibility lines are shifted by 1). Further parameters are $U = 12\Gamma$, $\beta = 1/(3\Gamma)$, $\epsilon(t) = -6\Gamma + 18\Gamma\cos(\Omega t)$.

HXC potential as well as the master Eq. (8.2). A comparison with td-DMRG data is outlined in Sec. 8.2.2.

We begin by analyzing the time-dependent charge flow between the quantum dot and the reservoir induced by a step-pulse gate-voltage driving, see Fig. 8.3 (a).[6] For weak reservoir-dot coupling, as considered here, the time-dependent density, $n(t)$, is well described by an exponential decay towards its new equilibrium value after each gate-voltage step. The characteristic decay rate is given by $\lambda_c(\epsilon)$ [99, 105], where ϵ is the new position of the energy level. This is shown by the solid line in Fig. 8.3 (a) and compared to the calculated TDDFT densities. Interestingly, the density related to $\epsilon_{\mathrm{HXC}}^{\mathrm{ad}}$ first follows the dashed-dotted line, which shows the exponential decay for a system without interaction ($U = 0$) obtained from a TDDFT calculation with $\epsilon_{\mathrm{HXC}} = 0$. Thus, we conclude that the adiabatic HXC potential leads to

[6] Numerical issues of our TDDFT time propagations are discussed in Sec. 7.4.

charge relaxation with the characteristic decay rate of a noninteracting system. The density eventually overestimates its equilibrium value and strongly decaying oscillations occur, which are visible in the inset (dotted line) of Fig. 8.3 (a), showing the time evolution of the adiabatic HXC potential. On the contrary, the TDDFT density in Fig. 8.3 (a), which corresponds to the nonadiabatic HXC potential $\epsilon_{\mathrm{HXC}}^{\mathrm{M}}$ (dashed) clearly features the expected exponential behavior with the decay rate of the interacting system. The time evolution of $\epsilon_{\mathrm{HXC}}^{\mathrm{M}}$ in the inset of Fig. 8.3 (a) also indicates that the density increases monotonically towards the new equilibrium value without any oscillating behavior. It is remarkable that the dependence on $\dot{n}(t)$ in the HXC potential is already sufficient to generate the charge-relaxation behavior of an interacting system in a noninteracting KS system. We also checked that at the time at which the two HXC potentials begin to differ, $t\Gamma \gtrsim 1/4$, the respective TDDFT densities in Fig. 8.3 (a) evolve with different decay rates. Finally, we note that minor differences between the TDDFT and the master-equation data, which are visible in the beginning of the time evolution are related to non-Markovian dynamics, which is fully neglected in Eq. (8.2) but partially included in a TDDFT calculation. Importantly, as we show in the next Sec. 8.2.2, the TDDFT data is highly accurate also in this short-time regime.

As a second application, we analyze a large-amplitude harmonic driving of the gate voltage, see Fig. 8.3 (b), presenting the resulting time-resolved currents, $I(t) = -\dot{n}(t)$. The two peaks correspond to the first and the second electron entering the initially empty quantum dot during a half period of the drive. The driving frequency increases linearly from bottom to top lines and all further parameters are chosen to illustrate the transition from the adiabatic to the nonadiabatic regime. The solid lines represent the result of Eq. (8.2) and serve as a reference point, allowing for a comparison with the TDDFT currents related to the adiabatic HXC potential, which reveals the breakdown of $\epsilon_{\mathrm{HXC}}^{\mathrm{ad}}$ for driving beyond the adiabatic regime. For larger frequencies, the left peak in the charge current is increasingly overestimated, while the right peak is underestimated. The poorly reproduced charge relaxation rate causes electrons in the KS system of the adiabatic HXC potential to tunnel too quickly. In contrast, the nonadiabatic potential leads to a good agreement between the TDDFT currents and the result of Eq. (8.2) for all displayed driving frequencies.

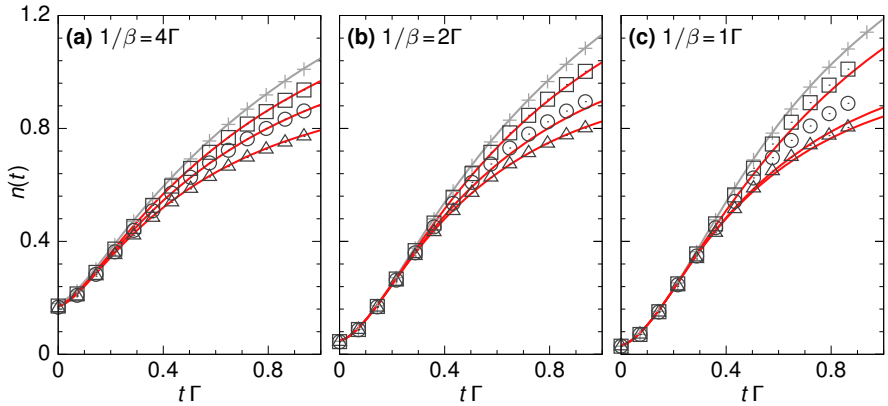

Figure 8.4: Comparison of TDDFT densities calculated using $\epsilon^{\mathrm{M}}_{\mathrm{HXC}}$ (lines) with accurate td-DMRG data (symbols) [203]. The quantum dot is subject to a square pulse with parameters $\epsilon(t<0)=10\Gamma$ and $\epsilon(t>0)=-6\Gamma$. Top to bottom lines/symbols show different interaction strengths, $U/\Gamma=0,4,8,16$, and panels (a)-(c) different temperatures.

8.2.2 Transient dynamics and comparison with td-DMRG

A crucial observation for the TDDFT approach presented here, based on $\epsilon^{\mathrm{M}}_{\mathrm{HXC}}$, is that the time evolution of the quantum dot is not only accurate at long time scales (previous section), but also at intermediate and short times, i. e., in the regime of transient dynamics (this section). In this transient regime, the Born-Markov result, which we used as a reference for long time scales in Fig. 8.3, clearly fails, since we neglected non-Markovian contributions in the master Eq. (8.2). As mentioned in the previous section, this failure is the reason for the visible difference in Fig. 8.3 (a) between the TDDFT result (long dashed) and the master-equation data (solid line) at the beginning of the time evolution. In order to assess the performance of TDDFT—employing the XC potential derived here—also in this transient regime, we compare the TDDFT results with accurate data obtained with time-dependent density-matrix renormalization-group theory (td-DMRG) [203, 204].

In Fig. 8.4 we present a comparison of TDDFT (lines) and td-DMRG results (symbols) for the interacting single-contact quantum

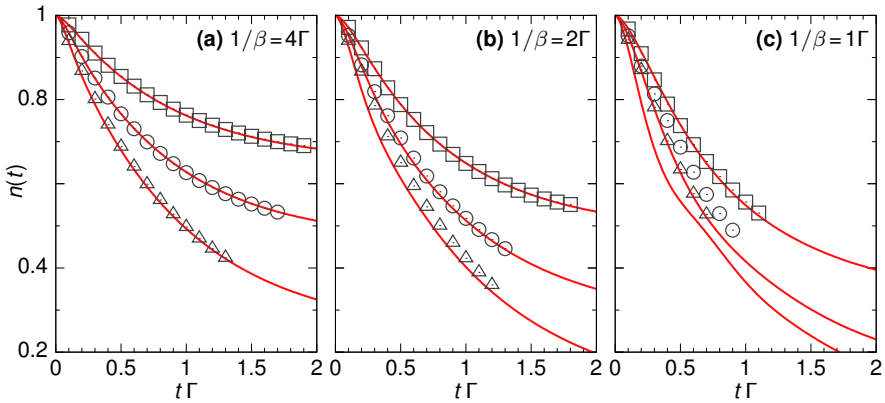

Figure 8.5: Comparison of TDDFT densities calculated using $\epsilon^{\mathrm{M}}_{\mathrm{HXC}}$ (lines) with accurate td-DMRG data (symbols) [203] for a square-pulse driving with parameters $\epsilon(t<0) = -U/2$ and $\epsilon(t>0) = U/2$. Top to bottom lines/symbols show different interaction strengths, $U/\Gamma = 4, 8, 16$, and panels (a)-(c) different temperatures.

dot subject to a sudden shift of the energy level. The panels (a)-(c) differ in the applied temperature, where the highest temperature is shown in panel (a). Here, we find that TDDFT precisely matches the td-DMRG data over the whole time evolution and for all interaction strengths plotted in the figure. This is a key result of this section, showing that the accuracy of TDDFT with $\epsilon^{\mathrm{M}}_{\mathrm{HXC}}$ significantly exceeds the accuracy of the Born-Markov master equation, which has been used to derive the XC potential $\epsilon^{\mathrm{M}}_{\mathrm{HXC}}$ in Eq. (8.7). This emphasizes the strength of the KS approach, where the interaction is modeled by an XC potential, while the KS system is otherwise solved exactly, without any approximation with respect to the time evolution.[7] The XC potential $\epsilon^{\mathrm{M}}_{\mathrm{HXC}}$ has thereby been tailored to describe the *long*-time behavior of the system in the presence of interaction and at high temperatures. Consequently, at high temperatures, we expect TDDFT and td-DMRG to differ only when the interaction plays a more important role in the *short*-time evolution, than it does for the *long*-time evolution. In panel (a), we conclude that this is not the

[7] See also Sec. 8.3.5, where we compare TDDFT, in the linear-response regime, with second-order perturbation theory.

case.[8] However, deviations are visible when we lower the temperature in panels (b) and (c). See in particular the data for $U = 8\Gamma$ (circles and second-to-lowest lines), where the level position after the shift is close to the electron-hole symmetric point. We attribute these deviations to the fact that $\epsilon^{\mathrm{M}}_{\mathrm{HXC}}$ is derived based on leading-order perturbation theory in the tunnel coupling, see Sec. 8.1. In the Coulomb-blockade regime and at intermediate temperatures, $\beta\Gamma \gtrsim 1$, it is known that relevant contributions to the time evolution appear in second order tunneling [99]. For accurate TDDFT calculations also in this regime, it is necessary to improve the approximation $\epsilon^{\mathrm{M}}_{\mathrm{HXC}}$ of Eq. (8.7).

As a second example, we compare TDDFT results and td-DMRG data for a quantum dot, which is initially singly occupied, see Fig. 8.5. At the initial time, the energy level is raised above the Fermi energy and the density on the quantum dot begins to decrease. Panels (a)-(c) show results calculated for three different temperatures and several interaction strengths. We again find that deviations between TDDFT and td-DMRG emerge at low temperatures [panel (c)] and for increasing interaction, for the reasons discussed in the previous paragraph. Importantly, at the high temperature in panel (a), the data agrees very well.

Finally, we want to emphasize the huge difference in computational effort, which is needed to obtain the TDDFT and the td-DMRG data of Figs. 8.4 and 8.5. On the one hand, the parallelized td-DMRG calculation takes, for each data set, roughly four days on an eight-core machine [203]. On the other hand, one of the TDDFT calculations only needs a few hours on a single processor.[9] What is more, the TDDFT time propagation is capable of reaching significantly longer times than td-DMRG, see, e. g., the time evolutions over several Γ^{-1} shown in Fig. 8.3 (b). This exemplifies the trade-off between accuracy and numerical efficiency, which we usually make when choosing a specific method of quantum many-body physics. It is therefore a significant

[8] Note that the dynamics at very short times after the sudden gate-voltage step is equally well described by the adiabatic HXC potential $\epsilon^{\mathrm{ad}}_{\mathrm{HXC}}$, see the left part of Fig. 8.3 (a), where the dashed and dotted lines agree.

[9] Besides that, we believe that the computation time of the employed TDDFT code can be significantly reduced by optimizing the implementation, e. g., by using a predictor-corrector scheme for the time evolution, which might allow larger time steps.

result that TDDFT with the master-equation based XC potential $\epsilon_{\mathrm{HXC}}^{\mathrm{M}}$ achieves both, accuracy and efficiency in the high temperature regime. We believe that this paves the way towards further applications of TDDFT for the theoretical description of nanoscale devices.

8.2.3 Dynamics of multiple quantum dots

As an example of a system, which is more complex than the single-electron source studied so far, we analyze the experiment reported in Ref. [196]. Here, a self-assembled layer of quantum dots is located on top of a two-dimensional electron gas. To model this setup in TDDFT, we use 70 quantum dots which are weakly coupled to a shared electron reservoir as shown in Fig. 8.1 (b). To include parameter variations of a real setup, we consider Gaussian-distributed energy levels (ϵ_l), reservoir-dot couplings (γ_l) and interaction strengths (U_l) for the quantum dots with site index l. The spatial distances between adjacent dots are modeled by multiplying γ_l with an energy-dependent phase factor [197], as explained in Sec. 7.2. In the experiment, these distances are larger than the reservoir coherence length, which justifies the application of the HXC potentials $\epsilon_{\mathrm{HXC}}^{\mathrm{M/ad}}$ for each dot separately. Figure 8.6 presents TDDFT calculations for a step-pulse gate-voltage driving, leading to the periodic charging/discharging of a fraction of quantum dots. While for both HXC potentials we observe the overall signature [196] of interaction, namely that the relaxation dynamics after positive/negative gate-voltage steps differ, the explicit evolution is *physical* only for $\epsilon_{\mathrm{HXC}}^{\mathrm{M}}$. For times exceeding the reservoir memory time, τ_{r}, the density changes in Fig. 8.6 have to lie in the gray region bounded by $|\Delta n(0)|e^{-\Gamma t}$ and $|\Delta n(0)|e^{-2\Gamma t}$, since $\Gamma \leq \lambda_{\mathrm{c}}(\epsilon) \leq 2\Gamma$ for a single dot. The charging process calculated with $\epsilon_{\mathrm{HXC}}^{\mathrm{ad}}$ violates this constraint, because each dot which is supposed to become singly occupied evolves towards double occupation initially, see also Fig. 8.3 (a).

The setup analyzed in Fig. 8.6 provides a first step towards more complex nanoscale devices, for which TDDFT can provide a description of the electron dynamics.[10] Since the TDDFT treatment described here includes the geometry of interest, it also allows for future analyses beyond the statistical method applied in Ref. [196], e. g., with reduced

[10] Note that the numerical costs of time evolving the setups of Figs. 8.3 and 8.6 are comparable.

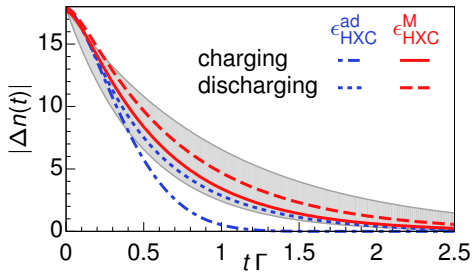

Figure 8.6: Absolute density change summed over all quantum dots, $|\Delta n(t)| = \sum_{l=1}^{N_{\rm dot}} \left| n_l(t) - n_l(t_1) \right|$ with $t_1 \gg t$, for a sudden rise (charging) or drop (discharging) of the gate voltage by the amount -3Γ at $t = 0$, calculated using either $\epsilon^{\rm M}_{\rm HXC}$ or $\epsilon^{\rm ad}_{\rm HXC}$ for all dots. See text for gray area. The calculation uses $N_{\rm dot} = 70$ quantum dots with Gaussian-distributed energy levels ϵ_l ($\mu = 0.7\Gamma, \sigma = 0.5\Gamma$), interaction strengths U_l ($\mu = 14\Gamma, \sigma = 0.5\Gamma$) and reservoir-dot couplings γ_l ($\mu = 1\Gamma, \sigma = 0.1\Gamma$), where Γ defines an energy scale. The inverse temperature is set to $\beta = 1/(2\Gamma)$.

quantum-dot distances. A central question, however, is in which way the XC potential needs to be modified in order to properly describe a more complex structure. To analyze this question, a promising first step would be a study of two quantum dots coupled to a shared electron reservoir, where the spatial distance between the dots is smaller than the reservoir coherence length. Another interesting setup is a quantum dot with multiple energy levels and tunnel coupling to a single reservoir. Both setups can in principle be studied with the method explained here.

8.3 Linear-response theory

8.3.1 Linear response in TDDFT

In this section, we leave the numerical time propagations studied up to here, and turn to a second application of TDDFT: the calculation of linear-response quantities. We focus on the interacting single-electron source modeled by Eq. (2.1), and begin with an initially equilibrated system, to which we apply a small harmonic gate voltage.

By calculating the emerging charge current in linear order in the applied perturbation, we extract the finite-frequency linear-response admittance of this system. We thereby investigate linear-response properties of the nonadiabatic XC potential developed in Sec. 8.1, see Eq. (8.7).

Importantly, a key benefit of TDDFT linear-response theory is that a numerical time evolution is not necessary in order to compute linear-response admittances. The reason lies in the linear-response admittance of the auxiliary KS system, which we derive exactly, being connected to the admittance of the interacting system by a Dyson equation (see below).[11] This equation includes the central quantity of TDDFT linear-response theory, namely the *XC kernel*, which is defined as a functional derivative of the XC potential with respect to the density, evaluated at the equilibrium density [78, 79, 82]. Here, we compare the XC kernel of the nonadiabatic XC potential with the kernel of the related adiabatic one, and we investigate how these kernels influence finite-frequency admittances of the single-contact quantum dot.

8.3.2 Derivation of the admittance

To obtain the linear-response admittance of the interacting single-electron source, $G(\omega)$, in TDDFT, we first calculate the admittance of the KS auxiliary system given in Eq. (3.9). The admittance in the KS system is defined by $G_{\mathrm{KS}}(\omega) = \frac{\partial I(\omega)}{\partial \epsilon_{\mathrm{KS}}[n](\omega)}\Big|_{\mathrm{eq}}$, and it depends on the position of the KS energy level, $\epsilon_{\mathrm{KS}}[n_{\mathrm{eq}}] = \bar{\epsilon} + \epsilon_{\mathrm{HXC}}[n_{\mathrm{eq}}]$, where $\bar{\epsilon}$ denotes the mean level position in the interacting system. Since the KS system describes noninteracting electrons, we can derive the KS admittance exactly, see, e. g., the result in Ref. [63]. The density value n_{eq} is calculated self-consistently from the exact KS expression for the quantum-dot's equilibrium density,

$$n_{\mathrm{eq}} = \frac{\Gamma}{\pi} \int_{-\infty}^{\infty} dE \, \frac{f^{+}(E)}{\left(\epsilon_{\mathrm{KS}}[n_{\mathrm{eq}}] - E\right)^2 + \Gamma^2/4}. \tag{8.11}$$

[11] A similar equation exists, e. g., for the density-density response function.

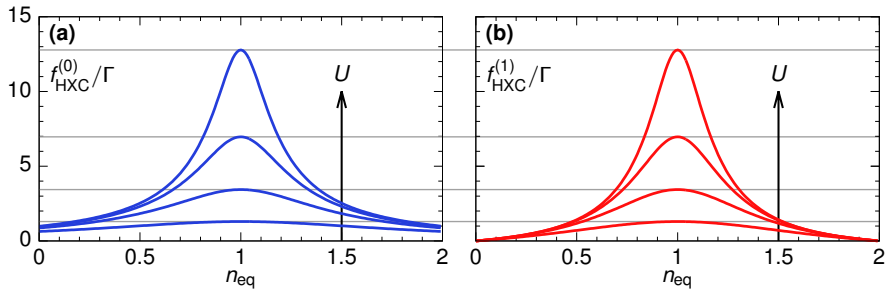

Figure 8.7: Coefficients of the HXC kernels in Eq. (8.14) for on-site interaction $U = 2\Gamma, 4\Gamma, 6\Gamma, 8\Gamma$ (bottom to top lines) and $\beta = 1/(2\Gamma)$. Thanks to the characteristic time scale $\tau_{\rm ch}$ (defined in the main text), the peak heights are identical for both coefficients, while differences appear for $n_{\rm eq} \to 0$ and $n_{\rm eq} \to 2$.

In TDDFT linear-response theory, the KS admittance is related to the admittance of the interacting system by the Dyson equation,

$$G(\omega) = G_{\rm KS}(\omega) - G_{\rm KS}(\omega)\frac{if_{\rm HXC}(n_{\rm eq},\omega)}{\omega}G(\omega). \tag{8.12}$$

This leads to the result

$$G(\omega) = \frac{\omega G_{\rm KS}(\omega)}{\omega + if_{\rm HXC}(n_{\rm eq},\omega)G_{\rm KS}(\omega)}, \tag{8.13}$$

with the frequency-dependent kernel, $f_{\rm HXC}(n_{\rm eq},\omega)$. The HXC kernel is defined as the Fourier transform of $f_{\rm HXC}(n_{\rm eq}, t-t') = \frac{\delta\epsilon_{\rm HXC}[n](t)}{\delta n(t')}\Big|_{\rm eq}$, see, e. g., Refs. [78, 79, 82]. Note that this kernel is always frequency independent, when derived from an adiabatic XC potential, while a nonadiabatic XC potential results in a nontrivial frequency dependence.

8.3.3 Nonadiabatic and adiabatic HXC kernels

From the definition of the HXC kernel given in the previous subsection, we derive the HXC kernels related to the specific approximations, $\epsilon^{\rm M}_{\rm HXC}$ and $\epsilon^{\rm ad}_{\rm HXC}$, see Eq. (8.7). For the nonadiabatic XC potential we find

$$f^{\rm M}_{\rm HXC}(n_{\rm eq},\omega) = f^{(0)}_{\rm HXC}(n_{\rm eq}) - i\omega\tau_{\rm ch}f^{(1)}_{\rm HXC}(n_{\rm eq}), \tag{8.14}$$

and $f_{\mathrm{HXC}}^{\mathrm{ad}}(n_{\mathrm{eq}}) = f_{\mathrm{HXC}}^{\mathrm{M}}(n_{\mathrm{eq}}, 0)$ for the adiabatic one, with the abbreviations $f_{\mathrm{HXC}}^{(0)}(n_{\mathrm{eq}}) = \frac{\partial \epsilon_{\mathrm{HXC}}^{\mathrm{M}}(n,\dot{n})}{\partial n}\Big|_{\mathrm{eq}}$ and $f_{\mathrm{HXC}}^{(1)}(n_{\mathrm{eq}}) = \tau_{\mathrm{ch}}^{-1} \frac{\partial \epsilon_{\mathrm{HXC}}^{\mathrm{M}}(n,\dot{n})}{\partial \dot{n}}\Big|_{\mathrm{eq}}$. Here, we also introduce a characteristic time scale, τ_{ch}, which for our approximations is convenient to define as $\tau_{\mathrm{ch}} = \tau_{\mathrm{c}}^{U=0} - \tau_{\mathrm{c}}^{U\neq 0}$, see also Eq. (8.10). This scale quantifies the dynamical step in the XC potential visible in Fig. 8.2 (a), and it is given by the difference between the charge relaxation times of the noninteracting and the interacting systems, evaluated at electron-hole symmetry [80].

The (real) coefficients, which appear on the right-hand side in Eq. (8.14), are plotted in Fig. 8.7 (a)-(b) for various interaction strengths. For increasing interaction parameter U, we observe that both coefficients develop a peak at single occupation. Therefore, the frequency dependence of $f_{\mathrm{HXC}}^{\mathrm{M}}$ adds a linear and imaginary contribution to the peak of the frequency-independent HXC kernel, $f_{\mathrm{HXC}}^{\mathrm{ad}}$.

8.3.4 Finite-frequency admittances

Figure 8.8 (a)-(b) present the real parts of finite-frequency linear-response admittances (i. e. conductances), which we obtain for the single-electron emitter studied here. The calculations in (a) and (b) differ by the applied temperature. As a reference, the black solid lines show analytic results, which are derived from perturbation theory in the tunnel coupling, i. e., the method described in Sec. 3.1. More specifically, the black lines are obtained from finite-frequency noise calculations, as outlined in Sec. 5.4. To extract the finite-frequency conductances from the noise, we employed the fluctuation-dissipation theorem [189], see Eq. (5.6).[12] In both plots in Fig. 8.8, three TDDFT curves are shown, which respectively correspond to the conductance in the KS system, $G_{\mathrm{KS}}(\omega)$, and the conductances calculated with Eq. (8.13), using the two HXC kernels defined in Eq. (8.14). For both temperatures, the conductances calculated in the KS system (dashed-dotted lines) deviate strongly from the reference data (solid), as it is expected for the unphysical KS system. For the chosen parameters, the KS energy level is positioned at the Fermi energy, and the conductance therefore increases strongly already at very low frequencies (note

[12] Note that, in the publication [85], we focus on equilibrium noise spectra instead of admittances. The fluctuation-dissipation theorem connects both.

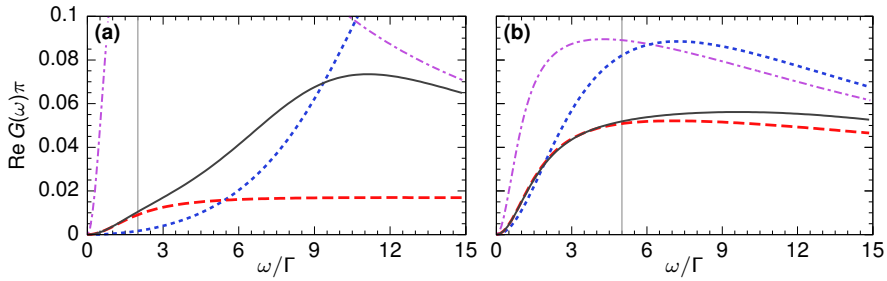

Figure 8.8: Finite-frequency conductances of the single-electron source for inverse temperatures (a) $\beta = 1/(2\Gamma)$ and (b) $\beta = 1/(5\Gamma)$, as indicated by the gray lines. Shown are the uncorrected conductances of the KS systems (purple dashed-dotted lines), and the corrected conductances [Eq. (8.13)], using the HXC kernels $f^{\mathrm{ad}}_{\mathrm{HXC}}$ (blue dotted lines) and $f^{\mathrm{M}}_{\mathrm{HXC}}$ (red dashed lines). Further parameters are $\bar{\epsilon} = -8\Gamma$, $U = 16\Gamma$. The black solid lines are plotted for reference and present perturbation-theory results.

that the zero-frequency conductance vanishes for the single-contact quantum dot). The dotted lines show conductances, corrected with the HXC kernel of the *adiabatic* HXC potential. Here, the discrepancy with the perturbative result is reduced only for very low frequencies. From Eq. (8.14) and Fig. 8.7 we estimate, that the frequency independent HXC kernel, $f^{\mathrm{ad}}_{\mathrm{HXC}}$, is reasonable for $\omega \ll 1/\tau_{\mathrm{ch}}$, i. e., when the frequency-dependent part of $f^{\mathrm{M}}_{\mathrm{HXC}}$ is small.[13] On the contrary, the kernel of the *nonadiabatic* HXC potential significantly improves the TDDFT result in the low and medium frequency regime (dashed lines). The agreement with the reference data is excellent for frequencies $\omega \lesssim \beta^{-1}$, as it is visible in both plots in Fig. 8.8. We emphasize that already the linear frequency dependence of the associated HXC kernel, $f^{\mathrm{M}}_{\mathrm{HXC}}$, is sufficient for the observed improvement. The failure for frequencies $\omega > \beta^{-1}$ can be understood from the derivation of the related HXC potential, which is based on a Markov approximation, see Sec. 8.1. Therefore, it misses dynamics which is fast compared to the reservoir memory time, $\tau_{\mathrm{r}} = \beta$. On the contrary, when memory effects in the reservoir are negligible for the system's time evolution, this

[13] In Fig. 8.8 (a) and (b), the scale $1/\tau_{\mathrm{ch}}$ is roughly 2 and 2.5. In panel (a), we observe that the adiabatic HXC kernel can already fail at much lower frequencies.

simple nonadiabatic HXC potential, depending only on the density and its first time derivative, considerably improves the TDDFT description of the electron dynamics, compared to its adiabatic counterpart. This is true in the linear-response regime (this section) as well as for non-linear response (Sec. 8.2).

8.3.5 RC times

A central question of the approach presented here is if the TDDFT results, based on the XC potential $\epsilon^{\mathrm{M}}_{\mathrm{HXC}}$, can be more accurate than first-order perturbation theory in the Markov approximation.[14] Importantly, in the analysis of nonadiabatic dynamics in Fig. 8.3 (a), we already pointed out that the TDDFT time evolution is in principle non-Markovian, in contrast to the also shown Born-Markov result, see also Sec. 8.2.2. To further investigate the difference between TDDFT and perturbation theory, we find that an instructive quantity is given by the *RC time* of the single-contact quantum dot. The *RC* time, $\tau_{\mathrm{RC}} = RC$, with resistance R and capacitance C, is based on the circuit analog sketched in Fig. 2.1 (b), see also the discussion in Sec. 2.1. The finite-frequency admittance of this classical circuit, expanded at zero frequency, is given by

$$G(\omega) = -i\omega C + \omega^2 C^2 R. \tag{8.15}$$

Using this classical analogy, we define a resistance and a capacitance of the single-electron source by expanding the TDDFT admittance in Eq. (8.13) around zero frequency and comparing the outcome to Eq. (8.15), see Refs. [94, 99]. We find that R and C are connected to the values R_{KS} and C_{KS} of the KS system by

$$R = \frac{R_{\mathrm{KS}}}{\left[1 + C_{\mathrm{KS}} f^{(0)}_{\mathrm{HXC}}(n_{\mathrm{eq}})\right]^2} + \frac{\tau_{\mathrm{ch}} f^{(1)}_{\mathrm{HXC}}(n_{\mathrm{eq}})}{\left[1 + C_{\mathrm{KS}} f^{(0)}_{\mathrm{HXC}}(n_{\mathrm{eq}})\right]^2}, \tag{8.16a}$$

$$C = \frac{C_{\mathrm{KS}}}{1 + C_{\mathrm{KS}} f^{(0)}_{\mathrm{HXC}}}. \tag{8.16b}$$

Note that the second term in the first equation only appears for the nonadiabatic HXC potential.

[14] We remind that we applied Born-Markov master eqs. to derive $\epsilon^{\mathrm{M}}_{\mathrm{HXC}}$ in Eq. (8.7).

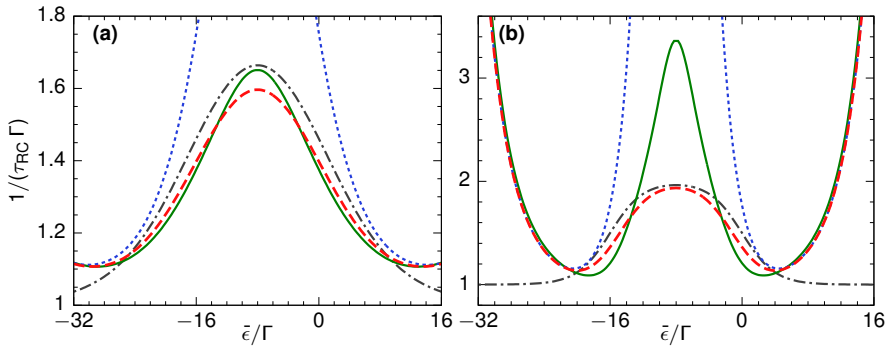

Figure 8.9: Inverse *RC* times of the single-electron source for two inverse temperatures (a) $\beta = 1/(5\Gamma)$ and (b) $\beta = 1/(2\Gamma)$. Shown are the *RC* times calculated in TDDFT using the HXC kernels $f_{\mathrm{HXC}}^{\mathrm{ad}}$ (blue dotted lines) and $f_{\mathrm{HXC}}^{\mathrm{M}}$ (red dashed lines), as well as the *RC* times derived in first-order and second-order perturbation theory in the tunnel-coupling [99] (black dashed-dotted and green solid lines). The interaction strength is $U = 16\Gamma$.

The calculated *RC* times are presented in Fig. 8.9 (a)-(b) for two different temperatures, where the higher temperature is applied in panel (a). Also shown are *RC* times derived in real-time diagrammatic perturbation theory in first-order as well as in second-order in the tunnel coupling, see Ref. [99]. Let us first study the dashed line in panel (a), which shows the TDDFT result based on the nonadiabatic HXC potential $\epsilon_{\mathrm{HXC}}^{\mathrm{M}}$ (more specifically: $f_{\mathrm{HXC}}^{\mathrm{M}}$). By comparing this line with the two perturbation-theory results, we find that the first-order-in-Γ *RC* times (dashed-dotted line) only poorly describe the TDDFT data, while *second-order* perturbation theory (solid line) provides a much better description. This is a striking result, showing that TDDFT with the HXC potential $\epsilon_{\mathrm{HXC}}^{\mathrm{M}}$—initially derived using first-order perturbation theory—can lead to *RC* times which agree with perturbation-theory results beyond the first order. The reason for this unintuitive behavior is that no perturbation-theory expansion is employed to solve the KS auxiliary system. On the one hand, interaction effects are modeled with an HXC potential from first-order perturbation theory, but, on the the other hand, the time evolution in the noninteracting KS system includes all orders in the tunnel

coupling. Therefore, we expect deviations between the TDDFT data and second-order perturbation theory to become significant, when interaction plays a dominant role in the dynamics. This is the case when the dot is close to electron-hole symmetry, $\bar{\epsilon} = -\frac{U}{2}$, as visible in Fig. 8.9 (a). In the region where the dot is singly occupied, $-U \lesssim \bar{\epsilon} \lesssim 0$, we also find that the *RC* time calculated with the adiabatic HXC kernel, $f_{\mathrm{HXC}}^{\mathrm{ad}}$, is strongly overestimated. On the contrary, when the dot is close to zero or double occupation, $\bar{\epsilon} \gg 0$ or $\bar{\epsilon} \ll -U$, the interaction on the quantum dot barely influences the *RC* time, and both TDDFT calculations thus lead to similar results close to the second-order perturbation-theory data [204].

Figure 8.9 (b) presents a calculation at lower temperatures, where the impact of second-order tunneling on the dynamics is more pronounced. This panel exemplifies a limit of the nonadiabatic HXC potential, which leads to an over-fitting of the TDDFT data (dashed line) to the first-order perturbation-theory result (dashed-dotted line), in particular close to the electron-hole symmetric point, see also the center of panel (a). We conclude that, when interaction is dominant, a reverse-engineering procedure similar to the one outlined in Sec. 8.1, but based on second or higher-order perturbation theory, would be necessary to obtain a HXC potential which correctly accounts for higher-order tunneling phenomena also in the Coulomb blockade region.

8.4 Final comments

In summary, we identified that XC contributions in the single-contact Anderson model can be approximated by a reverse-engineering procedure based on master equations. This led us to a key result, namely an expression for a nonadiabatic HXC potential, see Eq. (8.7). We connected a dynamical step in this approximation to physical charge-relaxation time scales, and we successfully applied the potential in TDDFT calculations of single as well as multiple time-dependently driven quantum dots weakly coupled an electron reservoir. To conclude this chapter, we comment on the quality and the limitations of the presented TDDFT method for describing single-electron transport.

Let us first remind ourselves that the only approximation included

in a TDDFT calculation is the one for the XC contributions (besides numerical errors introduced by the discretization of the Hamiltonian, see Sec. 7.4). The (open-boundary) Schrödinger equation of the non-interacting KS auxiliary system is solved numerically, without any approximation with respect to the time evolution or any perturbative expansion. Throughout this chapter, we have seen that this fact can result in an accuracy of TDDFT, which exceeds the Markovian perturbation theory, although the latter is initially employed to derive the XC potential of Eq. (8.7). For example, for the single-contact quantum dot, we discussed in Sec. 8.2.2 that the TDDFT time evolutions after sudden changes of the level position match with very precise td-DMRG results on short as well as long time scales (see also Sec. 8.3.5 on RC times).

Besides that, a limiting factor for the TDDFT calculations was discussed in Sec. 8.3: it is the frequency of a time-periodic drive. In this section, we calculated the finite-frequency linear-response admittance for the single-contact quantum dot with $\epsilon_{\mathrm{HXC}}^{\mathrm{M}}$, and it turned out to be only reasonable for driving frequencies below the reservoir temperature. This result raises the question, why the transient behavior after sudden parameter changes—which include all frequencies—is then properly described in the TDDFT calculations. It seems that the presence of interaction is less significant for the short-time dynamics after a parameter quench, than it is for the dynamics of a periodically driven system with high driving frequency. Here, it would be insightful to study nonadiabatic properties of the HXC potential beyond the dependence on the first time derivative of the density, e. g., by going beyond the Born-Markov master equations in the reverse-engineering procedure.

A further limitation of the TDDFT calculations is a restriction with respect to the justifiable temperature scale. From the derivation of the nonadiabatic HXC potential in Eq. (8.7), based on Markovian master equations, we expect this expression to only be reasonable for high temperatures, $\beta\Gamma \ll 1$. For lower temperatures, we already presented failures of $\epsilon_{\mathrm{HXC}}^{\mathrm{M}}$ in Sec. 8.2.2 (transient dynamics) and in Sec. 8.3 (RC times). Note that these failures are attributed to the XC part only, and are not a general limitation of TDDFT. To reach lower temperatures, it is important to conduct further research, in order to analyze how the approximation derived here needs to be modified.

9 Two-Contact Quantum Dot in TDDFT

We now present a major extension of the time-dependent density-functional-theory (TDDFT) approach studied in the previous two chapters. We find that the procedure to derive an exchange-correlation (XC) potential from master equations—along the lines of Sec. 8.1—is not only applicable to the single-contact quantum dot, but also to a quantum dot with *two* adjacent electron reservoirs. This extended setup is illustrated in Fig. 9.1. Besides applying a time-dependent gate voltage to the quantum dot, we also consider a (possibly time-dependent) bias voltage. Note that the system shown in Fig. 9.1 is an example of a single-electron transistor, with the characteristic feature of Coulomb blockade, i. e., due to Coulomb repulsion on the quantum dot, a significant bias voltage can be necessary to induce a steady-state current. In this chapter, as a first application of the TDDFT approach outlined below, we analyze how the system enters or leaves the Coulomb blockade region, when we apply a constant bias and a time-dependent gate voltage. In addition, the described method also allows us to calculate, e. g., the system's response to a time-dependently driven bias voltage or the transient dynamics after sudden bias and gate switches. The latter case is particularly interesting in order to analyze nanoscale devices which mostly operate with steady states, but are exposed to sudden parameter switches, such as the typical application of a (nanoscale) transistor. Here, we believe that a numerically feasible tool such as TDDFT is useful for related

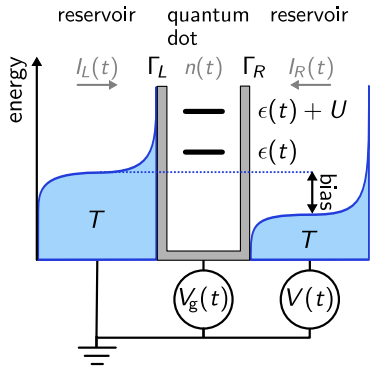

Figure 9.1: Energy diagram of a single-level quantum dot with tunnel coupling to two adjacent reservoirs and with an applied bias voltage $V(t)$ and gate voltage $V_g(t)$, see also Fig. 8.1 (a). Also indicated is the time-dependent electron density $n(t)$ of the quantum dot and the charge currents $I_{L/R}(t)$ in the reservoirs.

future experiments, to simulate the charge dynamics in single-electron tunneling devices.

Importantly, for the two-contact quantum dot studied here, the reverse-engineering procedure of Sec. 8.1 leads not only to a nonadiabatic XC potential, but also to a nonadiabatic XC bias correction [90, 132, 133]. We discuss how the results of this chapter are connected to the XC potential of the single-contact quantum dot and also to a steady-state density-functional method known as i-DFT [90–92].

In Sec. 9.1, we define the model and the corresponding Kohn-Sham (KS) system, and in Sec. 9.2.1 we discuss the reverse-engineering procedure for the two-contact quantum dot. The developed expressions for the XC potential and the XC bias are analyzed in Sec. 9.2.2, and applied in numerical TDDFT time evolutions in Sec. 9.3.

9.1 Interacting and Kohn-Sham systems

We describe the quantum dot with tunnel coupling to two reservoirs by an Anderson Hamiltonian similar to Eq. (2.1), see also Fig. 9.1. An additional index $\alpha = \mathrm{L}, \mathrm{R}$ is assigned to reservoir annihilation/creation operators, reservoir energies and the tunnel coupling, indicating the

associated left or right reservoir. Furthermore, during the time evolution, we take into account a possibly time-dependent bias voltage, $V(t) = 2V_{\mathrm{L}}(t) = -2V_{\mathrm{R}}(t)$, which shifts all reservoir energies symmetrically by the amount $V_\alpha(t)$. At the initial time we set $V_\alpha(t_0) = 0$ and consider the system to be in thermal equilibrium, where the Fermi energy is used as a reference energy as before. Note that this modeling describes the natural case of experiments, where a bias voltage is applied at some point in time to an initially equilibrated system [205, 206]. This stands in contrast to many other theoretical approaches, where the dot and the reservoirs are typically assumed to be decoupled and in local equilibrium in the past, see also Sec. 3.1 and references therein.

We define the Hamiltonian of the two-contact quantum dot as

$$\begin{aligned} H = & \sum_\sigma \epsilon(t) d_\sigma^\dagger d_\sigma + U d_\uparrow^\dagger d_\uparrow d_\downarrow^\dagger d_\downarrow + \sum_{\alpha,k,\sigma} \left[\epsilon_{\alpha k} + V_\alpha(t)\right] c_{\alpha k\sigma}^\dagger c_{\alpha k\sigma} \\ & + \sum_{\alpha,k,\sigma} \left(\gamma_\alpha c_{\alpha k\sigma} d_\sigma^\dagger + \mathrm{H.\,c.}\right). \end{aligned} \tag{9.1}$$

The tunnel-coupling strength between the quantum dot and the reservoir with index α is defined by $\Gamma_\alpha = 2\pi|\gamma_\alpha|^2\nu_{\alpha,0}$, with the respective density-of-states $\nu_{\alpha,0}$. Let us emphasize that we focus on charge currents in this Anderson model generated by electron tunneling only, i. e., we exclude additional contributions stemming from displacement currents. The latter are induced by time-varying gate and bias voltages and they add to the actual total current in a nanosystem, see Ref. [207] for details.

As discussed in Sec. 3.2.3, we proceed by assuming noninteracting v-representability and define a related noninteracting KS auxiliary system by setting the interaction in Eq. (9.1) to zero and including the Hartree (H) and XC potentials. In contrast to the single-reservoir case, Eq. (3.9), we here explicitly allow for XC contributions not only for the quantum-dot energy level, but also for the reservoir energies [90, 132, 133]. We model the latter by homogeneously[1] shifting all reservoir energies in terms of an *XC bias*, $V_{\mathrm{XC}}[n](t)$, with $V_{\mathrm{L/R,XC}}[n](t) = \pm V_{\mathrm{XC}}[n](t)/2$. The XC bias is added to the bias in

[1] Note that a homogeneous shift is a reasonable assumption for the wide-band-limit reservoirs included here, see Refs. [90, 92].

the KS system, and the KS Hamiltonian thus becomes

$$\begin{aligned} H_{\mathrm{KS}} = & \sum_{\sigma} \left[\epsilon(t) + \epsilon_{\mathrm{HXC}}[n](t)\right] d_\sigma^\dagger d_\sigma \\ & + \sum_{\alpha,k,\sigma} \left[\epsilon_{\alpha k} + V_\alpha(t) + V_{\alpha,\mathrm{XC}}[n](t)\right] c_{\alpha k\sigma}^\dagger c_{\alpha k\sigma} \\ & + \sum_{\alpha,k,\sigma} \left(\gamma_\alpha c_{\alpha k\sigma} d_\sigma^\dagger + \mathrm{H.\,c.}\right). \end{aligned} \tag{9.2}$$

To numerically time evolve this KS system, we employ the formalism outlined in Chap. 7, namely the open-boundary Schrödinger equation for single-particle KS states $|\psi(t)\rangle$. Along the lines of Sec. 7.2, we project each single-particle state onto the quantum-dot/reservoir orbitals, which leads to a wave function with a quantum-dot part, $\psi_{\mathrm{c}}(t)$, and two reservoir parts, $\psi_\alpha(t)$. By discretizing both reservoirs in k-space and following the steps described in Sec. 7.2, we derive the final equation

$$\begin{aligned} i\partial_t \psi_{\mathrm{c}}(t) = & \left[\epsilon(t) + \epsilon_{\mathrm{HXC}}[n](t) - \sum_\alpha \frac{i\Gamma_\alpha}{2}\right] \psi_{\mathrm{c}}(t) \\ & + \sum_{\alpha,k} \gamma_\alpha e^{-i\epsilon_{\alpha k}(t-t_0) - i\int_0^t dt' \left[V_\alpha(t') + V_{\alpha,\mathrm{XC}}[n](t')\right]} \psi_{\alpha,k}(t_0). \end{aligned} \tag{9.3}$$

The electron density on the quantum dot is calculated from the quantum-dot part of the projected wave functions, $\psi_{\mathrm{c}}(t)$, by evaluating $n(t) = \sum_{\{\psi\}} p_\psi |\psi_{\mathrm{c}}(t)|^2$, where the sum goes over all KS single-particle wave functions. As before, the weight of each wave function in the many-particle state of the KS system is given by p_ψ. As initial condition at time t_0, we always use the equilibrium KS density matrix of the unbiased and uncoupled system: $V = 0$ and $\gamma_\alpha = 0$.[2]

For a complete presentation of the technical details, we briefly report the numerical parameters of the calculations presented in this chapter, see also Sec. 7.4. To compute the data shown in Fig. 9.3, we used the time step $\Delta t = 4 \cdot 10^{-5}/\Gamma$ and $I_{\mathrm{res}} = [-50\Gamma, 50\Gamma]$ with 250 orbitals per reservoir. Note that we were able to use smaller numerical parameters than for the single-reservoir calculations of

[2] All time evolutions presented later in this chapter are shown for $t \gg t_0$.

Chap. 8, because we additionally implemented that time-dependent changes in XC contributions are smoothened over several time steps. Without this modification, we find the numerical time evolution in the presence of a bias voltage to be unstable.

9.2 Non-steady-state XC potential and XC bias

9.2.1 Derivation of the non-steady-state XC contributions

In order to develop an approximation for the XC contributions of the two-contact quantum dot, we again exploit a master-equation description, see Sec. 8.1. We first describe the dynamics of the quantum dot in terms of the diagonal part of the reduced quantum-dot density matrix, referred to as the occupation vector, $\boldsymbol{P}(t) = \big[P_0(t), P_1(t), P_2(t)\big]^{\mathrm{T}}$, where both spin configurations are summed up in $P_1(t) = P_\uparrow(t) + P_\downarrow(t)$. Assuming Markovian dynamics and applying leading-order perturbation theory with respect to the tunnel coupling to the model in Eq. (9.1), we obtain the master equation,

$$\partial_t \boldsymbol{P}(t) = \mathcal{W}_t^{(i)}\, \boldsymbol{P}(t), \tag{9.4}$$

with $W_t^{(i)} = \sum_\alpha \mathcal{W}_{\alpha,t}^{(i)}$, see also Eq. (3.6). The electron density on the quantum dot is calculated as $n(t) = \boldsymbol{n}^{\mathrm{T}}\boldsymbol{P}(t)$, with $\boldsymbol{n}^{\mathrm{T}} = [0,1,2]$. The two kernels $\mathcal{W}_{\alpha,t}^{(i)}$ are, in leading order in the tunnel-coupling strength, given by

$$\frac{\mathcal{W}_{\alpha,t}^{(i)}}{\Gamma_\alpha} = \begin{bmatrix} -2f^+\big(\epsilon_\alpha\big) & f^-\big(\epsilon_\alpha\big) & 0 \\ 2f^+\big(\epsilon_\alpha\big) & -f_\epsilon^- - f^+\big(\epsilon_\alpha + U\big) & 2f^-\big(\epsilon_\alpha + U\big) \\ 0 & f^+\big(\epsilon_\alpha + U\big) & -2f^-\big(\epsilon_\alpha + U\big) \end{bmatrix}, \tag{9.5}$$

where $\epsilon_\alpha = \epsilon(t) + V_\alpha(t)$, see also Eq. (8.3) for the single-contact quantum dot.

Note that, for deriving a XC approximation for the single-contact quantum dot in Sec. 8.1, it was sufficient to exploit that the time evolution of the electron density on the dot, $n(t)$, is identical in the interacting and the KS systems. As a consequence, the XC potential derived in Eq. (8.3) only depends on $n(t)$ and derivatives thereof. However, the XC potential of TDDFT generally depends on the electron

density of the whole system, i. e., also on the density in the reservoir(s) [78, 79, 82]. In the single-contact case, due to charge conservation, any density change in the reservoir is accompanied by a corresponding change of the electron density on the quantum dot, which justifies a dependence of the XC potential on $n(t)$ and its history only. This is different for the two-contact quantum dot considered here, where a current can flow between the two reservoirs without a change in $n(t)$, see, e. g., the steady-state current which arises when a constant bias voltage is applied. For the XC approximation of the two-contact quantum dot, which we derive below, to depend on the electron densities on the dot *and* in the reservoirs, we again exploit charge conservation, and, besides $n(t)$, include a dependence on the *currents* in the left and right reservoirs. In other words, since the interacting and the KS system share the identical density evolution, we exploit that the density on the quantum dot as well as the left and right charge currents are identical in both systems. For the interacting system, the charge current in reservoir α, calculated in Markov approximation, becomes

$$I_\alpha(t) = \frac{\boldsymbol{e}^{\mathrm{T}}}{2} \mathcal{W}^{(i)}_{\mathrm{I}_\alpha,t} \boldsymbol{P}(t), \tag{9.6}$$

with $\boldsymbol{e}^{\mathrm{T}} = (1,1,1)$, and the additional current kernels given by

$$\frac{\mathcal{W}^{(i)}_{\mathrm{I}_\alpha,t}}{\Gamma_\alpha} = \begin{bmatrix} 0 & 2f^-\big(\epsilon_\alpha\big) & 0 \\ -2f^+\big(\epsilon_\alpha\big) & 0 & 2f^-\big(\epsilon_\alpha + U\big) \\ 0 & -2f^+\big(\epsilon_\alpha + U\big) & 0 \end{bmatrix}. \tag{9.7}$$

Note the similarity between Eq. (9.6) and Eq. (6.5) for a single-contact quantum dot, as well as Eq. (4.7), where we analyze the charge current through a superconducting spin turnstile.

Next, we also assume Markovian dynamics in the KS system, and derive the master equation

$$\partial_t \boldsymbol{P}_{\mathrm{KS}}(t) = \mathcal{W}^{(i)}_{\mathrm{KS},t} \boldsymbol{P}_{\mathrm{KS}}(t), \tag{9.8}$$

and the current expressions

$$I_{\mathrm{KS},\alpha}(t) = \frac{\boldsymbol{e}^{\mathrm{T}}}{2} \mathcal{W}^{(i)}_{\mathrm{I}_{\mathrm{KS},\alpha},t} \boldsymbol{P}_{\mathrm{KS}}(t), \tag{9.9}$$

with the KS occupation vector $\boldsymbol{P}_{\mathrm{KS}}(t)$ and the KS current $I_{\mathrm{KS},\alpha}(t)$ in reservoir α. We emphasize that the currents in the two reservoirs can differ during a time evolution, and they are only equal (with opposite sign) when the system reaches a steady state. The kernels $\mathcal{W}^{(i)}_{\mathrm{KS},t}$ and $\mathcal{W}^{(i)}_{\mathrm{I}_{\mathrm{KS},\alpha},t}$ are obtained from $W^{(i)}_t$ and $\mathcal{W}^{(i)}_{\mathrm{I}_\alpha,t}$, respectively, by setting U to zero and replacing $\epsilon(t) \to \epsilon(t) + \epsilon^{\mathrm{M2}}_{\mathrm{HXC}}[n](t)$ and $V_\alpha(t) \to V_\alpha(t) + V^{\mathrm{M2}}_{\alpha,\mathrm{XC}}[n](t)$. We here add the superscript 'M2' to the XC quantities to indicate the underlying Markov approximation and to differentiate the two-reservoir case of this section from the single-reservoir result, $\epsilon^{\mathrm{M}}_{\mathrm{HXC}}$.

Finally, we exploit the fact that the density and its time derivatives are identical in the KS and the interacting systems. As mentioned before, charge conservation then demands that the charge currents between the dot and the left and right reservoirs are also identical in both systems.[3] By following the lines of Sec. 8.1.2 and expressing the occupation vector in terms of the density, see Eq. (8.1), we can extract a HXC potential and an XC bias voltage for the two-contact quantum dot. We find the key result

$$\epsilon^{\mathrm{M2}}_{\mathrm{HXC}}\left(n, I_{\mathrm{L}}, I_{\mathrm{R}}\right) = \frac{\epsilon^{\mathrm{M}}_{\mathrm{HXC}}(n, -I_{\mathrm{R}})\big|_{\Gamma_{\mathrm{R}}} + \epsilon^{\mathrm{M}}_{\mathrm{HXC}}(n, -I_{\mathrm{L}})\big|_{\Gamma_{\mathrm{L}}}}{2}, \tag{9.10a}$$

$$V^{\mathrm{M2}}_{\alpha,\mathrm{XC}}\left(n, I_{\mathrm{L}}, I_{\mathrm{R}}\right) = \alpha\frac{\epsilon^{\mathrm{M}}_{\mathrm{HXC}}(n, -I_{\mathrm{R}})\big|_{\Gamma_{\mathrm{R}}} - \epsilon^{\mathrm{M}}_{\mathrm{HXC}}(n, -I_{\mathrm{L}})\big|_{\Gamma_{\mathrm{L}}}}{2}, \tag{9.10b}$$

with $\alpha = \pm$ for the indices L/R and with $\epsilon^{\mathrm{M}}_{\mathrm{HXC}}$ given in Eq. (8.7), where Γ is replaced by $\Gamma_{\mathrm{L/R}}$ as indicated. All quantities in Eqs. (9.10) are evaluated at time t. These equations relate the XC contributions of the two-contact quantum dot to the previous result, $\epsilon^{\mathrm{M}}_{\mathrm{HXC}}(n, \dot{n})$, which is derived for a single-contact quantum dot. Note that this connection between the two-contact and the single-contact XC approximations only holds, because both XC expressions are based on first-order perturbation theory in the tunnel-coupling strength. We expect Eqs. (9.10) to fail if we include higher-order tunneling in the derivations of $\epsilon^{\mathrm{M}}_{\mathrm{HXC}}$, $\epsilon^{\mathrm{M2}}_{\mathrm{HXC}}$ and $V^{\mathrm{M2}}_{\alpha,\mathrm{XC}}$.

[3] The calculations presented here can also be interpreted in the framework of time-dependent *current* DFT, where the KS system is defined as a noninteracting system, which shares the identical density *and current* with the interacting system, see, e. g., Ref. [78]. Since we consider a one-dimensional system, the current is always fixed by the density.

For comparison, we also define a *steady-state* XC approximation related to Eqs. (9.10). This is motivated by the recent success of steady-state i-DFT [90, 91] to describe steady-state currents in the Anderson model studied here. In this approach, the XC potential and XC bias only depend on the density on the quantum dot and the total current through the system, $I = [I_\mathrm{R} - I_\mathrm{L}]/2$. The system is considered to be in the steady state, hence the currents are independent of time. In analogy to the adiabatic approximation of TDDFT, see Sec. 3.2.2, the XC approximation of steady-state i-DFT has been used in time-dependent (non-steady-state) calculations [92], by replacing I with $I(t)$, i. e., with the current at time t. Here, we want to analyze the relevance of including both currents, $I_\mathrm{L}(t)$ and $I_\mathrm{R}(t)$, separately in an XC approximation. For this purpose, we define the additional steady-state approximation as

$$\epsilon_\mathrm{HXC}^\mathrm{ss}\left(n(t), I(t)\right)(t) = \epsilon_\mathrm{HXC}^\mathrm{M2}\left(n(t), -I(t), I(t)\right)(t), \tag{9.11a}$$

$$V_{\alpha,\mathrm{XC}}^\mathrm{ss}\left(n(t), I(t)\right)(t) = V_{\alpha,\mathrm{XC}}^\mathrm{M2}\left(n(t), -I(t), I(t)\right)(t), \tag{9.11b}$$

and we abbreviate it with 'ss' in the following. The difference between the M2 and ss XC approximations is that the former still depends on the time derivative of the electron density on the quantum dot, $\dot{n}(t)$. Both approximations are equal for $\dot{n}(t) = 0$.

9.2.2 Properties of the non-steady-state XC contributions

The HXC potential and the XC bias of Eqs. (9.10) are plotted in Fig. 9.2. Note that in this and the subsequent section we consider symmetric couplings only, $\Gamma_L = \Gamma_\mathrm{R} = \Gamma$, and we leave a study of asymmetric couplings for the future. In Fig. 9.2, we illustrate the XC contributions for three different scenarios. First, panels (a) and (d) present the result for a system without bias, i. e., $I_\mathrm{L}(t) = I_\mathrm{R}(t)$. In this case, the XC bias also vanishes and the HXC potential is similar to the result of the single-contact quantum dot, see Fig. 8.2 (a). Second, when a bias voltage is applied across the quantum dot and the system reaches a steady state, we obtain $I_\mathrm{L}(t) = -I_\mathrm{R}(t)$, which is the scenario shown in panels (c) and (f). In panel (c), we find for the HXC potential that the dynamical step of the single-contact quantum dot, visible in (a), splits into *two* dynamical steps. Each step is related to the current

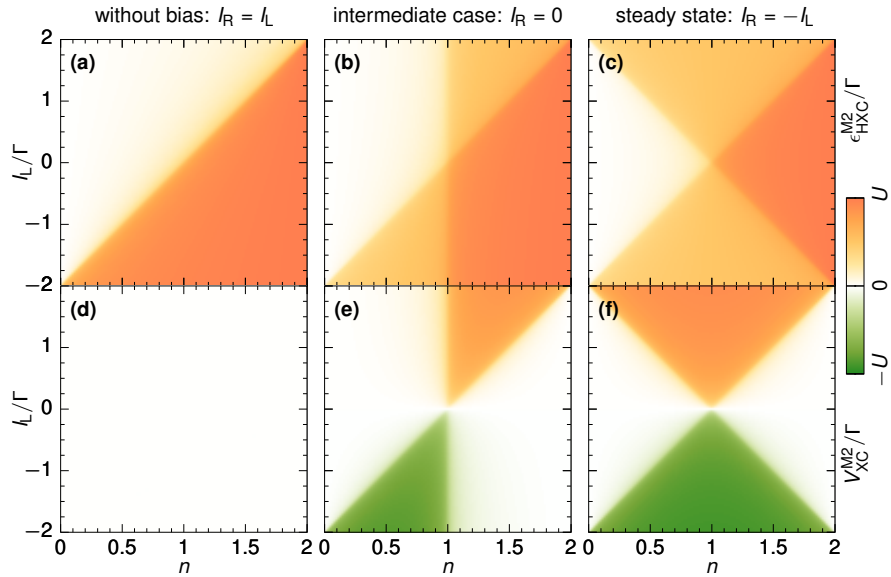

Figure 9.2: (a)-(c) Non-steady-state HXC potential and (d)-(f) XC bias M2 of Eqs. (9.10) for the quantum dot with two contacts, plotted as a function of the density and the left current, while the right current is fixed as indicated. Panels (d) and (f) show the special case, where the M2 and ss approximations agree, see Eqs. (9.11). Parameters are $U = 16\Gamma$, $\beta = 1/(2\Gamma)$ and $\Gamma_R = \Gamma_L = \Gamma$.

into one of the two reservoirs. Their positions depend on $n(t)$ and either $I_L(t)$ or $I_R(t)$, and they are located at

$$n = 1 + I_\alpha \left(\tau_{c,\alpha}^{U=0} - \tau_{c,\alpha}^{U\neq 0} \right), \tag{9.12}$$

with $\alpha = L, R$. The times $\tau_{c,\alpha}^{U=0}$ and $\tau_{c,\alpha}^{U\neq 0}$ in Eq. (9.12) are given by the charge-relaxation time scales of the interacting and the noninteracting quantum dot, see also the paragraph below Eq. (8.10). Both times are evaluated at the electron-hole symmetric point and calculated with respect to the reservoir α, i. e., with switched-off coupling to the opposite reservoir. Importantly, the relation given in Eq. (9.12) holds in the general dynamical case, where $I_L(t) \neq I_R(t)$, and also for asymmetric coupling, $\Gamma_L \neq \Gamma_R$. This equation connects steps in the HXC potential to *physical* charge relaxation time scales, see also the

discussion in Sec. (8.1.3). For the XC bias in panel (f) we also observe a two-step structure with identical step positions but different step heights. The XC-bias steps thereby counteract an applied bias voltage, which can be seen by the following example. Let us consider a quantum dot at electron hole symmetry, $n(t) = 1$, with a nonzero steady-state current, leading to, e. g., $I_{\mathrm{L}}(t) < 0$ in the left reservoir. From panel (f), we conclude that the XC bias in this situation is roughly given by $-U$.[4] Since the assumed current only occurs when the total bias in the KS system is positive, we find that the applied bias needs to be larger than $+U$. This is the expected behavior in the Coulomb-blockade region, which we here describe in a noninteracting KS system. We point out that similar two-step structures in the HXC potential and the XC bias have also been reported for steady-state i-DFT [90, 91]. The key difference in this section is that the M2 approximation in Eqs. (9.10) is not limited to an analysis of steady states, because $I_{\mathrm{L}}(t)$ and $I_{\mathrm{R}}(t)$ are treated separately. Finally, as a third case in Fig. 9.2, we present an intermediate scenario in panels (b) and (e), where we fix $I_{\mathrm{R}} = 0$. Note that this intermediate case does not describe an intuitive physical situation, and it is only shown here to give a more complete picture of the functions plotted in Fig. 9.2 depending on n, I_{L} and I_{R}. The additional panels (b) and (e) illustrate how the two-step structures in the potential and the bias emerge from the single HXC potential step and the vanishing XC bias in panels (a) and (d), respectively.

9.3 Conductances of a driven quantum dot

Before we present TDDFT time evolutions for the two-contact quantum dot, we comment on the expected precision of the approach. We first remind ourselves that the nonadiabatic XC potential for the single-contact quantum dot, derived in Eq. (8.3), leads to very accurate time evolutions on short and long time scales, as discussed in Sec. 8.2.2, see also Sec. 8.4. Importantly, we believe that this high accuracy also holds for the Anderson model with two reservoirs in the high temperature/weak coupling regime. This expectation is reasonable, because the two reservoirs are essentially independent at the high temperatures studied here, $\beta\Gamma \ll 1$, where co-tunneling is strongly

[4] The actual step height is slightly smaller due to the finite temperature.

suppressed. Consequently, we expect TDDFT for the two-contact quantum dot, using the M2 XC approximation, to be accurate not only on long time scales and for steady states, but also in the regime of transient dynamics. This accuracy, together with the possibility to propagate the system for long times, see Sec. 8.2.2, makes TDDFT with the M2 approximation a powerful tool to study numerous gate and bias-voltage driving schemes. It would be interesting to verify the expected accuracy in future studies, e. g., by comparing TDDFT results with td-DMRG data, as we do in Sec. 8.2.2 for the single-contact quantum dot.

We now present TDDFT time propagations for one particular driving scheme, and we leave the study of further driving schemes for the future. As mentioned previously, the TDDFT results shown in the following are used to compare the performance of the M2 and the ss XC approximations in nonadiabatic time evolutions. This is insightful in order to highlight the importance of including the left and right currents separately in a XC approximation, as it is the case for the M2 expressions in Eqs. (9.10). The M2 expressions thus extend, e. g., the i-DFT approximations of Ref. [92], which depend on the quantum-dot density and the total current only.

As an example, we analyze the dc conductance of the interacting quantum dot in the presence of a time-periodic driving of the gate voltage. A question which arises for this system is the fate of the Coulomb blockade, i. e. the interaction-induced suppression of a dc current, when we apply the ac gate-voltage driving in addition to a bias voltage. In the calculations, we apply a small constant bias, $V(t) = V$, and a harmonic gate voltage, $\epsilon(t) = \bar{\epsilon} + \delta\epsilon \sin(\Omega t)$, and we calculate the *time-averaged* dc conductance,

$$G_{\mathrm{dc}} = \left\langle \frac{dI}{dV} \right\rangle_t , \tag{9.13}$$

from the TDDFT time evolution of the current, $I(t)$, through the system. We consider the system to be in equilibrium at the initial time t_0, and we apply the bias and the harmonic gate voltage starting from $t > t_0$. The system is time propagated numerically, see Eq. (9.3), until periodicity is established.

The TDDFT results for the constant bias and harmonic gate-voltage driving are presented in Fig. 9.3. We first focus on the panels

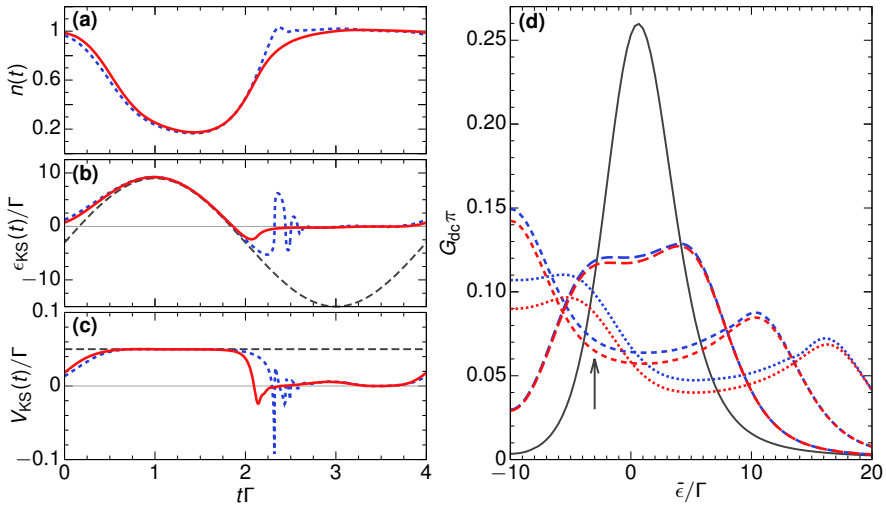

Figure 9.3: (a)-(c) Time evolution calculated in TDDFT using either Eqs. (9.10) (M2, red solid lines) or Eqs. (9.11) (ss, blue dotted lines) as XC approximations. We consider a small bias, V, and a harmonically driven energy level, $\epsilon(t) = \bar{\epsilon} + \delta\epsilon \sin(\Omega t)$. Shown are (a) the density, (b) the KS energy level, $\epsilon_{\mathrm{KS}}[n](t) = \epsilon(t) + \epsilon_{\mathrm{HXC}}[n](t)$, and (c) the KS bias, $V_{\mathrm{KS}}[n](t) = V + V_{\mathrm{XC}}[n](t)$. Bare quantities without HXC corrections are plotted as black dashed lines. Parameters are $\bar{\epsilon} = -3\Gamma$ [black arrow in (d)], $\delta\epsilon = 12\Gamma$, $V = 0.05\Gamma$, $\beta = 2/(\pi\Gamma)$, $U = 20\Gamma$, $\Omega = 0.5\pi\Gamma$. (d) Averaged dc conductances for amplitudes $\delta\epsilon/\Gamma = 0, 6, 12, 18$ (solid, long dashed, short dashed, dotted), calculated using the XC approximation M2 (red) and ss (blue). Further parameters are set as before. Without driving, both approximations produce the same conductance (black solid line).

(a)-(c), which present the time evolution of the density, the energy level and the bias voltage in the KS system for one set of parameters.[5] The average level position without HXC correction is set to $\bar{\epsilon} = -3\Gamma$, where the dot is singly occupied due to the presence of interaction. The driving of the energy level leads to a decreasing density in the beginning of the driving period, see panel (a). Here, we observe that the steady-state approximation (dotted line) generally leads to faster

[5] Numerical issues of the calculations are discussed in Sec. 7.4, see also Sec. 9.1.

density adjustments than the non-steady-state approximation (solid line). At the beginning of the second half of the driving period, where the density strongly increases, the dotted line even overshoots the value $n(t) = 1$, and small decaying oscillations occur. This failure of the steady-state approximation is similar to the behavior of the adiabatic single-contact XC potential, $\epsilon_{\mathrm{HXC}}^{\mathrm{ad}}$, see in particular Fig. (8.3) (a). Both approximations neglect a dependence on $\dot{n}(t)$, when compared to their nonadiabatic/non-steady-state counterparts in Eqs. (8.7) and (9.11).

As a consequence of the time-dependent driving, the system studied in Fig. 9.3 (a)-(c) periodically leaves and enters the Coulomb-blockade region during the drive. Hence, in the second half of the time evolutions in panels (b) and (c), we can analyze how Coulomb blockade is realized dynamically in the noninteracting KS system: in panel (b), the level position is kept at the electron-hole symmetric point, while in (c) the applied bias voltage is strongly suppressed, leading to a vanishing current through the system (not shown). We also find that the M2 approximation (solid line) leads to a smooth evolution of the KS energy level and bias. On the contrary, the ss approximation (dotted line) results in a damped oscillating behavior, when the system enters the Coulomb-blockade region. We attribute this effect to the discussed overshooting of the density, see panel (a).

To analyze the difference between the M2 and the ss approximations in calculations of linear-response conductances, we turn to Fig. 9.3 (d). Here, we plot TDDFT conductances as a function of the bare average level position, $\bar{\epsilon}$, and for four different amplitudes of the gate-voltage drive. Note that the conductances are symmetric around $\bar{\epsilon} = -U/2$, and, therefore, we only show the data for $\bar{\epsilon} \geq -U/2 = -10\Gamma$ in Fig. 9.3 (d). Without driving, the conductance has two peaks located at $\bar{\epsilon} \approx 0, -U$ (solid line, only one peak is shown). These peaks split in two, when we apply a harmonic gate-voltage driving, where the splitting equals twice the amplitude of the drive (peak-to-peak). By comparing the effect of both XC approximations in panel (d) (red and blue lines), we find that conductances calculated in the steady-state XC approximation differ from the result obtained with the non-steady-state one. For parameters, where the system enters Coulomb blockade during the drive, the ss conductance exceeds the conductance calculated with M2. The reason for this trend is that the M2 approximation of Eqs. (9.10) builds up the Coulomb blockade much faster than the

ss approximation of Eqs. (9.11), which is evident from panels (b) and (c). In contrast, when the ss approximation is employed, the damped oscillations of the KS energy level and bias lead to an increased current flow and thus an increased conductance. We conclude that the property of the XC approximation M2, namely to include an explicit dependence on $\dot{n}(t)$, is especially important for the dynamics, when the system, during a time-dependent change of parameters, enters the Coulomb-blockade region.

Besides the case presented here, we note that the outlined TDDFT method based on the M2 approximation can be readily applied to investigate other driving schemes. Anticipated future studies include an analysis of the dynamics in the presence of ac bias voltages [92] and of transient dynamics after sudden parameter switches [87]. These studies would be particularly interesting, when we compare the outcome to descriptions of the electron dynamics based on Markovian master equations (which are employed in other parts of this thesis, see, e. g., Chap. 4). Comparisons of this kind are instructive to highlight the relevance of the non-Markovian time evolution which is included in TDDFT for the KS system. We expect this asset of TDDFT to be even more significant for the two-contact quantum dot, than it is for the single-contact quantum dot of Chap. 8. Note, e. g., that a Markovian master equation for the two-contact quantum dot fails to describe transient behavior after a suddenly switched-on bias voltage: it immediately describes the steady state (if the density does not change due to the applied bias). A detailed discussion of TDDFT in this context is left for future investigations.

10 | Conclusion

A central aspect of this thesis was to analyze electron dynamics and current fluctuations in time-dependently driven single-electron tunneling devices. In Chap. 4, we proposed and outlined a concept to realize a quantized spin-current source, and in Chaps. 5-6 we provided new insights into finite-frequency noise spectra of interacting single-electron emitters. In Chaps. 7-9, we employed time-dependent density-functional theory (TDDFT) in the context of single-electron transport, to simulate the electron dynamics in single and multiple interacting quantum dots driven by time-dependent gate and bias voltages.

Besides detailed investigations of the physics in these nanosystems (summarized below), a second key aspect of this thesis was the development and application of complementary theoretical methods. We here applied this multi-method approach, on the one hand, to compare and cross-check results derived in different theories. On the other hand, by first gaining experience, specifically, with diagrammatic perturbation theory in the tunnel coupling and TDDFT, we were able to combine assets of these two methods in a novel way. In Chaps. 8-9, we transferred insights from the diagrammatic calculations to TDDFT, which significantly improved TDDFT simulations of the electron dynamics in the described nanosystems. To conclude, we briefly repeat key results and provide an outlook for possible future projects.

First, in Chap. 4, we proposed a new nanoscale device as an experimentally feasible clocked single-spin source, see Ref. [84]. The device consists of a superconducting single-electron transistor (SET) with ferromagnetic-insulator elements, and we considered the device to be exposed to a constant bias and a time-periodic gate voltage.

This extends previous studies of pure charge turnstiles, based on superconductor/normal-metal hybrid SETs, which are in demand for metrological purposes [36–38]. The theoretical analysis presented in Chap. 4 revealed that the proposed device can produce a precise spin current, thanks to a working principle, which exploits charging effects as well as a spin-split DOS of the superconductors. We provided estimates of leading error mechanisms reducing the device's accuracy, and we pointed out that the employed spin-active tunnel barriers can also significantly reduce error mechanisms for the related charge turnstiles [36, 39, 42]. For the future, it would be interesting to perform additional calculations, which yield an improved quantitative picture of the achievable precision in both devices.

Besides currents, a further key quantity which is useful to characterize single-electron tunneling devices is given by the current noise. The current noise contains information on a system's excitation spectrum, time scales of the dynamics and also the presence of interaction. In Chaps. 5-6, we investigated the charge-current noise of a single-contact quantum dot, which acts as a single electron emitter, due to a slow time-periodic gate voltage. In these chapters, we provided a comprehensive picture of finite-frequency noise spectra—as well as noise harmonics—in the presence of both, Coulomb interaction on the quantum dot and slow time-periodic driving of the quantum-dot levels. To derive the current noise, we extended a real-time diagrammatic perturbation theory in the tunnel coupling, see Ref. [55]. We distinguished a low, an intermediate and a high noise-frequency regime (depending on the ratio ω/Γ), and we provided detailed descriptions of the noise calculations for all three regimes. The key physical insights can be summarized in the following way: (1) many noise features are straightforward to interpret by comparing time scales of the system's dynamics; (2) noise harmonics in the high noise-frequency regime provide a spectroscopic tool to investigate specific fluctuation processes; (3) the interplay of Coulomb interaction and time-dependent driving leads to a unique signature in the noise, namely a non-vanishing zero-frequency first noise harmonic. Note that this thesis thus promotes the study of noise harmonics for future experiments. In addition, we believe that the detailed description of the real-time diagrammatic noise calculations is helpful to perform similar studies in related systems. An apparent extension would be to derive finite-frequency noise spectra of adiabatic

quantum pumps, consisting of a quantum dot coupled to two contacts, see also Ref. [54] for a related zero-frequency noise calculation.

Finally, in Chaps. 7-9, we turned to the numerical method TDDFT. This method is today successfully applied, e. g., to calculate excitation spectra of large molecules and to simulate atoms and molecules in strong laser fields. It is, however, less applied for simulations of the charge dynamics in single-electron tunneling devices, as we pointed out throughout this thesis. A central drawback of TDDFT is that available approximations of the exchange-correlation (XC) potential are almost exclusively time local, which is known to be, in many cases, insufficient to describe nonadiabatic dynamics. Therefore, it is a key result of this thesis that we found a procedure to reverse-engineer a nonadiabatic (i. e. time-nonlocal) XC potential for an interacting quantum dot coupled to an electron reservoir, see Chap. 8. This was possible due to insights we gained from the diagrammatic calculations of Chaps. 4-6, i. e., thanks to a multi-method perspective on single-electron transport. The procedure to develop a nonadiabatic XC potential is based on master-equation descriptions of the electron dynamics in the interacting quantum dot and in a corresponding non-interacting auxiliary system. Besides that, the additional insights outlined in Chap. 8 are summarized as follows: (1) the derived XC potential only depends on the quantum-dot charge density and its first time derivative; (2) its main nonadiabatic property is a dynamical step, which we related to physical charge-relaxation time scales; (3) this dynamical step is crucial for the dynamics in the linear- [80] and nonlinear-response regime [85]; (4) TDDFT with this simple nonadiabatic XC potential is already significantly more accurate than the master-equation description, which we used to derive the nonadiabatic XC potential initially. To show the latter point, we compared TDDFT results of the single-contact quantum dot to accurate data obtained in time-dependent density-matrix renormalization-group calculations (td-DMRG), as well as to results derived in second-order perturbation theory. Besides that, we presented time evolutions of many quantum dots coupled to a shared reservoir, to demonstrate the applicability of the TDDFT approach to more complex systems. This also exemplified the efficient numerics of TDDFT—a key asset of this theory—which makes it a promising tool for future simulations of the electron dynamics in complex single-electron tunneling devices. Note that, prior

to Chap. 8, we explained the employed TDDFT implementation in Chap. 7, where we also provided numerical details, which may be of interest for follow-up projects. Furthermore, in Chap. 9, we outlined an extension of the reverse-engineering procedure which is valid for a quantum dot coupled to two reservoirs. Here, we found novel approximations for the XC potential as well as for an XC correction to an applied bias voltage, both depending on the charge density on the quantum dot and the currents in the left and the right reservoirs. We emphasize that this extends related studies of a steady-state DFT approach (i-DFT) [90–92] to the dynamical case, where the system is not in a steady state and where the XC approximation depends on the left and right currents separately.

Importantly, the nonstandard approach of combining diagrammatic methods with TDDFT generates a starting point for numerous future research. We here sort possible follow-up projects which arise into three key questions:

1. How can the derived nonadiabatic XC potentials be extended to lower temperatures and strong reservoir-dot coupling?

2. What are the prospects of TDDFT calculations for more complex nanodevices which are still described by model Hamiltonians?

3. What are the implications for the XC potential of systems governed by long-ranged Coulomb interaction?

The first question is particularly interesting considering the recent success of steady-state DFT (i-DFT) to describe strong correlation in the Anderson model [90, 91]. An initial step to include memory in these calculations has been reported in Ref. [134], by proposing a low-temperature generalization of the method outlined in this thesis, see also Ref. [92]. However, further research is necessary to validate the accuracy of this generalization.

To discuss the second question, let us once more emphasize the central motivation for the TDDFT approach presented in Chaps. 7-9. We believe that many interesting nanoscale devices can be treated in TDDFT, by either applying the derived XC approximations, or by developing extensions thereof, starting from Markovian master equations. Promising future studies include a many-level quantum

dot, where we expect a repetition of the here reported dynamical step at integer density values. We also anticipate studies of double quantum dots with direct coupling between the two dots, as a step towards complex setups, which may include multiple mutually-coupled quantum dots. Note that in Chap. 7 we already laid the ground for a numerical implementation of arbitrary geometries of multiple quantum dots coupled to a shared reservoir (and an extension to multiple reservoirs is straightforward, see Chap. 9). The possibility to include multiple quantum dots and their real-space separation in a TDDFT calculation also highlights another benefit. In TDDFT, we can explicitly treat the propagation of electrons in the reservoir(s), in contrast to diagrammatic methods, where we trace out the reservoir degrees-of-freedom. This in principle allows us to analyze setups similar to the one reported in Ref. [24], where two single-electron sources emit electrons into separated one-dimensional channels, which then cross at a beam splitter. By modeling the single-electron sources individually with the TDDFT approach presented here, and the one-dimensional conductors—the electron reservoirs—as two tight-binding chains with a shared site, we can set up a TDDFT calculation for this and similar systems. Note that the Pauli exclusion principle at the shared site is already implemented by construction. This exemplifies the possibilities for future TDDFT calculations, which are opened up by this thesis.

Finally, the third question is natural to ask, because dynamical steps have recently also been reported for XC potentials of systems with long-ranged interaction [116, 123, 128–130]. Since we related the dynamical steps in the XC approximations derived here to physical charge-relaxation time scales, it is interesting to investigate if similar relations can be found for these systems as well. We leave this as an open question for future research.

A | Master Equation for a Single-Spin Source

In this appendix, we derive the Markovian master equation which models the charge and spin dynamics in the superconducting single-electron transistor studied in Chap. 4. Note that this appendix also appears in the paper *New Journal of Physics* **18** 083019 (2016).

We begin in App. A.1 by explaining a way to keep track of the charge and quasiparticle numbers on the superconducting island. Afterwards, the employed model for the distribution of island quasiparticles is discussed in App. A.2. The Markovian master equation and the respective tunnel rates between different island configurations are derived in App. A.3.

A.1 Charge and quasiparticle degrees-of-freedom

In order to derive a master equation describing the time evolution of the island's occupation probabilities, it is necessary to count the number of excess charges on the island. To achieve this, we extend the Hilbert space by charge states $\{|n\rangle\}$ [68]. These states allow us to keep track of the number of charges that enter or leave the island, without keeping track of their energy distribution. Note that no coherences between different charge states are included in the calculations, since the Josephson energies of the tunnel junctions are considered to be small compared to the charging energy E_c. Starting from the Hamiltonian in Eq. (4.1), the operator $\hat{n}$ in the Hamiltonian is reinterpreted as $\hat{n}\,|n\rangle = n\,|n\rangle$ and the tunneling part of the Hamiltonian

is redefined by adding operators in the $|n\rangle$-subspace, leading to

$$\begin{aligned} H = & \sum_{\alpha=\mathrm{L,R}} \sum_{\sigma,k} \epsilon_{\alpha k} c^\dagger_{\alpha\sigma k} c_{\alpha\sigma k} - \sum_{\alpha,k} \left(\Delta_\alpha c^\dagger_{\alpha\uparrow k} c^\dagger_{\alpha\downarrow -k} + \Delta^*_\alpha c_{\alpha\downarrow -k} c_{\alpha\uparrow k} \right) \\ & + \sum_{\sigma,k} \left(\epsilon_k - \sigma h \right) d^\dagger_{\sigma k} d_{\sigma k} - \sum_k \left(\Delta d^\dagger_{\uparrow k} d^\dagger_{\downarrow -k} + \Delta^* d_{\downarrow -k} d_{\uparrow k} \right) \\ & + E_\mathrm{c} \left(\hat{n} - n_\mathrm{g}(t) \right)^2 \\ & + \sum_{\alpha=\mathrm{L,R}} \sum_{\sigma,k,l} \sum_n \left(t^{a\sigma}_{kl} c_{\alpha\sigma l} d^\dagger_{\sigma k} |n+1\rangle\langle n| + \mathrm{H.\,c.} \right). \end{aligned} \tag{A.1}$$

The Hamiltonian in Eq. (A.1) is diagonalized by applying a Bogoliubov transformation to the electron operators both in the contacts and on the island,

$$\gamma^\dagger_{\downarrow -k} = u_k d^\dagger_{\downarrow -k} + v^*_k d_{\uparrow k}, \tag{A.2a}$$

$$\kappa^\dagger_{\alpha\downarrow -k} = u_{\alpha k} c^\dagger_{\alpha\downarrow -k} + v^*_{\alpha k} c_{\alpha\uparrow k}, \tag{A.2b}$$

$$\gamma_{\uparrow k} = u^*_k d_{\uparrow k} - v_k d^\dagger_{\downarrow -k}, \tag{A.2c}$$

$$\kappa_{\alpha\uparrow k} = u^*_{\alpha k} c_{\alpha\uparrow k} - v_{\alpha k} c^\dagger_{\alpha\downarrow -k}. \tag{A.2d}$$

The result is a description in terms of quasiparticles, where $\gamma^{(\dagger)}_{\sigma k}$ are the island and $\kappa^{(\dagger)}_{\alpha\sigma k}$ the contact quasiparticle operators. The prefactors of the Bogoliubov transformation fulfill $|u_k|^2 = \left(1 + \epsilon_k / \sqrt{\epsilon_k^2 + |\Delta|^2}\right)/2$ and $|v_k|^2 = 1 - |u_k|^2$ (equivalently for $|u_{\alpha k}|^2$ and $|v_{\alpha k}|^2$). Using the Eqs. (A.2), the Hamiltonian in Eq. (A.1) becomes (up to a constant)

$$\begin{aligned} H = & \sum_{\alpha=\mathrm{L,R}} \sum_{\sigma,k} E_{\alpha k} \kappa^\dagger_{\alpha\sigma k} \kappa_{\alpha\sigma k} + \sum_{\sigma,k} E_{\sigma k} \gamma^\dagger_{\sigma k} \gamma_{\sigma k} + E_\mathrm{c} \left(\hat{n} - n_\mathrm{g}(t) \right)^2 \\ & + \sum_{\alpha=\mathrm{L,R}} \sum_{k,l} \sum_n \Bigg[t^{\alpha\uparrow}_{kl} \left(u_{\alpha l} \kappa_{\alpha\uparrow l} + v_{\alpha l} \kappa^\dagger_{\alpha\downarrow -l} \right) \left(u^*_k \gamma^\dagger_{\uparrow k} + v^*_k \gamma_{\downarrow -k} \right) \\ & \times |n+1\rangle\langle n| + t^{\alpha\downarrow}_{kl} \left(u_{\alpha l} \kappa_{\alpha\downarrow -l} - v_{\alpha l} \kappa^\dagger_{\alpha\uparrow l} \right) \left(u^*_k \gamma^\dagger_{\downarrow -k} - v^*_k \gamma_{\uparrow k} \right) \\ & \times |n+1\rangle\langle n| + \mathrm{H.\,c.} \Bigg], \end{aligned} \tag{A.3}$$

where the quasiparticle energies are $E_{\alpha k} = E(\epsilon_{\alpha k}) = \sqrt{\epsilon_{\alpha k}^2 + |\Delta_\alpha|^2}$ for the contacts and $E_{\sigma k} = E(\epsilon_k, \sigma) = -\sigma h + \sqrt{\epsilon_k^2 + |\Delta|^2}$ for the Zeeman-split island.

As pointed out in the main text, the parity effect in the superconducting island [150, 164, 166] is crucial for the spin-turnstile operation. To account for the parity effect in the calculations, it is important to keep track of the island quasiparticle excitations of both spin directions by extending the introduced charge states by the quasiparticle numbers $N^\uparrow$ and $N^\downarrow$ to $\{|n, N^\uparrow, N^\downarrow\rangle\}$. Naturally, the charge number and the quasiparticle numbers are not fully independent of each other: the parity of excess charges $p(n)$ equals the parity $p(N^\uparrow + N^\downarrow)$ of the total number of quasiparticle excitations. Therefore, the Hamiltonian is modified to

$$\begin{aligned} H = & \sum_{\alpha=\mathrm{L,R}} \sum_{\sigma,k} E_{\alpha k} \kappa_{\alpha\sigma k}^\dagger \kappa_{\alpha\sigma k} + \sum_{\sigma,k} E_{\sigma k} \gamma_{\sigma k}^\dagger \gamma_{\sigma k} + E_\mathrm{c} \left(\hat{n} - n_\mathrm{g}(t)\right)^2 \\ & + \sum_{\alpha=\mathrm{L,R}} \sum_{k,l} \sum_{n,N^\uparrow,N^\downarrow}{}' \Bigg[t_{kl}^{\alpha\uparrow} \left(u_{\alpha l} \kappa_{\alpha\uparrow l} + v_{\alpha l} \kappa_{\alpha\downarrow -l}^\dagger \right) \\ & \times \left(u_k^* \gamma_{\uparrow k}^\dagger \hat{\mathrm{P}}_{n+1,N^\uparrow+1,N^\downarrow}^{n,N^\uparrow,N^\downarrow} + v_k^* \gamma_{\downarrow -k} \hat{\mathrm{P}}_{n+1,N^\uparrow,N^\downarrow-1}^{n,N^\uparrow,N^\downarrow} \right) \\ & + t_{kl}^{\alpha\downarrow} \left(u_{\alpha l} \kappa_{\alpha\downarrow -l} - v_{\alpha l} \kappa_{\alpha\uparrow l}^\dagger \right) \\ & \times \left(u_k^* \gamma_{\downarrow -k}^\dagger \hat{\mathrm{P}}_{n+1,N^\uparrow,N^\downarrow+1}^{n,N^\uparrow,N^\downarrow} - v_k^* \gamma_{\uparrow k} \hat{\mathrm{P}}_{n+1,N^\uparrow-1,N^\downarrow}^{n,N^\uparrow,N^\downarrow} \right) \\ & + \mathrm{H.\,c.} \Bigg], \end{aligned} \tag{A.4}$$

where we used the abbreviations $\hat{\mathrm{P}}_{n,N^\uparrow,N^\downarrow}^{n',N^{\uparrow\prime},N^{\downarrow\prime}} = |n, N^\uparrow, N^\downarrow\rangle\langle n', N^{\uparrow\prime}, N^{\downarrow\prime}|$ and $\sum'_{n,N^\uparrow,N^\downarrow} = \sum_{n,N^\uparrow,N^\downarrow,\ \text{with}\ p(n)=p(N^\uparrow+N^\downarrow)}$.

A.2 Density matrix and quasiparticle distribution

The added quasiparticle-resolved charge states lead us to a simplified description of the system's dynamics. More precisely, we do not need to take into account the exact distribution of quasiparticles and charges over the accessible energy states, when treating the time evolution

of the occupation probabilities, $P(n, N^{\uparrow}, N^{\downarrow}; t)$, of the island states $|n, N^{\uparrow}, N^{\downarrow}\rangle$. In the following, we often suppress the time-variable t, intending $P(n, N^{\uparrow}, N^{\downarrow}; t) \equiv P(n, N^{\uparrow}, N^{\downarrow})$. The density matrix for the extended Hilbert space of the full system is modeled by

$$\rho(t) = \rho_{\mathrm{L}}^{\mathrm{eq}} \otimes \rho_{\mathrm{R}}^{\mathrm{eq}} \otimes {\sum_{n,N^{\uparrow},N^{\downarrow}}}' \rho_{\mathrm{island}}^{n,N^{\uparrow},N^{\downarrow}} \otimes |n, N^{\uparrow}, N^{\downarrow}\rangle\langle n, N^{\uparrow}, N^{\downarrow}| \cdot P(n, N^{\uparrow}, N^{\downarrow}; t). \tag{A.5}$$

Again, coherent superpositions of island states $|n, N^{\uparrow}, N^{\downarrow}\rangle$ with different charge and/or quasiparticle numbers are not allowed due to the island's large charging energy and superconducting gap. In the considered model, both contacts are assumed to be large reservoirs, which can be described by equilibrium density matrices $\rho_{\mathrm{L,R}}^{\mathrm{eq}}$ for all times. Consequently, the quasiparticle distribution function of the contacts is given by a Fermi distribution The density matrix $\rho_{\mathrm{island}}^{n,N^{\uparrow},N^{\downarrow}}$ of the island sub-space is not known in detail, but the separate measurements of the excess charge number and the spin-resolved quasiparticle numbers yield $n, N^{\uparrow}, N^{\downarrow}$. The distribution function of island quasiparticles among the quasiparticle energies is defined by

$$F^{+}_{n,N^{\uparrow},N^{\downarrow}}(\sigma, k) = \mathrm{Tr}\left(\gamma^{\dagger}_{\sigma k}\gamma_{\sigma k}\,\rho_{\mathrm{island}}^{n,N^{\uparrow},N^{\downarrow}}\right). \tag{A.6}$$

Here, we make the assumptions that $F^{+}_{n,N^{\uparrow},N^{\downarrow}}(\sigma, k)$ only depends on the energy $E_{\sigma k}$ and on the number of quasiparticles with respective spin N^{σ} (thus being independent of the number of excess charges n):

$$F^{+}_{n,N^{\uparrow},N^{\downarrow}}(\sigma, k) \approx F^{+}_{N^{\sigma}}(E_{\sigma k}). \tag{A.7}$$

We then model $F^{+}_{N^{\sigma}}(E_{\sigma k})$ by a Fermi distribution featuring an effective temperature $T_{N^{\sigma}}$ [with $F^{-}_{N^{\sigma}}(E_{\sigma k}) = 1 - F^{+}_{N^{\sigma}}(E_{\sigma k})$]. The effective temperature, which should not be confused with a physical temperature, is a free parameter which is used to keep track of the number of quasiparticle excitations on the island. This means that $T_{N^{\sigma}}$ depends on the number of already excited σ-spin quasiparticles, and is implicitly fixed by the equation

$$N^{\sigma} = \sum_{k} F^{+}_{N^{\sigma}}(E_{\sigma k}) = 2\,\nu_0 V_{\mathrm{I}} \int_0^{\infty} dE\, g_{\sigma}(E) F_{N^{\sigma}}(E). \tag{A.8}$$

Here, V_I is the island's volume, ν_0 is the DOS at the Fermi level in the normal state and $g_\sigma(E)$ is the unitless DOS of the superconducting island. The model thereby ensures that the occupation numbers of the density matrix in the island quasiparticle subspace are in agreement with the number of quasiparticle excitations counted in the additional states $|n, N^\uparrow, N^\downarrow\rangle$. In this way, we take care of the parity effect in the model, since the sequential tunnel rates of the master equation, derived in App. A.3, explicitly depend on $F^+_{N^\sigma}$ and thus on the number of excited quasiparticles. In a real system, the distribution of quasiparticles on the island might differ from the Fermi distribution. However, the precise form of $F^+_{N^\sigma}$ should not influence the working principle of the proposed clocked spin pump, as long as $F^+_{N^\sigma} \ll 1$ [166].

A.3 Master equation in Born-Markov approximation

We now come to the derivation of the master equation, which describes the time evolution of the occupation probabilities $P(n, N^\uparrow, N^\downarrow)$. The master equation is calculated in Born-Markov approximation, i. e., restricted to sequential tunneling while neglecting memory effects, see also Sec. 3.1.2. The starting point for the derivation is the Liouville-von Neumann equation

$$i\partial_t \rho(t) = [H, \rho(t)]\,. \tag{A.9}$$

As a first step, we switch to the interaction picture with respect to the perturbation H_T, where interaction-picture operators are marked by a $\sim$ symbol. We obtain the Liouville-von Neumann equation in Born-Markov approximation

$$\partial_t \tilde{\rho}(t) = (-i)^2 \int_{-\infty}^{t} dt' \left[\tilde{H}_\mathrm{T}(t), \left[\tilde{H}_\mathrm{T}(t'), \tilde{\rho}(t)\right]\right]. \tag{A.10}$$

The time evolution of the probabilities $P(n, N^\uparrow, N^\downarrow)$ is calculated by taking the time derivative of the expectation value of the projector $\hat{P}_{n,N^\uparrow,N^\downarrow} = \hat{P}^{n,N^\uparrow,N^\downarrow}_{n,N^\uparrow,N^\downarrow} = |n, N^\uparrow, N^\downarrow\rangle\langle n, N^\uparrow, N^\downarrow|$. With Eq. (A.10)

follows

$$\partial_t P(n,N^\uparrow,N^\downarrow) = \mathrm{Tr}\left(\hat{P}_{n,N^\uparrow,N^\downarrow}\,\partial_t\rho(t)\right) \tag{A.11}$$
$$= (-i)^2\int_{-\infty}^{t} dt'\,\mathrm{Tr}\left(\hat{P}_{n,N^\uparrow,N^\downarrow}\left[\tilde{H}_\mathrm{T}(t),\left[\tilde{H}_\mathrm{T}(t'),\tilde{\rho}(t)\right]\right]\right).$$

Before evaluating the double commutator in Eq. (A.11), we write the tunnel Hamiltonian as

$$\tilde{H}_\mathrm{T}(t) = \sum_{\alpha,\beta=\pm}\sum_{\sigma,k} e^{iH_0t}H^{\alpha\beta}_{\sigma k}e^{-iH_0t} \tag{A.12}$$

where H_0 represents the unperturbed Hamiltonian, $\alpha=\pm$ indicates if a charge is added or subtracted from the island and $\beta=\pm$ marks the excitation or annihilation of an island quasiparticle during the tunnel process ($\bar{\alpha}=-\alpha,\bar{\beta}=-\beta$). The operators $H^{\alpha\beta}_{\sigma k}$, with $H^{\alpha\beta}_{\sigma k}=\left(H^{\bar{\alpha}\bar{\beta}}_{\sigma k}\right)^\dagger$, read as

$$H^{++}_{\uparrow k} = \sum_{\alpha=\mathrm{L,R}}\sum_{n,N^\uparrow,N^\downarrow}{}'\sum_l t^{\alpha\uparrow}_{kl} \tag{A.13a}$$
$$\times\left(u_{\alpha l}\kappa_{\alpha\uparrow l}+v_{\alpha l}\kappa^\dagger_{\alpha\downarrow -l}\right)u^*_k\gamma^\dagger_{\uparrow k}\hat{\mathrm{P}}^{n,N^\uparrow,N^\downarrow}_{n+1,N^\uparrow+1,N^\downarrow},$$
$$H^{+-}_{\uparrow k} = \sum_{\alpha=\mathrm{L,R}}\sum_{n,N^\uparrow,N^\downarrow}{}'\sum_l t^{\alpha\uparrow}_{kl} \tag{A.13b}$$
$$\times\left(u_{\alpha l}\kappa_{\alpha\uparrow l}+v_{\alpha l}\kappa^\dagger_{\alpha\downarrow -l}\right)v^*_k\gamma_{\downarrow -k}\hat{\mathrm{P}}^{n,N^\uparrow,N^\downarrow}_{n+1,N^\uparrow,N^\downarrow-1},$$
$$H^{++}_{\downarrow k} = \sum_{\alpha=\mathrm{L,R}}\sum_{n,N^\uparrow,N^\downarrow}{}'\sum_l t^{\alpha\downarrow}_{kl} \tag{A.13c}$$
$$\times\left(u_{\alpha l}\kappa_{\alpha\downarrow -l}-v_{\alpha l}\kappa^\dagger_{\alpha\uparrow l}\right)u^*_k\gamma^\dagger_{\downarrow -k}\hat{\mathrm{P}}^{n,N^\uparrow,N^\downarrow}_{n+1,N^\uparrow,N^\downarrow+1},$$
$$H^{+-}_{\downarrow k} = \sum_{\alpha=\mathrm{L,R}}\sum_{n,N^\uparrow,N^\downarrow}{}'\sum_l t^{\alpha\downarrow}_{kl} \tag{A.13d}$$
$$\times\left(u_{\alpha l}\kappa_{\alpha\downarrow -l}-v_{\alpha l}\kappa^\dagger_{\alpha\uparrow l}\right)(-1)v^*_k\gamma_{\uparrow k}\hat{\mathrm{P}}^{n,N^\uparrow,N^\downarrow}_{n+1,N^\uparrow-1,N^\downarrow}.$$

Inserting these expressions into Eq. (A.11) and only keeping the parts of the double commutator that do not vanish under the trace leads to

$$\begin{aligned}\partial_t P(n,N^{\uparrow},N^{\downarrow}) = {} & (-i)^2 \int_{-\infty}^{t} dt' \,\mathrm{Tr}\left(\hat{P}_{n,N^{\uparrow},N^{\downarrow}}\right. \\ & \left.\times \sum_{\alpha,\beta,\sigma,k}\left[\tilde{H}^{\alpha\beta}_{\sigma k}(t),\left[\tilde{H}^{\bar{\alpha}\bar{\beta}}_{\sigma k}(t'),\tilde{\rho}(t)\right]\right]\right) \\ = {} & 2\,\mathrm{Re}\int_{-\infty}^{t} dt' \sum_{\alpha,\beta,\sigma,k}\mathrm{Tr}\left(\tilde{H}^{\alpha\beta}_{\sigma k}(t)\hat{P}_{n,N^{\uparrow},N^{\downarrow}}\tilde{H}^{\bar{\alpha}\bar{\beta}}_{\sigma k}(t')\tilde{\rho}(t)\right. \\ & \left.-\tilde{H}^{\bar{\alpha}\bar{\beta}}_{\sigma k}(t')\tilde{H}^{\alpha\beta}_{\sigma k}(t)\hat{P}_{n,N^{\uparrow},N^{\downarrow}}\tilde{\rho}(t)\right)\end{aligned} \tag{A.14}$$

The 16 objects defined by $I^{\alpha\beta}_{\sigma k}(t,t') = \mathrm{Tr}\left\{\tilde{H}^{\bar{\alpha}\bar{\beta}}_{\sigma k}(t')\tilde{H}^{\alpha\beta}_{\sigma k}(t)\hat{P}_{n,N^{\uparrow},N^{\downarrow}}\tilde{\rho}(t)\right\}$ and $J^{\alpha\beta}_{\sigma k}(t,t') = \mathrm{Tr}\left\{\tilde{H}^{\alpha\beta}_{\sigma k}(t)\hat{P}_{n,N^{\uparrow},N^{\downarrow}}\tilde{H}^{\bar{\alpha}\bar{\beta}}_{\sigma k}(t')\tilde{\rho}(t)\right\}$ in Eq. (A.14) are calculated by applying standard manipulations. We then summarize all terms appearing on the r. h. s of Eq. (A.14) in products containing an occupation probability and a transition rate. This leads to the master equation for the occupation probabilities

$$\begin{aligned}\partial_t P(n,N^{\uparrow},N^{\downarrow}) = \sum_{n',N^{\uparrow\prime},N^{\downarrow\prime}}{}'' \Big[& W^{n',N^{\uparrow\prime},N^{\downarrow\prime}}_{n,N^{\uparrow},N^{\downarrow}} P(n',N^{\uparrow\prime},N^{\downarrow\prime}) \\ & - W^{n,N^{\uparrow},N^{\downarrow}}_{n',N^{\uparrow\prime},N^{\downarrow\prime}} P(n,N^{\uparrow},N^{\downarrow})\Big].\end{aligned} \tag{A.15}$$

Here, $\sum''$ is defined as the sum over all combinations of $n', N^{\uparrow\prime}, N^{\downarrow\prime}$ for which $n'-n = \pm 1$ and $N^{\uparrow\prime}+N^{\downarrow\prime}-(N^{\uparrow}+N^{\downarrow}) = \pm 1$. In Eq. (A.15), a transition from $(n,N^{\uparrow},N^{\downarrow})$ to $(n',N^{\uparrow\prime},N^{\downarrow\prime})$ is characterized by the transition rate $W^{n,N^{\uparrow},N^{\downarrow}}_{n',N^{\uparrow\prime},N^{\downarrow\prime}}$, where the indices describe the island excess charges and quasiparticle excitations before and after the tunnel process. In total, starting from the islands occupation $(n,N^{\uparrow},N^{\downarrow})$, eight different sequential tunnel processes can in principle occur. The tunneling of one charge *towards* the island is divided in four different processes: the involved electron features either an up spin or a down spin and, during the process, a quasiparticle of the same spin is generated or a quasiparticle of the opposite spin is annihilated. The tunnel

rates of these four processes are

$$W^{n,N^\uparrow,N^\downarrow}_{n+1,N^\uparrow+1,N^\downarrow} = \sum_{\alpha=\mathrm{L,R}} \frac{1}{R_\uparrow} \int_0^\infty dE\, g_\alpha\left(E+\delta E^{\alpha,n}_+\right) \times g_\uparrow(E)\, f^+\left(E+\delta E^{\alpha,n}_+\right) F^-_{N^\uparrow}(E) \tag{A.16a}$$

$$W^{n,N^\uparrow,N^\downarrow}_{n+1,N^\uparrow,N^\downarrow-1} = \sum_{\alpha=\mathrm{L,R}} \frac{1}{R_\uparrow} \int_0^\infty dE\, g_\alpha\left(-E+\delta E^{\alpha,n}_+\right) \times g_\downarrow(E)\, f^+\left(-E+\delta E^{\alpha,n}_+\right) F^+_{N^\downarrow}(E) \tag{A.16b}$$

$$W^{n,N^\uparrow,N^\downarrow}_{n+1,N^\uparrow,N^\downarrow+1} = \sum_{\alpha=\mathrm{L,R}} \frac{1}{R_\downarrow} \int_0^\infty dE\, g_\alpha\left(E+\delta E^{\alpha,n}_+\right) \times g_\downarrow(E)\, f^+\left(E+\delta E^{\alpha,n}_+\right) F^-_{N^\downarrow}(E) \tag{A.16c}$$

$$W^{n,N^\uparrow,N^\downarrow}_{n+1,N^\uparrow-1,N^\downarrow} = \sum_{\alpha=\mathrm{L,R}} \frac{1}{R_\downarrow} \int_0^\infty dE\, g_\alpha\left(-E+\delta E^{\alpha,n}_+\right) \times g_\uparrow(E)\, f^+\left(-E+\delta E^{\alpha,n}_+\right) F^+_{N^\uparrow}(E), \tag{A.16d}$$

in which we defined $R_{\alpha\sigma} = 1/[2\pi|t^{\alpha\sigma}|^2\nu_0^2 V_\alpha V_\mathrm{I})] = R_\sigma$ as the tunnel resistances (spin dependent), with the volumes V_α (contact) and V_I (island) and ν_0 is the DOS per spin at the Fermi level in the normal state, We also assume $t^{\alpha\sigma}_{kl} = t^{\alpha\sigma}$ to be momentum independent. The dimensionless DOS $g_\alpha(E_\alpha)$ and $g_\sigma(E)$ of the island and the contacts are defined in Eq. (4.2). The tunneling of one charge *off* the island is equivalently divided in four processes, where the respective tunnel rates are

$$W^{n,N^\uparrow,N^\downarrow}_{n-1,N^\uparrow,N^\downarrow+1} = \sum_{\alpha=\mathrm{L,R}} \frac{1}{R_\uparrow} \int_0^\infty dE\, g_\alpha\left(-E-\delta E^{\alpha,n}_-\right) \times g_\downarrow(E)\, f^-\left(-E-\delta E^{\alpha,n}_-\right) F^-_{N^\downarrow}(E) \tag{A.17a}$$

$$W^{n,N^\uparrow,N^\downarrow}_{n-1,N^\uparrow-1,N^\downarrow} = \sum_{\alpha=\mathrm{L,R}} \frac{1}{R_\uparrow} \int_0^\infty dE\, g_\alpha\left(E-\delta E^{\alpha,n}_-\right) \times g_\uparrow(E)\, f^-\left(E-\delta E^{\alpha,n}_-\right) F^+_{N^\uparrow}(E) \tag{A.17b}$$

$$W^{n,N^\uparrow,N^\downarrow}_{n-1,N^\uparrow+1,N^\downarrow} = \sum_{\alpha=\mathrm{L,R}} \frac{1}{R_\downarrow} \int_0^\infty dE\, g_\alpha\left(-E-\delta E^{\alpha,n}_-\right) \times g_\uparrow(E)\, f^-\left(-E-\delta E^{\alpha,n}_-\right) F^-_{N^\uparrow}(E) \tag{A.17c}$$

$$W^{n,N^{\uparrow},N^{\downarrow}}_{n-1,N^{\uparrow},N^{\downarrow}-1} = \sum_{\alpha=\mathrm{L,R}} \frac{1}{R_{\downarrow}} \int_0^{\infty} dE\, g_{\alpha}\left(E - \delta E_{-}^{\alpha,n}\right) \times g_{\downarrow}(E)\, f^{-}\left(E - \delta E_{-}^{\alpha,n}\right) F^{+}_{N^{\downarrow}}(E). \tag{A.17d}$$

Each of the eight tunnel processes can only take place if the addition energy $\delta E_{\pm}^{\alpha,n}$ defined in Eq. (4.3) is brought up. This includes the change of charging energy and a contribution from an applied bias voltage V. Notably, the tunnel rates in Eqs. (A.15)-(A.17) depend on time via the addition energies.

B | Details on the Noise Derivations

We provide technical details of the real-time diagrammatic noise calculations of Sec. 5.4. The following appendices are part of a paper, which is available under the reference *arXiv* 1805.03130 (preprint).

The structure is as follows. First, in App. B.1, we motivate the definition of the auxiliary function, $\tilde{S}(t;\omega)$ in Eq. (5.4), for the diagrammatic noise calculations. The slow-driving expansion of this function is discussed in detail in App. B.2, leading to Eqs. (5.16) of the main text. For this expansion we also define another helpful function, $\tilde{I}(t,z;\omega)$, which is calculated explicitly in App. B.3. The derivation of the reduced propagator, $\overline{\Pi}(t,z;\omega)$, is outlined in App. B.4. To evaluate the noise expressions derived in this thesis, we give expressions for all relevant kernels in App. B.5. Finally, in App. B.6, we provide technical details on the high noise-frequency approximation, see Sec. 5.4.3.

B.1 The auxiliary function $\tilde{S}(t;\omega)$

We begin by deriving Eq. (5.3) of the main text by rewriting Eq. (5.2) in terms of the auxiliary function $\tilde{S}(t;\omega)$ given in Eq. (5.4). First, in Eq. (5.2), we split the second integration into two parts and obtain

$$\mathcal{S}(n;\omega) = \lim_{t_0\to-\infty}\Bigg[\int_0^T \frac{dt}{T}\int_{t_0}^0 d\tau e^{in\Omega t+i\omega\tau}\mathcal{C}(t,\tau) + \int_0^T \frac{dt}{T}\int_{t_0}^0 d\tau e^{in\Omega t-i\omega\tau}\mathcal{C}(t,-\tau)\Bigg], \tag{B.1}$$

with $\mathcal{C}(t,\tau) = \langle\{\delta I(t), \delta I(t+\tau)\}\rangle$. To treat the second term in the square brackets, we swap its two integrations and, by exploiting periodicity, shift the interval of the integration over t by the amount $-\tau$. Incorporating the latter shift into a shift of the variable t, swapping the integration order a second time and exploiting the symmetrized form of $\mathcal{C}(t,\tau) = \mathcal{C}(t+\tau,-\tau)$, we derive

$$\mathcal{S}(n;\omega) = \lim_{t_0\to-\infty}\left[\int_0^T \frac{dt}{T}\int_{t_0}^0 d\tau e^{in\Omega t+i\omega\tau}\mathcal{C}(t,\tau)\right. \\ \left. + \int_0^T \frac{dt}{T}\int_{t_0}^0 d\tau e^{in\Omega(t+\tau)-i\omega\tau}\mathcal{C}(t,\tau)\right]. \tag{B.2}$$

Since at finite temperatures considered here, temporal correlations of current fluctuations, given by $\mathcal{C}(t,\tau)$, decay quickly for large values of τ, we expect the limit in Eq. (B.2) to converge separately for both terms in the square brackets. Therefore, we can replace t_0 with $-\infty$ at the integration bounds. The final step to obtain Eq. (5.3) of the main text is then to write the resulting equation in terms of the auxiliary function, which has been defined in Eq. (5.4), where the time difference τ has been replaced by $t' - t$.

B.2 Expansion of $\tilde{S}(t;\omega)$ for slow driving

In Sec. 5.3.3 we explain that, for slow periodic driving, it is justified to expand the noise expression in Eq. (5.3) order-by-order in the small parameter $\delta\epsilon\,\Omega\beta/\Gamma$. To evaluate the zeroth and first order of the resulting series [Eqs. (5.5)]—referred to as the instantaneous and the adiabatic-response contributions to the noise—we first need to derive the respective terms in the slow-driving expansion of the auxiliary function defined in Eq. (5.4). For this expansion, we start from the expression introduced in Sec. 5.4.2 and split the frequency-dependent propagator on the right-hand side of Eq. (5.10) into a decaying and a non-decaying part, as defined in Eq. (5.12). By inserting the reduced

propagator into Eq. (5.10), we obtain

$$\begin{aligned}\tilde{S}(t;\omega) = \lim_{t_0\to-\infty} \frac{\boldsymbol{e}^{\mathrm{T}}}{2}\Bigg[&\int_{t_0}^{t} dt_1 \int_{t_0}^{t_1} dt_2 \int_{t_0}^{t_2} dt_3 \\ &\times \mathcal{W}_I^{<}(t,t_1;\omega)\overline{\Pi}(t_1,t_2;\omega)\mathcal{W}_I^{>}(t_2,t_3;\omega)\boldsymbol{P}(t_3) \\ &+ \int_{t_0}^{t} dt_1 \mathcal{W}_{II}(t,t_1;\omega)\boldsymbol{P}(t_1) - \int_{t_0}^{t} dt_1 \int_{t_0}^{t_1} dt_2 \int_{t_0}^{t_1} dt_3 \\ &\times e^{i\omega(t_1-t)}\mathcal{W}_I(t,t_2)\boldsymbol{P}(t_2)\otimes \boldsymbol{e}^{\mathrm{T}}\mathcal{W}_I(t_1,t_3)\boldsymbol{P}(t_3)\Bigg].\end{aligned} \tag{B.3}$$

In Sec. 5.4.2 we introduced how the integrand of the kinetic equation (3.4) is expanded around the reference time t. Here, we proceed in a similar way, expanding all occupation vectors in the integrands in Eq. (B.3) around t. In addition, also the first time arguments of all kernels and of the reduced propagator are expanded around the reference time. These expansions are justified for slow driving, due to the short support times of all kernels, given by the reservoir correlation time β, and the short support time of the reduced propagator, given by Γ^{-1}. In addition, again following the same principle as introduced for the kinetic equation in Sec. 5.4.2, all objects $\boldsymbol{P}, \mathcal{W}$ and $\overline{\Pi}$ have to be expanded individually order by order in $\delta\epsilon\,\Omega\beta/\Gamma$. Collecting all terms in zeroth (first) order, we find the instantaneous contribution (adiabatic response) of the auxiliary function as given in Eqs. (5.16) in the main text,

$$\begin{aligned}\tilde{S}^{(\mathrm{i})}(t;\omega) = \frac{\boldsymbol{e}^{\mathrm{T}}}{2}\Big\{\mathcal{W}_I^{<}\overline{\Pi}\mathcal{W}_I^{>}\boldsymbol{P}\Big\}_{t;\omega}^{(\mathrm{i})} + \frac{\boldsymbol{e}^{\mathrm{T}}}{2}\Big\{\mathcal{W}_{II}\boldsymbol{P}\Big\}_{t;\omega}^{(\mathrm{i})} \\ - 2\Big\{\tilde{I}I\Big\}_{t;\omega}^{(\mathrm{i})},\end{aligned} \tag{B.4a}$$

$$\begin{aligned}\tilde{S}^{(\mathrm{a})}(t;\omega) = \frac{\boldsymbol{e}^{\mathrm{T}}}{2}\Big\{\mathcal{W}_I^{<}\overline{\Pi}\mathcal{W}_I^{>}\boldsymbol{P}\Big\}_{t;\omega}^{(\mathrm{a})} + \frac{\boldsymbol{e}^{\mathrm{T}}}{2}\Big\{\mathcal{W}_{II}\boldsymbol{P}\Big\}_{t;\omega}^{(\mathrm{a})} \\ - 2\Big\{\tilde{I}I\Big\}_{t;\omega}^{(\mathrm{a})},\end{aligned} \tag{B.4b}$$

where we applied several abbreviations, which we now explain. We have given the definition of the curly brackets for an operator product in Eqs. (5.14). Extended to a four-operator product, this explicitly

reads as [54]

$$\{ABCD\}^{(\mathrm{i})} = A^{(\mathrm{i})}B^{(\mathrm{i})}C^{(\mathrm{i})}D^{(\mathrm{i})}, \tag{B.5a}$$

$$\begin{aligned}\{ABCD\}^{(\mathrm{a})} = {} & A^{(\mathrm{i})}B^{(\mathrm{i})}C^{(\mathrm{i})}D^{(\mathrm{a})} + A^{(\mathrm{i})}B^{(\mathrm{i})}C^{(\mathrm{a})}D^{(\mathrm{i})} \\ & + A^{(\mathrm{i})}B^{(\mathrm{a})}C^{(\mathrm{i})}D^{(\mathrm{i})} + A^{(\mathrm{a})}B^{(\mathrm{i})}(t)C^{(\mathrm{i})}D^{(\mathrm{i})} \\ & + \partial A^{(\mathrm{i})}\,\partial_t\Big[B^{(\mathrm{i})}C^{(\mathrm{i})}D^{(\mathrm{i})}\Big] + A^{(\mathrm{i})}\,\partial B^{(\mathrm{i})}\,\partial_t\Big[C^{(\mathrm{i})}D^{(\mathrm{i})}\Big] \\ & + A^{(\mathrm{i})}B^{(\mathrm{i})}\,\partial C^{(\mathrm{i})}\dot{D}^{(\mathrm{i})}.\end{aligned} \tag{B.5b}$$

In Eqs. (B.4), the curly brackets carry a subscript for the reference time t, as well as a frequency argument ω, which have to be associated to all objects depending on these parameters. The new function $\tilde{I}$ is discussed in App. B.3.

To proceed with the evaluation of Eqs. (B.4), we need to derive the instantaneous contributions and the adiabatic responses of all objects appearing in the curly brackets individually. These derivations are outlined for the occupation vector and the current in the Sec. 5.4.2 in the main text, for the function $\tilde{I}$ in App. B.3 and for the reduced propagator in App. B.4. The adiabatic expansion of kernels is discussed in detail in Refs. [54, 67]. Explicit expressions in lowest order in the tunnel coupling, needed for the evaluation of the noise in the limits studied in this manuscript, are given in App. B.5. The final abbreviation in Eqs. (B.4) is that we write I for $\langle I(t)\rangle$.

B.3 The function $\tilde{I}(t,z;\omega)$

In this appendix, we discuss properties of the function $\tilde{I}$, which appears in Eqs. (B.4) and (5.16). We start from the third term on the right-hand side of Eq. (B.3), which stems from the product of current operators at different times and a contribution containing the non-decaying part of the propagator Π. The first part of this integral is similar to a current at time t_1, but not identical to it, and it also contains a frequency-dependent exponential function. It is this term that we want to analyze here and that we abbreviate as

$$\tilde{I}(t,t_1;\omega) = \frac{\boldsymbol{e}^{\mathrm{T}}}{2}\int_{-\infty}^{t_1} dt_2 e^{i\omega(t_1-t)}\mathcal{W}_I(t,t_2)\boldsymbol{P}(t_2). \tag{B.6}$$

The Laplace transform of Eq. (B.6) with respect to t_1 is given by

$$\begin{aligned}\tilde{I}(t,z;\omega) &= \int_{-\infty}^{t} dt_1 e^{z(t_1-t)} \frac{\boldsymbol{e}^{\mathrm{T}}}{2} \int_{-\infty}^{t_1} dt_2 e^{i\omega(t_1-t)} \mathcal{W}_I(t,t_2)\boldsymbol{P}(t_2) \qquad \text{(B.7)}\\ &= \int_{-\infty}^{t} dt_2 \int_{t_2}^{t} dt_1 e^{(z+i\omega)(t_1-t)} \frac{\boldsymbol{e}^{\mathrm{T}}}{2} \mathcal{W}_I(t,t_2)\boldsymbol{P}(t_2)\\ &= \int_{-\infty}^{t} dt_2 \frac{\boldsymbol{e}^{\mathrm{T}}}{2} \mathcal{W}_I(t,t_2)\boldsymbol{P}(t_2) \frac{1-e^{(z+i\omega)(t_2-t)}}{z+i\omega}\\ &= \frac{1}{z+i\omega}\left[\langle I(t)\rangle - I(t,z+i\omega)\right].\end{aligned}$$

In the last line, we inserted Eq. (3.5) for the expectation value of the current, as well as $I(t,z) = \frac{\boldsymbol{e}^{\mathrm{T}}}{2}\int_{-\infty}^{t} dt_2 e^{z(t_2-t)}\mathcal{W}_I(t,t_2)\boldsymbol{P}(t_2)$. We now outline the steps to derive the instantaneous part and the adiabatic response of the function $\tilde{I}(t,z;\omega)$. Using the form given in the last line in Eq. (B.7), we can expand $\tilde{I}(t,z;\omega)$ in powers of $\delta\epsilon\,\Omega\beta/\Gamma$, following the lines of the current expansion discussed in Sec. 5.4.2. In the limit $z \to 0^+$, which is of interest here, we find

$$\tilde{I}^{(\mathrm{i})}(t,0^+;\omega) = \frac{\boldsymbol{e}^{\mathrm{T}}}{2i\omega}\left[\left\{\mathcal{W}_I\boldsymbol{P}\right\}_t^{(\mathrm{i})} - \left\{\mathcal{W}_I\boldsymbol{P}\right\}_{t;\omega}^{(\mathrm{i})}\right], \qquad \text{(B.8a)}$$

$$\tilde{I}^{(\mathrm{a})}(t,0^+;\omega) = \frac{\boldsymbol{e}^{\mathrm{T}}}{2i\omega}\left[\left\{\mathcal{W}_I\boldsymbol{P}\right\}_t^{(\mathrm{a})} - \left\{\mathcal{W}_I\boldsymbol{P}\right\}_{t;\omega}^{(\mathrm{a})}\right]. \qquad \text{(B.8b)}$$

Note that the expression for $\tilde{I}^{(\mathrm{a})}(t,0^+;\omega)$ in Eq. (B.8b) is only given for completeness and is not needed for the calculations performed here. The reason is that in the auxiliary function in Eq. (B.4b) it is always multiplied with $\langle I(t)\rangle^{(\mathrm{i})}$, which vanishes for the single-contact quantum dot.

B.4 The reduced propagator $\overline{\Pi}(t,z;\omega)$

Equations (B.4) of the auxiliary function also include the instantaneous part and the adiabatic response of the Laplace-transformed reduced propagator, $\overline{\Pi}(t,z;\omega)$. The derivation of these parts is discussed in this appendix. By combining the definition of the reduced propagator, Eq. (5.12), with the Dyson equation of the full propagator, Eq. (5.11),

we find

$$\begin{aligned}\overline{\Pi}(t,t_1;\omega) = &\left[\mathbf{1}-\boldsymbol{P}(t)\otimes\boldsymbol{e}^{\mathrm{T}}\right]e^{i\omega(t_1-t)} \\ &+\int_{t_1}^{t}dt_2\int_{t_1}^{t_2}dt_3\,e^{i\omega(t_2-t)}\mathcal{W}(t_2,t_3;\omega) \\ &\times\left[\overline{\Pi}(t_3,t_1;\omega)+\boldsymbol{P}(t_3)\otimes\boldsymbol{e}^{\mathrm{T}}e^{i\omega(t_1-t_3)}\right].\end{aligned} \tag{B.9}$$

An important property of $\overline{\Pi}(t,t_1;\omega)$ is that this function decays for $|t-t_1|\gg\Gamma^{-1}$, in other words, when the difference in the time arguments exceeds the relaxation time of the quantum dot. This property, together with the assumption of slow driving, $\delta\epsilon\,\Omega\beta/\Gamma\ll 1$, justifies the expansion of the t_2-dependence of the kernel $\mathcal{W}(t_2,t_3;\omega)$ in Eq. (B.9) around the time t. In a similar way, we expand the t_3-dependence of the term in the (second) square brackets in Eq. (B.9) around the time t.

At this point, the Laplace transform $\overline{\Pi}(t,z;\omega)$ can be calculated, where we make use of the fact that the Laplace transform of a convolution of three functions, $A(t,t_1)$, $B(t,t_1)$ and $C(t,t_1)$, which we write as $\int_{-\infty}^{t}dt_1e^{z(t_1-t)}\int_{t_1}^{t}dt_2\int_{t_2}^{t}dt_3A(t,t_1)B(t_1,t_2)C(t_2,t_3)$, can be expressed as $e^{\partial}A(t,z)B(t,z)C(t,z)$, with $e^{\partial}=\exp\big(\partial_z^A\partial_t^B+\partial_z^A\partial_t^C+\partial_z^B\partial_t^C\big)$, see also Ref. [54]. The derivatives in this abbreviation only act on the quantities indicated by their superscripts. We obtain the equation

$$\begin{aligned}\overline{\Pi}(t,z;\omega) = &\frac{\mathbf{1}-\boldsymbol{P}(t)\otimes\boldsymbol{e}^{\mathrm{T}}}{z+i\omega} \\ &+e^{\partial}\,\frac{1}{z+i\omega}\mathcal{W}(t,z;\omega)\left[\overline{\Pi}(t,z;\omega)+\frac{\boldsymbol{P}(t)\otimes\boldsymbol{e}^{\mathrm{T}}}{z+i\omega}\right].\end{aligned} \tag{B.10}$$

The derivatives abbreviated by the symbol e^{∂} act on the three functions $A(t,z;\omega)=(z+i\omega)^{-1}$, $B(t,z;\omega)=\mathcal{W}(t,z;\omega)$, and $C(t,z;\omega)=\overline{\Pi}(t,z;\omega)+\boldsymbol{P}(t)\otimes\boldsymbol{e}^{\mathrm{T}}(z+i\omega)^{-1}$. We can write Eq. (B.10) in a more compact form by using the property that $\overline{\Pi}(t,z;\omega)=\overline{\Pi}(t,z+i\omega,0)=\overline{\Pi}(t,z+i\omega)$, and similarly for $W(t,z;\omega)$. The reason for this is that both objects only contain diagrams in which the frequency line runs

over the whole diagram. The final expression for $\overline{\Pi}(t,z)$ is

$$\overline{\Pi}(t,z) = \frac{\mathbf{1} - \boldsymbol{P}(t)\otimes \boldsymbol{e}^{\mathrm{T}}}{z} + e^{\partial}\,\frac{1}{z}\mathcal{W}(t,z)\left[\overline{\Pi}(t,z) + \frac{\boldsymbol{P}(t)\otimes \boldsymbol{e}^{\mathrm{T}}}{z}\right]. \tag{B.11}$$

The limit $\lim_{z\to 0^+}\overline{\Pi}(t,z;\omega)$, which is of interest for the noise calculations, is obtained from Eq. (B.11) by calculating $\lim_{z\to i\omega}\overline{\Pi}(t,z)$. Importantly, for the finite-frequency noise, this limit can be taken by replacing z with $i\omega$ in Eq. (B.11), in contrast to the zero-frequency noise [54], where the limit must be taken carefully.

We continue by deriving the instantaneous part and the adiabatic response of the function $\overline{\Pi}(t,z)$ given in Eq. (B.11). To extract these contributions, we proceed as previously and expand the reduced propagator in the small parameter $\delta\epsilon\,\Omega\beta/\Gamma$. In Eq. (B.11) we use the replacement $\overline{\Pi}(t,z) \to \overline{\Pi}^{(i)}(t,z) + \overline{\Pi}^{(a)}(t,z) + \ldots$ and similarly for $\mathcal{W}(t,z)$ as well as for $\boldsymbol{P}(t)$. We then collect all contributions in zeroth and first order in $\delta\epsilon\,\Omega\beta/\Gamma$. The result for the instantaneous part of the reduced propagator is the algebraic equation

$$\left[\mathbf{1} - \frac{\mathcal{W}^{(i)}}{z}\right]\overline{\Pi}^{(i)} = \frac{\mathbf{1} - \boldsymbol{P}^{(i)}\otimes \boldsymbol{e}^{\mathrm{T}}}{z} + \frac{\mathcal{W}^{(i)}\boldsymbol{P}^{(i)}\otimes \boldsymbol{e}^{\mathrm{T}}}{z^2}, \tag{B.12a}$$

For readability, we suppress the arguments (t,z) for kernels and the reduced propagator and (t) for the occupation vector in Eq. (B.12a) and also in Eq. (B.12b) below. The adiabatic response of the reduced

propagator is calculated by subsequently solving the equation

$$\begin{aligned}\left[\mathbf{1}-\frac{\mathcal{W}^{(i)}}{z}\right]\overline{\Pi}^{(a)} = &-\frac{\dot{\mathcal{W}}^{(i)}\,\overline{\Pi}^{(i)}}{z^2}-\frac{\mathcal{W}^{(i)}\,\dot{\overline{\Pi}}^{(i)}}{z^2}+\frac{\mathcal{W}^{(a)}\,\overline{\Pi}^{(i)}}{z}\\ &+\frac{\partial\mathcal{W}^{(i)}\,\dot{\overline{\Pi}}^{(i)}}{z}-\frac{\dot{\mathcal{W}}^{(i)}\,\boldsymbol{P}^{(i)}\otimes\boldsymbol{e}^{\mathrm{T}}}{z^3}\\ &-\frac{\mathcal{W}^{(i)}\,\dot{\boldsymbol{P}}^{(i)}\otimes\boldsymbol{e}^{\mathrm{T}}}{z^3}+\frac{\partial\mathcal{W}^{(i)}\,\dot{\boldsymbol{P}}^{(i)}\otimes\boldsymbol{e}^{\mathrm{T}}}{z^2}\\ &+\frac{\mathcal{W}^{(i)}\,\boldsymbol{P}^{(a)}\otimes\boldsymbol{e}^{\mathrm{T}}}{z^2}+\frac{\mathcal{W}^{(a)}\,\boldsymbol{P}^{(i)}\otimes\boldsymbol{e}^{\mathrm{T}}}{z^2}\\ &-\frac{\boldsymbol{P}^{(a)}\otimes\boldsymbol{e}^{\mathrm{T}}}{z}.\end{aligned}\tag{B.12b}$$

The solutions of Eqs. (B.12) are necessary to calculate the instantaneous part and adiabatic response of the auxiliary function in Eqs. (B.4) and (5.16).

A further insight of Eqs. (B.12) is the conclusion that an order-by-order expansion scheme in the tunnel-coupling strength is not generally applicable to the auxiliary noise function. The reason for this is that the reduced propagator, which is part of the auxiliary noise function, has no well defined order-by-order expansion, because the matrix $\left[\mathbf{1}-\frac{\mathcal{W}^{(i)}}{z}\right]$ on the left-hand side in Eqs. (B.12) mixes the orders: the first term is of order unity, while the second term scales with Γ/ω. Therefore, only for high noise frequencies, where $\Gamma/\omega \ll 1$, the usual order-by-order scheme can be applied, as shown in App. B.6. Otherwise, we use a crossover scheme, where all terms in Eqs. (B.12) are kept, with kernels derived in leading order in the tunnel-coupling strength.

B.5 Explicit kernels from diagrammatic rules

We now discuss explicit expressions for the various $\mathcal{W}$ kernels, which appear in this thesis, see Secs. 3.1 and 5.4. Throughout this work, all kernels are evaluated in the sequential-tunneling regime, namely up to linear order in Γ. Each kernel is therefore given by a sum over all possible diagrams containing a single tunneling line. This line connects either two tunnel vertices [$\mathcal{W}(t,t')$ and $\mathcal{W}(t,t';\omega)$], a tunnel and a

current vertex $[\mathcal{W}_{\mathrm{I}}(t,t'), \mathcal{W}_{\mathrm{I}}^{<}(t,t';\omega)$ and $\mathcal{W}_{\mathrm{I}}^{>}(t,t';\omega)]$ or two current vertices $[\mathcal{W}_{\mathrm{II}}(t,t';\omega)]$. At zero frequency, $\omega = 0$, the diagrammatic rules to calculate instantaneous contributions as well as adiabatic responses of these kernels are outlined in detail in the appendix of Ref. [54]. To derive the diagrams relevant here, we have to take into account that some kernels become frequency dependent due to the exponential factor $e^{i\omega(t'-t)}$ in the auxiliary function defined in Eq. (5.4). As explained in Sec. 5.4.1, we include this frequency dependence by adding a line in the respective diagrams, carrying the frequency ω. This additional frequency line only leads to a small modification of the diagrammatic rules of Ref. [54], which we now outline. In Laplace space, a linear-in-Γ diagram in instantaneous order is proportional to $1/\Delta E(t)$, where $\Delta E(t)$ is given by the difference of all backward-going minus all forward-going energies. If we evaluate a diagram which contains an additional frequency line, the only modification is that we have to include this frequency as a forward-going energy in $\Delta E(t)$, hence the frequency line in the diagrammatic picture. Analogous rules have to be applied for the adiabatic-response diagrams. However, for the here considered system, we can show that these expressions can always be simplified to $\mathcal{W}^{(\mathrm{a})}(t,z;\omega) = \frac{1}{2}\partial_z \dot{\mathcal{W}}^{(\mathrm{i})}(t,z;\omega)$.

For completeness, we give the instantaneous contribution to all kernels in Laplace representation. The kernels are shown for the spin-degenerate case, $\epsilon = \epsilon_\uparrow = \epsilon_\downarrow$, and with finite interaction parameter U, since this case is the main focus of this thesis. Extensions to spin-split single-particle energies $\epsilon_\uparrow \neq \epsilon_\downarrow$ at vanishing interaction, as discussed in Secs. 6.1 and 6.2, are straightforward. The instantaneous kernels in linear order in Γ read as

$$\frac{\mathcal{W}^{(\mathrm{i})}}{\Gamma} = \begin{bmatrix} -F^+(\epsilon) & \frac{1}{2}F^-(\epsilon) & \frac{1}{2}F^-(\epsilon) & 0 \\ \frac{1}{2}F^+(\epsilon) & -\frac{1}{2}\big[F^-(\epsilon) & 0 & \frac{1}{2}F^-(\epsilon{+}U) \\ & +F^+(\epsilon{+}U)\big] & & \\ \frac{1}{2}F^+(\epsilon) & 0 & -\frac{1}{2}\big[F^-(\epsilon) & \frac{1}{2}F^-(\epsilon{+}U) \\ & & +F^+(\epsilon{+}U)\big] & \\ 0 & \frac{1}{2}F^+(\epsilon{+}U) & \frac{1}{2}F^+(\epsilon{+}U) & -F^-(\epsilon{+}U) \end{bmatrix}_{z;\omega}, \tag{B.13}$$

$$\frac{\mathcal{W}_{\mathrm{I}}^{(\mathrm{i})}}{\Gamma} = \begin{bmatrix} 0 & f^{-}(\epsilon,z;0) & f^{-}(\epsilon,z;0) & 0 \\ -f^{+}(\epsilon,z;0) & 0 & 0 & f^{-}(\epsilon+U,z;0) \\ -f^{+}(\epsilon,z;0) & 0 & 0 & f^{-}(\epsilon+U,z;0) \\ 0 & -f^{+}(\epsilon+U,z;0) & -f^{+}(\epsilon+U,z;0) & 0 \end{bmatrix}, \tag{B.14}$$

$$\frac{\mathcal{W}_{\mathrm{II}}^{(\mathrm{i})}}{\Gamma} = \begin{bmatrix} F^{+}(\epsilon) & \frac{1}{2}F^{-}(\epsilon) & \frac{1}{2}F^{-}(\epsilon) & 0 \\ \frac{1}{2}F^{+}(\epsilon) & \frac{1}{2}\big[F^{-}(\epsilon) + F^{+}(\epsilon+U)\big] & 0 & \frac{1}{2}F^{-}(\epsilon+U) \\ \frac{1}{2}F^{+}(\epsilon) & 0 & \frac{1}{2}\big[F^{-}(\epsilon) + F^{+}(\epsilon+U)\big] & \frac{1}{2}F^{-}(\epsilon+U) \\ 0 & \frac{1}{2}F^{+}(\epsilon+U) & \frac{1}{2}F^{+}(\epsilon+U) & F^{-}(\epsilon+U) \end{bmatrix}_{z;\omega}. \tag{B.15}$$

Here, we suppressed for readability the arguments $(t, z; \omega)$ for the kernels in Eqs. (B.13) and (B.15), and the arguments (t, z) for the kernel in Eq. (B.14). The frequency-independent kernel $\mathcal{W}^{(\mathrm{i})}(t, z)$ equals $\mathcal{W}^{(\mathrm{i})}(t, z; 0)$. The subscript $(z; \omega)$ in the expressions for the kernels denotes that $F^{\pm}(x) \to F^{\pm}(x, z; \omega)$, and we introduce the additional abbreviations

$$f^{\pm}(x, z; \omega) = f^{\pm}(x + \omega - iz) + f^{\pm}(x - \omega + iz), \tag{B.16}$$

$$F^{\pm}(x, z; \omega) = f^{\pm}(x, z; \omega) \mp \psi(x, z; \omega), \tag{B.17}$$

$$\begin{aligned} \psi(x, z; \omega) = \frac{1}{2\pi i}\Big[&\tilde{\psi}(\epsilon + \omega - iz) + \tilde{\psi}(-\epsilon - \omega + iz) \\ &- \tilde{\psi}(\epsilon - \omega + iz) - \tilde{\psi}(-\epsilon + \omega - iz)\Big], \end{aligned} \tag{B.18}$$

where $f^{\pm}(x) = (1 + e^{\pm\beta x})^{-1}$ is the Fermi function of the reservoir and $\tilde{\psi}(x) = \psi\left(\frac{1}{2} + \frac{\beta x}{2\pi i}\right)$ with the Digamma function ψ. Note that for $\omega \to 0$ and $z \to 0^{+}$ we find $\psi(x, 0; 0) = 0$ and $F^{\pm}(x, 0; 0) = 2f^{\pm}(x)$. To also write the explicit expressions for the two remaining kernels, $\mathcal{W}_{\mathrm{I}}^{>,(\mathrm{i})}(t, z; \omega)$ and $\mathcal{W}_{\mathrm{I}}^{<,(\mathrm{i})}(t, z; \omega)$, we define the further abbreviation $g_x^{\pm\pm}(z; \omega) = f^{\pm}(x, z; 0) \pm F^{\pm}(x, z; \omega)$. The first superscript on the left-hand side refers to the superscripts of the two functions on the right-hand side, while the second superscript defines if the two functions are summed up or subtracted. Using this abbreviation and writing the

arguments $(z;\omega)$ also as a subscript, the kernels become

$$\frac{\mathcal{W}_{\mathrm{I}}^{>,(\mathrm{i})}}{\Gamma} = \begin{bmatrix} -g_\epsilon^{+-} & \frac{1}{2}g_\epsilon^{-+} & \frac{1}{2}g_\epsilon^{-+} & 0 \\ -\frac{1}{2}g_\epsilon^{++} & \frac{1}{2}\left[g_\epsilon^{--}-g_{\epsilon+U}^{+-}\right] & 0 & \frac{1}{2}g_{\epsilon+U}^{-+} \\ -\frac{1}{2}g_\epsilon^{++} & 0 & \frac{1}{2}\left[g_\epsilon^{--}-g_{\epsilon+U}^{+-}\right] & \frac{1}{2}g_{\epsilon+U}^{-+} \\ 0 & -\frac{1}{2}g_\epsilon^{++}+U & -\frac{1}{2}g_{\epsilon+U}^{++} & g_{\epsilon+U}^{--} \end{bmatrix}_{z;\omega}, \tag{B.19}$$

$$\frac{\mathcal{W}_{\mathrm{I}}^{<,(\mathrm{i})}}{\Gamma} = \begin{bmatrix} g_\epsilon^{+-} & \frac{1}{2}g_\epsilon^{-+} & \frac{1}{2}g_\epsilon^{-+} & 0 \\ -\frac{1}{2}g_\epsilon^{++} & -\frac{1}{2}\left[g_\epsilon^{--}-g_{\epsilon+U}^{+-}\right] & 0 & \frac{1}{2}g_{\epsilon+U}^{-+} \\ -\frac{1}{2}g_\epsilon^{++} & 0 & -\frac{1}{2}\left[g_\epsilon^{--}-g_{\epsilon+U}^{+-}\right] & \frac{1}{2}g_{\epsilon+U}^{-+} \\ 0 & -\frac{1}{2}g_{\epsilon+U}^{++} & -\frac{1}{2}g_{\epsilon+U}^{++} & -g_{\epsilon+U}^{--} \end{bmatrix}_{z;\omega}. \tag{B.20}$$

Note that we suppressed the arguments $(t, z;\omega)$ on the kernels for readability. Finally, we note that all contributions stemming from the Digamma functions, which we included here for completeness, are neglected in the noise calculations. The reason is that we denote these contributions to renormalization effects. Since tunneling beyond the first order studied here also leads to renormalization of system parameters [99], the contributions stemming from the Digamma functions should be excluded for a consistent sequential-tunneling derivation. In a calculation in second order in Γ (not part of this thesis), care must be taken for a proper inclusion of renormalization effects in the finite-frequency noise.

B.6 Expressions for high noise frequencies

In this appendix we derive a simple expression for the reduced propagator, $\overline{\Pi}(t, z)$, which is valid for high noise frequencies, $\omega \gg \Gamma$. This eventually leads to Eq. (5.18) of the main text. We begin with Eq. (B.11) for the reduced propagator, which has been derived in App. B.4. We remind that the dependence on the noise frequency ω has been absorbed in the z argument, which we set to $i\omega$ at the end of the calculation. The main observation is that the kernel $\mathcal{W}(t, z)$ in Eq. (B.11) has a magnitude of the scale Γ, while the factor $1/z$ in front turns into a factor $1/(i\omega)$. We conclude that the second term on the right-hand side of Eq. (B.11) scales with Γ/ω and is therefore strongly suppressed for high noise frequencies [173]. This suppression cannot be lifted by the derivatives included in the abbreviation e^{∂} in Eq. (B.11), which

only lead to minor corrections for the driving schemes considered in this work. Hence, in the high noise-frequency regime we write

$$\overline{\Pi}^{(\mathrm{HF})}(t,z) = \frac{\mathbf{1} - \boldsymbol{P}(t) \otimes \boldsymbol{e}^{\mathrm{T}}}{z}. \tag{B.21}$$

From this equation we extract the instantaneous part and the adiabatic response of the reduced propagator,

$$\overline{\Pi}^{(\mathrm{i,HF})}(t,z) = \frac{\mathbf{1} - \boldsymbol{P}^{(\mathrm{i})}(t) \otimes \boldsymbol{e}^{\mathrm{T}}}{z}, \tag{B.22a}$$

$$\overline{\Pi}^{(\mathrm{a,HF})}(t,z) = -\frac{\boldsymbol{P}^{(a)}(t) \otimes \boldsymbol{e}^{\mathrm{T}}}{z}. \tag{B.22b}$$

Interestingly, the reduced propagator in the high noise-frequency regime, i.e., Eq. (B.21), has an order-by-order expansion scheme in the tunnel-coupling strength, which means in the small parameter $\Gamma\beta$. The reason is that this expansion scheme is well defined for the occupation vector on the right-hand side, see also Sec. 5.4.3. We now use this observation to derive Eq. (5.18), which gives the auxiliary function, $\tilde{S}^{(l,\mathrm{HF})}(t;\omega)$, in the high-noise frequency regime and in lth order in the slow-driving expansion. The instantaneous part is included as the case $l = 0$ and the adiabatic response as $l = 1$. We first remind that for the occupation vector calculated in lth order in the slow-driving expansion, the leading-order term in the additional expansion in the tunnel-coupling strength is given by the $-l$th order [67]. From Eq. (B.21) we conclude that the same is true for leading contributions of the reduced propagator, when the latter is evaluated at high noise frequencies. Besides that, all kernels begin to contribute in first order in Γ, irrespective of their order in the slow-driving expansion. The leading contribution to the current in lth order in the slow-driving expansion is of order $-l + 1$ in the expansion in the tunnel-coupling strength. By only keeping the terms in lowest order in Γ for each order in the slow-driving expansion, we arrive at the general Eq. (5.18) for the auxiliary function calculated in the high-noise frequency regime.

Finally, we also give an explicit expression for the instantaneous fluctuation vector of Eq. (6.2) for a spin-split system. At high noise

frequencies, we find the expression

$$\frac{\boldsymbol{F}^{(\mathrm{i,HF})}(t;\omega)}{\Gamma} = \begin{pmatrix} f^{+}(\epsilon_{\uparrow};\omega) + f^{+}(\epsilon_{\downarrow};\omega) \\ f^{-}(\epsilon_{\uparrow};\omega) + f^{+}(\epsilon_{\downarrow}+U;\omega) \\ f^{-}(\epsilon_{\downarrow};\omega) + f^{+}(\epsilon_{\uparrow}+U;\omega) \\ f^{-}(\epsilon_{\uparrow}+U;\omega) + f^{-}(\epsilon_{\downarrow}+U;\omega) \end{pmatrix}^{\mathrm{T}} . \tag{B.23}$$

Bibliography

[1] R. A. Millikan, "The Isolation of an Ion, a Precision Measurement of its Charge, and the Correction of Stokes's Law," *Phys. Rev. (Series I)*, vol. 32, pp. 349–397, Apr 1911.

[2] R. A. Millikan, "On the Elementary Electrical Charge and the Avogadro Constant," *Phys. Rev.*, vol. 2, pp. 109–143, Aug 1913.

[3] T. A. Fulton and G. J. Dolan, "Observation of single-electron charging effects in small tunnel junctions," *Phys. Rev. Lett.*, vol. 59, pp. 109–112, Jul 1987.

[4] J. P. Pekola, O.-P. Saira, V. F. Maisi, A. Kemppinen, M. Möttönen, Y. A. Pashkin, and D. V. Averin, "Single-electron current sources: Toward a refined definition of the ampere," *Rev. Mod. Phys.*, vol. 85, pp. 1421–1472, Oct 2013.

[5] B. Kaestner and V. Kashcheyevs, "Non-adiabatic quantized charge pumping with tunable-barrier quantum dots: a review of current progress," *Rep. Prog. Phys.*, vol. 78, p. 103901, Sep 2015.

[6] C. Bäuerle, D. C. Glattli, T. Meunier, F. Portier, P. Roche, P. Roulleau, S. Takada, and X. Waintal, "Coherent control of single electrons: a review of current progress," *Rep. Prog. Phys.*, vol. 81, p. 056503, Apr 2018.

[7] "Single-electron control in solid state devices," in *Phys. Stat. Sol. B* (J. Splettstoesser and R. J. Haug, ed.), vol. 254, no. 3, March 2017.

[8] L. J. Geerligs, V. F. Anderegg, P. A. M. Holweg, J. E. Mooij, H. Pothier, D. Esteve, C. Urbina, and M. H. Devoret, "Frequency-locked turnstile device for single electrons," *Phys. Rev. Lett.*, vol. 64, pp. 2691–2694, May 1990.

[9] H. Pothier, P. Lafarge, C. Urbina, D. Esteve, and M. H. Devoret, "Single-Electron Pump Based on Charging Effects," *Eur. Phys. Lett.*, vol. 17, p. 249, Jan 1992.

[10] L. P. Kouwenhoven, A. T. Johnson, N. C. van der Vaart, C. J. P. M. Harmans, and C. T. Foxon, "Quantized current in a quantum-dot turnstile using oscillating tunnel barriers," *Phys. Rev. Lett.*, vol. 67, pp. 1626–1629, Sep 1991.

[11] T. Ando, A. B. Fowler, and F. Stern, "Electronic properties of two-dimensional systems," *Rev. Mod. Phys.*, vol. 54, pp. 437–672, Apr 1982.

[12] L. P. Kouwenhoven, D. G. Austing, and S. Tarucha, "Few-electron quantum dots," *Rep. Prog. Phys.*, vol. 64, p. 701, Jun 2001.

[13] S. M. Reimann and M. Manninen, "Electronic structure of quantum dots," *Rev. Mod. Phys.*, vol. 74, pp. 1283–1342, Nov 2002.

[14] F. A. Zwanenburg, A. S. Dzurak, A. Morello, M. Y. Simmons, L. C. L. Hollenberg, G. Klimeck, S. Rogge, S. N. Coppersmith, and M. A. Eriksson, "Silicon quantum electronics," *Rev. Mod. Phys.*, vol. 85, pp. 961–1019, Jul 2013.

[15] E. A. Laird, F. Kuemmeth, G. A. Steele, K. Grove-Rasmussen, J. Nygård, K. Flensberg, and L. P. Kouwenhoven, "Quantum transport in carbon nanotubes," *Rev. Mod. Phys.*, vol. 87, pp. 703–764, Jul 2015.

[16] D. V. Averin and K. K. Likharev, "Coulomb blockade of single-electron tunneling, and coherent oscillations in small tunnel junctions," *J. Low Temp. Phys.*, vol. 62, pp. 345–373, Feb 1986.

[17] K. Likharev, "Single-electron transistors: Electrostatic analogs of the DC SQUIDS," *IEEE Trans. Magn.*, vol. 23, pp. 1142–1145, Mar 1987.

[18] M. A. Kastner, "The single-electron transistor," *Rev. Mod. Phys.*, vol. 64, pp. 849–858, Jul 1992.

[19] N.-H. Kaneko, S. Nakamura, and Y. Okazaki, "A review of the quantum current standard," *Meas. Sci. Technol.*, vol. 27, p. 032001, Feb 2016.

[20] E. Gibney, "New definitions of scientific units are on the horizon," *Nat. News*, vol. 550, p. 312, Oct 2017.

[21] G. Fève, A. Mahé, J.-M. Berroir, T. Kontos, B. Plaçais, D. C. Glattli, A. Cavanna, B. Etienne, and Y. Jin, "An On-Demand Coherent Single-Electron Source," *Science*, vol. 316, pp. 1169–1172, May 2007.

[22] J. Gabelli, G. Fève, J.-M. Berroir, B. Plaçais, A. Cavanna, B. Etienne, Y. Jin, and D. C. Glattli, "Violation of Kirchhoff's Laws for a Coherent RC Circuit," *Science*, Jul 2006.

[23] E. Bocquillon, F. D. Parmentier, C. Grenier, J.-M. Berroir, P. Degiovanni, D. C. Glattli, B. Plaçais, A. Cavanna, Y. Jin, and G. Fève, "Electron Quantum Optics: Partitioning Electrons One by One," *Phys. Rev. Lett.*, vol. 108, p. 196803, May 2012.

[24] E. Bocquillon, V. Freulon, J.-M. Berroir, P. Degiovanni, B. Plaçais, A. Cavanna, Y. Jin, and G. Fève, "Coherence and Indistinguishability of Single Electrons Emitted by Independent Sources," *Science*, vol. 339, pp. 1054–1057, Mar 2013.

[25] V. Freulon, A. Marguerite, J.-M. Berroir, B. Plaçais, A. Cavanna, Y. Jin, and G. Fève, "Hong-Ou-Mandel experiment for temporal investigation of single-electron fractionalization," *Nat. Comm.*, vol. 6, p. 6854, Apr 2015.

[26] N. Ubbelohde, F. Hohls, V. Kashcheyevs, T. Wagner, L. Fricke, B. Kästner, K. Pierz, H. W. Schumacher, and R. J. Haug, "Partitioning of on-demand electron pairs," *Nat. Nanotechnol.*, vol. 10, p. 46, Dec 2014.

[27] A. Marguerite, C. Cabart, C. Wahl, B. Roussel, V. Freulon, D. Ferraro, C. Grenier, J.-M. Berroir, B. Plaçais, T. Jonckheere,

J. Rech, T. Martin, P. Degiovanni, A. Cavanna, Y. Jin, and G. Fève, "Decoherence and relaxation of a single electron in a one-dimensional conductor," *Phys. Rev. B*, vol. 94, p. 115311, Sep 2016.

[28] B. Roussel, C. Cabart, G. Fève, E. Thibierge, and P. Degiovanni, "Electron quantum optics as quantum signal processing," *Phys. Stat. Sol. B*, vol. 254, p. 1600621, Mar 2017.

[29] M. D. Blumenthal, B. Kaestner, L. Li, S. Giblin, T. J. B. M. Janssen, M. Pepper, D. Anderson, G. Jones, and D. A. Ritchie, "Gigahertz quantized charge pumping," *Nat. Phys.*, vol. 3, pp. 343–347, May 2007.

[30] B. Kaestner, V. Kashcheyevs, S. Amakawa, M. D. Blumenthal, L. Li, T. J. B. M. Janssen, G. Hein, K. Pierz, T. Weimann, U. Siegner, and H. W. Schumacher, "Single-parameter nonadiabatic quantized charge pumping," *Phys. Rev. B*, vol. 77, p. 153301, Apr 2008.

[31] S. P. Giblin, S. J. Wright, J. D. Fletcher, M. Kataoka, M. Pepper, T. J. B. M. Janssen, D. A. Ritchie, C. A. Nicoll, D. Anderson, and G. A. C. Jones, "An accurate high-speed single-electron quantum dot pump," *New J. Phys.*, vol. 12, no. 7, p. 073013, 2010.

[32] S. Giblin, M. Kataoka, J. Fletcher, P. See, T. Janssen, J. Griffiths, G. Jones, I. Farrer, and D. Ritchie, "Towards a quantum representation of the ampere using single electron pumps," *Nat. Comm.*, vol. 3, p. 930, Mar 2012.

[33] J. D. Fletcher, P. See, H. Howe, M. Pepper, S. P. Giblin, J. P. Griffiths, G. A. C. Jones, I. Farrer, D. A. Ritchie, T. J. B. M. Janssen, and M. Kataoka, "Clock-controlled emission of single-electron wave packets in a solid-state circuit," *Phys. Rev. Lett.*, vol. 111, p. 216807, Nov 2013.

[34] J. Waldie, P. See, V. Kashcheyevs, J. P. Griffiths, I. Farrer, G. A. C. Jones, D. A. Ritchie, T. J. B. M. Janssen, and M. Kataoka, "Measurement and control of electron wave packets

from a single-electron source," *Phys. Rev. B*, vol. 92, p. 125305, Sep 2015.

[35] G. Yamahata, S. P. Giblin, M. Kataoka, T. Karasawa, and A. Fujiwara, "Gigahertz single-electron pumping in silicon with an accuracy better than 9.2 parts in 10^7," *Appl. Phys. Lett.*, vol. 109, pp. 013101–5, Jul 2016.

[36] J. P. Pekola, J. J. Vartiainen, M. Möttönen, O.-P. Saira, M. Meschke, and D. V. Averin, "Hybrid single-electron transistor as a source of quantized electric current," *Nat. Phys.*, vol. 4, p. 120, 2008.

[37] A. Kemppinen, M. Meschke, M. Möttönen, D. V. Averin, and J. P. Pekola, "Quantized current of a hybrid single-electron transistor with superconducting leads and a normal-metal island," *Eur. Phys. J. Spec. Top.*, vol. 172, no. 1, pp. 311–321, 2009.

[38] V. F. Maisi, Y. A. Pashkin, S. Kafanov, J.-S. Tsai, and J. P. Pekola, "Parallel pumping of electrons," *New J. Phys.*, vol. 11, p. 113057, Nov 2009.

[39] D. V. Averin and J. P. Pekola, "Nonadiabatic charge pumping in a hybrid single-electron transistor," *Phys. Rev. Lett.*, vol. 101, p. 066801, Aug 2008.

[40] T. Aref, V. F. Maisi, M. V. Gustafsson, P. Delsing, and J. P. Pekola, "Andreev tunneling in charge pumping with SINIS turnstiles," *Eur. Phys. Lett.*, vol. 96, no. 3, p. 37008, 2011.

[41] O.-P. Saira, A. Kemppinen, V. F. Maisi, and J. P. Pekola, "Vanishing quasiparticle density in a hybrid Al/Cu/Al single-electron transistor," *Phys. Rev. B*, vol. 85, p. 012504, 2012.

[42] A. Di Marco, V. F. Maisi, F. W. J. Hekking, and J. P. Pekola, "Effect of photon-assisted Andreev reflection in the accuracy of a SINIS turnstile," *Phys. Rev. B*, vol. 92, p. 094514, Sep 2015.

[43] J. Dubois, T. Jullien, F. Portier, P. Roche, A. Cavanna, Y. Jin, W. Wegscheider, P. Roulleau, and D. C. Glattli, "Minimal-excitation states for electron quantum optics using levitons," *Nature*, vol. 502, p. 659, Oct 2013.

[44] R. P. G. McNeil, M. Kataoka, C. J. B. Ford, C. H. W. Barnes, D. Anderson, G. A. C. Jones, I. Farrer, and D. A. Ritchie, "On-demand single-electron transfer between distant quantum dots," *Nature*, vol. 477, pp. 439–442, Sep 2011.

[45] S. Hermelin, S. Takada, M. Yamamoto, S. Tarucha, A. D. Wieck, L. Saminadayar, C. Bauerle, and T. Meunier, "Electrons surfing on a sound wave as a platform for quantum optics with flying electrons," *Nature*, vol. 477, pp. 435–438, Sep 2011.

[46] D. M. T. van Zanten, D. M. Basko, I. M. Khaymovich, J. P. Pekola, H. Courtois, and C. B. Winkelmann, "Single Quantum Level Electron Turnstile," *Phys. Rev. Lett.*, vol. 116, p. 166801, Apr 2016.

[47] B. Roche, R.-P. Riwar, B. Voisin, E. Dupont-Ferrier, R. Wacquez, M. Vinet, M. Sanquer, J. Splettstoesser, and X. Jehl, "A two-atom electron pump," *Nat. Comm.*, vol. 4, p. 1581, Mar 2013.

[48] R. Landauer, "Condensed-matter physics: The noise is the signal," *Nature*, vol. 392, p. 658, Apr 1998.

[49] Y. Blanter and M. Büttiker, "Shot noise in mesoscopic conductors," *Phys. Rep.*, vol. 336, no. 1-2, pp. 1–166, 2000.

[50] A. A. Clerk, M. H. Devoret, S. M. Girvin, F. Marquardt, and R. J. Schoelkopf, "Introduction to quantum noise, measurement, and amplification," *Rev. Mod. Phys.*, vol. 82, pp. 1155–1208, Apr 2010.

[51] M. Moskalets and M. Büttiker, "Time-resolved noise of adiabatic quantum pumps," *Phys. Rev. B*, vol. 75, p. 035315, Jan 2007.

[52] M. Moskalets and M. Büttiker, "Heat production and current noise for single- and double-cavity quantum capacitors," *Phys. Rev. B*, vol. 80, p. 081302, Aug 2009.

[53] M. Moskalets, "Noise of a single-electron emitter," *Phys. Rev. B*, vol. 88, p. 035433, Jul 2013.

[54] R.-P. Riwar, J. Splettstoesser, and J. König, "Zero-frequency noise in adiabatically driven interacting quantum systems," *Phys. Rev. B*, vol. 87, p. 195407, May 2013.

[55] N. Dittmann and J. Splettstoesser, "Finite-frequency noise of interacting single-electron emitters: Spectroscopy with higher noise harmonics," *Phys. Rev. B*, vol. 98, p. 115414, Sep 2018.

[56] A. Mahé, F. D. Parmentier, E. Bocquillon, J.-M. Berroir, D. C. Glattli, T. Kontos, B. Plaçais, G. Fève, A. Cavanna, and Y. Jin, "Current correlations of an on-demand single-electron emitter," *Phys. Rev. B*, vol. 82, p. 201309, Nov 2010.

[57] F. D. Parmentier, E. Bocquillon, J.-M. Berroir, D. C. Glattli, B. Plaçais, G. Fève, M. Albert, C. Flindt, and M. Büttiker, "Current noise spectrum of a single-particle emitter: Theory and experiment," *Phys. Rev. B*, vol. 85, p. 165438, Apr 2012.

[58] M. Moskalets and M. Büttiker, "Floquet scattering theory of quantum pumps," *Phys. Rev. B*, vol. 66, p. 205320, Nov 2002.

[59] M. Moskalets and M. Büttiker, "Adiabatic quantum pump in the presence of external ac voltages," *Phys. Rev. B*, vol. 69, p. 205316, May 2004.

[60] M. V. Moskalets, *Scattering Matrix Approach to Non-Stationary Quantum Transport*. World Scientific Publishing Company, Sep 2011.

[61] Y. Meir and N. S. Wingreen, "Landauer formula for the current through an interacting electron region," *Phys. Rev. Lett.*, vol. 68, pp. 2512–2515, Apr 1992.

[62] N. S. Wingreen, A.-P. Jauho, and Y. Meir, "Time-dependent transport through a mesoscopic structure," *Phys. Rev. B*, vol. 48, pp. 8487–8490, Sep 1993.

[63] A.-P. Jauho, N. S. Wingreen, and Y. Meir, "Time-dependent transport in interacting and noninteracting resonant-tunneling systems," *Phys. Rev. B*, vol. 50, pp. 5528–5544, Aug 1994.

[64] H. Schoeller and G. Schön, "Mesoscopic quantum transport: Resonant tunneling in the presence of a strong coulomb interaction," *Phys. Rev. B*, vol. 50, pp. 18436–18452, Dec 1994.

[65] J. König, H. Schoeller, and G. Schön, "Zero-bias anomalies and boson-assisted tunneling through quantum dots," *Phys. Rev. Lett.*, vol. 76, pp. 1715–1718, Mar 1996.

[66] J. König, J. Schmid, H. Schoeller, and G. Schön, "Resonant tunneling through ultrasmall quantum dots: Zero-bias anomalies, magnetic-field dependence, and boson-assisted transport," *Phys. Rev. B*, vol. 54, pp. 16820–16837, Dec 1996.

[67] J. Splettstoesser, M. Governale, J. König, and R. Fazio, "Adiabatic pumping through a quantum dot with coulomb interactions: A perturbation expansion in the tunnel coupling," *Phys. Rev. B*, vol. 74, p. 085305, Aug 2006.

[68] H. Schoeller, "Transport theory of interacting quantum dots," in *Mesoscopic Electron Transport* (L. L. Sohn, L. P. Kouwenhoven, and G. Schön, eds.), p. 291, Kluwer, 1997. Habilitation thesis, Karlsruhe.

[69] H. Schoeller, "Dynamics of open quantum systems," in *Lecture Notes of the 45th IFF Spring School 2014* (S. Blügel, N. Helbig, V. Meden, and D. Wortmann, eds.), p. B5, Forschungszentrum Jülich, 2014.

[70] A. J. Daley, C. Kollath, U. Schollwöck, and G. Vidal, "Time-dependent density-matrix renormalization-group using adaptive effective Hilbert spaces," *J. Stat. Mech.*, vol. 2004, p. P04005, Apr 2004.

[71] S. R. White and A. E. Feiguin, "Real-Time Evolution Using the Density Matrix Renormalization Group," *Phys. Rev. Lett.*, vol. 93, p. 076401, Aug 2004.

[72] P. Schmitteckert, "Nonequilibrium electron transport using the density matrix renormalization group method," *Phys. Rev. B*, vol. 70, p. 121302, Sep 2004.

[73] F. Heidrich-Meisner, A. E. Feiguin, and E. Dagotto, "Real-time simulations of nonequilibrium transport in the single-impurity Anderson model," *Phys. Rev. B*, vol. 79, p. 235336, Jun 2009.

[74] E. Runge and E. K. U. Gross, "Density-functional theory for time-dependent systems," *Phys. Rev. Lett.*, vol. 52, pp. 997–1000, Mar 1984.

[75] P. Hohenberg and W. Kohn, "Inhomogeneous electron gas," *Phys. Rev.*, vol. 136, pp. B864–B871, Nov 1964.

[76] W. Kohn and L. J. Sham, "Self-Consistent Equations Including Exchange and Correlation Effects," *Phys. Rev.*, vol. 140, pp. A1133–A1138, Nov 1965.

[77] R. O. Jones, "Density functional theory: Its origins, rise to prominence, and future," *Rev. Mod. Phys.*, vol. 87, pp. 897–923, Aug 2015.

[78] M. A. L. Marques, N. T. Maitra, F. M. S. Nogueira, E. K. U. Gross, A. Rubio, "Fundamentals of time-dependent density functional theory," in *Lecture Notes in Physics*, vol. 827, Springer Berlin Heidelberg, 2012.

[79] Carsten A. Ullrich, *Time-Dependent Density-Functional Theory: Concepts and Applications.* Oxford University Press, 2011.

[80] N. Dittmann, J. Splettstoesser, and N. Helbig, "Nonadiabatic Dynamics in Single-Electron Tunneling Devices with Time-Dependent Density-Functional Theory," *Phys. Rev. Lett.*, vol. 120, p. 157701, Apr 2018.

[81] R. van Leeuwen, "Mapping from Densities to Potentials in Time-Dependent Density-Functional Theory," *Phys. Rev. Lett.*, vol. 82, pp. 3863–3866, May 1999.

[82] N. T. Maitra, "Perspective: Fundamental aspects of time-dependent density functional theory," *J. Chem. Phys.*, vol. 144, p. 220901, Jun 2016.

[83] C. A. Ullrich and Z.-h. Yang, "A Brief Compendium of Time-Dependent Density Functional Theory," *Braz. J. Phys.*, vol. 44, pp. 154–188, Feb 2014.

[84] N. Dittmann, J. Splettstoesser, and F. Giazotto, "Clocked single-spin source based on a spin-split superconductor," *New J. Phys.*, vol. 18, p. 083019, Aug 2016.

[85] N. Dittmann, J. Splettstoesser, and N. Helbig, "Equilibrium finite-frequency noise of an interacting mesoscopic capacitor studied in time-dependent density-functional theory," *J. Phys. Conf. Ser.*, vol. 969, p. 012145, Mar 2018.

[86] S. Kurth, G. Stefanucci, E. Khosravi, C. Verdozzi, and E. K. U. Gross, "Dynamical Coulomb Blockade and the Derivative Discontinuity of Time-Dependent Density Functional Theory," *Phys. Rev. Lett.*, vol. 104, p. 236801, Jun 2010.

[87] A.-M. Uimonen, E. Khosravi, A. Stan, G. Stefanucci, S. Kurth, R. van Leeuwen, and E. K. U. Gross, "Comparative study of many-body perturbation theory and time-dependent density functional theory in the out-of-equilibrium Anderson model," *Phys. Rev. B*, vol. 84, p. 115103, Sep 2011.

[88] G. Stefanucci and S. Kurth, "Towards a Description of the Kondo Effect Using Time-Dependent Density-Functional Theory," *Phys. Rev. Lett.*, vol. 107, p. 216401, Nov 2011.

[89] E. Perfetto and G. Stefanucci, "Missing derivative discontinuity of the exchange-correlation energy for attractive interactions: The charge Kondo effect," *Phys. Rev. B*, vol. 86, p. 081409, Aug 2012.

[90] G. Stefanucci and S. Kurth, "Steady-State Density Functional Theory for Finite Bias Conductances," *Nano Lett.*, vol. 15, pp. 8020–8025, Nov 2015.

[91] S. Kurth and G. Stefanucci, "Nonequilibrium Anderson model made simple with density functional theory," *Phys. Rev. B*, vol. 94, p. 241103, Dec 2016.

[92] G. Stefanucci and S. Kurth, "AC transport in correlated quantum dots: From Kondo to Coulomb blockade regime," *Phys. Rev. B*, vol. 97, p. 245415, Jun 2018.

[93] M. Büttiker, A. Prêtre, and H. Thomas, "Dynamic conductance and the scattering matrix of small conductors," *Phys. Rev. Lett.*, vol. 70, pp. 4114–4117, Jun 1993.

[94] M. Büttiker, H. Thomas, and A. Prêtre, "Mesoscopic capacitors," *Phys. Lett. A*, vol. 180, pp. 364–369, Sep 1993.

[95] A. Prêtre, H. Thomas, and M. Büttiker, "Dynamic admittance of mesoscopic conductors: Discrete-potential model," *Phys. Rev. B*, vol. 54, pp. 8130–8143, Sep 1996.

[96] S. E. Nigg, R. López, and M. Büttiker, "Mesoscopic Charge Relaxation," *Phys. Rev. Lett.*, vol. 97, p. 206804, Nov 2006.

[97] D. V. Averin, A. N. Korotkov, and K. K. Likharev, "Theory of single-electron charging of quantum wells and dots," *Phys. Rev. B*, vol. 44, pp. 6199–6211, Sep 1991.

[98] M. Moskalets, P. Samuelsson, and M. Büttiker, "Quantized dynamics of a coherent capacitor," *Phys. Rev. Lett.*, vol. 100, p. 086601, Feb 2008.

[99] J. Splettstoesser, M. Governale, J. König, and M. Büttiker, "Charge and spin dynamics in interacting quantum dots," *Phys. Rev. B*, vol. 81, p. 165318, Apr 2010.

[100] D. Litinski, P. W. Brouwer, and M. Filippone, "Interacting mesoscopic capacitor out of equilibrium," *Phys. Rev. B*, vol. 96, p. 085429, Aug 2017.

[101] C. W. J. Beenakker, "Theory of Coulomb-blockade oscillations in the conductance of a quantum dot," *Phys. Rev. B*, vol. 44, pp. 1646–1656, Jul 1991.

[102] M. Switkes, C. M. Marcus, K. Campman, and A. C. Gossard, "An Adiabatic Quantum Electron Pump," *Science*, vol. 283, pp. 1905–1908, Mar 1999.

[103] Jürgen König, *Quantum Fluctuations in the Single-Electron Transistor*. Shaker Verlag, 1999. PhD thesis.

[104] G. Schaller, "Open quantum systems far from equilibrium," in *Lecture Notes in Physics*, vol. 881, Springer, 2014.

[105] F. Cavaliere, M. Governale, and J. König, "Nonadiabatic pumping through interacting quantum dots," *Phys. Rev. Lett.*, vol. 103, p. 136801, Sep 2009.

[106] M. Koentopp, C. Chang, K. Burke, and R. Car, "Density functional calculations of nanoscale conductance," *J. Phys. Cond. Mat.*, vol. 20, p. 083203, Feb 2008.

[107] M. Ruggenthaler and R. van Leeuwen, "Global fixed-point proof of time-dependent density-functional theory," *Eur. Phys. Lett.*, vol. 95, p. 13001, Jun 2011.

[108] M. Ruggenthaler, M. Penz, and R. van Leeuwen, "Existence, uniqueness, and construction of the density-potential mapping in time-dependent density-functional theory," *J. Phys. Cond. Mat.*, vol. 27, no. 20, p. 203202, 2015.

[109] J. F. Dobson, "Harmonic-potential theorem: Implications for approximate many-body theories," *Phys. Rev. Lett.*, vol. 73, pp. 2244–2247, Oct 1994.

[110] G. Vignale, "Center of mass and relative motion in time dependent density functional theory," *Phys. Rev. Lett.*, vol. 74, pp. 3233–3236, Apr 1995.

[111] N. T. Maitra, K. Burke, and C. Woodward, "Memory in time-dependent density functional theory," *Phys. Rev. Lett.*, vol. 89, p. 023002, Jun 2002.

[112] J. I. Fuks, K. Luo, E. D. Sandoval, and N. T. Maitra, "Time-resolved spectroscopy in time-dependent density functional theory: An exact condition," *Phys. Rev. Lett.*, vol. 114, p. 183002, May 2015.

[113] N. T. Maitra and K. Burke, "Demonstration of initial-state dependence in time-dependent density-functional theory," *Phys. Rev. A*, vol. 63, p. 042501, Mar 2001.

[114] P. Elliott and N. T. Maitra, "Propagation of initially excited states in time-dependent density-functional theory," *Phys. Rev. A*, vol. 85, p. 052510, May 2012.

[115] M. Thiele, E. K. U. Gross, and S. Kümmel, "Adiabatic approximation in nonperturbative time-dependent density-functional theory," *Phys. Rev. Lett.*, vol. 100, p. 153004, Apr 2008.

[116] K. Luo, J. I. Fuks, E. D. Sandoval, P. Elliott, and N. T. Maitra, "Kinetic and interaction components of the exact time-dependent correlation potential," *J. Chem. Phys.*, vol. 140, p. 18A515, May 2014.

[117] K. Capelle and V. L. Campo, "Density functionals and model Hamiltonians: Pillars of many-particle physics," *Phys. Rep.*, vol. 528, pp. 91–159, Jul 2013.

[118] N. A. Lima, M. F. Silva, L. N. Oliveira, and K. Capelle, "Density Functionals Not Based on the Electron Gas: Local-Density Approximation for a Luttinger Liquid," *Phys. Rev. Lett.*, vol. 90, p. 146402, Apr 2003.

[119] C. Verdozzi, "Time-Dependent Density-Functional Theory and Strongly Correlated Systems: Insight from Numerical Studies," *Phys. Rev. Lett.*, vol. 101, p. 166401, Oct 2008.

[120] J. P. Perdew, R. G. Parr, M. Levy, and J. L. Balduz, "Density-functional theory for fractional particle number: Derivative discontinuities of the energy," *Phys. Rev. Lett.*, vol. 49, pp. 1691–1694, Dec 1982.

[121] J. P. Perdew and M. Levy, "Physical Content of the Exact Kohn-Sham Orbital Energies: Band Gaps and Derivative Discontinuities," *Phys. Rev. Lett.*, vol. 51, pp. 1884–1887, Nov 1983.

[122] M. Mundt and S. Kümmel, "Derivative discontinuities in time-dependent density-functional theory," *Phys. Rev. Lett.*, vol. 95, p. 203004, Nov 2005.

[123] M. Lein and S. Kümmel, "Exact time-dependent exchange-correlation potentials for strong-field electron dynamics," *Phys. Rev. Lett.*, vol. 94, p. 143003, Apr 2005.

[124] D. Vieira, K. Capelle, and C. A. Ullrich, "Physical signatures of discontinuities of the time-dependent exchange–correlation potential," *Phys. Chem. Chem. Phys.*, vol. 11, pp. 4647–4654, May 2009.

[125] M. Hellgren and E. K. U. Gross, "Discontinuities of the exchange-correlation kernel and charge-transfer excitations in time-dependent density-functional theory," *Phys. Rev. A*, vol. 85, p. 022514, Feb 2012.

[126] C. Toher, A. Filippetti, S. Sanvito, and K. Burke, "Self-interaction errors in density-functional calculations of electronic transport," *Phys. Rev. Lett.*, vol. 95, p. 146402, Sep 2005.

[127] F. Evers and P. Schmitteckert, "Broadening of the derivative discontinuity in density functional theory," *Phys. Chem. Chem. Phys.*, vol. 13, pp. 14417–14420, 2011.

[128] M. J. P. Hodgson, J. D. Ramsden, and R. W. Godby, "Origin of static and dynamic steps in exact Kohn-Sham potentials," *Phys. Rev. B*, vol. 93, p. 155146, Apr 2016.

[129] P. Elliott, J. I. Fuks, A. Rubio, and N. T. Maitra, "Universal dynamical steps in the exact time-dependent exchange-correlation potential," *Phys. Rev. Lett.*, vol. 109, p. 266404, Dec 2012.

[130] J. D. Ramsden and R. W. Godby, "Exact density-functional potentials for time-dependent quasiparticles," *Phys. Rev. Lett.*, vol. 109, p. 036402, Jul 2012.

[131] G. Xianlong, A.-H. Chen, I. V. Tokatly, and S. Kurth, "Lattice density functional theory at finite temperature with strongly density-dependent exchange-correlation potentials," *Phys. Rev. B*, vol. 86, p. 235139, Dec 2012.

[132] S. Kurth and G. Stefanucci, "Dynamical Correction to Linear Kohn-Sham Conductances from Static Density Functional Theory," *Phys. Rev. Lett.*, vol. 111, p. 030601, Jul 2013.

[133] Z.-F. Liu and K. Burke, "Density functional description of Coulomb blockade: Adiabatic versus dynamic exchange correlation," *Phys. Rev. B*, vol. 91, p. 245158, Jun 2015.

[134] S. Kurth and G. Stefanucci, "Time-dependent i-DFT exchange-correlation potentials with memory: applications to the out-of-equilibrium Anderson model," *Eur. Phys. J. B*, vol. 91, p. 118, Jun 2018.

[135] S. A. Wolf, D. D. Awschalom, R. A. Buhrman, J. M. Daughton, S. von Molnár, M. L. Roukes, A. Y. Chtchelkanova, and D. M. Treger, "Spintronics: a spin-based electronics vision for the future," *Science*, vol. 294, pp. 1488–1495, Nov 2001.

[136] I. Žutić, J. Fabian, and S. Das Sarma, "Spintronics: Fundamentals and applications," *Rev. Mod. Phys.*, vol. 76, pp. 323–410, Apr 2004.

[137] B. Bertrand, S. Hermelin, S. Takada, M. Yamamoto, S. Tarucha, A. Ludwig, A. D. Wieck, C. Bäuerle, and T. Meunier, "Fast spin information transfer between distant quantum dots using individual electrons," *Nat. Nanotechnol.*, vol. 11, p. 672, May 2016.

[138] A. Brataas, Y. Tserkovnyak, G. E. W. Bauer, and B. I. Halperin, "Spin battery operated by ferromagnetic resonance," *Phys. Rev. B*, vol. 66, p. 060404, Aug 2002.

[139] F. Mahfouzi, B. K. Nikolić, S.-H. Chen, and C.-R. Chang, "Microwave-driven ferromagnet-topological-insulator heterostructures: The prospect for giant spin battery effect and quantized charge pump devices," *Phys. Rev. B*, vol. 82, p. 195440, Nov 2010.

[140] M. V. Costache and S. O. Valenzuela, "Experimental Spin Ratchet," *Science*, vol. 330, pp. 1645–1648, Dec 2010.

[141] J. Linder and J. W. A. Robinson, "Superconducting spintronics," *Nat. Phys.*, vol. 11, p. 307, Apr 2015.

[142] C. H. L. Quay, M. Weideneder, Y. Chiffaudel, C. Strunk, and M. Aprili, "Quasiparticle spin resonance and coherence in superconducting aluminium," *Nat. Comm.*, vol. 6, p. 8660, Oct 2015.

[143] R. Meservey, P. M. Tedrow, and J. S. Moodera, "Electron spin polarized tunneling study of ferromagnetic thin films," *J. Magn. Magn. Mat.*, vol. 35, pp. 1–6, Mar 1983.

[144] H. Yang, S.-H. Yang, S. Takahashi, S. Maekawa, and S. S. P. Parkin, "Extremely long quasiparticle spin lifetimes in superconducting aluminium using MgO tunnel spin injectors," *Nat. Mat.*, vol. 9, p. 586, Jun 2010.

[145] C. H. L. Quay, D. Chevallier, C. Bena, and M. Aprili, "Spin imbalance and spin-charge separation in a mesoscopic superconductor," *Nat. Phys.*, vol. 9, p. 84, Jan 2013.

[146] M. Eschrig, "Spin-polarized supercurrents for spintronics: a review of current progress," *Rep. Prog. Phys.*, vol. 78, p. 104501, Sep 2015.

[147] M. Eschrig, "Spin-polarized supercurrents for spintronics," *Phys. Today*, vol. 64, p. 43, Dec 2010.

[148] J. S. Moodera, T. S. Santos, and T. Nagahama, "The phenomena of spin-filter tunnelling," *J. Phys. Cond. Mat.*, vol. 19, p. 165202, Apr 2007.

[149] B. Li, G.-X. Miao, and J. S. Moodera, "Observation of tunnel magnetoresistance in a superconducting junction with zeeman-split energy bands," *Phys. Rev. B*, vol. 88, p. 161105, Oct 2013.

[150] V. F. Maisi, S. V. Lotkhov, A. Kemppinen, A. Heimes, J. T. Muhonen, and J. P. Pekola, "Excitation of single quasiparticles in a small superconducting al island connected to normal-metal leads by tunnel junctions," *Phys. Rev. Lett.*, vol. 111, p. 147001, Oct 2013.

[151] F. Giazotto and F. Taddei, "Superconductors as spin sources for spintronics," *Phys. Rev. B*, vol. 77, p. 132501, Apr 2008.

[152] X. Hao, J. S. Moodera, and R. Meservey, "Spin-filter effect of ferromagnetic europium sulfide tunnel barriers," *Phys. Rev. B*, vol. 42, pp. 8235–8243, Nov 1990.

[153] R. Meservey and P. M. Tedrow, "Spin-polarized electron tunneling," *Phys. Rep.*, vol. 238, pp. 173–243, Mar 1994.

[154] F. Giazotto, T. T. Heikkilä, and F. S. Bergeret, "Very Large Thermophase in Ferromagnetic Josephson Junctions," *Phys. Rev. Lett.*, vol. 114, p. 067001, Feb 2015.

[155] T. Tokuyasu, J. A. Sauls, and D. Rainer, "Proximity effect of a ferromagnetic insulator in contact with a superconductor," *Phys. Rev. B*, vol. 38, pp. 8823–8833, Nov 1988.

[156] R. C. Dynes, J. P. Garno, B. Hertel, and T. P. Orlando, "Tunneling study of superconductivity near the metal-insulator transition," *Phys. Rev. Lett.*, vol. 53, p. 2437, 1984.

[157] J. P. Pekola, T. T. Heikkilä, A. M. Savin, J. T. Flyktman, F. Giazotto, and F. W. J. Hekking, "Limitations in cooling electrons using normal-metal-superconductor tunnel junctions," *Phys. Rev. Lett.*, vol. 92, p. 056804, 2004.

[158] T. S. Santos, J. S. Moodera, K. V. Raman, E. Negusse, J. Holroyd, J. Dvorak, M. Liberati, Y. U. Idzerda, and E. Arenholz, "Determining exchange splitting in a magnetic semiconductor by spin-filter tunneling," *Phys. Rev. Lett.*, vol. 101, p. 147201, Sep 2008.

[159] B. Li, N. Roschewsky, B. A. Assaf, M. Eich, M. Epstein-Martin, D. Heiman, M. Münzenberg, and J. S. Moodera, "Superconducting spin switch with infinite magnetoresistance induced by an internal exchange field," *Phys. Rev. Lett.*, vol. 110, p. 097001, Feb 2013.

[160] Y. M. Xiong, S. Stadler, P. W. Adams, and G. Catelani, "Spin-resolved tunneling studies of the exchange field in EuS/Al bilayers," *Phys. Rev. Lett.*, vol. 106, p. 247001, Jun 2011.

[161] T. J. Liu, J. C. Prestigiacomo, and P. W. Adams, "Electrostatic tuning of the proximity-induced exchange field in EuS/Al bilayers," *Phys. Rev. Lett.*, vol. 111, p. 027207, Jul 2013.

[162] K. Senapati, M. G. Blamire, and Z. H. Barber *Nat. Mat.*, vol. 10, p. 849, 2011.

[163] A. Pal, Z. H. Barber, J. W. A. Robinson, and M. G. Blamire *Nat. Comm.*, vol. 5, p. 3340, 2014.

[164] D. V. Averin and Y. V. Nazarov, "Single-electron charging of a superconducting island," *Phys. Rev. Lett.*, vol. 69, pp. 1993–1996, Sep 1992.

[165] P. Lafarge, P. Joyez, D. Esteve, C. Urbina, and M. H. Devoret, "Measurement of the even-odd free-energy difference of an isolated superconductor," *Phys. Rev. Lett.*, vol. 70, pp. 994–997, Feb 1993.

[166] A. Heimes, V. F. Maisi, D. S. Golubev, M. Marthaler, G. Schön, and J. P. Pekola, "Tunneling and relaxation of single quasiparticles in a normal-superconductor-normal single-electron transistor," *Phys. Rev. B*, vol. 89, p. 014508, Jan 2014.

[167] F. Giazotto, F. Taddei, P. D'Amico, R. Fazio, and F. Beltram, "Nonequilibrium spin-dependent phenomena in mesoscopic superconductor-normal metal tunnel structures," *Phys. Rev. B*, vol. 76, p. 184518, 2007.

[168] N. Ubbelohde, C. Fricke, C. Flindt, F. Hohls, and R. J. Haug, "Measurement of finite-frequency current statistics in a single-electron transistor," *Nat. Comm.*, vol. 3, p. 612, Jan 2012.

[169] L. Saminadayar, D. C. Glattli, Y. Jin, and B. Etienne, "Observation of the $e/3$ Fractionally Charged Laughlin Quasiparticle," *Phys. Rev. Lett.*, vol. 79, pp. 2526–2529, Sep 1997.

[170] R. De-Picciotto, M. Reznikov, M. Heiblum, V. Umansky, G. Bunin, and D. Mahalu, "Direct observation of a fractional charge," *Nature*, vol. 389, p. 162, Sep 1997.

[171] E. Onac, F. Balestro, B. Trauzettel, C. F. J. Lodewijk, and L. P. Kouwenhoven, "Shot-noise detection in a carbon nanotube quantum dot," *Phys. Rev. Lett.*, vol. 96, p. 026803, Jan 2006.

[172] J. Basset, A. Y. Kasumov, C. P. Moca, G. Zaránd, P. Simon, H. Bouchiat, and R. Deblock, "Measurement of Quantum Noise in a Carbon Nanotube Quantum Dot in the Kondo Regime," *Phys. Rev. Lett.*, vol. 108, p. 046802, Jan 2012.

[173] A. Käck, G. Wendin, and G. Johansson, "Full-frequency voltage noise spectral density of a single-electron transistor," *Phys. Rev. B*, vol. 67, p. 035301, Jan 2003.

[174] H.-A. Engel and D. Loss, "Asymmetric Quantum Shot Noise in Quantum Dots," *Phys. Rev. Lett.*, vol. 93, p. 136602, Sep 2004.

[175] M. Braun, J. König, and J. Martinek, "Frequency-dependent current noise through quantum-dot spin valves," *Phys. Rev. B*, vol. 74, p. 075328, Aug 2006.

[176] E. A. Rothstein, O. Entin-Wohlman, and A. Aharony, "Noise spectra of a biased quantum dot," *Phys. Rev. B*, vol. 79, p. 075307, Feb 2009.

[177] N. Gabdank, E. A. Rothstein, O. Entin-Wohlman, and A. Aharony, "Noise spectra of an interacting quantum dot," *Phys. Rev. B*, vol. 84, p. 235435, Dec 2011.

[178] D. Marcos, C. Emary, T. Brandes, and R. Aguado, "Non-markovian effects in the quantum noise of interacting nanostructures," *Phys. Rev. B*, vol. 83, p. 125426, Mar 2011.

[179] C. P. Orth, D. F. Urban, and A. Komnik, "Finite-frequency noise properties of the nonequilibrium Anderson impurity model," *Phys. Rev. B*, vol. 86, p. 125324, Sep 2012.

[180] S. Y. Müller, M. Pletyukhov, D. Schuricht, and S. Andergassen, "Magnetic field effects on the finite-frequency noise and ac conductance of a Kondo quantum dot out of equilibrium," *Phys. Rev. B*, vol. 87, p. 245115, Jun 2013.

[181] C. P. Moca, P. Simon, C.-H. Chung, and G. Zaránd, "Finite-frequency-dependent noise of a quantum dot in a magnetic field," *Phys. Rev. B*, vol. 89, p. 155138, Apr 2014.

[182] J. Jin, S. Wang, X. Zheng, and Y. Yan, "Current noise spectra and mechanisms with dissipaton equation of motion theory," *J. Chem. Phys.*, vol. 142, p. 234108, Jun 2015.

[183] S. Droste, J. Splettstoesser, and M. Governale, "Finite-frequency noise in a quantum dot with normal and superconducting leads," *Phys. Rev. B*, vol. 91, p. 125401, Mar 2015.

[184] R. Zamoum, M. Lavagna, and A. Crépieux, "Finite-frequency noise in a non-interacting quantum dot," *J. Stat. Mech.*, vol. 2016, p. 054013, May 2016.

[185] P. Stadler, G. Rastelli, and W. Belzig, "Finite frequency current noise in the Holstein model," *Phys. Rev. B*, vol. 97, p. 205408, May 2018.

[186] A. Crépieux, S. Sahoo, T. Q. Duong, R. Zamoum, and M. Lavagna, "Emission noise in an interacting quantum dot: Role of inelastic scattering and asymmetric coupling to the reservoirs," *Phys. Rev. Lett.*, vol. 120, p. 107702, Mar 2018.

[187] H.-K. Zhao and Q. Chen, "Noise spectrum of charge current in a quantum dot system under the irradiation of quantum electromagnetic field," *Phys. Lett. A*, vol. 377, pp. 3235–3241, Dec 2013.

[188] A. Marguerite, B. Roussel, R. Bisognin, C. Cabart, M. Kumar, J. M. Berroir, E. Bocquillon, B. Plaçais, A. Cavanna, U. Gennser, Y. Jin, P. Degiovanni, and G. Fève, "Extracting single electron wavefunctions from a quantum electrical current," *arXiv 1710.11181 (preprint)*, Oct 2017.

[189] H. B. Callen and T. A. Welton, "Irreversibility and generalized noise," *Phys. Rev.*, vol. 83, pp. 34–40, Jul 1951.

[190] A. Thielmann, M. H. Hettler, J. König, and G. Schön, "Shot noise in tunneling transport through molecules and quantum dots," *Phys. Rev. B*, vol. 68, p. 115105, Sep 2003.

[191] O. Kashuba, H. Schoeller, and J. Splettstoesser, "Nonlinear adiabatic response of interacting quantum dots," *Eur. Phys. Lett.*, vol. 98, p. 57003, Jun 2012.

[192] R.-P. Riwar, B. Roche, X. Jehl, and J. Splettstoesser, "Readout of relaxation rates by nonadiabatic pumping spectroscopy," *Phys. Rev. B*, vol. 93, p. 235401, Jun 2016.

[193] M. Moskalets, P. Samuelsson, and M. Büttiker, "Quantized Dynamics of a Coherent Capacitor," *Phys. Rev. Lett.*, vol. 100, p. 086601, Feb 2008.

[194] J. H. Shirley, "Solution of the Schrödinger Equation with a Hamiltonian Periodic in Time," *Phys. Rev.*, vol. 138, pp. B979–B987, May 1965.

[195] F. Reckermann, J. Splettstoesser, and M. R. Wegewijs, "Interaction-Induced Adiabatic Nonlinear Transport," *Phys. Rev. Lett.*, vol. 104, p. 226803, Jun 2010.

[196] A. Beckel, A. Kurzmann, M. Geller, A. Ludwig, A. D. Wieck, J. König, and A. Lorke, "Asymmetry of charge relaxation times in quantum dots: The influence of degeneracy," *Eur. Phys. Lett.*, vol. 106, no. 4, p. 47002, 2014.

[197] S. Alexander and P. W. Anderson, "Interaction between localized states in metals," *Phys. Rev.*, vol. 133, pp. A1594–A1603, Mar 1964.

[198] S. Kurth, G. Stefanucci, C.-O. Almbladh, A. Rubio, and E. K. U. Gross, "Time-dependent quantum transport: A practical scheme using density functional theory," *Phys. Rev. B*, vol. 72, p. 035308, Jul 2005.

[199] G. Stefanucci and C.-O. Almbladh, "Time-dependent quantum transport: An exact formulation based on TDDFT," *Eur. Phys. Lett.*, vol. 67, no. 1, p. 14, 2004.

[200] G. Stefanucci, S. Kurth, A. Rubio, and E. K. U. Gross, "Time-dependent approach to electron pumping in open quantum systems," *Phys. Rev. B*, vol. 77, p. 075339, Feb 2008.

[201] R.-P. Riwar, B. Roche, X. Jehl, and J. Splettstoesser, "Readout of relaxation rates by nonadiabatic pumping spectroscopy," *Phys. Rev. B*, vol. 93, p. 235401, Jun 2016.

[202] J. Schulenborg, R. B. Saptsov, F. Haupt, J. Splettstoesser, and M. R. Wegewijs, "Fermion-parity duality and energy relaxation in interacting open systems," *Phys. Rev. B*, vol. 93, p. 081411, Feb 2016.

[203] D. Kennes, "private communication." 2018.

[204] N. Dittmann, N. Helbig, and D. M. Kennes, "Dynamics of the anderson impurity model: benchmarking a non-adiabatic exchange-correlation potential in time-dependent density functional theory," *arXiv 1810.00183 (preprint)*, Oct 2018.

[205] M. Cini, "Time-dependent approach to electron transport through junctions: General theory and simple applications," *Phys. Rev. B*, vol. 22, pp. 5887–5899, Dec 1980.

[206] G. Stefanucci and C.-O. Almbladh, "Time-dependent quantum transport: an exact formulation based on TDDFT," *Eur. Phys. Lett.*, vol. 67, p. 14, Jul 2004.

[207] C. Bruder and H. Schoeller, "Charging effects in ultrasmall quantum dots in the presence of time-varing fields," *Phys. Rev. Lett.*, vol. 72, pp. 1076–1079, Feb 1994.